Fall 2019

Self-Assembly and Emergent Properties of Urea Tethered Triphenylamines for the Formation of Regenerable Radicals

Ammon J. Sindt

Self-Assembly and Emergent Properties of Urea Tethered Triphenylamines for the Formation of Regenerable Radicals

by

Ammon J. Sindt

Bachelor of Science
Missouri Western State University, 2015

Submitted in Partial Fulfillment of the Requirements

For the Degree of Doctor of Philosophy in

Chemistry

College of Arts and Sciences

University of South Carolina

2019

Accepted by:

Linda S. Shimizu, Major Professor

Aaron K. Vannucci, Chair, Examining Committee

Dmitry V. Peryshkov, Committee Member

Christopher T. Williams, Committee Member

Cheryl L. Addy, Vice Provost and Dean of the Graduate School

DEDICATION

This work is dedicated to my mom, Alicia Negaard, my late dad, Lauri Sindt, my stepdad, James Negaard, my two older brothers, Andrew and Aaron Sindt, and little sister, Amy Sindt, for their continual support and encouragement.

ACKNOWLEDGEMENTS

I would not have reached this point without the support of others. First and foremost, I would like to thank God for his continual mercies and blessings throughout my education.

I would also like to thank my advisor, Dr. Shimizu, for mentoring me throughout my time as a graduate student. She encouraged me to be a better scientist every day and helped me realize my potential. I am very grateful to have an advisor as kind she is.

Next, I would like thank the University of South Carolina (SPARC Graduate Research Grant) and the NSF (CHE-1608874, CHE-1305136, CHE-1904386, and OIA-1655740) for their financial support.

I must also express my sincere gratitude to all of my labmates that assisted me along the way. Sahan and Bozumeh guided in my first steps as a chemist. Baillie attempted to keep me in line. Dustin and I did almost everything together. Muhammad and Faizul are some of the most uplifting people I know. Julia Ladson, Gyubin Shin, Julia Raffetto, David McEachern Jr., Paul Wesarg, and Johannes Hartel each made the lab much more entertaining and allowed me to accomplish more.

Lastly, I would like to thank my collaborators. Their advice and insight on the various projects I worked on were invaluable and helped me immensely throughout my graduate career. I would like to especially thank Dr. Smith for solving so many of my "small needle-like crystals" as this data was absolutely vital to my graduate work.

ABSTRACT

Self-assembly of photoactive compounds in the solid-state can give rise to new photophysical properties. Key to these properties, is how these compounds can be organized in a uniform way. For this, hydrogen bonding building blocks can be used to guide the assembly of these compounds into organized structures. For instance, ureas, thioureas, and squaramides which contain both hydrogen bond donors and acceptors can guide the assembly of small *m*-xylene macrocycles in three distinct manners: 1-D columns, edge-to-face Herringbone patterns, and interdigitated networks. The former of these is commonly employed in our group to make either linear or macrocyclic dimers to study the effects self-assembly has on the stability of photogenerated radicals. For example, UV-irradiation of urea assembled triphenylamine linear dimers results in the formation of persistent radicals, whereas in solution any generated radicals are unstable and quickly terminate. In this case, approximately 1 in 150 molecules generate a radical upon UV-irradiation with a half-life of one week. Most intriguingly, re-exposure to UV-irradiation can restore the radical concentration to its original amount without damaging the bulk material. For the macrocyclic case, the 1-D columns that are formed from self-assembly are permeable to small guests which can be loaded into the framework in a single-crystal-to-single-crystal fashion. When loaded, the guest molecules play a major role in how much radical is formed upon UV-irradiation, and still display radical regenerative properties similar to the linear dimer case. Overall, this work will highlight how supramolecular assembly controls the resulting photophysical properties of a material.

TABLE OF CONTENTS

LIST OF TABLES

LIST OF SCHEMES

LIST OF EQUATIONS

LIST OF FIGURES

CHAPTER 1

INTRODUCTION

1.0 ABSTRACT

Self-assembly and self-organization of small molecules into hierarchal materials is a convenient method for designing materials with functional properties. These properties range from forming porous materials with one-dimensional channels that can facilitate the binding and reaction of small guests to stabilizing photogenerated radicals. This chapter aims to introduce these properties, highlight their importance, and understand how molecular structure leads to material function.

1.1 INTRODUCTION INTO SUPRAMOLECULAR ASSEMBLY

Self-assembly describes the spontaneous formation of supramolecular structures from discrete building blocks under thermodynamic equilibrium.[1] This provides a route for forming functional materials with synergistic properties.[2] These properties include proton conductivity,[3] CO_2 capture,[4] solid-state dichromism[5] and many others. Typically, functional materials are formed with directing groups that help guide assembly in the solid-state. This guidance can be the result of many different types of strong and weak interactions that work in tandem to stabilize a particular structure. Some examples of these interactions are as halogen,[6] covalent,[7] and coordination bonds[8] among numerous others.

Hydrogen bonds, which is a type of guiding interaction, are a class of intermediate intermolecular interactions between an electron-deficient hydrogen and a region of high electron density (usually an electron pair).[9] These bonds are important because of their reversible and directional nature.[10] The interaction between a hydrogen bond donor and a hydrogen bond acceptor tends to be linear (180°), which minimizes the repulsions between the heavy atoms.[11] The hydrogen bond is also relatively weak, ranging from 0 kcal mol^{-1} in a competitive solvent such as water to up to 5-40 kcal mol^{-1} in non-polar solvents or in

the gas phase. The reversibility of these weak interactions enables thermodynamically unfavorable structures to be disassembled and helps to drive the dynamic assembly process to a thermodynamically favorable structure. The directionality and reversibility of hydrogen bonds helps build predictable assemblies.[12]

Some organic functional groups can hydrogen bond with themselves to direct supramolecular assembly. For instance, urea, thiourea, and squaramide functional groups each contain strong hydrogen bond donors (amide protons) and strong hydrogen bond acceptors (carbonyls and thiocarbonyls). Thus, each of these groups can direct the assembly of small molecules. However, these assemblies are different due to the size or hydrogen bonding nature of the directing group.[13,14] As seen in Figure 1.1, when comparing similar dibenzyl substituted ureas, squaramides, and thioureas, different structures are found for each case. The urea[15] and squaramide[16] are quite similar initially with both forming hydrogen bonded tapes. However, due to the squaramide's size it increases the molecular repeat distance along the hydrogen bonded tape from 4.62 to 6.03 Å versus the urea causing the benzyl groups to be further apart. The thiourea[17] directs quite differently from these structures as it prefers dimer formation instead of hydrogen bonded tape formation. Thus, these three-hydrogen bond driven directing groups lead to different supramolecular assemblies. In addition to these groups, other organic functional groups can also direct hydrogen bonded assemblies such as oxalylamides[18] and carboxylic acids.[19] Overall, hydrogen bonds can be used in concert with many other intermolecular interactions to direct crystal growth, build complex networks, and form functional materials.

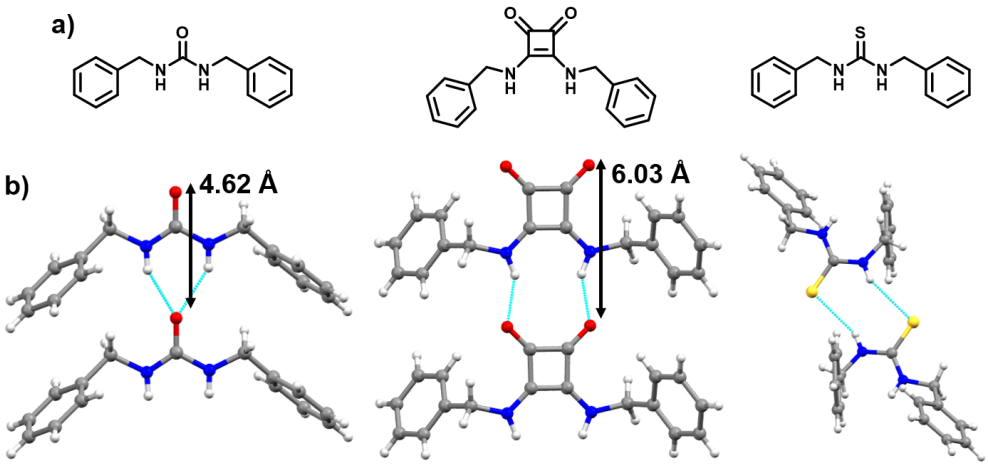

Figure 1.1. Different types of hydrogen-bonding shown from different types of organic functional groups with two benzyl substituents. (A) Molecular structures of compounds. From left to right the hydrogen bonding groups are urea,[15] squaramide,[16] and thiourea.[17] (B) Hydrogen bonding for each structure. For the taped structure (urea and squaramide) the molecular repeat distance is given.

Porous materials are one type of functional supramolecular structure. Porous molecular frameworks have inner cavities that may or may not contain guests. Examples of these materials include zeolites,[20] metal organic frameworks,[21] hydrogen bonded organic frameworks,[22] covalent organic frameworks,[23] and porous organic materials (POMs).[24] These materials find uses in catalysis,[25] molecular confinement,[26] storage,[27] sensing,[28] and separations.[29] The discrete nano-environments contribute to the unique functional properties. The porosity in these systems can be variable with some structures exhibiting vast 3D networks while other structures exhibit simple 1D porosity (i.e. channels). The latter has received considerable attention in recent years due to the simplicity of 1D channels, which facilitates computational modeling of these systems. The homogeneous 1D structures have been employed for fundamental studies of host-guest interactions,[30] catalysis,[31] and diffusion.[32] For example, the 1D channels formed from carbon nanotubes[33]

and POMs organized by *bis*-urea macrocycles[34] have been used to probe normal Fickian versus single file diffusion on a molecular scale.

One reliable way to form 1D porous materials is to construct a POM by the self-assembly of small organic building units. POMs have great flexibility since a vast number of simple organic molecules are commercial or are readily synthesized, which allows for a vast range of structures to be constructed. Some of the earliest examples of 1D channels using POMs are seen with cyclic peptides. One example of these, *cyclo*[(Gln-D-Ala-Glu-D-Ala)$_3$], self-assembles upon the slow acidification of an alkaline solution to form small, columnar nanotubes with an internal diameter of 13 Å.[35] These tubes are held together with β-sheet formations between closely spaced macrocycles with a repeat distance of 4.8 Å between macrocycles. Similarly, the Seebach group found that all three stereoisomers of the cyclic tetramer of 3-aminobutanoic acid could form small nanotubes (Figure 1.2).[36] Although the crystals were too small for SC-XRD, crystals diffracted well with PXRD to allow for their structural determination. In this case, each macrocycle was organized through four non-linear C=O···H-N hydrogen bonds resulting in tubular packing.

Later examples of 1D channels being formed from organic materials can be seen for pillar[6]arene, cucurbit[6]uril, and cyclobenzoin ester. For the first of these, pillar[6]arene, both it and its [5] analog form nanotubes with intrinsic 1D channels upon the slow evaporation of ethyl benzene.[37] However, for the [6] derivative it can either be activated and loaded with styrene or suspended in styrene vapors to lose its original 1D channel forming a new framework with encapsulated styrene. In fact, this is favorable enough that it can selectively remove styrene from 1:1 ethyl benzene/styrene mixtures. For cucurbit[6]uril, it organizes into honeycomb-like structures with 1D channels organized

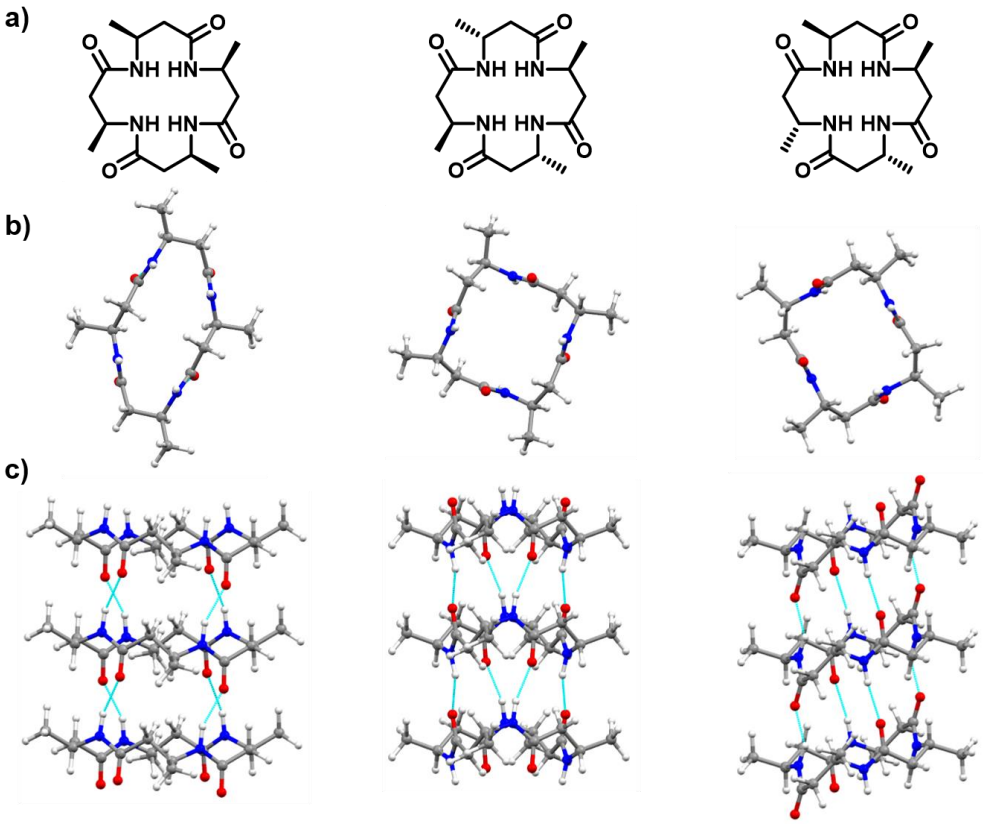

Figure 1.2. Nanotubes made from the three different cyclic tetramers of 3-aminobutanic acid.[36] (a) Molecular structures of the cyclic peptides. (b) View down the channels. (c) View of hydrogen bonding holding tubes together.

within 6 cucurbit[6]uril units (Figure 1.3).[38] These channels are ~6 Å in diameter are held together with C-H···O hydrogen bonding resulting in a distorted square planar geometry. This results in robust nanotubes that can be activated under vacuum and later loaded with acetylene without harming the crystalline framework. Lastly, for cyclobenzoin ester, several different derivatives can be crystallized in 1D porous materials.[39] This is quite surprising as there are no strong covalent or non-covalent bonds holding the structures together. Nevertheless, crystals are still quite robust with methyl substituted derivatives shown in Figure 1.3 displaying porosity after activation (or desolvation).

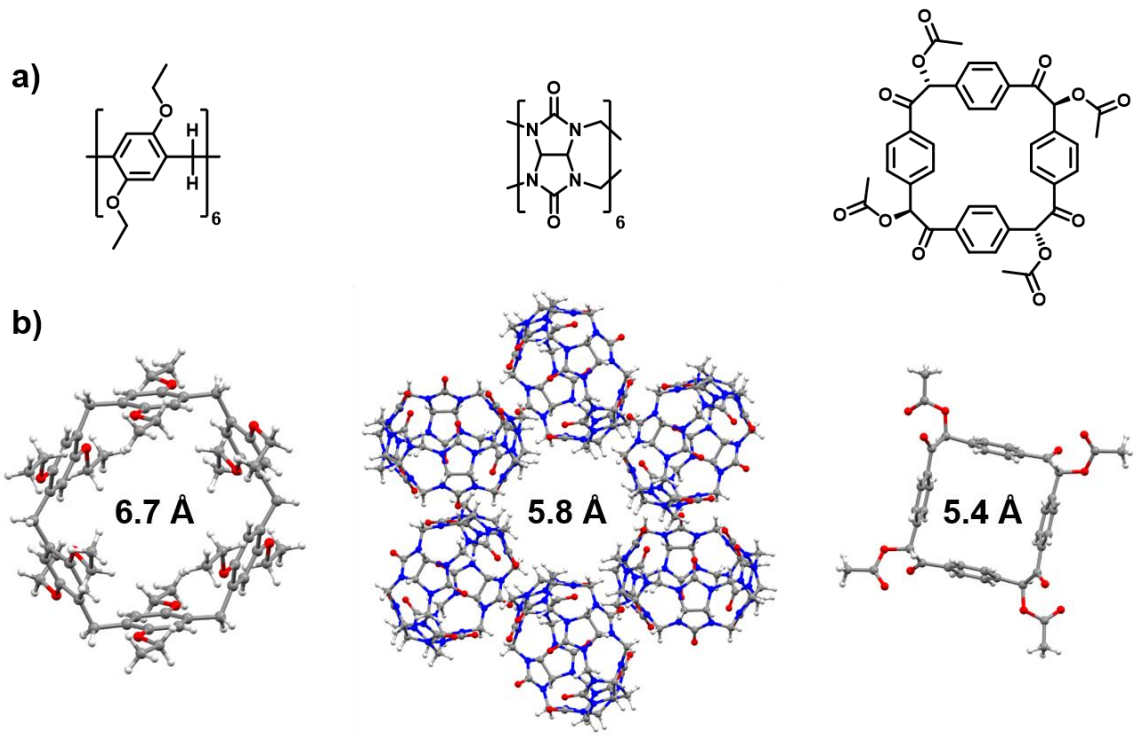

Figure 1.3. Nanotubes made from the three different types or organic molecules.[37-39] (a) Molecular structures of compounds. (b) View down the pores for each structure showing the approximate size of each pore. For the cyclobenzoin ester (far right), only the square pore is shown.

Sometimes it is advantageous to see how different guests, or a lack of guests affect a host framework in a host-guest complex. One way to view this is through single-crystal-to-single-crystal (SC-SC) transformations. During this process a crystal undergoes a change from one crystal structure to another without losing its crystallinity. For example, the cyclic peptide shown in Figure 1.4, organizes into 1D columns with chloroform guests contained within its architecture.[40] Chloroform can be removed by heating the crystals at 165 °C activating the host and causing the crystal structure to change. The host can then be exposed to chloroform vapors reforming the original crystal structure and causing the 1D columns to reform. Another example of SC-SC transformations in a 1D channel is seen for a 'sugar sponge', made by the Fujita group.[41] This sponge which is made of a dimannose

para substituted benzene ligand coordinated to sodium atoms can exchange guests in a SC-SC manner. The original guest, diethyl ether, inside the 1D channels of the sponge can be exchanged for a number of new guests including *n*-propyl alcohol. This is done by soaking the sponge in a 1:1 mixture of *n*-propyl alcohol and diisopropyl ether at 50 °C resulting in the new host-guest complex. Similarly, the Jung group also made a framework with *tris*(isonicotinoyloxyl-methyl)benzene coordinated to Ag^{+} with PF_6^{-} as the counter anion.[42] This framework resulted in 1D pores, 4.4 Å in diameter, that could exchange an upwards of 41 guests at varying temperature via SC-SC transformations.

The Shimizu group also assembles 1D porous materials that can undergo SC-SC transformations. Our group synthesizes *bis*-urea macrocycles from two ureas and two C-shaped spacers to afford building blocks that assemble into columnar motifs with intrinsic

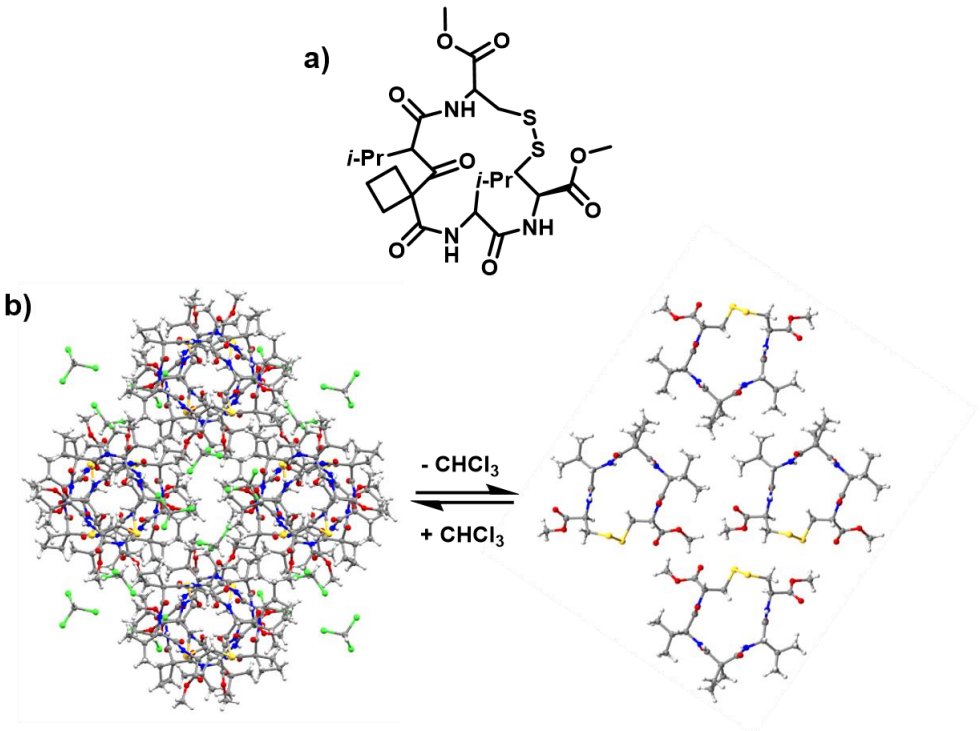

Figure 1.4. SC-SC shown for a cyclic peptide in the solid-state.[40] (a) Molecular structure of cyclic peptide. (b) SC-SC transformation for peptide upon the removal or the addition of chloroform.

porosity.[43] These macrocycles are depicted in Figure 1.5. The urea units are organized perpendicular to the plane of the macrocycles and hydrogen bond with each other through the characteristic three-centered urea hydrogen bond resulting in the tubular structure. Each macrocycle is spaced ~ 4.7 Å away from each other inside the tubes due to the urea repeat distance which is also ~ 4.7 Å. This results in nanotubes which are typically organized into hexagonal arrays and appear as needle-like crystals. The C-shape spacers, which are the other unit of the macrocycles, control the size and functionality of the channel. The sizes range from 1.0 × 1.4 Å for the smallest spacer, *m*-xylene, to 8.4 × 13.0 Å for the largest spacer, *m*-di(phenylethynyl)benzene (PHY).[44] Functionality ranges from binding metals as is the case for the 2,2'-bipyridyl spacer, to sensitizing molecular oxygen upon UV-exposure in the benzophenone (BP) spacers in air.[43] It should be noted that not every *bis*-urea macrocycle forms the same structure. An example is the 3,5-dimethylpyridine spacer.[45] In this case the pyridines of the spacer can hydrogen bond with ureas forming 1D columns where the spacer is part of the hydrogen bonding network.

Thus far, the main application of these macrocycle has been for the use as small nanochambers for selective photoreactions of small molecules.[43] Typically, in solution small photoreactive guests can react a number of ways due to free rotation giving rise to a large number of possible products. However, reactants encapsulated within small nanochambers have more limited modes of geometric and vibrational freedom which results in altered reactivity. Thus, two reactants may be forced along a different reaction pathway than in free solution. To prepare the assembled macrocycles for use as nanoreactors, macrocycles are first activated with a moderate amount of heat to remove the

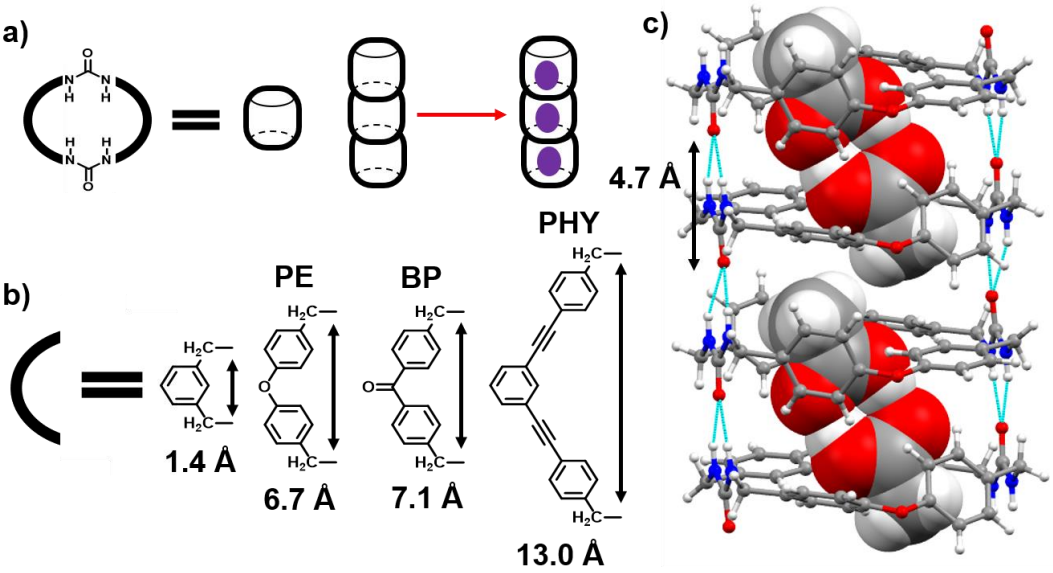

Figure 1.5. Overview of *bis*-urea macrocycles.[43] (a) Macrocycles are made from two ureas and two C-shape spacers, which self-assemble into straws (or channels) which can uptake small guests. (b) Examples of C-shape spacers, approximate aperture size of columns given underneath. (c) An example of a *bis*-urea macrocycle column made from a PE spacer. Acetic acid guests inside the columns are shown as space-filled models. Repeat distance of macrocycles is given as well.[46]

guest from the channels. The initial guest, DMSO for the PHY and BP hosts or acetic acid for the phenyl ether (PE) host, is present from the initial crystallization conditions and must be removed before a new guest can be added. After the initial guest is removed, a new guest can be added either by exposing the activated crystals to vapors of a new guest, a solution of the guest as a neat liquid, or as a guest solution in a solvent that is non-competitive with loading. Once the new inclusion complex has been obtained, exposure to UV-light of an appropriately selected wavelength can cause photoreactive guests to react. The photoproducts can then be extracted from the host material using an acceptable solvent.

Three *bis*-urea macrocycles have been applied as nanoreactors, namely the PE, PHY, and BP hosts. The PE host has been used to control the reactivity of α, β-unsaturated

ketones[47,48] while the PHY host has been used to control the selectivity of photodimerizations of coumarins[49] and chromones.[50] The BP host, which is a photosensitizer that can form singlet oxygen, has been used for the selective oxidation of 2-methyl-2-butene[51] and 1-methyl-1-cyclohexene.[52] While it is assumed that the processes of guest loading, guest reaction, and product extraction all follow SC-SC processes due to the excellent PXRD data of the crystals, prior to this work, no single crystal data had been obtained of host-guest complexes with photoactive guests. The first examples of SC-SC loading in *bis*-urea crystals are presented in Chapters 4 and 5.

1.2 INTRODUCTION INTO PHOTOGENERATED RADICALS

Subvalent compounds are a class of compounds which have less bonds than expected based on valent structure considerations.[53] Free radicals are an example of such compounds. Due to their free valent nature, they are often highly reactivity. Many common radical reactions such as hydrogen abstraction and dimerization are thermodynamically favorable. Nonetheless, some radical compounds exhibit high stability. Organic radicals (including those in the organomain group) have uses in spin labeling,[54] spin trapping,[55] EPR[56] and MRI imaging,[57] magnetic[58] and conductive materials,[59] and catalysis.[60] These applications arise from the unique chemistry that radicals provide due to their unpaired electron. These stable radical compounds can be broadly separated into two groups. Stable radicals, which can be isolated and handled as pure compounds, or persistent radicals, which are sufficiently long-lived to be observed with conventional spectroscopic techniques but cannot be isolated as a pure compound.[61]

Three general organic frameworks are responsible for a large portion of organic radicals. These are hydrocarbon-based radicals, nitrogen/oxygen-based radicals, and

thiazyl-based frameworks.[53] Many of these systems exhibit resonance which enables delocalization of the radical center on multiple atoms through π systems. This lowers the reactivity of individual atoms involved with the radical site thus increasing the overall stability of the molecule. An example of one of these compounds is the triphenylmethyl radical, which was first proposed in 1900.[62] This persistent hydrocarbon-based radical is formed upon reacting triphenylmethyl chloride with silver. It can only be observed in solution in equilibrium with its dimeric species (Figure 1.6a) and cannot be isolated as a pure compound. The dimer consists of a relatively weak bond (~11 kcal/mol) between the σ bond between the central methyl carbon of one radical and a *para* carbon of another.[63] The *para* carbon is involved as some radical spin density is delocalized onto the *ortho* and *para* carbons of the molecule. This as evidenced with electron paramagnetic resonance (EPR) and electron nuclear double resonance (ENDOR) spectroscopies.[64,65] Overall, the radical is stabilized through a combination of π-delocalization and sterics (phenyl rings surrounding the central methyl center) giving it its unusual stability.

Nitrogen/oxygen-based radicals and thiazyl-based also see use as organic radicals. For the former, (2,2,6,6-tetramethylpiperidin-1-yl)oxy (TEMPO) is an example of a stable radical that sees usage a commercial spin-trapping agent.[66] In this molecule, the cyclic

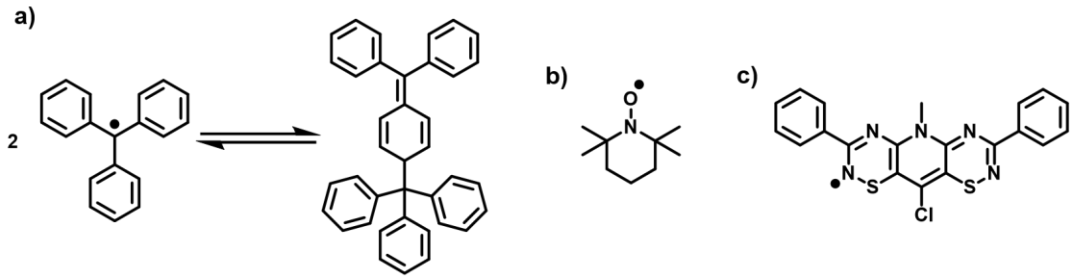

Figure 1.6. Examples of organic radicals. (a) Persistent triphenylmethyl radical exists in equilibrium with its dimeric species in solution.[63] (b) TEMPO is a stable nitrogen/oxygen-based radical. (c) An example of a stable thiazyl-based radical.[68]

nitroxide has fully methyl substituted α positions relative to the nitroxyl group (Figure 1.6b). This helps prevent radical-radical dismutation reactions among other degradation pathways.[67] This stability allows it to be unreactive enough that it can be isolated as pure compound, hence its term as a stable radical. An example of a thiazyl-based radical is shown in Figure 1.6c.[68] This molecule stabilizes its radical through delocalization on the exterior nitrogens and carbon bridges as evidenced through EPR and computational experiments. This results in a moderate amount of stability enabling it to be crystallized as a pure material.

Many strategies to form organic radicals involve strategic synthetic plans and molecular designs to stabilize the radical. Another strategy for radical stability could involve locking the radical in the solid-state for stabilization. This limits the radical's ability to interact with other molecules leading to possible degradation and provides stabilization to the radical species. However, one major issue arises with this method. If the radical is not stable, how does one organize it into the solid-state before it degrades? One possible solution to this issue is to freeze a radical bound material in the solid-state with liquid nitrogen immediately after forming the material. However, this only stabilizes the radical bound compound at cyro temperatures and does not help radical stability under standard conditions. This constraint limits the practical applications of any radical material reliant off using this method. An alternative method includes crystallizing a radical precursor in the solid-state and generating the radical in a solid-to-solid or crystal-to-crystal process. Since the radical would already be in the solid-state it would not need to be frozen with liquid nitrogen as long as the crystalline state is maintained. Potentially, this would afford radicals with more utility.

Previously, our group demonstrated this strategy is viable in the case of self-assembled benzophenones. Indeed, the self-assembled BP host (Figure 1.7) formed stable radical species upon UV-irradiation.[51] The stable diradicals were observed with EPR spectroscopy and were surprisingly long lived under optimal conditions (in the dark under argon). This host could selectively facilitate the oxidation of 2-methyl-2-butene or 1-methyl-1-cyclohexene[52] as described earlier. Due to the radical formation it was suggested that this radical might enhance singlet oxygen formation or help facilitate radical pathways for oxidation process to occur.[51] The radical persisted for weeks and could be employed as a radical polarizing agent for solid-state dynamic nuclear polarization magic angle spinning NMR spectroscopy.[69] The mechanism of radical formation was suggested to occur via excitation to the S_1, followed by intersystem crossing to give a triplet, which abstracts a nearby proton to afford a resonance stabilized radical pair. While this is reasonable, given BP's photophysics, ultrafast spectroscopy studies have yet to be carried out.

To further explore the BP case, two additional BP compounds were also tested to see if they also exhibited photogenerated persistent radicals upon self-assembly similar to the BP macrocycle.[70] These molecules were linear analog (LA) counterparts to the macrocycle, and they only contained one methylene urea tether between the BP moieties. Nevertheless, they still formed robust crystals whose photophysical properties could be measured. It was found the 4,4'-LA which only had aryl protons next to the BP carbonyl produced the most and longest-lived radicals, while the 3,5-LA which had methyl, methylene, and aryl protons next to the BP carbonyl produced lower quantities of shorter-lived radical species. Thus, it is inferred that aryl proton abstraction results in more stable radical formation over the methylene or methyl equivalents. These studies suggest that the

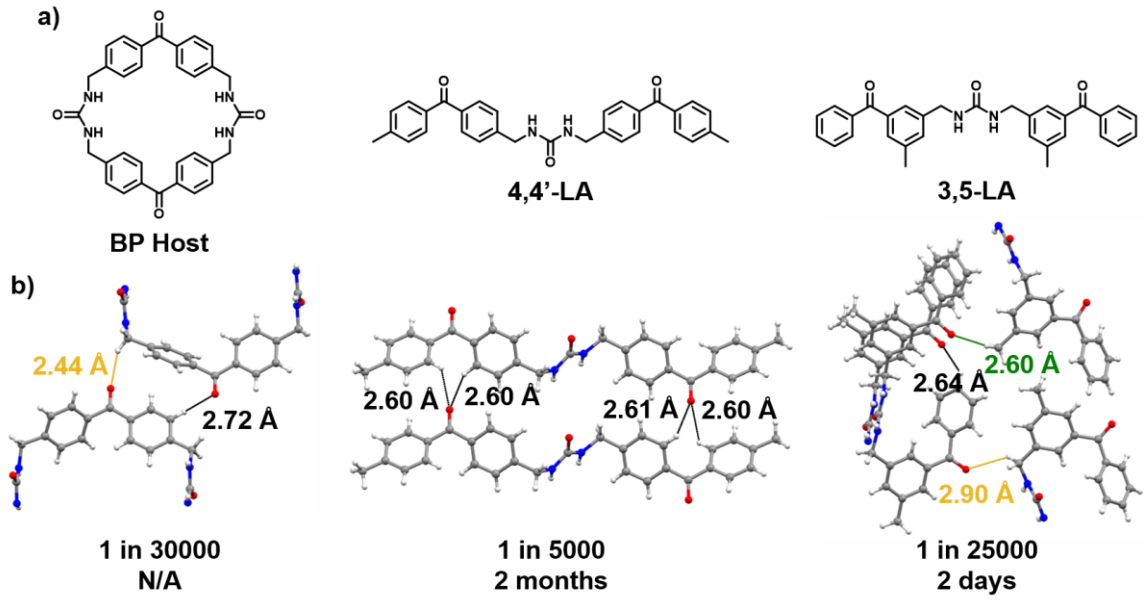

Figure 1.7. Overview photogenerated radical formation in self-assembled BPs.[51,70] (a) BPs of interest. (b) Crystal structures of BP compounds along with the hydrogen distances from the carbonyls with the following code: black (aryl), orange (methylene), and green (methyl). Radical concentrations and half-lives of radicals are given underneath if known.

supramolecular environment played a large role in photogenerated radical formation. It should be noted that in solution no radicals are generated upon UV-irradiation as observed via EPR spectroscopy. This is similar to what is observed for simple benzophenone, as any ketyl radicals formed quickly dimerize or terminate. Overall, these BP compounds provide a proof of concept for the supramolecular strategy of radical stabilization.

Can self-assembly of urea systems provide a general strategy for stabilize other unstable radicals? A potential candidate to organize and test are triphenylamine (TPA) radicals. TPA radicals and their radical cations are employed in battery cathodes,[71] high-spin polymers,[72] and as hole-transport layers in photo-materials.[73] TPAs radical cations are generally only considered stable radicals if all three *para* sites on the TPA moiety have substitution. An example of this is Magic Blue, which is a tribromo TPA hexachloroantimonate salt. This commercial one-electron oxidant has bromine substitution

on all three *para* sites of the TPA cation. TPAs without this substitution have been shown to undergo degradation reactions such as benzidine formation.[74,75] TPA radical cations have been formed under a number of conditions including chemical and electrochemical oxidation.[76] However, others have been formed by photoinduced oxidation.[77]

Using the photoinduced oxidations of TPAs, amide substituted TPAs can be compelled to undergo supramolecular polymerization into nanowires.[77] When in a sufficiently oxidizing solvent such as chloroform, these TPAs can undergo oxidation upon light exposure.[78] When oxidized, the TPAs becomes flattened relative to their nitrogen center from their original propeller shape. They can then interact with other oxidized TPAs through π-stacking interactions through the phenyl rings and/or hydrogen bonding interactions through the amide groups. Once the columnar assembly is started, neutral TPAs can be added to the nanowire since the energy gain of attachment to the nanowire is now greater than the energy loss of flattening the TPA structure. The TPA shown in Figure 1.8a can undergo this process when about 0.1 to 1% of the molecules become oxidized in 1 to 10 mM solutions.

Other TPAs in this family of molecules can also undergo photo-induced self-assembly. When assembled these nanowires adopt primarily two different supramolecular structures namely: the "snowflake" and "Mercedes-Benz" structures.[77] In both of these structures the nitrogens of the TPA core are in collinear alignment (or stacked directly upon each other). However, differences arise in the π-stacking interactions. In the snowflake structure TPAs alternate between D and L chiralities resulting in edge-to face π-stacking between the phenyl rings as seen in Figure 1.8b.[79] The difference between the D and L chiralities is shown in Figure 1.8c. In the Mercedes-Benz structure, similar chirality

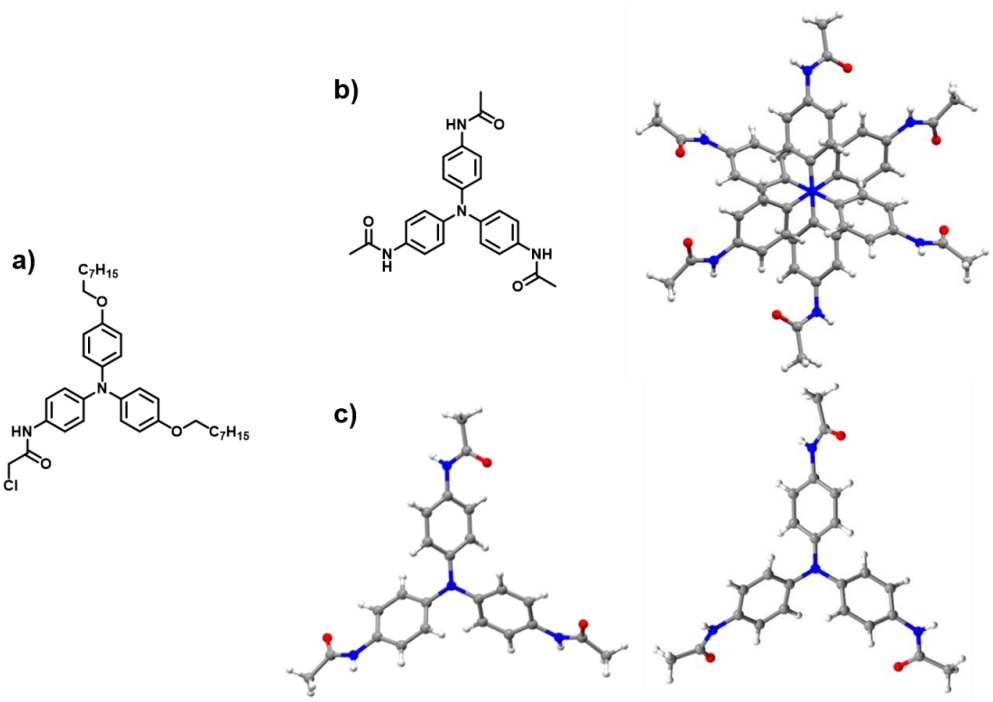

Figure 1.8. (a) Example of a TPA that can undergo photoinduced self-assembly in solution.[78] (b) Example of a TPA showing the snowflake structure.[79] On the left is the molecular structure of the compound while on the right is the structure of the compound in the solid-state. (c) Difference between the D (left structure) and L (right structure) chiralities of the TPA shown in part b.

structures stack directly upon each other forming either M or P helices for any given nanowire.[77] This results in face-to-face π stacking between the phenyl rings of the TPAs. Overall, the assembly of these structures have been found to be quite reliable and have led to their use as conductive nanowires.[80] Considering the similarities between the urea and amide functional groups this suggests that urea-based TPAs may also exhibit similar properties.

1.3 CONCLUSIONS

In summary, self-assembly of small molecules in the solid-state can give rise to emergent functional materials. This functionality ranges from forming nanotubular materials with columnar porosity to stabilizing photogenerated radicals. Nanotubes with

1D porosity can be formed from small organic molecules assembled through hydrogen bonding interactions and can be useful in host-guest chemistries. Photogenerated radicals can be stabilized through induced or pre-organized assembly and can be useful as DNP NMR polarizing agents. The following chapters will discuss these functionalities and properties. First, the assemblies of small *m*-xylene macrocycles containing ureas, thioureas, and squaramides will be synthesized and compared to analyze the differences between each hydrogen bond directing group when interconnected in small macrocycles. In chapter 3, urea tethered assemblies of TPAs will be crystallized and evaluated to see if photogenerated radical formation can be stabilized in pre-organized TPAs. Chapter 4 examines the synthesis and crystallization of *bis*-urea macrocycles containing TPA units. The process of removing the encapsulated solvent and loading a new guest will also be examined. Chapter 5 studies the UV-irradiation of assembled TPA macrocycles and evaluates the quantity and stability of radical generated. The goal of these studies is to understand how supramolecular structure and guest encapsulation modulates radical formation. Lastly, chapter 6 will summarize this work and give suggestions for future work for these materials. Overall, this research aims to examine how supramolecular elements come together and how they affect the functionality of a material.

1.4 REFERENCES

1. Ercolani, G. *J. Phys. Chem. B* **1998**, *102*, 5699-5703.
2. Mahadevi, A. S.; Sastry, G. N. *Chem. Rev.* **2016**, *116*, 2775-2825.
3. Meng, X.; Wang, H.-N.; Song, S.-Y.; Zhang, H.-J. *Chem. Soc. Rev.* **2017**, *46*, 464-480.
4. Samanta, A.; Zhao, A.; Shimizu, G. K. H.; Sarkar, P.; Gupta, R. *Ind. Eng. Chem. Res.* **2012**, *51*, 1438-1463.

5. Liu, M.; Zhang, L.; Wang, T. *Chem. Rev.* **2015**, *115*, 7304-7397.
6. Cavallo, G.; Metrangolo, P.; Milani, R.; Pilati, T.; Priimagi, A.; Resnati, G.; Terraneo, G. *Chem. Rev.* **2016**, *116*, 2478-2601.
7. Wang, H.; Zeng, Z.; Xu, P.; Li, L.; Zeng, G.; Xiao, R.; Tang, Z.; Huang, D.; Tang, L.; Lai, C.; Jiang, D.; Liu, Y.; Yi, H.; Qin, L.; Ye, S.; Ren, X.; Tang, W. *Chem. Soc. Rev.* **2019**, *48*, 488-516.
8. Yuan, S.; Feng, L.; Wang, K.; Pang, J.; Bosch, M.; Lollar, C.; Sun, Y.; Qin, J.; Yang, X.; Zhang, P.; Wang, Q.; Zou, L.; Zhang, Y.; Zhang, L.; Fang, Y.; Li, J.; Zhou, H.-C. *Adv. Mater.* **2018**, *30*, 1704303.
9. Kollman, P. A.; Allen, L. C. *Chem. Rev.* **1972**, *72*, 283-303.
10. Legon, A. C.; Millen, D. J. *Acc. Chem. Res.* **1987**, *20*, 39-46.
11. Steiner, T. *Angew. Chem., Int. Ed.* **2002**, *41*, 48-76.
12. Hisaki, I.; Chen, X.; Takahashi, K.; Nakamura, T. *Angew. Chem., Int. Ed.* **2019**, *58*, 11160-11170.
13. Custelcean, R. *Chem. Commun.* **2008**, 295-307.
14. Marchetti, L. A.; Kumawat, L. K.; Mao, N.; Stephens, J. C.; Elmes, R. B. P. *Chem* **2019**, *5*, 1398-1485.
15. Pulacchini, S.; Abrahams, I.; Eames, J.; Watkinson, M. *Supramol. Chem.* **2002**, *14*, 353-357.
16. Portell, A.; Barbas, R.; Braga, D.; Polito, M.; Puigjaner, C.; Prohens, R. *CrystEngComm* **2009**, *11*, 52-54.
17. Ramnathan, A.; Sivakumar, K.; Subramanian, K.; Meerarani, D.; Ramadas, K.; Fun, H.-K. *Acta Crystallogr. C* **1996**, *52*, 139-142.

18. Coe, S.; Kane, J. J.; Nguyen, T. L.; Toledo, L. M.; Wininger, E.; Fowler, F. W.; Lauher, J. W. *J. Am. Chem. Soc.* **1997**, *119*, 86-93.

19. Gavezzotti, A. *Acta Crystallogr. B* **2008**, *64*, 401-403.

20. Přech, J.; Pizarro, P.; Serrano, D. P.; Čejka, J. *Chem. Soc. Rev.* **2018**, *47*, 8263-8306.

21. Alhamami, M.; Doan, H.; Cheng, C.-H. *Materials* **2014**, *7*, 3198-3250.

22. Lin, R.-B.; He, Y.; Li, P.; Wang, H.; Zhou, W.; Chen, B. *Chem. Soc. Rev.* **2019**, *48*, 1362-1389.

23. Kandambeth, S.; Dey, K.; Banerjee, R. *J. Am. Chem. Soc.* **2019**, *141*, 1807-1822.

24. Das, S.; Heasman, P.; Ben, T.; Qiu, S. *Chem. Rev.* **2017**, *117*, 1515-1563.

25. Dhakshinamoorthy, A.; Alvaro, M.; Garcia, H. *Chem. Commun.* **2012**, *48*, 11275-11288.

26. Tabacchi, G. *ChemPhysChem* **2018**, *19*, 1249-1297.

27. Kitagawa, S.; Kitaura, R.; Noro, S. *Angew. Chem., Int. Ed.* **2004**, *43*, 2334-2375.

28. Wales, D. J.; Grand, J.; Ting, V. P.; Burke, R. D.; Edler, K. J.; Bowen, C. R.; Mintova, S.; Burrows, A. D. *Chem. Soc. Rev.* **2015**, *44*, 4290-4321.

29. Sumida, K.; Rogow, D. L.; Mason, J. A.; McDonald, T. M.; Bloch, E. D.; Herm, Z. R.; Bae, T.-H.; Long, J. R. *Chem. Rev.* **2012**, *112*, 724-781.

30. Song, N.; Kakuta, T.; Yamagishi, T.; Yang, Y.-W.; Ogoshi, T. *Chem* **2018**, *4*, 2029-2053.

31. Ma, L.; Abney, C.; Lin, W. *Chem. Soc. Rev.* **2009**, *38*, 1248-1256.

32. Meersmann, T.; Logan, J. W.; Simonutti, R.; Caldarelli, S.; Comotti, A.; Sozzani, P.; Kaiser, L. G.; Pines, A. *J. Phys. Chem. A* **2000**, *104*, 11665-11670.

33. Chen, Q.; Moore, J. D.; Liu, Y.-C.; Roussel, T. J.; Wang, Q.; Wu, T.; Gubbins, K. E. *J. Chem. Phys.* **2010**, *133*, 094501.

34. Bowers, C. R.; Dvoyashkin, M.; Salpage, S. R.; Akel, C.; Bhase, H.; Geer, M. F.; Shimizu, L. S. *ACS Nano*, **2015**, *9*, 6343-6353.

35. Khazanovich, N.; Granja, J. R.; McRee, D. E.; Miligan, R. A.; Ghadiri, M. R. *J. Am. Chem. Soc.* **1994**, *116*, 6011-6012.

36. Seebach, D.; Matthews, J. L.; Meden, A.; Wessels, T.; Baerlocher, C.; McCusker, L. B. *Helv. Chim. Acta* **1997**, *80*, 173-182.

37. Jie, K.; Liu, M.; Zhou, Y.; Little, M. A.; Bonakala, S.; Chong, S. Y.; Stephenson, A.; Chen, L.; Huang, F.; Cooper, A. I. *J. Am. Chem. Soc.* **2017**, *139*, 2908-2911.

38. Lim, S.; Kim, H.; Selvapalam, N.; Kim, K.-J.; Cho, S. J.; Seo, G.; Kim, K. *Angew. Chem., Int. Ed.* **2008**, *47*, 3352-3355.

39. McHale, C. M.; Stegemoller, C. R.; Hashim, M. I.; Wang, X.; Miljanić, O. Š. *Cryst. Growth Des.* **2019**, *19*, 562-567.

40. Guha, S.; Drew, M. G. B.; Banerjee, A. *CrystEngComm* **2009**, *11*, 756-762.

41. Ning, G.-H.; Matsumura, K.; Inokuma, Y.; Fujita, M. *Chem. Commun.* **2016**, *52*, 7013-7015.

42. Choi, D.; Lee, H.; Lee, J. J.; Jung, O.-S. *Cryst. Growth Des.* **2017**, *17*, 6677-6683.

43. Shimizu, L. S.; Salpage, S. R.; Korous A. A. *Acc. Chem. Res.* **2014**, *47*, 2116-2127.

44. Sindt, A. J.; Smith, M. D.; Berens, S.; Vasenkov, S.; Bowers, C. R.; Shimizu, L. S. *Chem. Commun.* **2019**, *55*, 5619-5622.

45. Roy, K.; Wang, C.; Smith, M. D.; Dewal, M. B.; Wibowo, A. C.; Brown, J. C.; Ma, S.; Shimizu, L. S. *Chem. Commun.* **2011**, *47*, 277-279.

46. Shimizu, L. S.; Hughes, A. D.; Smith, M. D.; Davis, M. J.; Zhang, B. P.; zur Loye, H.-C.; Shimizu, K. D. *J. Am. Chem. Soc.* **2003**, *125*, 14972-14973.

47. Yang, J.; Dewal, M. B.; Shimizu, L. S. *J. Am. Chem. Soc.* **2006**, *128*, 8122-8123.

48. Yang, J.; Dewal, M. B.; Profeta, S.; Smith, M. D.; Li, Y.; Shimizu, L. S. *J. Am. Chem. Soc.* **2008**, *130*, 612-621.

49. Dawn, S.; Salpage, S. R.; Koscher, B. A.; Bick, A.; Wibowo, A. C.; Pellechia, P. J.; Shimizu, L. S. *J. Phys. Chem. A* **2014**, *118*, 10563-10574.

50. Salpage, S. R.; Donevant, L. S.; Smith, M. D.; Bick, A.; Shimizu, L. S. *J. Photochem. Photobiol. A-Chem.* **2016**, *315*, 14-24.

51. Geer, M. F.; Walla, M. D.; Solntsev, K. M.; Strassert, C. A.; Shimizu, L. S. *J. Org. Chem.* **2013**, *78*, 5568-5578.

52. DeHaven, B. A.; Liberatore, H. K.; Greer, A.; Richardson, S. D.; Shimizu, L. S. *ACS Omega*, **2019**, *4*, 8290-8298.

53. Hicks, R. G. *Org. Biomol. Chem.* **2007**, *5*, 1321-1338.

54. Hubbell, W. L.; McConnel, H. M. *Proc. Natl. Acad. Sci. USA* **1968**, *61*, 12-16.

55. Scott, M. J.; Billiar, T. R.; Stoyanovsky, D. A. *Sci. Rep.* **2016**, *6*, 38773.

56. Kuppusamy, P.; Chzhan, M.; Vij, K.; Shteynbuk, M.; Lefer, D. J.; Giannella, E.; Zweier, J. L. *Proc. Natl. Acad. Sci. USA* **1994**, *91*, 3388-3392.

57. Nguyen, H. V.-T.; Chen, Q.; Paletta, J. T.; Harvey, P.; Jiang, Y.; Zhang, H.; Boska, M. D.; Ottaviani, M. F.; Jasanoff, A.; Rajca, A.; Johnson, J. A. *ACS Cent. Sci.* **2017**, *3*, 800-811.

58. Alberola, A.; Less, R. J.; Pask, C. M.; Rawson, J. M.; Palacio, F.; Oliete, P.; Paulsen, C.; Yamaguchi, A.; Farley, R. D.; Murphy, D. M. *Angew. Chem., Int. Ed.* **2003**, *42*, 4782-4785.

59. Mailman, A.; Winter, S. M.; Yu, X.; Robertson, C. M.; Yong, W.; Tse, J. S.; Secco, R. A.; Liu, Z.; Dube, P. A.; Howard, J. A. K.; Oakley, R. T. *J. Am. Chem. Soc.* **2012**, *134*, 9886-9889.

60. Wertz, S.; Studer, A. *Green Chem.* **2013**, *15*, 3116-3134.

61. Griller, D.; Ingold, K. U. *Acc. Chem. Res.* **1976**, *9*, 13-19.

62. Gomberg, M. *J. Am. Chem. Soc.* **1900**, *22*, 757-771.

63. Neumann, W. P.; Uzick, W.; Zarkadis, A. K. *J. Am. Chem. Soc.* **1986**, *108*, 3762-3770.

64. Neumann, W. P.; Penenory, A.; Stewen, U.; Lehnig, M. *J. Am. Chem. Soc.* **1989**, *111*, 5845-5851.

65. Maki, A. H.; Allendoerfer, R. D.; Danner, J. C.; Keys, R. T. *J. Am. Chem. Soc.* **1968**, *90*, 4225-4231.

66. Cooper, D. R.; Dimitrijevic, N. M.; Nadeau, J. L. *Nanoscale* **2010**, *2*, 114-121.

67. Soule, B. P.; Hyodo, F.; Matsumoto, K.; Simone, N. L.; Cook, J. A.; Krishna, M. C.; Mitchell, J. B. *Free Radical Bio. Med.* **2007**, *42*, 1632-1650.

68. Beer, L.; Haddon, R. C.; Itkis, M. E.; Leitch, A. A.; Oakley, R. T.; Reed, R. W.; Richardson, J. F.; VanderVeer, D. G. *Chem. Commun.* **2005**, 1218-1220.

69. DeHaven, B. A.; Tokarski, J. T.; Korous, A. A.; Mentink-Vigier, F.; Makris, T. M.; Brugh, A. M.; Forbes, M. D. E.; van Tol, J.; Bowers, C. R.; Shimizu, L. S. *Chem.-Eur. J.* **2017**, *23*, 8315-8319.

70. DeHavent, B. A.; Goodlett, D. W.; Sindt, A. J.; Noll, N.; De Vetta, M.; Smith, M. D.; Martin, C. R.; González, L.; Shimizu, L. S. *J. Am. Chem. Soc.* **2018**, *140*, 13064-13070.
71. Su, C.; He, H.; Xu, L.; Zhao, K.; Zheng, C.; Zhang, C. *J. Mater. Chem. A* **2017**, *5*, 2701-2709.
72. Skorka, L.; Kurzep, P.; Chauviré, T.; Dubois, L.; Mouesca, J.-M.; Maurel, V.; Kulszewicz-Bajer, I. *J. Phys. Chem. B* **2017**, *121*, 4293-4298.
73. Agrarwala, P.; Kabra, D. *J. Mater. Chem. A* **2017**, *5*, 1348-1373.
74. Ito, A.; Ino, H.; Tanaka, K.; Kanemoto, K.; Kato, T. *J. Org. Chem.* **2002**, *67*, 491-498.
75. Yano, M.; Sato, K.; Shiomi, D.; Ichimura, A.; Abe, K.; Takui, T.; Itoh, K. *Tetrahedron Lett.* **1996**, *37*, 9207-9210.
76. Quinton, C.; Alain-Rizzo, V.; Dumas-Verdes, C.; Miomandre, F.; Clavier, G.; Audebert, P. *RSC Adv.* **2014**, *4*, 34332-34342.
77. Moulin, E.; Armao, J. J.; Giuseppone, N. *Acc. Chem. Res.* **2019**, *52*, 975-983.
78. Nyrkova, I.; Moulin, E.; Armao, J. J.; Maaloum, M.; Heinrick, B.; Rawiso, M.; Niess, F.; Cid, J.-J.; Jouault, N.; Buhler, E.; Semenov, A. N.; Giuseppone, N. *ACS Nano* **2014**, *8*, 10111-10124.
79. Armao, J. J.; Rabu, P.; Moulin, E.; Giuseppone, N. *Nano Lett.* **2016**, *16*, 2800-2805.
80. Faramarzi, V.; Niess, F.; Moulin, E.; Maaloum, M.; Dayan, J.-F.; Beaufrand, J.-B.; Zanettini, S.; Doudin, B.; Giuseppone, N. *Nat. Chem.* **2012**, *4*, 485-490.

CHAPTER 2

THIOUREAS AND SQUARAMIDES: COMPARISON WITH UREAS AS ASSEMBLY DIRECTING MOTIFS FOR M-XYLENE MACROCYCLES*

* Reprinted with permission from **Sindt, A. J.**; Smith, M. D.; Pellechia, P. J.; Shimizu, L. S. *Cryst. Growth Des.* **2018**, *18*, 1605-1612.

2.0 ABSTRACT

Intentional design of crystalline frameworks requires a good understanding of how inter- and intramolecular forces act together to afford solid-state structures. Herein, we synthesize and crystallize *bis*-thiourea and *bis*-squaramide *m*-xylene macrocycles and compare the conformational preferences of these functional groups as well as their assembled structures to their *bis*-urea counterpart. Four new crystal structures of the *bis*-thiourea macrocycle and the *bis*-squaramide macrocycle are reported. The *m*-xylene macrocycles of urea, thiourea, and squaramide each display *trans–trans* conformers in their pure crystal forms. The thiourea macrocycles show edge to face interactions driven by sulfur bonding to afford 2D sheets. This macrocycle also shows an ethylene diamine solvate that displays both *trans–trans* and *cis–trans* conformers in the same structure. Solution 2D EXSY NMR studies suggest that these and additional conformations interconvert at room temperature. Squaramide macrocycles display 2D hydrogen bonding networks forming interdigitated cycles using only one of the two available carbonyls for hydrogen bonding. Additionally, the *bis*-squaramide macrocycle can crystallize as a solvate, where it maintains its original 2D framework with propylene carbonate imbedded in-between its layers. Overall, these findings help build a foundation for predicting how assembly motifs are modulated by macrocyclic building units.

2.1 INTRODUCTION

Deliberate design of solid-state assemblies requires knowledge of how supramolecular elements come together to form crystalline frameworks. Within this context, supramolecular assembly through hydrogen bonding has proven to be quite useful in designing purposeful hydrogen bonding materials.[1–3] Urea, thiourea, and squaramide functional groups contain hydrogen bond donors and acceptors that can be used to direct

supramolecular assembly.[4,5] In particular, substituted ureas have been used extensively as a molecular building block due to their propensity to adopt a single *trans*−*trans* conformation and assemble into tapes and chains via the three centered urea−urea assembly motif.[6,7] For example, robust urea−urea hydrogen bonding interactions organize phenylethynylene bis-urea macrocycles into porous columnar structures in the solid-state. These nanochannels facilitate selective photoreactions of encapsulated chromones, coumarins, and acenapthalene.[8] In comparison to urea, thiourea and squaramide are employed less frequently. Thioureas form strong, directional frameworks but show a greater conformational flexibility. As seen in Figure 2.1b, thioureas can exist as three stable conformers: *trans*−*trans*, *cis*−*trans*, and *cis*−*cis* with the first two being the most prevalent. Typically, these conformers form zigzagged chains and dimers in the solid-state, respectively (Figure 2.1c).[4] The *cis*−*cis* conformer is rare and is observed when a benzene "locks" the thiourea into place resulting in tapes, which can be thought of as extended dimers.[9] Squaramides are usually found in head-to-tail chains as *trans*−*trans* conformers.[10] Their preference for the *trans*−*trans* conformer is attributed to cooperative induction effects as each addition of a squaramide in the chain reinforces the hydrogen bonding interaction of the following squaramide due to increased electronic polarization.[11] Although, the *trans*−*trans* conformer is the most common, the *cis*−*cis* conformer can be enforced through a ring locking strategy, similar to what was employed for thioureas.[11]

The attached organic substituents on these assembly motifs also influence the assemblies of these groups in the solid-state. For thioureas, bulky substituents selectively destabilize some conformers and direct which conformer is present in the solid-state. For

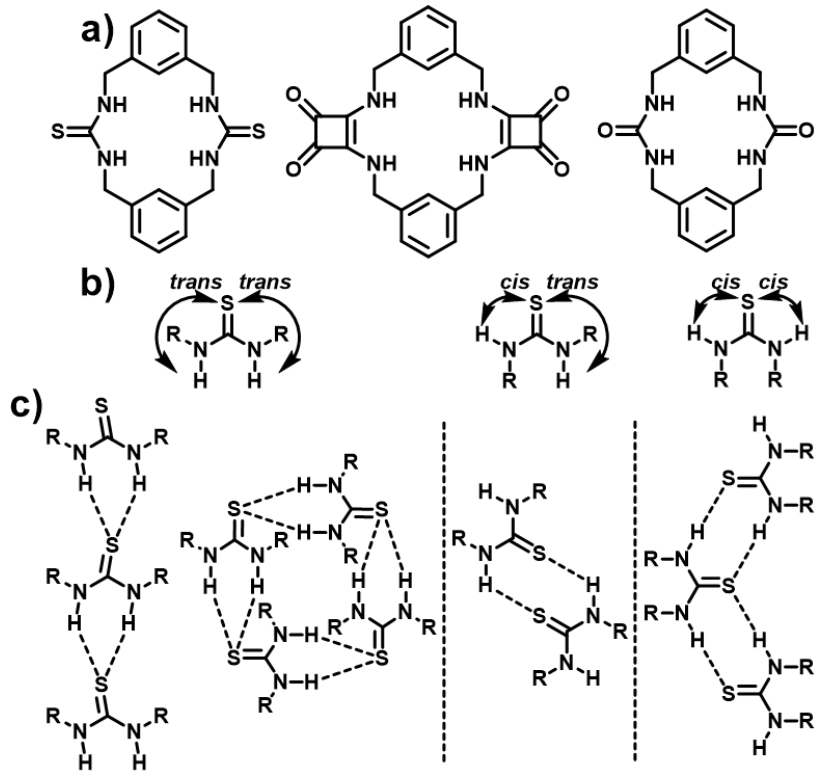

Figure 2.1. *m*-Xylene macrocycles incorporating different directing functional groups including thiourea, squaramide, and urea. (b) Thioureas (and other functional groups) can adopt three distinct conformers. (c) Typical hydrogen bonding seen for each of the thiourea conformers.

instance, bulky R groups encourage the chain motif (with *trans*−*trans* conformers) over dimer formation (*cis*−*trans* conformers) as the *trans* hydrogen in the *cis*−*trans* conformer is too congested to hydrogen bond, lowering the dimer favorability in which only the *cis* hydrogen can participate in hydrogen bonding.[12] Conformers can also be "frozen" into the solid-state through intermolecular interactions. For example, if an *ortho*-pyridine is present, it can force the thiourea into a cis−trans conformation resulting in the dimer structure.[13] A similar effect is seen for squaramide assemblies using N-carbamoyl instead of an ortho-pyridine,[14] as squaramides still adopt the chain motif even with the ortho-pyridine.[15] The π-stacking of the squaramide cyclobutene ring or carbonyls favors antiparallel structures.[16,17]

Herein, we examine the substituent effect exerted upon constraint of the thiourea and squaramide functional groups within a *m*-xylene macrocycle and evaluate their subsequent assembly patterns through a screen of crystallization conditions. While macrocyclization of thioureas and squaramides can limit conformational flexibility, *bis*-thiourea macrocycles made by α,α′-trehalose exhibited conformational flexibility of the thiourea unit in solution at room temperature.[18] Two *m*-xylene linkers combined with either two urea, thiourea or squaramide functional groups generates the small macrocycles in Figure 2.1a. Our prior work with the *bis*-urea macrocycle indicated that there was little flexibility in this system, which assembled in high fidelity into columns from acetic acid.[19] Here, we examine the corresponding thiourea and squaramide macrocycles to determine: 1) organization of the functional groups within a single macrocycle, 2) if these building blocks exhibit greater conformational flexibility than the corresponding ureas and 3) if they afford multiple crystal forms. The latter was accomplished by synthesizing the compounds in gram quantities and screening multiple crystallization conditions. Then, we compared their solid-state structures to the urea macrocycle and also other analogous compounds to probe the effects of macrocyclization on the crystalline assemblies of squaramides and thioureas.

2.2 MATERIALS AND METHODS

General. Chloroform and *m*-xylylenediamine were purchased from Sigma-Aldrich and used without further purification. Di(1*H*-imidazol1-yl)methanethione and 3,4-diethoxy-3-cyclobutene-1,2-dione were purchased from OxChem and Alfa Aesar, respectively. *bis*-Squaramide macrocycles were made according to previous procedures.[20,21] Column chromatography was carried out using silica gel (60 Å, 40−63 μm, Sorbtech). NMR spectra were recorded on a Bruker AVANCE III-HD 300 or 400 MHz

spectrometer at ambient temperature. Two-dimensional exchange spectroscopy (EXSY) were recorded with a mixing time of 0.8 s at 298 K on a 400 MHz Bruker AVANCE III-HD spectrometer.

***bis*-Thiourea *m*-Xylene Macrocycle 1**. Solutions of *m*-xylylenediamine (0.2 g, 1.46 mmol) in chloroform (200 mL) and 1,1′-thiocarbonyldiimidazol (0.2619 g, 1.46 mmol) in chloroform (200 mL) were added dropwise, simultaneously to 100 mL of chloroform at 60 °C over 3 h. The solution stirred at reflux for an additional hour. The solution was cooled to room temperature and filtered to give the crude product as a white solid. Crystallization by vapor diffusion of water into **1** in DMF (20 mg per 1.5 mL) yielded almond-shaped plate-like crystals (28%). ^{1}H NMR (300 MHz, DMSO-d_6): δ = 8.40−7.77 (m, 4H, N−H), 7.37−6.94 (m, 8H, Ar−H), 5.71−3.99 (m, 8H, C−H). HRMS (DEP): [M+] calculated, 356.1129; found, 356.1135.

C-Shape Intermediate for *bis*-Squaramide Macrocycle. First, 3,4-diethoxy-3-cyclobutene-1,2-dione (0.5 g, 2.94 mmol, 435 μL) was dissolved in 0.5 mL of dry diethyl ether. Then 0.131 g of *m*-xylylenediamine (0.96 mmol, 127 μL) dissolved in 25 mL of dry diethyl ether was added dropwise over 10 min. After stirring overnight at room temperature, the reaction was evaporated to dryness and was purified via flash chromatography (94:6 DCM/MeOH) to yield a beige colored solid (96%). Spectra matched that previously reported.[20] ^{1}H NMR (300 MHz, DMSO-d_6): δ = 1.34 (m, 6H), 4.46 (m, 2H), 4.66 (m, 6H), 7.23 (d, J = 6.7 Hz, 3H), 7.36 (t, J = 7.4 Hz, 1H), 9.08 (s, 1H), 9.29 (s, 1H).

***bis*-Squaramide Macrocycle 2**. The previous C-shape spacer (0.177 g, 0.46 mmol) was dissolved in 250 mL of ethanol and was heated under reflux. Then *m*-xylylenediamine

(0.063 g, 0.46 mmol, 61 μL) dissolved in 30 mL of ethanol was added via syringe pump at 1.7 mL/h. After 3 days of heating at reflux, the reaction was cooled to room temperature, and the macrocycle was filtered off. Washing this product with ethanol yielded the material as a pale yellow solid (76%). Spectra matched that previously reported.[21] ^{1}H NMR (300 MHz, DMSO-d_6): δ = 4.70 (s, 3 H), 4.82 (d, 5H), 7.30 (m, 8H), 7.90 (s, 3H), 8.45 (s, 1H).

Single Crystal X-ray Diffraction. X-ray intensity data of all single crystals were collected at 100(2) K using a Bruker D8 QUEST diffractometer equipped with a PHOTON 100 CMOS area detector and an Incoatec microfocus source (Mo Kα radiation, λ = 0.71073 Å).[22] The raw area detector data frames were reduced and corrected for absorption effects using the SAINT+ and SADABS programs.[22] Final unit cell parameters were determined by least-squares refinement of a large set of reflections taken from each data set. The structures were solved with SHELXT.[23,24] Subsequent difference Fourier calculations and full-matrix least-squares refinement against F2 were performed with SHELXL[23,24] using OLEX2.[25] All non-hydrogen atoms were refined with anisotropic displacement parameters. Hydrogen atoms bonded to carbon were located in Fourier difference maps before being placed in geometrically idealized positions and included as riding atoms with d(C−H) = 0.95 Å and U_{iso}(H) = 1.2U_{eq}(C) for aromatic hydrogen atoms, d(C−H) = 0.99 Å and U_{iso}(H) = 1.2U_{eq}(C) for methylene hydrogens, and d(C−H) = 0.98 Å and U_{iso}(H) = 1.5U_{eq}(C) for methyl hydrogens. The methyl hydrogens were allowed to rotate as a rigid group to the orientation of maximum observed electron density. All hydrogen atoms bonded to nitrogen were located in Fourier difference maps and refined freely. Crystal data are given in Table 2.1.

Table 2.1. Data Collection and Refinement for Crystals Incorporating **1** or **2**.

Identification code	**1**	**1**·($NH_2CH_2CH_2NH_2$)	**2**	**2**·$(PC)_2$

CCDC Number	1581583	1581581	1581584	1581582
Empirical formula	$C_{18}H_{20}N_4S_2$	$C_{20}H_{28}N_6S_2$	$C_{24}H_{20}N_4O_4$	$C_{32}H_{32}N_4O_{10}$
Formula weight	356.50	416.60	428.44	632.61
Temperature/K	100(2)	100(2)	100(2)	100(2)
Crystal system	monoclinic	triclinic	monoclinic	monoclinic
Space group	$P2_1/c$	P-1	$P2_1/c$	$P2_1/c$
a/Å	10.3919(5)	9.4135(5)	11.2164(5)	16.298(2)
b/Å	9.0882(4)	9.7739(6)	11.5991(5)	11.4936(14)
c/Å	8.8029(4)	11.5974(6)	8.0989(3)	8.1148(11)
α/°	90	91.632(2)	90	90
β/°	92.021(2)	105.178(2)	107.2930(10)	101.457(4)
γ/°	90	97.791(2)	90	90
Volume/$Å^3$	830.86(7)	1018.02(10)	1006.04(7)	1489.8(3)
Z	2	2	2	2
$\rho_{calc}g/cm^3$	1.425	1.359	1.414	1.410
μ/mm^{-1}	0.328	0.281	0.099	0.106
F(000)	376.0	444.0	448.0	664.0
Crystal size/mm^3	0.2 × 0.12 × 0.06	0.46 × 0.36 × 0.24	0.24 × 0.18 × 0.04	0.06 × 0.05 × 0.02
Radiation	MoKα (λ = 0.71073)	MoKα (λ = 0.71073)	MoKα (λ = 0.71073)	MoKα (λ = 0.71073)
2Θ range for data collection/°	5.956 to 56.612	4.534 to 65.246	5.178 to 55.406	4.366 to 50.052
Index ranges	-13 ≤ h ≤ 13, -12 ≤ k ≤ 12, -11 ≤ l ≤ 11	-14 ≤ h ≤ 14, -14 ≤ k ≤ 14, -17 ≤ l ≤ 17	-14 ≤ h ≤ 14, -15 ≤ k ≤ 15, -10 ≤ l ≤ 10	-19 ≤ h ≤ 19, -13 ≤ k ≤ 13, -9 ≤ l ≤ 9
Reflections collected	37851	64732	42677	36972
Independent reflections	2060 [R_{int} = 0.0351, R_{sigma} = 0.0140]	7428 [R_{int} = 0.0307, R_{sigma} = 0.0195]	2363 [R_{int} = 0.0362, R_{sigma} = 0.0146]	2625 [R_{int} = 0.1434, R_{sigma} = 0.0650]
Data/restraints/parameters	2060/0/125	7428/0/305	2363/0/153	2625/133/265
Goodness-of-fit on F^2	1.085	1.059	1.067	1.023
Final R indexes [I>=2σ (I)]	R_1 = 0.0323, wR_2 = 0.0850	R_1 = 0.0321, wR_2 = 0.0822	R_1 = 0.0420, wR_2 = 0.1011	R_1 = 0.0529, wR_2 = 0.1009
Final R indexes [all data]	R_1 = 0.0403, wR_2 = 0.0890	R_1 = 0.0387, wR_2 = 0.0852	R_1 = 0.0518, wR_2 = 0.1060	R_1 = 0.0966, wR_2 = 0.1169
Largest diff. peak/hole / e $Å^{-3}$	0.40/-0.27	0.57/-0.32	0.32/-0.25	0.32/-0.28

2.3 RESULTS AND DISCUSSION

To investigate the effects of macrocyclization on the conformations and assembly directing ability of thioureas and squaramides, we incorporated these functional groups into the m-xylene containing macrocycles in Figure 2.1a. To the best of our knowledge,

the thiourea macrocycle has not yet been reported, although Sasaki et al.[26] studied similar macrocycles for selective anion complexation, which had periphery *t*-butyl and *O*-butyl groups attached for solubility. Open chain equivalents have been reported that combine two thioureas through a *m*-xylene spacer.[27,28] These structures form cyclic dimers with other networks being formed on the basis of sterics, hydrogen bonding efficiency, and packing density. The squaramide macrocycle was first made by Qin et al.[21] and was used as an anion binding agent. They also prepared an equivalent with a glycol tail which was shown to assemble in 1D columns similar to the urea macrocycle. Open forms, with one squaramide substituted with two benzyl groups, exhibit temperature dependent polymorphism and afforded multiple crystal forms.[29,30]

We synthesized and tested crystallization conditions for the pure forms of *bis*-thiourea and *bis*-squaramide macrocycles to investigate if their conformations and assembly patterns resemble their analogous counterparts or if the macrocycles adopt new conformations and structures. The *bis*-thiourea macrocycle (**1**) was synthesized in one step using readily available *m*-xylylenediamine and 1,1'-thiocarbonyldiimidazol using a strategy similar to Sasaki et al. (Scheme 2.1).[26] This employs the simultaneous, dropwise addition of both macrocycle precursors at reflux in high dilution. A crude mixture of **1** was separated by collecting the precipitate from the reaction. Macrocycle **1** was insoluble in most common solvents but dissolved with gentle heating in DMSO, DMF and ethylene diamine and remained dissolved when cooled to room temperature. Therefore, we screened a range of crystallization conditions using vapor diffusion of an anti-solvent (water, diethyl ether, acetonitrile) into solutions of **1** (~ 6 mg / mL). Vapor diffusion of

water into DMF or ethylene diamine solutions of **1** afforded colorless crystals suitable for X-ray diffraction.

Macrocycle **1** crystallized from DMF in the monoclinic system with the $P2_1/c$ space group. The crystal structure shows the expected macrocycle **1**, which adopts a relatively planar structure similar to the reported *bis*-urea structures.[6] The thioureas display a *trans*−*trans* arrangement and are oriented approximately perpendicular to the *m*-xylene backbone. Hydrogen bonds converge on the sulfur from two different macrocycles with N−H−S angles of 143.2(17)° and 149.1(17)°. This is atypical of usual *trans*−*trans* bonding for thioureas, which usually engage in a zigzag motif with bifurcating hydrogen bonds (both hydrogens come from the same thiourea as opposed to the hydrogens coming from different thoiureas as is the case here).[12,31] Overall, the hydrogen bonding forms 12 atom circuits with four different thioureas engaging in each circuit as seen in Figure 2.1a. This hydrogen bonding defines edge-to-face slabs of **1** that lie parallel to the crystallographic (100) plane stacking along the [100] direction (Figure 2.2b,c). Each unit cell contains one-half of one macrocycle on an inversion center. The donor/acceptor lengths of 3.2731(14) and 3.3708(13) Å (N···S distances) and a C=S bond length of 1.7021(15) Å are all well within previous literature values.[32]

A second solvated crystal of **1** was prepared by using vapor diffusion of water into a solution of 1 in ethylene diamine. Large colorless parallelogram-shaped crystals of a 1:1 solvate crystallize in the triclinic system in the $P\bar{1}$ space group with one-half of two independent macrocycles and ethylene diamines on inversion centers making up the asymmetric unit. The **1**·($NH_2CH_2CH_2NH_2$) crystal contains both the *trans*−*trans* and the *cis*−*trans* thiourea conformations of the macrocycle. Similar to the first crystal form, the

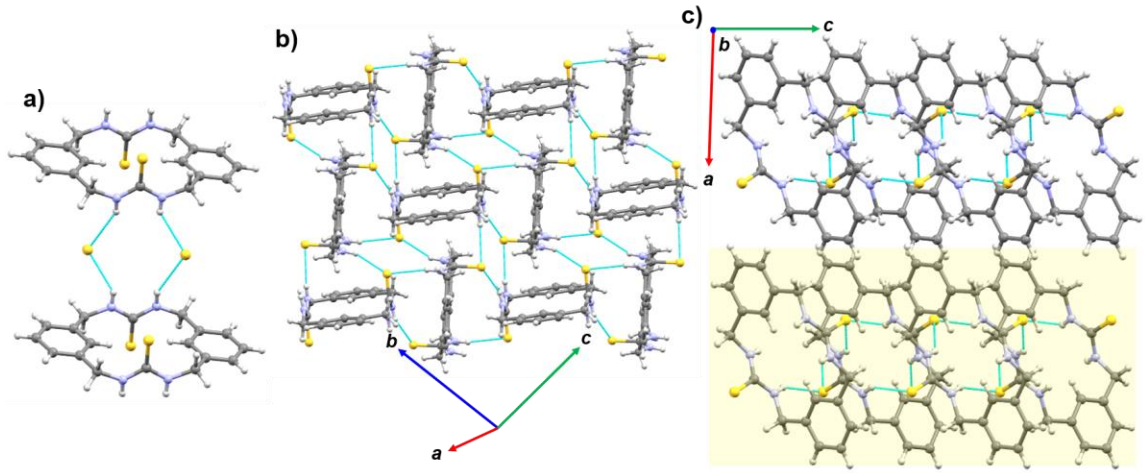

Figure 2.2. Views from **1**. Hydrogen bonds are given in light blue. (a) One circuit of hydrogen bonding (middle two macrocycles have been omitted for clarity). (b) One slab of **1**. (c) Two slabs of **1** stacked on top of each other (in the [100] direction, yellow indicates one of the two slabs).

trans−*trans* conformer is relatively planar with the thioureas perpendicular to the plane (Figure 2.3a); however, the *cis*−*trans* conformer gives the macrocycle more curvature resulting in an elongated Z-shape with the thioureas making the bend of the Z (Figure 2.3b). Hydrogen bonding from ethylene diamines holds the crystal together by interconnecting the conformers of **1** by accepting hydrogen bonds from one conformer and donating to the other (Figure 2.3d). As illustrated in Figure 2.7, one nitrogen on one of the two distinct ethylene diamines within this crystal accepts a hydrogen bond from a *cis*−*trans* **1** (2.9115(12) Å, N···N) and donates a hydrogen bond to a *trans*−*trans* **1** (3.5465(10) Å, N···S). Both nitrogens on this ethylene diamine are equivalent. The second ethylene diamine is similar except the conformers are flipped in that it accepts hydrogen bonds from *trans*−*trans* **1** and donates to *cis*−*trans* **1** (2.9773(13) and 3.5465(10) Å, Figure 2.8). The *cis*−*trans* conformer hydrogen bonds with itself to form chains with dimer structures on either side of the macrocycle at hydrogen bond lengths of 3.3223(8) Å (Figure 2.3c, N···S). Additionally, the *cis*−*trans* conformer accepts a hydrogen from the *trans*−*trans* conformer

with an N···S length of 3.5029(9) Å. This gives the sulfur three hydrogen bonds with an additional close contact from a hydrogen from a different *trans*−*trans* conformer proximal to it (Figures 2.3b and 2.9). The sulfur for the *trans*−*trans* conformer only has ethylene diamine as a hydrogen bond donor with two close contacts with methylene and aromatic hydrogens from two different *cis*−*trans* conformers.

The ^{1}H NMR of freshly dissolved crystals of **1** displayed broad peaks for the methylene groups from 4.0 to 5.6 ppm and amide hydrogens from 7.8 to 8.3 ppm, which suggests multiple exchanging conformations or oligomer/polymer formation (Figure 2.10). A PXRD of the bulk material (Figure 2.11, **1**) demonstrates that the sample is single phase and that the observed PXRD pattern correlated well with the pattern predicted using the single-crystal XRD coordinates. We turned to 2D EXchange SpectrometrY (EXSY) NMR

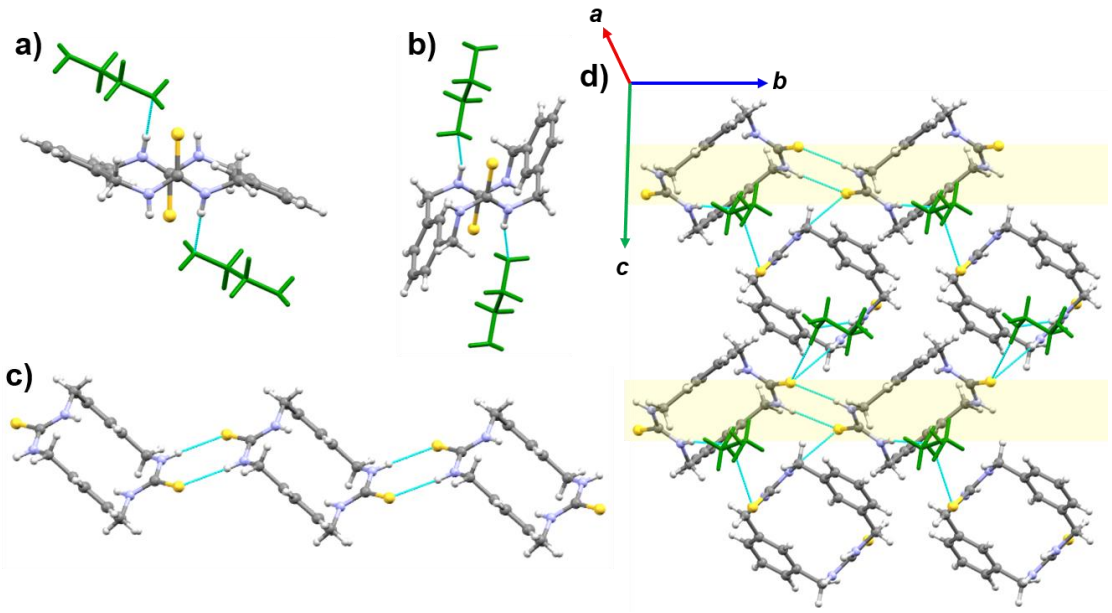

Figure 2.3. Views from **1**·($NH_2CH_2CH_2NH_2$). Hydrogen bonds are given in light blue. (a) *trans–trans* conformer of **1** (ball and stick) donating hydrogen bonds to one distinct ethylene diamine (green capped sticks, both shown are equivalent). (b) Similar to panel (a), except it is the *cis–trans* conformer of **1**. (c) Chain of *cis–trans* macrocycles. (d) Overall crystal structure of **1**·($NH_2CH_2CH_2NH_2$) with *cis–trans* chains highlighted in yellow. Additional crystal views are shown in Figures 2.7-2.9.

experiments to investigate if the sample was undergoing rotation between conformers in solution on the NMR time scale. This technique enables one to correlate the exchanging signals in a wide range of chemical exchange regimes (slow and fast). The EXSY spectra was collected at 298 K with a mixing time of 0.8 s (Figure 2.4b) and displays numerous cross-peaks for the thiourea NHs and methylene resonances. Specifically, the three resonances at 8.2, 8.0, and 7.85 ppm (Figure 2.4c) were assigned to the thiourea NHs and all display cross-peaks indicating at least two distinct states. Evidence from the **1**·($NH_2CH_2CH_2NH_2$) crystals suggest that two of these states are the *trans*−*trans* and *cis*−*trans* conformers (Figure 2.4a). The major conformer (∼50% by relative integration) is likely the *trans*−*trans* conformation given that there is only one kind of NH as opposed to the two that are predicted for the *cis*−*trans* conformer. Spin simulations (Figure 2.12) show that the large NH peak is coupled to the two large diastereotopic methylene peaks (J = 8.7 and 3.2 Hz). These methylene peaks are also coupled to each other (J = 16.0 Hz). The multiple broad resonances in the 4−6 ppm range (Figure 2.4d) also show multiple cross-peaks indicative of exchanging signals for the respective methylene protons.

Squaramide macrocycle **2** was synthesized through the C-shape intermediate[20] according to literature procedures, which is subsequently cyclized at high dilution (Scheme 2.2).[21] Macrocycle **2** displayed a greater solubility relative to **1**. Therefore, we screened a range of crystallization conditions using acetic acid, DMF, DMSO, propylene carbonate, and ethylene diamine (∼6 mg/mL). Vapor diffusion of water into a DMSO, DMF, or propylene carbonate solution of **2** at room temperature afforded three crystal forms: the

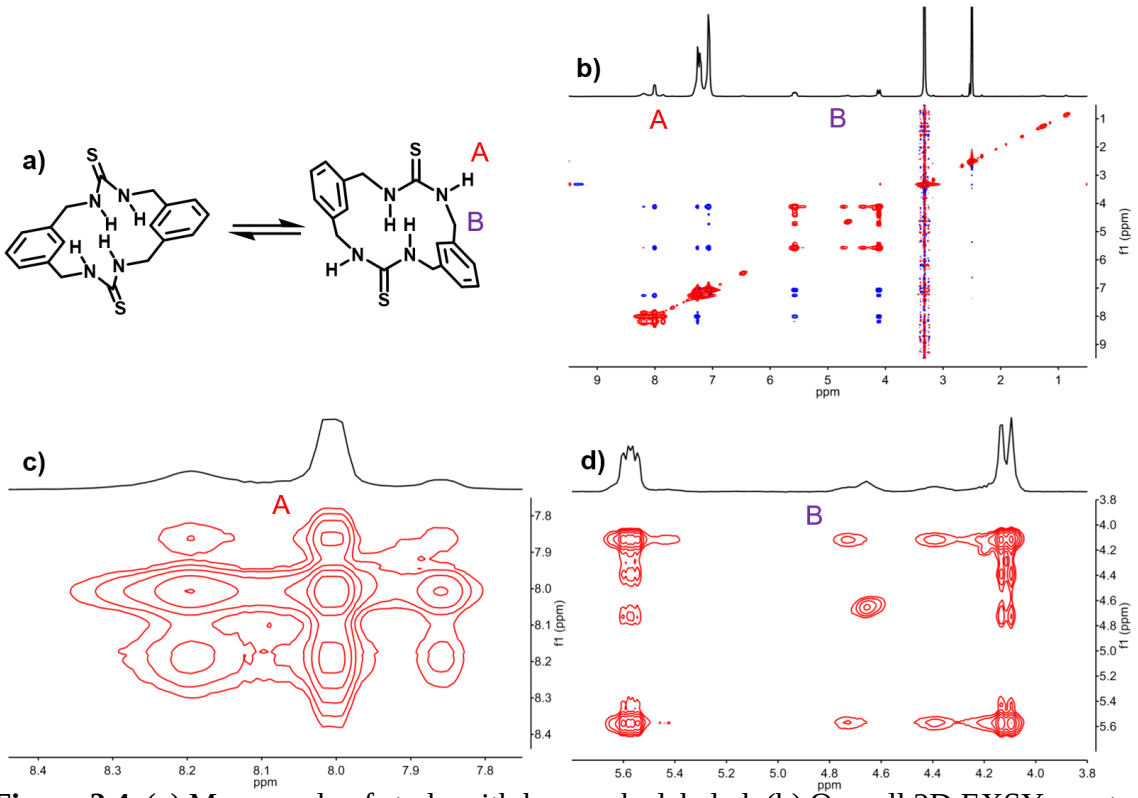

Figure 2.4. (a) Macrocycle of study with key peaks labeled. (b) Overall 2D EXSY spectra (peaks in red, NOESY peaks in blue). (c) Zoom of amide region. (d) Zoom of methylene region.

pure macrocycle, a propylene carbonate solvate, and a DMSO solvate. The first two are new crystal forms and will be discussed in detail. The DMSO solvate was identical to the structure recently reported from the Jolliffe group.[21]

Colorless parallelogram-shaped plate crystals of **2** were obtained in the monoclinic system in the $P2_1/c$ space group with one-half of **2** on an inversion center making up the asymmetric unit. In this crystal, only one of the squarate carbonyls participates in hydrogen bonding (Figure 2.5a) with a bifurcated hydrogen bond at lengths of 2.8694(17) and 2.8652(16) Å (N···O distances). The second carbonyl only has a close contact with one aromatic hydrogen. This is uncharacteristic for squaramides as they usually have both amide protons going to both carbonyls (one per each) as opposed to both protons going to

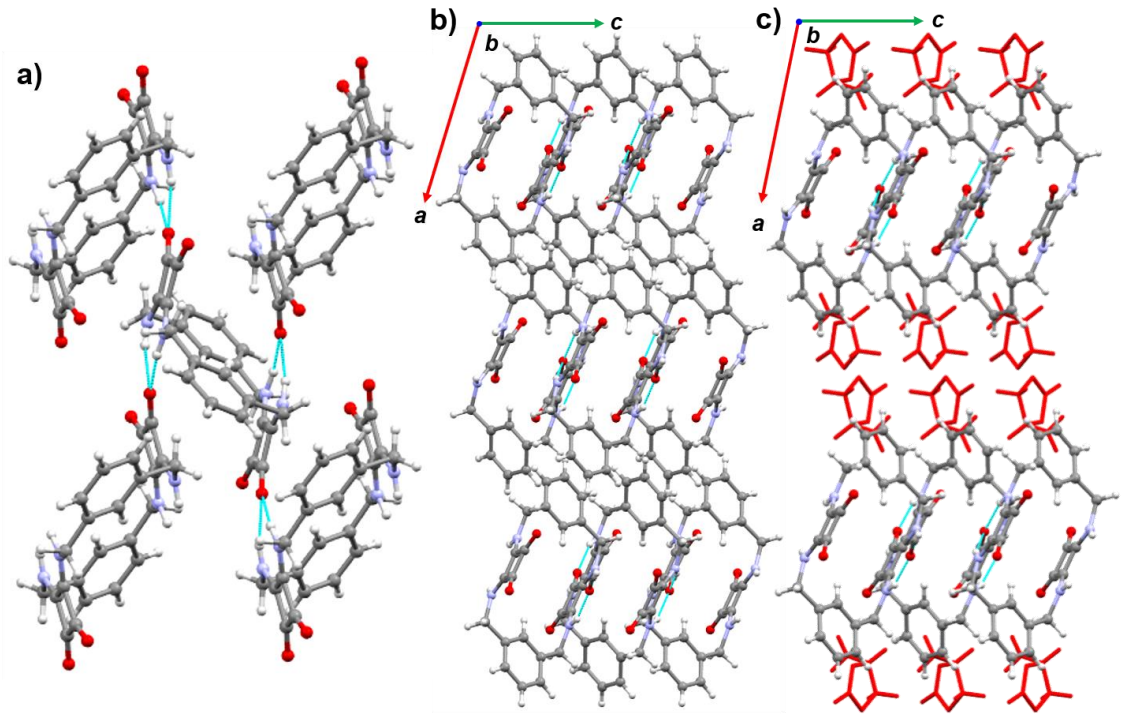

Figure 2.5. (a) Hydrogen bonding (light blue) in both **2** and **2**·$(PC)_2$. (b) Crystal structure of **2**. (c) Crystal structure of **2**·$(PC)_2$.

one carbonyl when they are in the *trans*−*trans* conformer as discussed earlier. In fact, a search of the CSD database (CSD 5.37, September 20, 2017) indicates this type of bonding for squaramides has only occurred three other times as opposed to 23 times for the normal bonding.[33] Overall, **2** forms an interdigitated 2D network with each macrocycle hydrogen bonded to four other macrocycles forming layers parallel to the crystallographic (100) plane, which then stack upon each along [100] (Figure 2.5b).

A second crystal form was obtained by vapor diffusion of water into a solution of **2** in propylene carbonate. These colorless rhombus-shaped plates crystallized in the monoclinic system in the $P2_1/c$ space group with one propylene carbonate (PC) and half of a macrocycle per asymmetric unit, resulting in a macrocycle to solvent ratio of 1:2. This solvated crystal **2**·$(PC)_2$ exhibits NH···O hydrogen bonding that defines 2D slabs along the crystallographic (100) plane with only one carbonyl participating in hydrogen bonding

(2.865(3) and 2.872(3) Å, N···O). Between these slabs lie enantiomerically scrambled propylene carbonate in the interstitial gaps between the 2D nets formed by the NH···O bonding between cycles as seen in Figure 2.5c. This results in a crystal that is very similar to **2**, except the 2D layers of hydrogen bonding have been separated by a layer of disordered solvent. Interestingly, this is only the second purely organic crystal incorporating propylene carbonate according to a CSD scan (CSD 5.37, September 20, 2017).[33]

The DMSO solvate **2**·$(DMSO)_2$ matched the structure previously reported in *Chem. Sci.*[21] in which the Jolliffe group demonstrated that macrocyclic squaramides bound sulfates in high affinity in aqueous solution. In this structure, the macrocycle displays a *trans*−*trans* squaramide conformation, and each of the NH groups are engaged in bifurcated hydrogen bonding to the DMSO oxygen. The macrocyclic conformation found here is similar to both **2** and **2**·$(PC)_2$ (Figure 2.13), suggesting that the squaramide macrocycle is more like the *bis*-urea macrocycle in terms of its limited flexibility.

The urea, thiourea, and squaramide macrocycles each display crystal forms where their functional groups adopt *trans*−*trans* conformers (Figure 2.6). A comparison of these *trans*−*trans* conformers shows that the three bis-functional groups are oriented at different angles (Figure 2.14) with respect to the *m*-xylene macrocycles and display very different hydrogen bond motifs. In the urea system, the ureas are tilted ∼69° from the plane of the macrocycle with bifurcated hydrogen bonds and offset aryl stacking interactions driving the columnar stacking of macrocycles into 1D columns.[19] The squaramides show a similar tilt ∼55° from the plane of its respective macrocycle and organize through 2D networks of hydrogen bonds with both NHs engaging in hydrogen bonding but with only one carbonyl

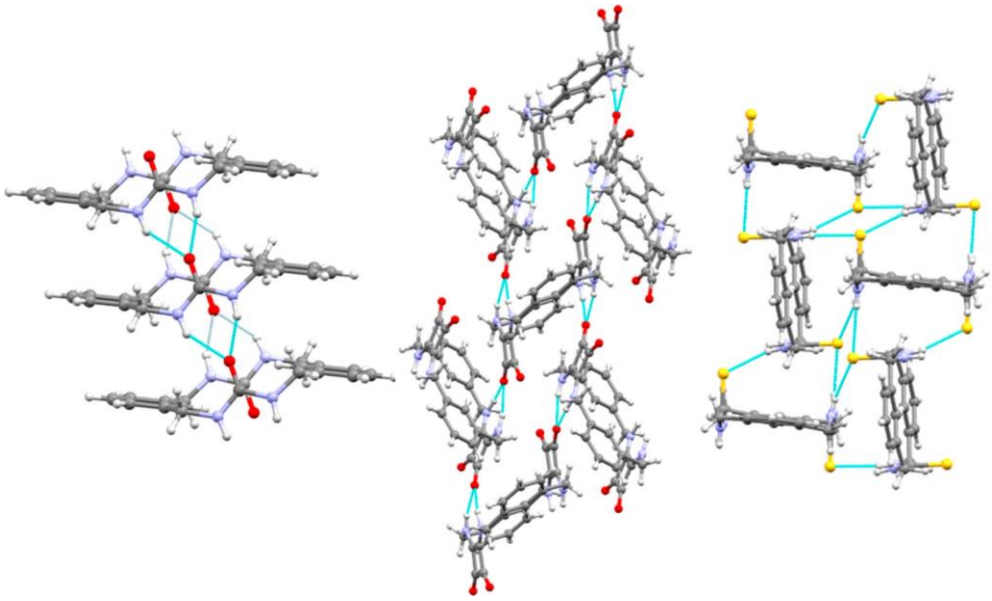

Figure 2.6. Hydrogen bonding (light blue) seen for the urea,[19] squaramide, and thiourea *m*-xylene macrocycles.

in participation. The thioureas are nearly perpendicular (~87°) from the plane of the macrocycle and organize through 2D networks of hydrogen bonds forming layers driven by the perpendicular bonding of the sulfur in the thiourea unit. These layers are further connected through edge-to-face aryl stacking interactions. Building on these and other experimental studies with computational investigations will help to further understand how these interactions are modulated by outside influences and lead to better predictions of which functional group is most suited for a specific application.

2.4 CONCLUSIONS

In conclusion, this chapter presents the synthesis of a new *bis*-thiourea *m*-xylene macrocycle along with a screen of crystallization conditions for both *bis*-thiourea *m*-xylene and *bis*-squaramide *m*-xylene macrocycles. Four new crystal structures were obtained that incorporate either the thiourea macrocycle or the squaramide equivalent. A comparison of these structures to literature reported structures of the *bis*-squaramide and *bis*-urea macrocycles suggests that when constrained within these small rings, these functional

groups favor *trans–trans* conformers. Indeed, the urea and squaramide analogues display exclusively *trans–trans* conformers, while the thiourea macrocycle appears to be less constrained and gave a solvate with ethylene diamine displaying both the *trans–trans* and *cis–trans* thiourea conformers within the same structure. Two-dimensional EXSY NMR studies suggest that both thiourea conformations are accessible and interconvert in solution at room temperature. Within the *trans–trans* structures, the thiourea and squaramide show markedly different assembly motifs, favoring 2D hydrogen bonding networks as opposed to the 1D columns formed by the urea derivative. The thiourea macrocycles crystallize in an edge-to-face fashion, while the squaramide equivalent crystallizes as interdigitated macrocycles. Currently, we are investigating the synthesis and assembly by experiment and computations of "mixed" macrocycles that contain two different assembly guiding groups: urea/thiourea, urea/squaramide, or thiourea/squaramide groups. Computations and crystal structures will help determine what hydrogen bonding is preferred when two of these groups are in direct competition with each other. Overall, these findings give insight into how macrocycles with different building units crystallize in the solid state and should lead to better designs and predictions for supramolecular assemblies.

2.5 EXPERIMENTAL

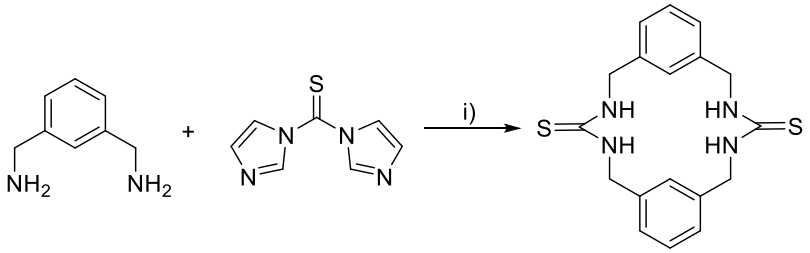

Scheme 2.1. Synthesis of the *bis*-thiourea *m*-xylene macrocycle. i) 1 eq. diamine and thione, $CHCl_3$, Δ, 4 hours; further recrystallization using vapor diffusion of water into DMF is required.

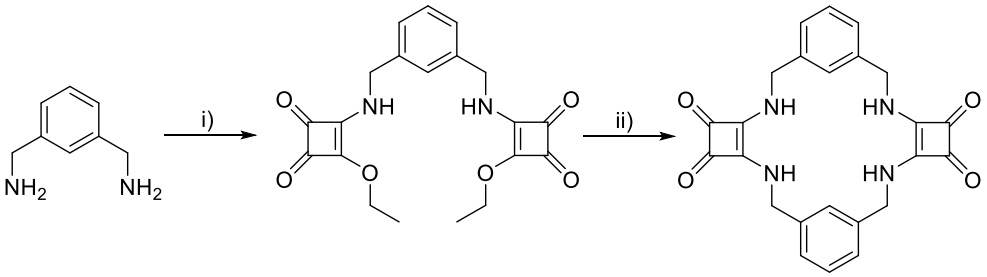

Scheme 2.2. Synthesis of the *bis*-squaramide *m*-xylene macrocycle. i) 3 eq. squarate, EtO_2, r.t., overnight ii) 1 eq. diamine, EtOH, Δ, 3 days.

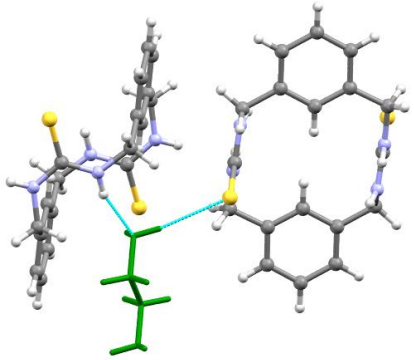

Figure 2.7. Additional view of the hydrogen bonding (light blue) in the **1**·($NH_2CH_2CH_2NH_2$) crystal. As seen here this ethylene diamine connects the two conformers of the macrocycle by accepting a hydrogen bond from the *cis-trans* **1** and donating to *trans-trans* **1**. Going from left they right they are *cis-trans* **1**, ethylene diamine, and *trans-trans* **1**.

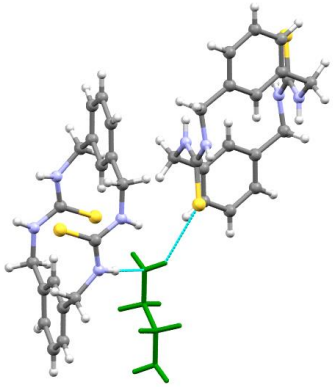

Figure 2.8. Additional view of the hydrogen bonding (light blue) in the **1**·($NH_2CH_2CH_2NH_2$) crystal. As seen here the other ethylene diamine (first shown in Figure 2.8) connects the two conformers as well, but it accepts a hydrogen bond from *trans-trans* **1** and donates to *cis-trans* **1**, opposite from the first ethylene diamine. Going from left they right they are *trans-trans* **1**, ethylene diamine, and *cis-trans* **1**.

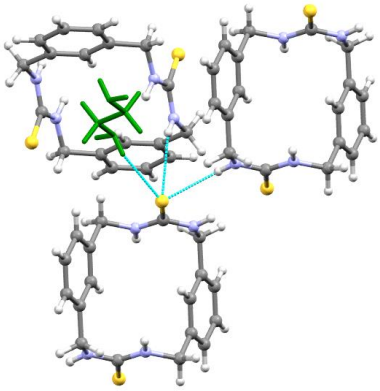

Figure 2.9. Additional view of the hydrogen bonding (light blue) in the **1**·($NH_2CH_2CH_2NH_2$) crystal. As seen here the sulfur on the *cis-trans* macrocycle has three hydrogen bonds. Going from left they right they come from an ethylene diamine, a *trans-trans* macrocycle, and another *cis-trans* macrocycle.

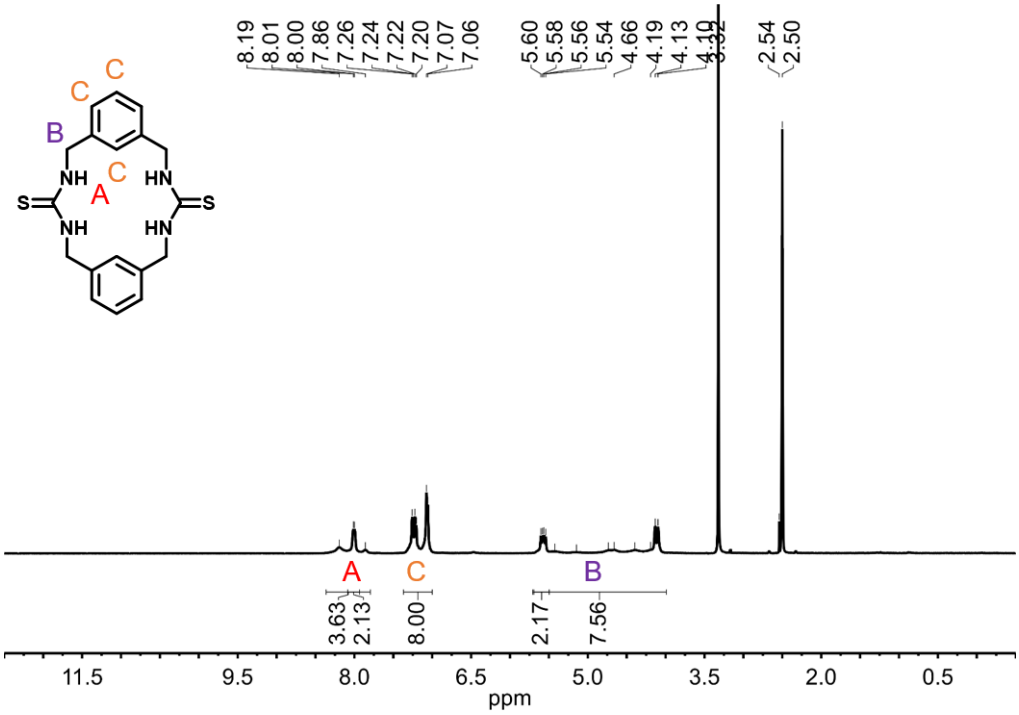

Figure 2.10. ^{1}H NMR of the thiourea macrocycle (400 MHz, DMSO-d_6): δ = 4.02-5.96 (m, 8H), 6.96-7.31 (m, 8H), 7.80-8.36 (m, 4H). Water present in NMR solvent. Initially, the spectra displayed large DMF peaks despite washing the crystals with water and leaving under vacuum for 3 days. To remove the DMF, crystals were dissolved in DMSO and precipitated out with water. This process was done again to ensure all removal of the DMF (this left behind residual DMSO, but DMSO did not interfere with the spectra of **1**, unlike DMF). An approximation of *trans-trans* **1** compared to other conformers was made by taking the average relative integral of the peaks at δ = 8.01 and 5.57 ppm (amide and methylene, respectively). This was 50%.

2.5.1 Powder X-ray Diffraction

PXRD data was collected on a Rigaku D/Max-2100 powder X-ray diffractometer using Cu Kα radiation. The step can covered an angular range of 10-50˚ 2Θ in steps of 0.02˚.

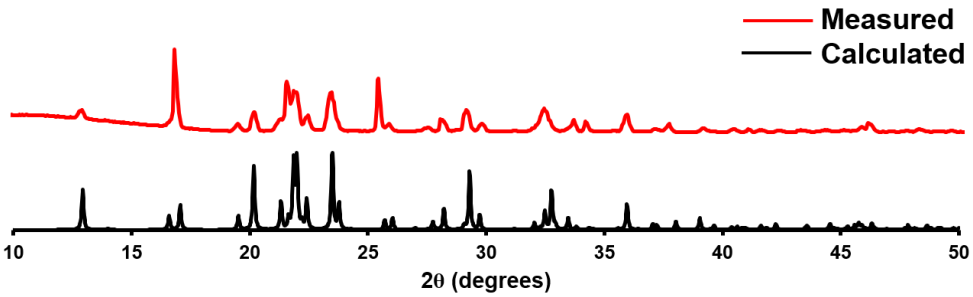

Figure 2.11. PXRD of **1**.

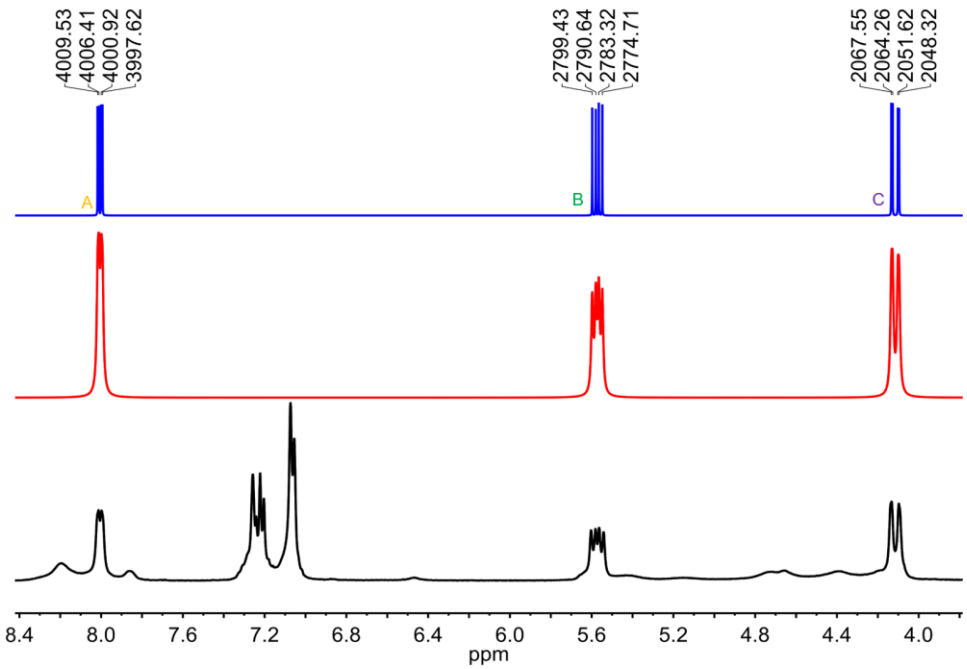

Figure 2.12. Spin simulation of the ^{1}H NMR of **1** (400 MHz, DMSO-d_6) of the amide and methylene peaks. Experimental spectra is given in black (zoom of Figure 2.10). In blue is the simulated spins at 0 Hz width. In red is the simulated spins at 5 Hz width. Coupling constants were as follows: δ = 8.00 (J = 8.7 Hz [B] and 3.2 Hz [C]), 5.57 (J = 8.7 Hz [A] and 16.0 Hz [C]), 4.12 (J = 3.2 Hz [A] and 16.0 Hz [B]). Spin simulations were performed in MestReNova Version 6.1.0-6224.

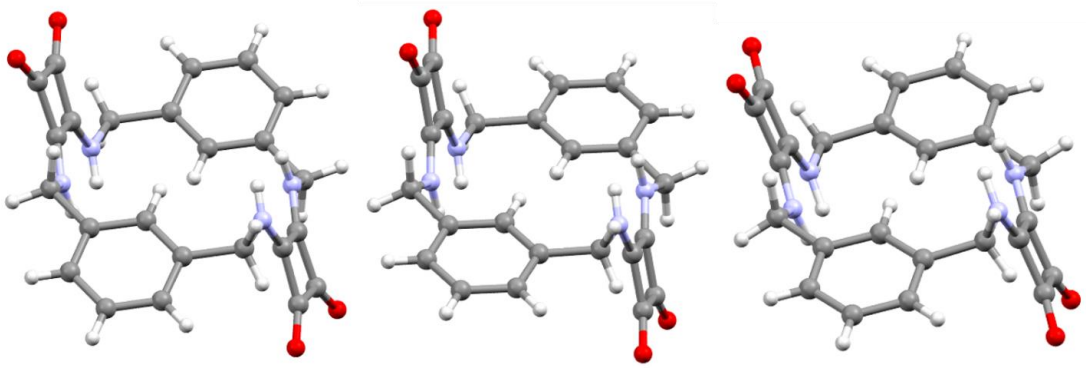

Figure 2.13. Comparison of the squaramide macrocycles found in three different crystals. From left to right these squramide macrocycles come from the following crystals: **2**·$(DMSO)_2$,[21] **2**, **2**·$(PC)_2$.

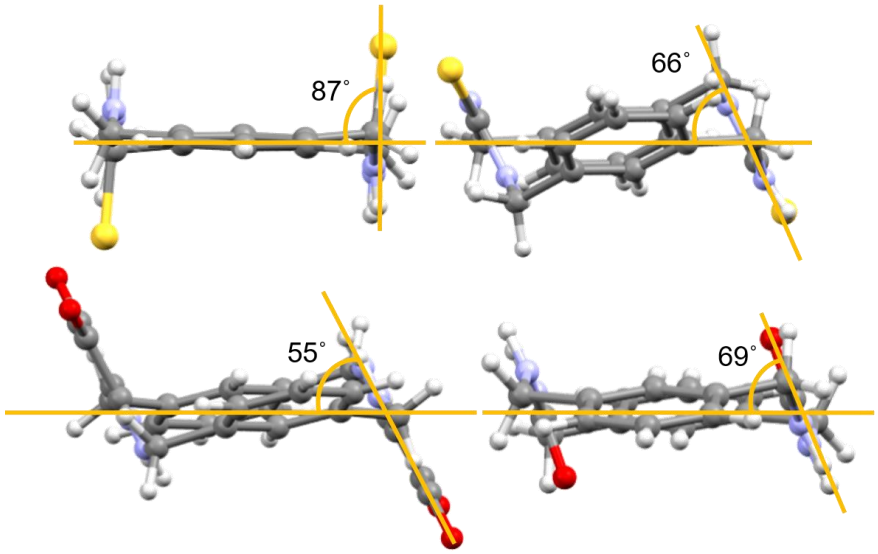

Figure 2.14. Angles of assembly for the different macrocycles. Angles are given as the plane of the macrocycle versus the plane of the building unit. For the thiourea cycles on top the *trans-trans* conformer of **1** (left) was taken from **1**, while the *cis-trans* conformer of **1** was taken from **1**·($NH_2CH_2CH_2NH_2$). The squaramide macrocycle was taken from **2**. The urea macrocycle was taken from reference.[19]

2.6 REFERENCES

1. Karmakar, A.; Illathvalappil, R.; Anothumakkool, B.; Sen, A.; Samanta, P.; Desai, A. V.; Kurungot, S.; Ghosh, S. K. *Angew. Chem., Int. Ed.* **2016**, *55*, 10667-10671.

2. Adachi T.; Ward, M. D. *Acc. Chem. Res.* **2016**, *49*, 2669-2679.

3. Chen S.; Binder W. H. *Acc. Chem. Res.* **2016**, *49*, 1409-1420.
4. Custelcean R. *Chem. Commun.* **2008**, 295-307.
5. Liu, Y.; Lam, A. H. W.; Fowler, F. W.; Lauher, J. W. *Mol. Cryst. Liq. Cryst.* **2002**, *389*, 39-46.
6. Shimizu, L. S.; Salpage, S. R.; Korous A. A. *Acc. Chem. Res.* 2014, **47**, 2116-2127.
7. Steed J. W. *Chem. Soc. Rev.* **2010**, *39*, 3686-3699.
8. Salpage, S. R.; Donevant, L. S.; Smith, M. D.; Bick, A.; Shimizu L. S. *J. Photochem. Photobiol. A-Chem.* **2016**, *315*, 14-24.
9. McBride, M. T.; Luo, T.-J. M.; Palmore G. T. R. *Cryst. Growth Des.* **2001**, *1*, 39-46.
10. Storer, R. I.; Aciro C.; Jones L. H. *Chem. Soc. Rev.* **2011**, *40*, 2330-2346.
11. Prohens, R.; Portell, A.; Puigjaner, C.; Barbas, R.; Alcobé, X.; Font-Bardia, M.; Tomàs, S. *CrystEngComm* **2012**, *14*, 5745-5748.
12. Custelcean, R.; Gorbunova M. G.; Bonnesen P. V. *Chem.-Eur. J.* **2005**, *11*, 1459-1466.
13. Suksai, C.; Pakawatchai C.; Tuntulani T. *J. Chem. Crystallogr.* **2009**, *39*, 348-352.
14. Davis, A. P.; Draper, S. M.; Dunne G.; Ashton P. *Chem. Commun.* **1999**, 2265-2266.
15. Prohens, R.; Portell, A.; Puigjaner, C.; Tomàs, S.; Fujii, K.; Harris, K. D. M.; Alcobé, X.; Font-Bardia, M.; Barbas R. *Cryst. Growth Des.* **2011**, *11*, 3725-3730.
16. Prohens, R.; Portell, A.; Font-Bardia, M.; Bauzá, A.; Frontera, A. *CrystEngComm* **2016**, *18*, 6437-6443.
17. Prohens, R.; Portell, A.; Font-Bardia, M.; Bauzá A.; Frontera, A. *CrystEngComm* **2017**, *19*, 3071-3077.
18. Fernández, J. M. G.; Blanco, J. L. J.; Mellet, C. O.; Fuentes, J. *J. Chem. Soc., Chem. Commun.* **1995**, 57-58.

19. Shimizu, L. S.; Smith, M. D.; Hughes, A. D.; Shimizu K. D. *Chem. Commun.* **2001**, 1592-1593.

20. Prohens, R.; Tomàs, S.; Morey, J.; Deyà, P. M.; Ballester, P. Costa, A. *Tetrahedron Lett.* **1998**, *39*, 1063-1066.

21. Qin, L.; Hartley, A.; Turner, P.; Elmes, R. B. P.; Jolliffe, K. A. *Chem. Sci.* **2016**, *7*, 4563-4572.

22. APEX2 Version 2014.9-0, SAINT+ Version 8.34A and SADABS Version 2014/4. Bruker Analytical X-ray Systems, Inc., Madison, Wisconsin, USA, 2014.

23. Sheldrick, G.M. *Acta Crystallogr. A* **2015**, *71*, 3-8.

24. Sheldrick, G.M. *Acta Crystallogr. C* **2015**, *71*, 3-8.

25. Dolomanov, O. V., Bourhis, L. J., Gildea, R. J., Howard J. A. K.; Puschmann, H. J. *Appl. Cryst.* **2009**, *42*, 339-341.

26. Sasaki, S.; Mizuno, M.; Naemura, K.; Tobe, Y. *J. Org. Chem.* **2000**, *65*, 275-283.

27. Succaw, G. L.; Weakley, T. J. R.; Han, F.; Doxsee, K. M. *Cryst. Growth Des.* **2005**, *5*, 2288-2298.

28. Tobe, Y.; Sasaki, S.; Mizuno, M.; Hirose, K.; Naemura, K. *J. Org. Chem.* **1998**, *63*, 7481-7489.

29. Portell, A.; Barbas, R.; Braga, D.; Polito, M.; Puigjaner, C.; Prohens, R. *CrystEngComm* **2009**, *11*, 52-54.

30. Portell, A.; Alcobé, X.; Daku, L. M. L.; Cerny, R.; Prohens, R. *Powder Diffr.* **2013**, *28*, S470-S480.

31. Zhao, X.; Chang, Y.; Fowler, F. W.; Lauher, J. W. *J. Am. Chem. Soc.* **1990**, *112*, 6627-6634.

32. Allen, F. H.; Bird, C. M.; Rowland, R. S.; Raithby, P. R. *Acta Crystallogr. B* **1997**, *53*, 680-695.

33. Groom, C. R.; Bruno, I. J.; Lightfoot, M. P.; Ward, S. C. *Acta Crystallogr. B* **2016**, *72*, 171-179.

CHAPTER 3

UV-IRRADIATION OF SELF-ASSEMBLED TRIPHENYLAMINES AFFORDS PERSISTENT AND REGERABLE RADICALS*

* **Sindt, A. J.**; DeHaven, B. A.; McEachern, D. F.; Dissanayake, D. M. M. M.; Smith, M. D.; Vannucci, A. K.; Shimizu, L. S. *Chem. Sci.* **2019**, *10*, 2670-2677. Published by The Royal Society of Chemistry.

3.0 ABSTRACT

UV-irradiation of assembled urea-tethered triphenylamine dimers results in the formation of persistent radicals, whereas radicals generated in solution are reactive and quickly degrade. In the solid-state, high quantities of radicals (approximately 1 in 150 molecules) are formed with a half-life of one week with no significant change in the single crystal X-ray diffraction. Remarkably, after decay, re-irradiation of the solid sample regenerates the radicals to their original concentration. The photophysics upon radical generation are also altered. Both the absorption and emission are significantly quenched without external oxidation likely due to the delocalization of the radicals within the crystals. The factors that influence radical stability and generation are correlated to the rigid supramolecular framework formed by the urea tether of the triphenylamine dimer. Electrochemical evidence demonstrates that these compounds can be oxidized in solution at 1.0 V vs. SCE to generate radical cations, whose EPR spectra were compared with spectra of the solid-state photogenerated radicals. Additionally, these compounds display changes in emission due to solvent effects from fluorescence to phosphorescence. Understanding how solid-state assembly alters the photophysical properties of triphenylamines could lead to further applications of these compounds for magnetic and conductive materials.

3.1 INTRODUCTION

Intentional design of functional supramolecular assemblies requires precise control of intermolecular interactions as well as an understanding of how complex structures modulate chemical and physical properties to produce materials with emergent qualities.[1-3] This understanding is key for designing compounds used to probe the enhancement or quenching of luminescence of small molecules in the solid-state.[4,5] Controlled assembly of

structures can also modulate conductivity[6,7] and dichroism in photoactive materials.[8] Here, we synthesize urea tethered triphenylamines (TPAs), and determine their photophysical properties in solution and in crystalline assemblies. Upon UV-irradiation, in both solution and the solid-state, these materials displayed radical formation with solid-state samples proving to be quite stable (Figure 3.1). Remarkably, solid-state samples yield high quantities of persistent radicals with ~1 in 150 molecules containing a radical. Moreover, after decay, reirradiation with UV light can regenerate the radicals in similar quantities. Thus, solid-state assembly alters the photophysical properties of TPAs and could prove helpful in the design of conductive and magnetic materials that integrate TPA components.

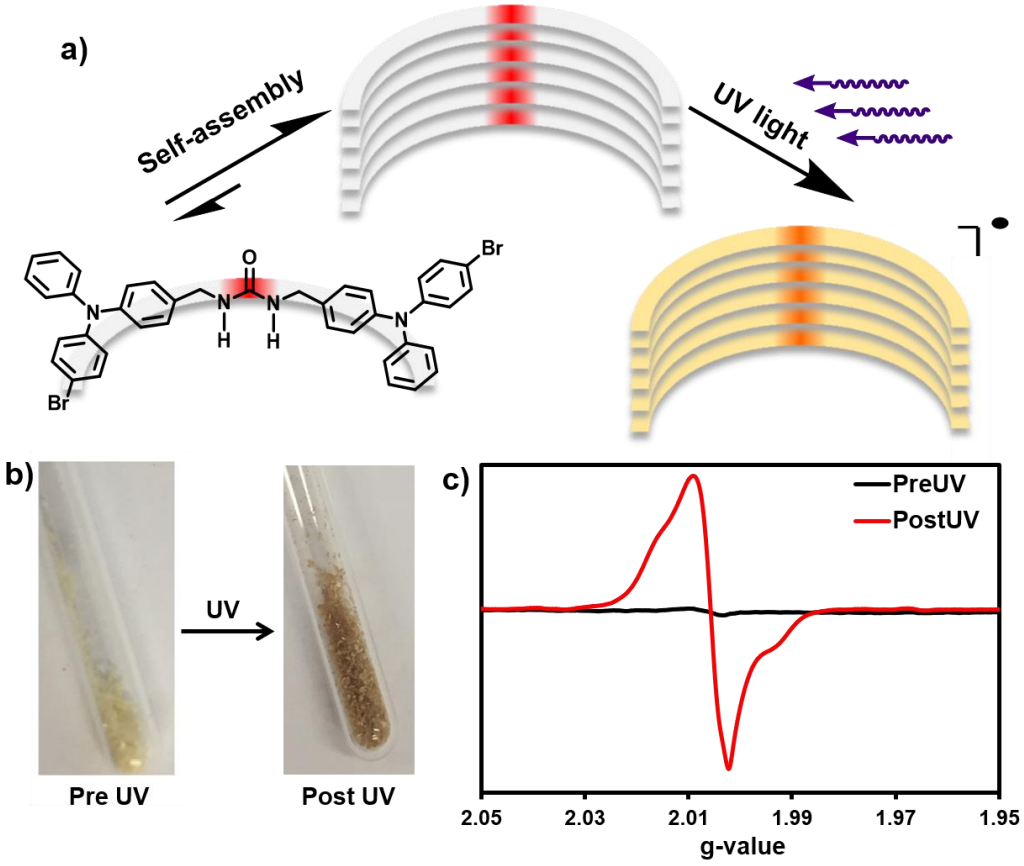

Figure 3.1. (a) Self-assembly of a triphenylamine derivative affords persistent radicals upon irradiation with UV light. (b) UV-irradiation induces a noticeable change in color. (c) A significant radical signal is observed which corresponds to 1 in ~600 molecules displaying a radical after 1 h of UV-irradiation and up to 1 in ~150 after 8–11 h.

Para substituted TPAs are prevalent examples of molecules that exhibit persistent radicals.[9] For example, Magic Blue, an antimony salt of tribromo TPA, is a commercial one-electron oxidant employed for many chemical processes.[10,11] The stability of substituted TPA radicals, has led to their use as promising spin-containing units for organic polymer based magnets.[12,13] These organic magnets are designable offering moldability and tunability. The oxidation of the TPA also alters its photophysics, leading to quenching of its fluorescence.[14,15] Typically, TPA compounds require para substitution on all the phenyl rings to generate stable radical cations.[16,17] The extra substitution helps to slow down degradation reactions such as benzidine formation.[16] Usually, chemical or electrochemical oxidation is required to generate the radicals.[14,15] Even without the oxidation to a radical, TPAs still find many uses as two-photon absorbers,[18,19] organic light emitting diode materials,[20] solvatofluorochromatic intramolecular charge transfer (ICT) molecules,[21] and as aggregation induced emission (AIE) compounds.[22,23]

The Shimizu group utilizes the three-centered urea interaction to drive assembly of linear and macrocyclic monomers into tapes, rods, and columns.[24] In the case of benzophenone containing monomers, assembly influences the photophysics and affords surprisingly stable radicals upon UV-irradiation.[25,26] For comparison, unassembled structures in solution show no radical formation upon UV-irradiation. Our hypothesis is that supramolecular assembly significantly enhances radical stability. Here, we test if urea-tethered triphenylamines will be affected in a similar manner.

We synthesized and compared the structures and properties of a methylene urea bridged 4-bromo TPA dimer (**3**) against 4-bromo TPA (**1**) and a protected urea analog (**2**). The structure of dimer **3** features one bromine on each TPA adduct to assist in intersystem

crossing (ISC) from the excited singlet to the triplet state which can be aided by the heavy atom effect and should help promote radical generation from UV-irradiation. The heavy atom effect increases ISC due to spin orbit coupling.[27] Additionally, one para position on each TPA unit of **3** was left intentionally unsubstituted. Typically, fully substituted TPA's are required for radical stability.[9] Here, we test if supramolecular assembly can provide stability to unsubstituted TPA radicals, which in turn, would allow for greater variability in TPA structures with stable radical characteristics. Radical formation was investigated by two methods: electrochemical oxidation and UV-irradiation. Both of these methods can generate radical cations in TPA compounds, with the former being well-known,[14,15] and the latter requiring a reducible agent in the molecule itself[28] or in molecules close-by (i.e. solvent).[29] Our goal is to characterize these systems by electron paramagnetic resonance (EPR) spectroscopy to understand how solid-state organization influences their ability to generate stable radicals versus dissolution. Specifically, we are testing (1) if self-assembly can stabilize radicals and (2) if UV-irradiation is a useful tool to generate TPA radicals in reasonable quantities. Additionally, we will examine the solvent dependent photophysics of the triplet and singlet emissions of these molecules.

3.2 RESULTS AND DISCUSSION

The urea tethered triphenylamine **3** was synthesized in five steps from commercial 4-bromotriphenylamine using a Vilsmeier–Haack reaction with phosphoryl chloride to yield the aldehyde,[30] which was subsequently converted to the alcohol via hydride reduction (Figure 3.1).[31] After bromination of the alcohol,[32] two TPA units were tethered through triazinanone under basic conditions. Deprotection of the urea afforded **3** as a pale yellow powder. Colorless needles were regularly obtained by slow evaporation of ethyl

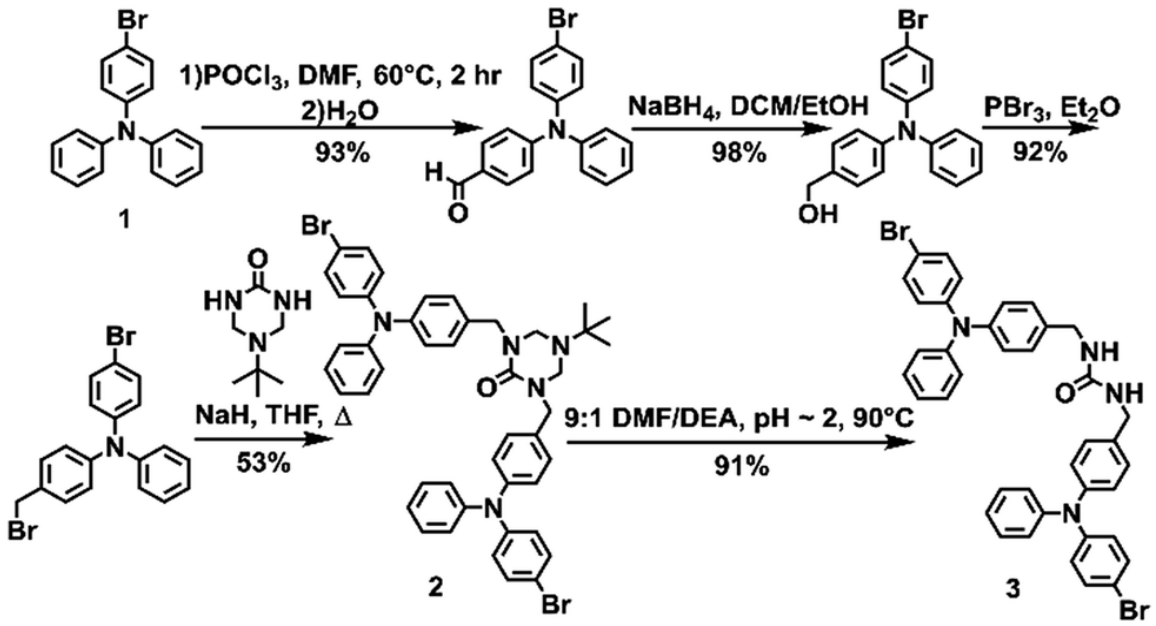

Scheme 3.1. Synthetic scheme for **2** and **3**.

acetate solutions (~20 mg mL−1) and were used for all solid-state measurements. The crystals were also subjected to X-ray diffraction analysis.

Triphenylamine **3** crystallized in the orthorhombic system in the *Pccn* space group. The X-ray structure revealed the desired compound with a linear *trans–trans* arrangement of the ureas with the two TPA units outstretched on both sides of the methylene urea tether in an anti-parallel manner. Crystallographically, the structure is disordered with two molecular orientations present (Figure 3.14) with the major component population of 91%. The urea carbonyl, which is located on a crystallographic C_2 axis, is common to both components. The individual molecules are organized into chains extending along the crystallographic *c*-axis through characteristic three-centered urea hydrogen bonds with a twisting angle of 51.6(1)°. The hydrogen-bonded urea groups (N(H)···O distances of 2.823(3) and 2.70(2) Å, (Figure 3.2a)) generate an X-shaped chain when viewed down the *c*-axis (Figure 3.2b). The twisting is likely caused by the extra steric bulk of the TPA since

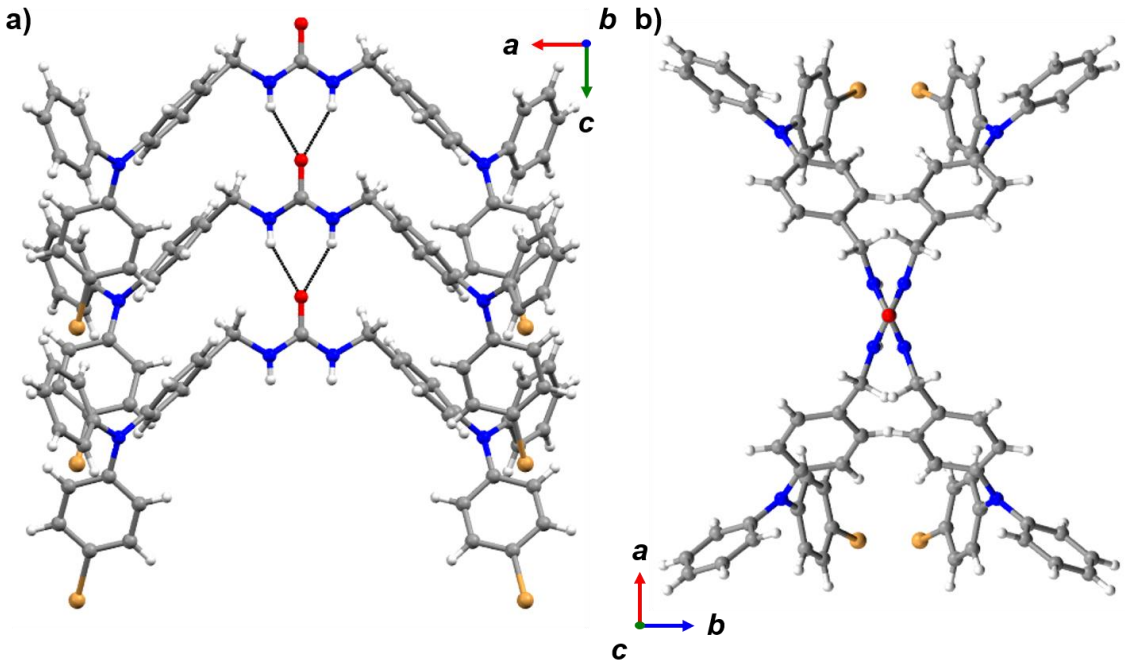

Figure 3.2. Views from **3** in the solid-state. Disorder was omitted for clarity. (a) Packing is driven through zig-zagged chains of urea hydrogen bonding. (b) Ureas adopt a twisting orientation creating an X-shape looking down the *c*-axis.

similar dibenzylic systems typically have straight urea chains according to a Cambridge Structural Database survey (CSD 5.39, September 28, 2018).[33]

To examine how solvent and assembly affects the photophysics of the TPA compounds, the absorption and emission for **1**, **2**, and **3** were taken in six solvents and in the solid-state at room temperature. The studies in dichloromethane, dimethyl sulfoxide, ethyl acetate, ethanol, acetonitrile, and tetrahydrofuran are summarized in Table 3.1 and 3.3. In all the tested solvents, the absorption spectra of **1**–**3** were nearly identical, with a strong $\pi\pi^*$ transition at approximately 300 nm dominating the spectra with no other bands readily apparent (Figure 3.1a). This suggests that in solution the proximity of the two TPA units have little effect on the absorption properties. On average, **2** and **3** were red-shifted by 2 nm compared to **1**. As expected, the molar absorptivity for **2** and **3** were very similar

and twice that of **1** with values ranging from 4.70–5.53 × 10^4 $M^{-1}cm^{-1}$ and 2.12–2.68 × 10^4 M^{-1} cm^{-1}, respectively.

Table 3.1. Data Collection and Refinement for Crystals Incorporating **1** or **2.**

Compound	Solvent	λ_{abs} (nm)[a]	ε (× 10^4 M^{-1} × cm^{-1})	λ_{ems} (nm)[b]	$\tau_{<avg>}$ (ns)[c]
2	DCM	304	5.11	365, 435*	0.8
	DMSO	302	5.42	451	5.1
	EtOAc	301	5.34	365	0.1
	EtOH	301	4.95	361	0.1
	MeCN	300	4.70	371, 451*	3.0
	THF	302	5.47	366*, 444	<0.1
3	DCM	303	5.20	366, 449*	2.2
	DMSO	302	5.41	369, 452*	4.1
	EtOAc	301	5.53	364*, 453	0.1
	EtOH	300	5.45	362*, 437	0.1
	MeCN	300	5.01	497	2.8
	THF	302	5.22	367*, 457	<0.1
	Solid	358	--	447	1.0

[a] Peak position at largest absorption band. [b] Peak positions at largest emission bands in nm (largest denoted with * if applicable, excited at λ_{abs}). [c] Average lifetime of largest emission peak.

For solid-state samples, crystals of **3** were first examined by PXRD to probe if the bulk crystalline material was similar in structure to the single crystal of **3**. Figure 3.16 compares the experimentally observed PXRD pattern to the predicted powder pattern simulated from the SC-XRD data. Seen here is an excellent correlation, suggesting that the bulk material is single phase and similar in structure to the solved crystal structure. This indicates that the photophysical measurements of the bulk material would be representative of the single crystals. Self-assembly of **3** resulted in a red shift of the absorbance of about 60 nm with slight broadening of the main peak (Figure 3.3a). A similar red shift has been reported before for other triphenylamine derivatives on the basis of J-aggregates;[34] however, this is more common for planar dyes.[35]

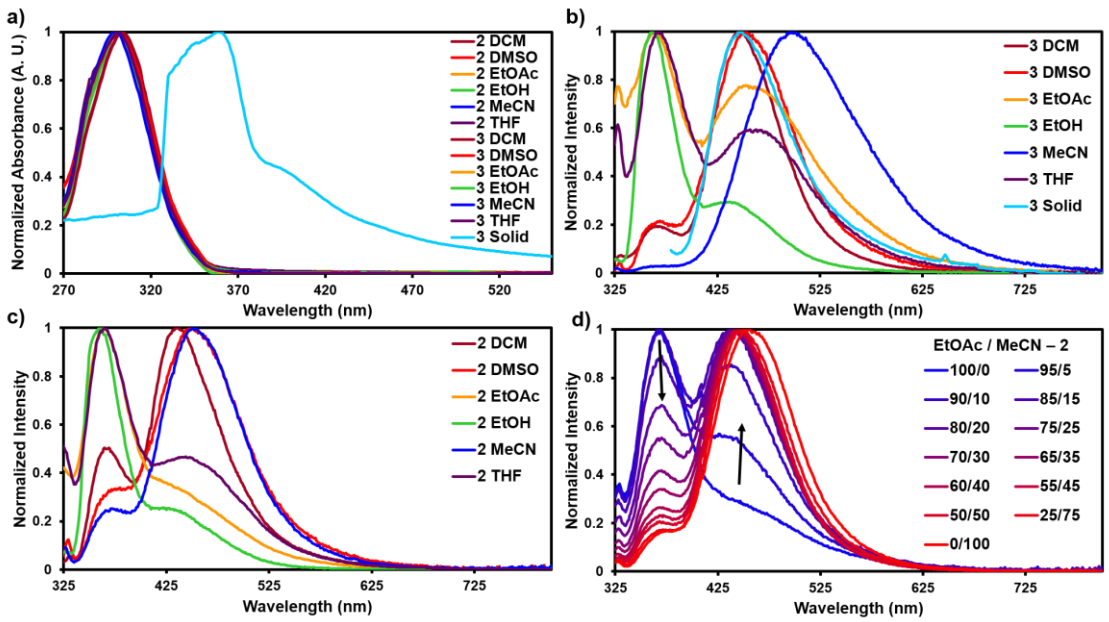

Figure 3.3. Absorbance and emission spectra of **2** and **3** at room temperature. (a) Normalized absorbance of **2** and **3** in different solvents and **3** in the solid-state. (b) Emission of **3** in different solvents and the solid-state. (c) Emission of **2** in different solvents. (d) Peak shift for **2** in the emission spectra changing from ethyl acetate to acetonitrile.

The emission spectra recorded in solution for **2** and **3** exhibited two main transitions either at approximately 370 nm (Band 1) and/or 450 nm (Band 2). As seen in Figure 3.3b and c, the intensities of these bands varied widely on the basis of solvent with **2** exhibiting more Band 1 character and **3** more Band 2. Band 1 is generally considered the fluorescence band for TPA systems.[21] To identify Band 2, further experiments were carried out.

First, the emission of **1** was taken in different solvents to probe if Band 2 was derived from an ICT process. Although ICT typically requires a donor–π–acceptor system,[36] the TPA units of **2** and **3** could rotate over to each other allowing the TPA units on either side of the urea tether to act as both the donor and acceptor in the ICT exchange without the need for a π-system intermediate. For this case, the TPAs would have to adopt

acceptor characteristics since TPAs are typically only the donor in ICT systems.[37] As seen in Figure 3.20, **1**, which is only a single TPA unit, also exhibited Band 2. This suggests that band 2 is not due to an ICT process.

Second, DOSY NMR studies were carried out on **3** to probe if Band 2 originated from an AIE process. Since AIE has been known to create new emissive bands,[38] ureas are known aggregators,[39] and AIE has been observed in TPA systems before[22,23] it seems reasonable that Band 2 could be derived from this process. For DOSY NMR, aggregation is detected when the observed hydrodynamic radius is significantly higher than the radius of the monomer. DOSY studies were conducted on solutions of **3** in deuterated acetonitrile (1 mM and 100 μM). This solution was chosen since it displayed the most significant Band 2 character of all the trials. As seen in Figures 3.23 and 3.24, no aggregation was observed for **3** in acetonitrile since the observed hydrodynamic radius of approximately 8 Å for both solutions is only slightly higher than that calculated from the crystal structure monomer of **3** (~6 Å). The slightly higher radius may be from solvation or a slight amount of dimerization, but definitively no large-scale aggregation was observed. Considering that more dilute solutions (10 μM) were used for photophysical measurements and no aggregation was observed in more concentrated samples, this suggests that AIE is not responsible for Band 2.

With ICT and AIE ruled out for the occurrence of Band 2, phosphorescence is suggested as the likely origin. Phosphorescence is common for structures containing TPAs that are employed in OLED materials.[40,41] Additionally, the peak position in the emission spectra is in good agreement for where phosphorescence is typically observed in TPA compounds. The bromine substituent can increase spin-orbital coupling via the heavy atom

effect, which gives access to the triplet state thus enhancing phosphorescence.[27] This effect can occur with either the heavy atom being directly connected into in the π-system,[41] or in close proximity.[42] The former case could explain why all three compounds exhibit Band 2, while the latter case could explain the intensity of this band (3 > 2 > 1). The emission spectra were also measured in the presence of a triplet quencher (triethylamine) and in an oxygen-saturated solution of dichloromethane. The emission was reduced in both cases (Figures 3.36 and 3.37), further suggesting that this band arises from phosphorescence.

For **1**–**3**, increasing solvent polarity resulted in increased phosphorescence, except in the case of polar protic solvents (ethanol) which showed little to no phosphorescence (Figures 3.3b and c). Solvent dependent phosphorescence has been observed before when S_1 and T_n were similar in energy.[44] In this situation, different solvents stabilized either state in varying degrees resulting in different phosphorescent quantum yields for each solvent, which may be the case here as well. To further investigate the solvent dependence, we examined if phosphoresce could be 'turned on' by the addition of a polar solvent to a non-polar system (Figure 3.3d). Starting with a fluorescent non-polar system (**2** in EtOAc), the addition of acetonitrile slowly turned on phosphorescence until the system was mostly phosphorescence clearly showing the solvent dependent nature of these emissive bands.

The luminescent lifetimes for **2** and **3** were found to be quite short for TPA derivatives with fluorescence and phosphorescent lifetimes estimated to be around 0.1 ns and 3 ns, respectively (Table 1, Figures S20 and S21). This may be due to competing non-radiative decay processes introduced by the heavy atoms. Typically, fluorescent lifetimes for TPA containing compounds tend to hover around 2 ns,[45,46] but heavy atom containing TPA derivatives with small π-systems have be seen to exhibit shorter lifetimes (<0.1 ns).[32]

For the phosphorescent lifetimes, while the heavy atom effect does increase phosphorescence intensity[27] it can shorten the lifetimes as well.[47]

In the solid-state it was not indicatively clear if fluorescence or phosphorescence was occurring as both the Stoke's shift (89 nm) and lifetime (1.0 ns) were in-between the expected values for fluorescence (65 nm, 0.1 ns) and phosphorescence (150 nm, 2.0 ns) determined from solution studies. Additionally, attempts at measuring accurate quantum yields for these compounds were unsuccessful due to radical generation and its subsequent effects on the photophysical properties.

The short observed lifetimes could be explained by the formation of stable radicals or by other non-radiative pathways. Thus, we turned to X-band EPR spectroscopy to probe radical formation within solution samples. First, a solution of **3** (~1 mM) was prepared in degassed DCM and was sealed under argon. While no EPR signal was observed pre UV, UV-irradiation (1 h) of the sample resulted in an EPR signal with a *g*-value of 2.005 (Figure 3.27). However, this radical was unstable and found to rapidly undergo degradation reactions. Figure 3.31 compares the ^{1}H NMR spectra of **3** in solution before and after UV-irradiation. The post UV sample shows nearly a complete loss of all of the parent resonances. Post-UV absorption and emission spectra also followed this trend (Figure 3.19 and 3.22) clearly indicating that radicals of **3** generated in solution are not stable. This is not unexpected since electrochemical studies of control **1** indicate an unstable radical cation in solution[48] and radical cations generated from TPAs with unsubstituted para positions are known to be unstable in solution.[16,17]

Next, EPR spectra were recorded on crystals of **3** in order to investigate how solid-state assembly influences the formation of radicals. First, EPR spectroscopy was performed on a triply recrystallized sample of **3** (3.9 mg) which was UV-irradiated for 6 h. Figure 3.28 shows the recorded EPR spectra, which displays a broad signal with an axial powder pattern shape. The observed g-value is 2.006, which is in the range of TPA radical cations in solution (2.002–2.005).[9] Singly recrystallized samples of **3** (10 mg) were also examined pre and post UV-irradiation (Figure 3.1c). As expected, no signal was seen pre irradiation; however, after 1 hour of UV-irradiation a broad EPR signal identical to the triply recrystallized sample was observed.

The persistence of the photogenerated radicals was examined using dark decay studies in which the recrystallized sample was irradiated for one hour and then stored in the dark at room temperature under argon. The EPR spectrum was monitored over a month to estimate its stability (Figure 3.4a). EPR signals were doubly integrated to obtain the area, which was plotted versus time after UV-irradiation (Figure 3.4a, inset). A reliable radical signal persists up to a month with a half-life of approximately one week. After two months,

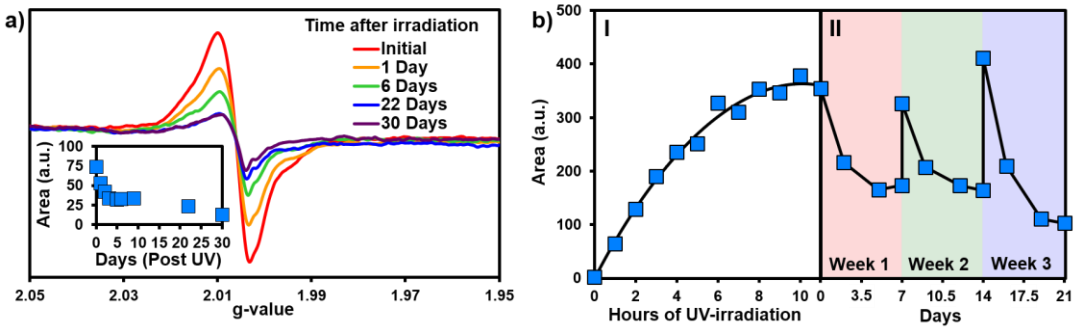

Figure 3.4. EPR data for **3** in the solid-state. (a) Dark decay after 1 hour of UV irradiation. Inset: the double integration of the dark decay spectra plotted versus time post UV irradiation. (b) (I) The double integration of the EPR spectra over time of UV irradiation followed by (II) a regeneration/decay study of the radicals. For part II, after the initial irradiation to the maximum radical concentration, the sample was irradiated for an additional 6 hours at the start of weeks 2 and 3.

when no radical signal was observable, we took a ^{1}H NMR of the sample to see if the sample had degraded similarly to the solution study. Remarkably, the NMRs were identical to the initially synthesized materials indicating that **3** is photostable in its crystal form (Figure 3.32).

Next, we estimated the maximum concentration of radicals that could be generated through UV-irradiation by plotting the area of the EPR signal versus time exposed to UV light. The amount of radicals increases steadily with irradiation time (1 to 6 h) as seen in Figure 3.4b part I. The plot of the double integration of the EPR signal versus time starts to plateau after 7–11 h of UV-irradiation with the crystals of **3** turning deep brown in color during the process (Figure 3.1b). The concentration of radicals was approximated using a calibration with standard solutions of Magic Blue in DCM. Comparing the area of the EPR spectra of the solid-sample versus the Magic Blue calibration can give an approximate concentration of radicals generated in the solid-state. After 11 hours of UV-exposure, 9.0 mg of **3** generated the same number of radicals as 100 μL of a 0.82 mM solution of Magic Blue, suggesting that 1 in 150 molecules of **3** have a radical (or 1 in 300 TPA units, Figure 3.30). Similar calculations for the 3.9 mg of the triply recrystallized sample were of a similar magnitude with ∼1 in 250 molecules exhibiting a radical after only 6 h of irradiation.

With no noticeable degradation of **3** occurring after radical formation in crystalline samples (Figure 3.32), we investigated if the radicals could be 'regenerated' after decay with repeated UV exposure. Typically, with chemical or electrochemical oxidations of TPAs to their corresponding radical cations, loss of the radical signal likely means the sample has degraded, and samples must be resynthesized. Remarkably, once the signal of

3 decays to half signal, irradiation with UV-light restores the radical concentration back to its maximum value (Figure 3.4b, Part II). The samples were re-irradiated for 6 hours at the start of weeks 2 and 3 to regenerate the signal. As seen in Figure 3.4b part II, the radicals decay at approximately the same rate over the three week long cycles. Also notable is that similar quantities of radicals are generated each time the crystals of **3** are UV-irradiated, demonstrating the exceptional stability and reproducible nature of the assembled structure versus in solution.

Next, we probed how the photogenerated radicals influenced the properties of the crystals as a whole. First, we compared the photophysics of the crystals before and after UV-irradiation (4 h). Both the absorption and emission were significantly quenched upon radical formation (Figure 3.18 and 3.21). This was quite striking considering the radical concentration was relatively low compared to the bulk sample. Oxidation of TPAs to radical cations is known to quench the photophysical properties,[14,15] but typically it is quantitative in nature, at least in solution. This indicates that the generated radical is strongly delocalized to effect the whole system and behaves similarly to a radical cation.

To further probe the nature of the radical, irradiated (4 h) brown crystals of **3** were subjected to SC-XRD and IR spectroscopy. No change was observed in the overall single crystal structure; however, we noticed a minor change in the amount of disorder in the crystal going from 91% major conformer to 95%. This is likely correlated to the specific single crystal chosen for SC-XRD and is probably unrelated to radical formation. We expect that the TPA units are too bulky to self-correct during crystal formation leading to an array of different conformer percentages depending on the single crystal. For the IR studies, pre and post UV spectra were found to be nearly identical with no visible changes

(Figure 3.33). The combination of SC-XRD and IR suggest that either the radical is highly delocalized and/or is not concentrated enough to be characterized by these methods.

Cyclic voltammetry (CV) was used to further characterize the electronic structure of **3** in solution. Since the radicals in the solid-state acted similarly to TPA radical cations, this method could further characterize the types of radicals generated in this system. The oxidation of **3** in DCM shows two pseudo-reversible oxidation waves at 1.0 V and 1.2 V vs. SCE (Figure 3.5a). In comparison, the oxidation of parent compound **1** leads to a degradation that was immediately visible in the CV,[48] which suggests that **3** is more stable towards oxidation than the parent compound. Controlled potential electrolysis performed on **3** at +1.2 V passed at total of 3.98 electrons per molecule (Figure 3.35). Thus, each oxidative wave in Figure 3.5a is attributed to a $2e^-$ oxidation of the symmetric compound **3**. Each electron is expected to come from the TPA units of the molecule, which would be consistent with previously reported results that have only one TPA unit per molecule.[48] For comparison, an electrochemical study on compound **2** showed that slower scan rates (40 mV s−1) were required to obtain pseudo-reversible oxidation waves also near 1.0 V and 1.2 V vs. SCE (Figure 3.34). This indicates the rigidity of backbone of **2** has a clear impact on electron transfer kinetics.

Bulk electrolysis on a ∼1 mM solution of **3** in DCM was performed at the first oxidation peak to generate a radical cation in solution. The first peak was chosen for the oxidation since it likely affords an overall dication with each TPA unit being oxidized once. Electrolysis was performed for ∼5 hours to afford a bright yellow solution; however, once electrolysis was completed the resulting sample was unstable at room temperature and turned teal within 15 min. EPR analysis showed no signal. Thus, the electrolysis was

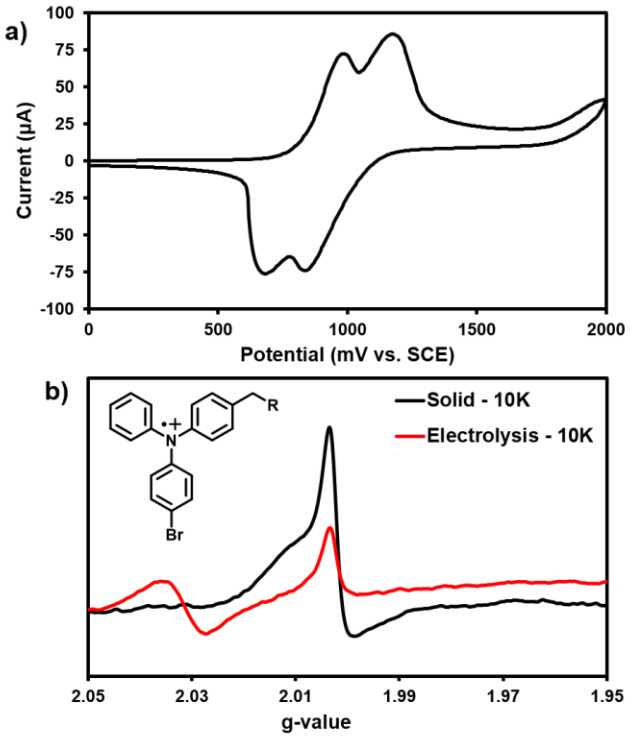

Figure 3.5. (a) CV for 1 mM **3** in a 0.1 M $(n\text{-Bu})_4N^+PF_6^-$ DCM solution, scan rate 100 mV s^{-1}. SCE = saturated calomel electrode. (b) Solution EPR for **3** at 10 K after bulk electrolysis at first oxidative peak (red) along with a solid-state EPR for **3** also at 10 K EPR after 3 hours of UV irradiation (black). Inset: proposed structure of radical responsible for EPR signal.

performed on a new sample that was immediately immersed in liquid nitrogen for transportation and the EPR recorded at 10 K. As seen in Figure 3.5b, two peaks for the electrolytic sample can be seen at g-values of 2.031 and 2.002.

The UV-generated radicals of crystalline **3** were also recorded at 10 K for comparison and showed no change in the line width and a slight shift in *g*-value to 2.002 compared to its room temperature spectrum, consistent with population of lower energy states. The peak at g-value = 2.002 was consistent in the electrolytic solution sample and the UV-irradiated crystals **3**. This suggests that crystalline **3** may form a similar radical species to electrolytic sample. Additionally, this is in good agreement with where TPA

radical cations typically appear in EPR spectra.[9] Thus, it is likely that the photogenerated radicals in assembled **3** are similar to radical triphenylamine cations formed by electrolysis (at *g*-value = 2.002), although it is not clear what anion is being formed in the crystalline sample for this process to occur. We are currently examining macrocyclic derivatives and are planning high field EPR studies that could help probe this question. The second isotropic signal at *g*-value = 2.031 was exclusive to the electrolyte sample and is attributed to degradation products.

Self-assembly of TPA urea dimers can stabilize the UV generated organic radicals in stark contrast to their solution counterparts. The concentration of the radicals is readily controlled by irradiation time up to a maximum of 1 in ∼150 molecules. The presence of the radicals can be visualized simply through their photophysical quenching behavior. Advantageous to this system is that the radicals can be generated in the solid-state without noticeable degradation to the starting materials and display a half-life up to a week. Additionally, these radicals can be regenerated upon re-irradiation without any loss in radical concentration. A comprehensive study on how different halogen substituents on these TPA compounds influences the radical generation, stability, and concentrations may be invaluable in revealing the factors that govern the photophysics of these compounds.

3.3 CONCLUSIONS

In summary, a TPA methylene urea-tethered dimer was synthesized and readily afforded single crystals that organized the TPA through urea hydrogen bonding interactions. This solid-state assembly significantly stabilizes UV-generated radicals. Radicals formed in solution were unstable, as expected for incomplete *para* substituted TPA systems. In the solid-state, high quantities of radicals were formed, up to 1 in ∼150

molecules, which were persistent at room temperature with no observable degradation or significant changes in the single crystal X-ray diffraction. Further, radicals generated within the assembled framework have been shown to last up to a month with a half-life around a week. Most remarkably, after radical decay, radicals can be regenerated to their original maximum concentration with re-exposure to UV light. The photophysics of these materials were significantly quenched likely due to TPA hole transport properties even with relatively low radical concentration. Electrochemical evidence demonstrates that these compounds can be oxidized in solution at 1.0 V vs. SCE to generate radical cations, whose EPR spectra are similar to the UV-generated radicals in the solid-state. This suggests that the TPA radical cation is being formed in the solid-state and this electron transfer is reversible and reforms the parent compound over time. We are currently planning to carry out high-field EPR experiments as well as Dynamic Nuclear Polarization Magic Angle Spinning solid-state C13-NMR to further examine this process. Future work includes the synthesis of additional halogenated on the TPA analogs to elucidate the factors that govern radical formation, persistence, and quantity. Understanding how assembly enhances the stability of radicals would be exceedingly helpful in the end goal of making better conductive and magnetic materials that incorporate TPA scaffolds.

3.4 EXPERIMENTAL

3.4.1 General Experimental

NMR spectra were recorded on Bruker Avance 300 or 400 MHz spectrometers. Chemical shifts are reported in ppm (δ) and were internally referenced with the solvent peak. All chemicals were purchased from chemical suppliers and were used as received unless otherwise noted. High-resolution mass spectrum data were recorded using a direct

exposure probe (DEP) in electron ionization mode on a Waters QTOF-I quadrupole time-of-flight mass spectrometer. UV-irradiation of all materials were carried out with a Hanovia 450 W medium pressure mercury arc lamp cooled in a quartz immersion well. Samples were purged with argon before irradiation. All other instrument protocols are described in their own sections hereafter.

3.4.2 Synthesis and Characterization of Compounds

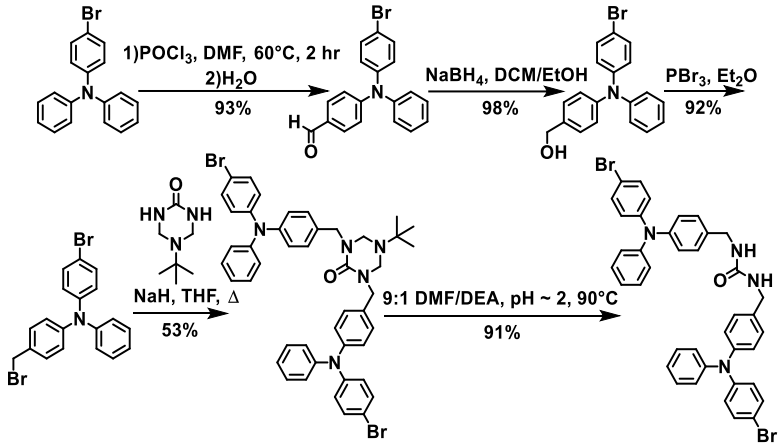

Scheme 3.2. Synthesis of compounds.

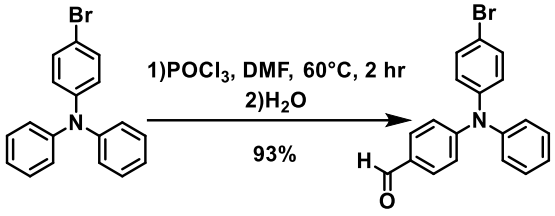

4-((4-Bromophenyl)(phenyl)amino)benzaldehyde: Compound was made according to previous procedures.[30] Phosphoryl chloride (840 μL, 9.0 mmol) was added dropwise to dry *N, N*-dimethylformamide (830 μL, 10.8 mmol) at 0˚C and the mixture was stirred at room temperature for 20 minutes. Then 4-bromo-*N, N*-diphenylaniline (2.590 g, 8.0 mmol) was added and this mixture was heated to 110˚ C then cooled to stir at 60˚ C for 2 hours. After cooling to room temperature, 50 mL of ice-cold water was added to the

mixture and the solution was neutralized with saturated $NaHCO_{3(aq)}$. The mixture was extracted with chloroform (3 × 50 mL) and the organics were washed with water (1 × 50 mL), then brine (1 × 50 mL), and dried with $MgSO_4$. The solvent was removed via rotary evaporation and the crude material was further purified by column chromatography (Hexanes/Ethyl Acetate = 3:1) to yield the product as a yellow solid (93%). Spectra matched that as previously reported.[30] ^{1}H NMR (300 MHz, $CDCl_3$): δ (ppm) 9.82 (s, 1H), 7.69 (d, *J* = 8.5 Hz, 2H), 7.44 (t, *J* = 8.5 Hz, 2H), 7.35 (t, *J* = 7.8 Hz, 2H), 7.22-7.11 (m, 3H), 7.08-6.99 (m, 4H).

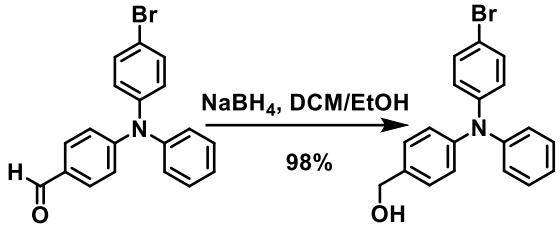

(4-((4-Bromophenyl)(phenyl)amino)phenyl)methanol: Compound was made according to previous procedures.[31] The previous aldehyde (2.609 g, 7.4 mmol) was dissolved in 120 mL of a 3:1 mixture of dry dichloromethane and ethanol. Sodium borohydride (0.308 g, 8.2 mmol) was added after and the mixture stirred at room temperature for 1 day in the dark. Then 180 mL of water was added and the mixture was extracted with dichloromethane (3 × 70 mL) and dried with $MgSO_4$. Solvent was removed via rotary evaporation leaving behind the alcohol as a sticky solid (98%). ^{1}H NMR (300 MHz, $(CD_3)_2SO$): δ (ppm) 7.41 (d, *J* = 8.8 Hz, 2H), 7.34-7.24 (m, 4H), 7.09-6.97 (m, 5H), 6.86 (d, *J* = 9.0 Hz, 2H), 5.14 (t, *J* = 5.8 Hz, 1H), 4.45 (d, *J* = 5.9 Hz, 2H). ^{13}C NMR (75 MHz, $CDCl_3$): δ (ppm) 147.42, 147.11, 147.07, 135.73, 132.32, 129.55, 128.51, 125.32, 124.59, 124.47, 123.49, 115.06, 65.18. HRMS (DEP): [M+] calculated, 353.0415; found, 353.0409.

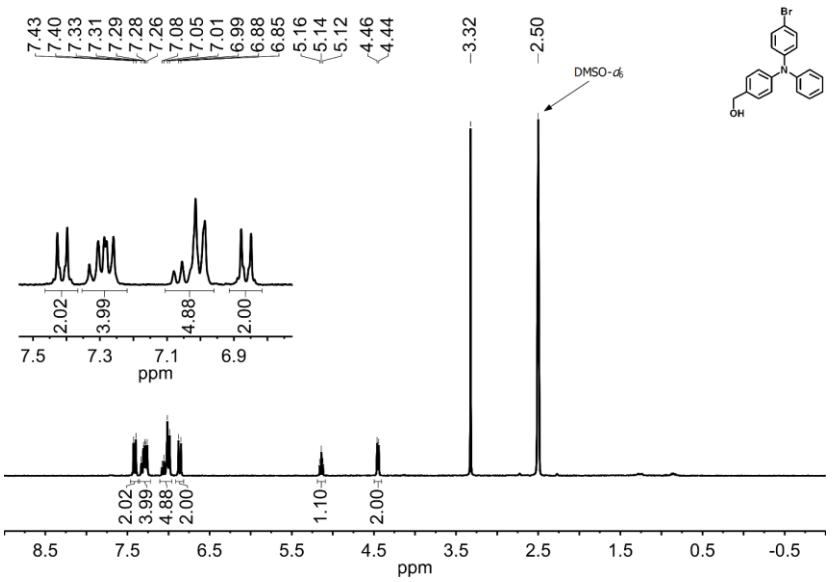

Figure 3.6. ^{1}H NMR of alcohol **2** ($(CD_3)_2SO$, 300 MHz).

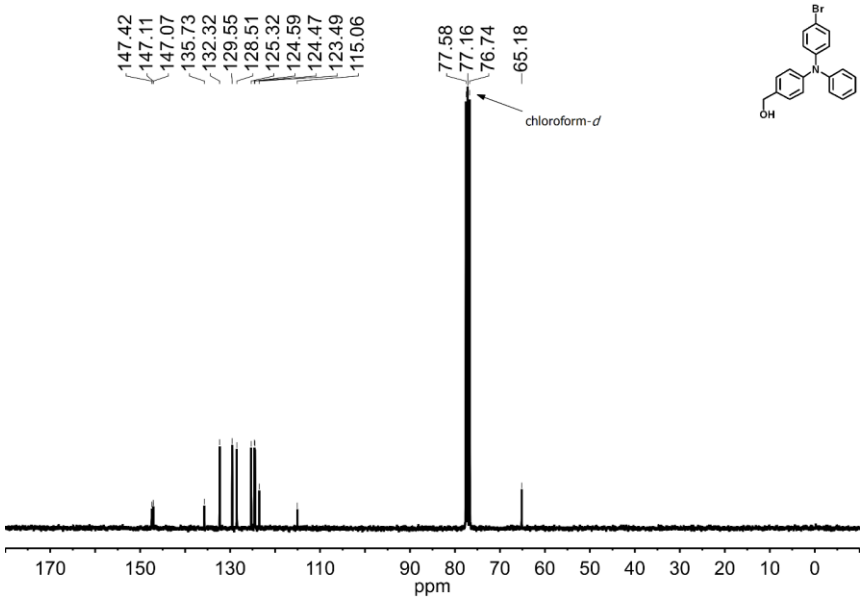

Figure 3.7. ^{13}C NMR of alcohol **2** ($CDCl_3$, 75 MHz).

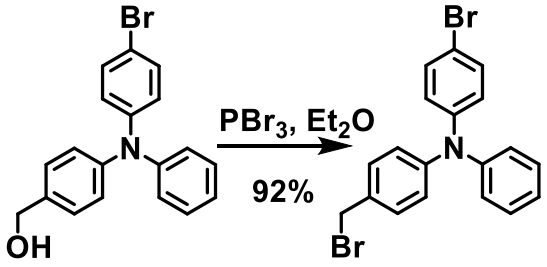

4-Bromo-*N*-(4-(bromomethyl)phenyl)-*N*-phenylaniline: Compound was made according to previous procedures.[32] The previous alcohol (2.253 g, 6.4 mmol) was suspended in 80 mL of dry diethyl ether and was cooled to 0 ˚C. Then a solution of phosphorus tribromide (363 μL, 3.8 mmol) in 10 mL dry diethyl ether was added dropwise over 5 minutes. The reaction stirred at room temperature overnight in the dark. In the morning, ice cold water (90 mL) and saturated $NaHCO_{3(aq)}$ (45 mL) was added to quench the reaction. The mixture was extracted with (1 × 90 mL) of dichloromethane and the organics were washed with brine (3 × 45 mL) and dried with $MgSO_4$. The solvent was removed under rotary evaporation to yield the bromide as a sticky solid (92%). ^{1}H NMR (300 MHz, CD_2Cl_2): δ (ppm) 7.40-7.23 (m, 6H), 7.13-7.04 (m, 3H), 7.03-6.92 (m, 4H), 4.51 (s, 2H). ^{13}C NMR (75 MHz, CD_2Cl_2): δ (ppm) 147.99, 147.36, 147.06, 132.63, 132.34, 130.58, 129.90, 126.09, 125.43, 124.27, 123.69, 115.69, 34.46. HRMS (DEP): [M+] calculated, 414.9571; found: 414.9580.

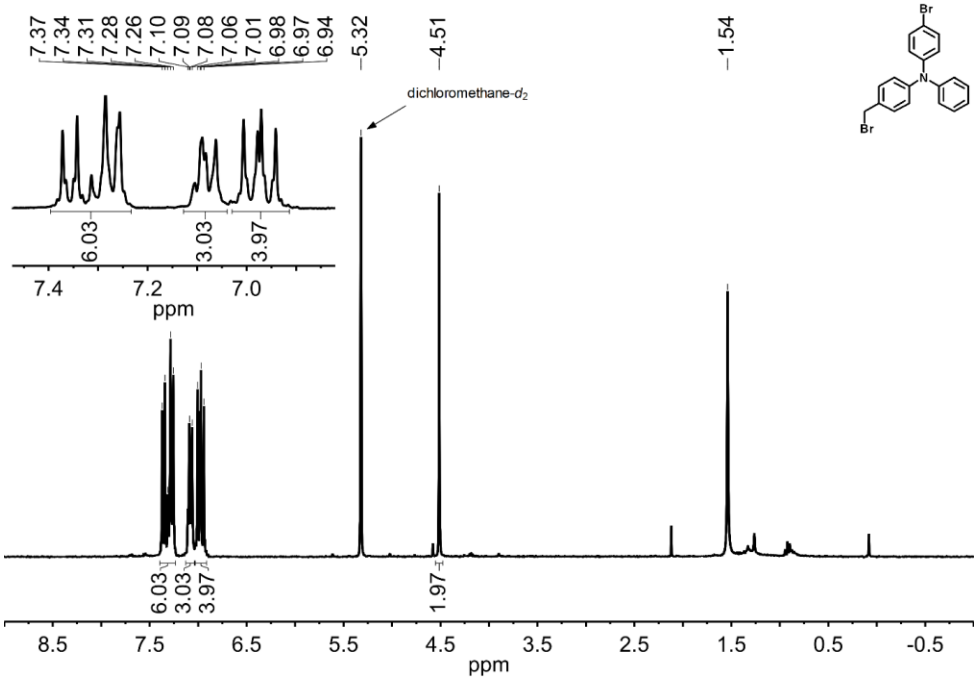

Figure 3.8. ^{1}H NMR of bromide **2** (CD_2Cl_2, 300 MHz).

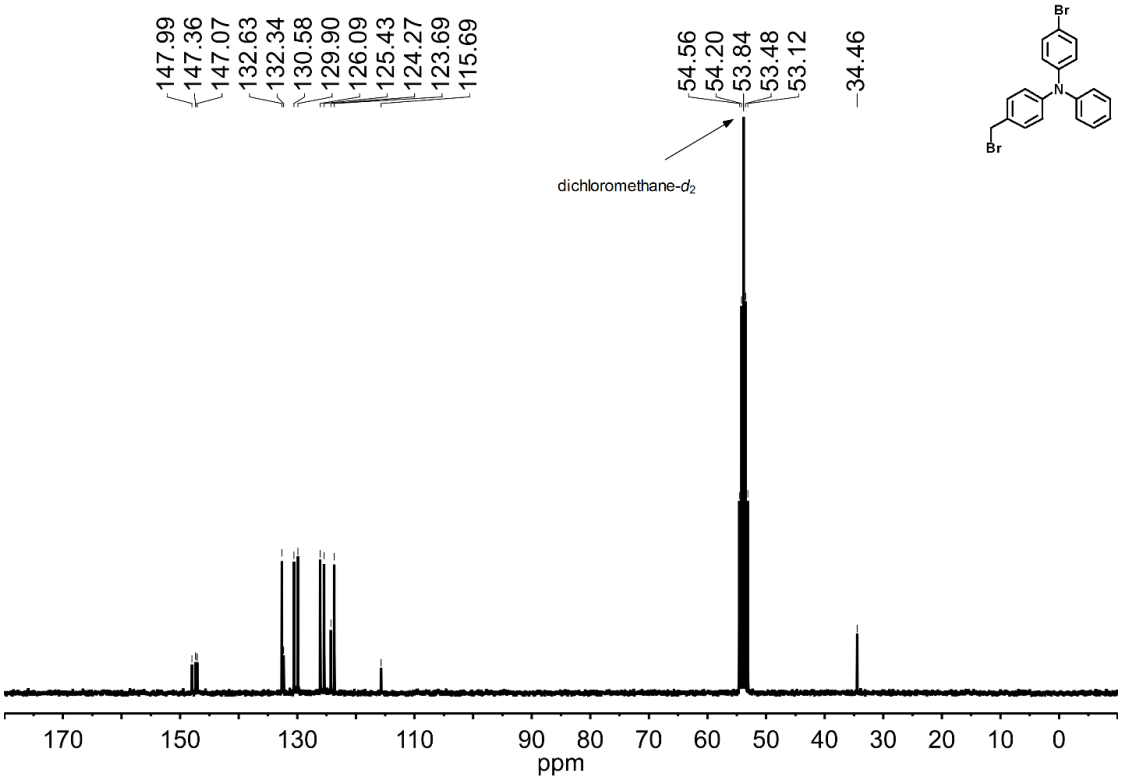

Figure 3.9. ^{13}C NMR of bromide **2** (CD_2Cl_2, 75 MHz).

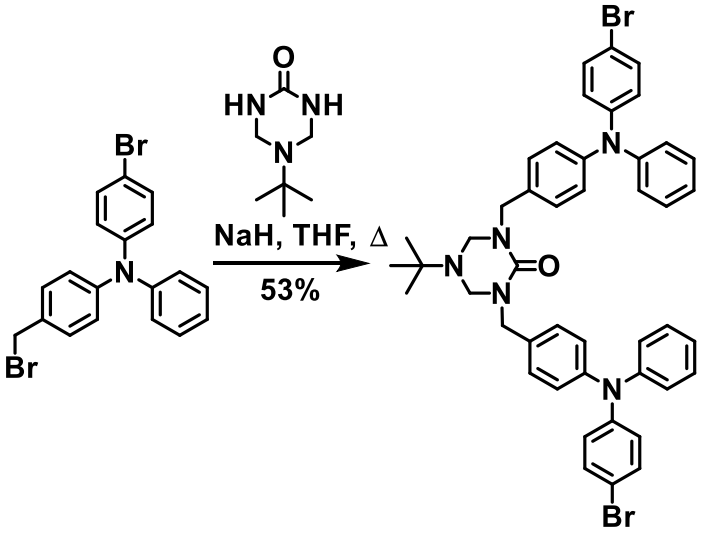

1,3-*bis*(4-((4-bromophenyl)(phenyl)amino)benzyl)-5-(*tert*-butyl)-1,3,5-triazinan-2-one: *tert*-Butyl triazinanone (0.209 g, 1.3 mmol) and sodium hydride (60% suspension in paraffin oil, 0.160 g, 4.0 mmol) were suspended in 20 mL of dry tetrahydrofuran and

was stirred for 10 minutes. Then the previous bromide (1.111 g, 2.7 mmol) was added as a solution in 20 mL of dry tetrahydrofuran. The reaction stirred at reflux in the dark overnight. After cooling to room temperature, 6 mL of both 1 N $HCl_{(aq)}$ and water were added to quench the reaction. This solution was extracted with dichloromethane (3 × 60 mL). The organics were washed with brine (1 × 60 mL) and dried with $MgSO_4$. The solvents were removed under rotary evaporation, and the product was isolated using column chromatography (Hexanes/Ethyl Acetate = 2:1) to yield the product as a sticky solid (53%). ^{1}H NMR (300 MHz, $(CD_3)_2CO$): δ (ppm) 7.43-7.26 (m, 12H), 7.10-7.01 (m, 10H), 6.93 (d, *J* = 8.9 Hz, 4H), 4.51 (s, 4H), 4.34 (s, 4H), 1.02 (s, 9H). ^{13}C NMR (75 MHz, $(CD_3)_2CO$): δ (ppm) 156.50, 148.27, 148.24, 147.16, 135.49, 132.99, 130.63, 130.36, 125.63, 125.44, 125.16, 124.27, 114.80, 62.39, 54.83, 48.39, 28.74. HRMS (DEP): [M+] calculated, 828.1907; found, 828.1927.

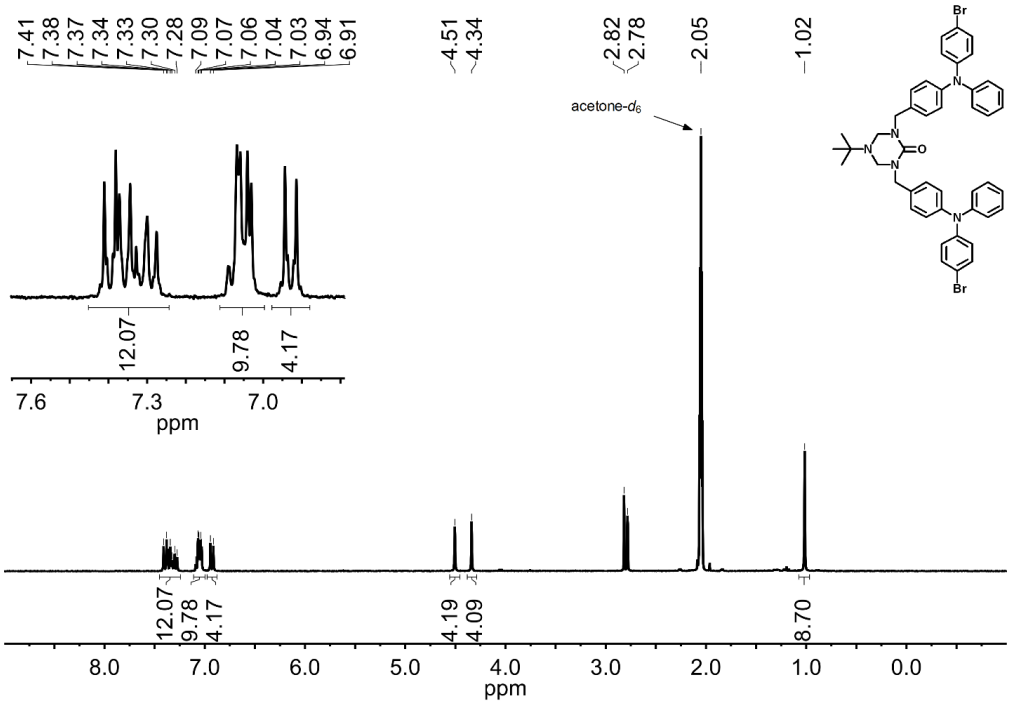

Figure 3.10. ^{1}H NMR of **2** ($(CD_3)_2CO$, 300 MHz).

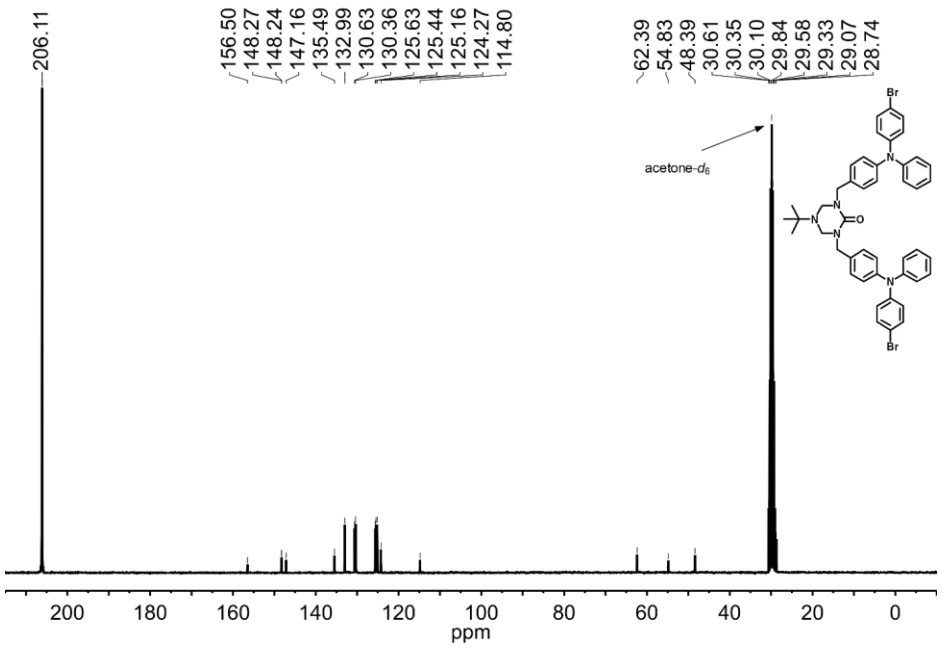

Figure 3.11. ^{13}C NMR of **2** ($(CD_3)_2CO$, 75 MHz).

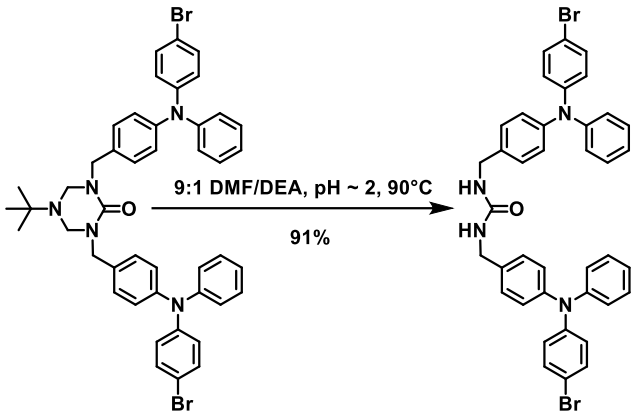

1,3-*bis*(4-((4-bromophenyl)(phenyl)amino)benzyl)urea: The previous protected urea (0.100 g, 0.1 mmol) was suspended in 50 mL of a 9:1 solution of *N*, *N*-dimethylformamide and diethanol amine and the pH was adjusted to 2 using 12 M $HCl_{(aq)}$. This mixture was heated at 90˚C for 2 days in the dark. The pH was readjusted to 2 using 12 M $HCl_{(aq)}$ every 12 hours until completion. After cooling to room temperature, the reaction was filtered and the residue was washed with 50 mL of water leaving behind the

product as a beige solid (91%). ^{1}H NMR (300 MHz, CD_2Cl_2): δ (ppm) 7.36-7.13 (m, 12H), 7.09-6.96 (m, 10H), 6.90 (d, *J* = 8.8 Hz, 4H), 4.70 (t, *J* = 5.8 Hz, 2H), 4.32 (d, *J* = 5.8 Hz, 4H). ^{13}C NMR (75 MHz, $CDCl_3$): δ (ppm) 158.04, 147.35, 147.00, 146.79, 133.81, 132.33, 129.56, 128.64, 125.27, 124.57, 124.47, 123.53, 115.07, 44.30. HRMS (DEP): [M+] calculated, 731.1016 found, 731.1025.

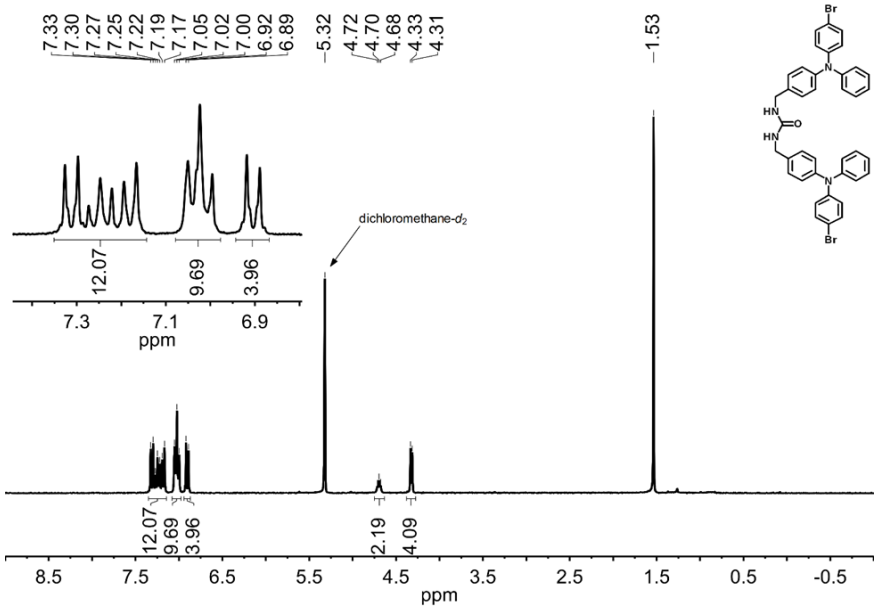

Figure 3.12. ^{1}H NMR of **3** (CD_2Cl_2, 300 MHz).

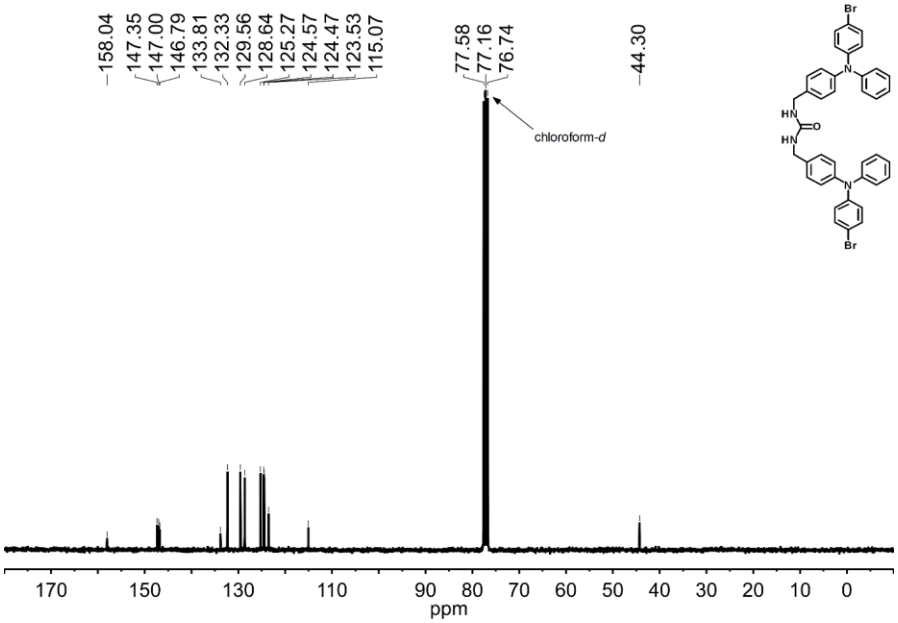

Figure 3.13. ^{13}C NMR of **3** ($CDCl_3$, 75 MHz).

3.4.3 Single Crystal X-ray Diffraction (SC-XRD)

X-ray intensity data from a colorless needle were collected at 100(2) K using a Bruker D8 QUEST diffractometer equipped with a PHOTON-100 CMOS area detector and an Incoatec microfocus source (Mo Kα radiation, λ = 0.71073 Å). The raw area detector data frames were reduced and corrected for absorption effects using the Bruker APEX3, SAINT+ and SADABS programs.[49,50] Final unit cell parameters were determined by least-squares refinement of 9851 reflections taken from the data set. The structure was solved with SHELXT.[51,52] Subsequent difference Fourier calculations and full-matrix least-squares refinement against F^2 were performed with SHELXL-20183 using OLEX2.[53]

The compound crystallizes in the orthorhombic system. The pattern of systematic absences in the intensity data was uniquely consistent with the space group Pccn, which was verified by structure solution. The asymmetric unit consists of half of one molecule, which is located on a two-fold axis of rotation. The structure is disordered. After routine location and anisotropic refinement of the unique half of the molecule, a very large residual electron density peak (magnitude 4.3 e-/$Å^3$) was observed in a chemically implausible site, ca. 2.0 Å from Br1. After ruling out data processing errors (crystal slippage, poor integration parameters, absorption correction, e.g.) the peak was eventually interpreted as the bromine atom of a minor 'whole-molecule' disorder component. Refinement of the site occupancy of this peak assigned as bromine and the major component bromine atom site occupancy summed to near one, providing support for this model. Subsequently, other peaks were picked from difference Fourier maps to complete the unique half of the minor disorder component, also located on the two-fold axis. The carbonyl C and O atoms are common to both disorder components. 1,2- and 1,3-distances in the minor disorder

component (atoms label suffixes “B”) were restrained to be similar to those in the major component (atom label suffixes “A”) via a SHELX SAME instruction. Anisotropic displacement parameters for atoms which are overlapped were held equal. An additional FLAT instruction was necessary for ring C9B-C14B, and Br1B was restrained to be equidistant from C11B and C13B. The disorder fractions were constrained to sum to one, and refined to A/B = 0.910(1) / 0.090(1). The same large residual peak / whole molecule disorder was observed in two other crystals. No sign of the disorder was evident in the diffraction frames, and no resolving twin law was found from the TwinRotMat program.[54,55] The modeled disorder suggests a deviation from ideal C_2 point symmetry in approximately 9% of molecules throughout the crystal. Solution in lower space groups lacking imposed C_2 symmetry showed the same disorder. All non-hydrogen atoms were refined with anisotropic displacement parameters. Hydrogen atoms bonded to carbon were placed in geometrically idealized positions and included as riding atoms with d(C-H) = 0.95 Å and Uiso(H) = 1.2Ueq(C) for aromatic hydrogen atoms, and d(C-H) = 0.99 Å and Uiso(H) = 1.2Ueq(C) for methylene hydrogen atoms. One unique position for the hydrogen atoms bonded to the urea nitrogen was located. It was refined isotropically with distances to both N1A and N1B restrained to be 0.84(2) Å. The largest residual electron density peak in the final difference map is 0.86 e-/Å^3, located 0.67Å from H11B. Crystal data are given in Table 3.2.

Table 3.2. Data Collection and Refinement for Crystals.

Identification Code	**3**
CCDC	1873066
Color of Crystal	Colorless
Empirical formula	$C_{39}H_{32}Br_2N_4O$
Formula weight	732.50

Temperature/K	100(2)
Crystal system	orthorhombic
Space group	Pccn
a/Å	18.5184(8)
b/Å	19.9443(7)
c/Å	9.0043(4)
α/deg	90
β/deg	90
γ/deg	90
Volume/Å^3	3325.6(2)
Z	4
ρ_{calc}g/cm^3	1.463
μ/mm^{-1}	2.475
F(000)	1488.0
Crystal size/mm^3	0.18 × 0.12 × 0.1
Radiation	MoKα (λ = 0.71073)
2Θ range for data collection/deg	4.4 to 54.368
Index ranges	-23 ≤ h ≤ 23, -25 ≤ k ≤ 25, -11 ≤ l ≤ 11
Reflections collected	123401
Independent reflections	3695 [R_{int} = 0.0442, R_{sigma} = 0.0136]
Data/restraints/parameters	3695/68/292
Goodness-of-fit on F^2	1.047
Final R indexes [I ≥ 2σ (I)]	R_1 = 0.0440, wR_2 = 0.1210
Final R indexes [all data]	R_1 = 0.0561, wR_2 = 0.1294

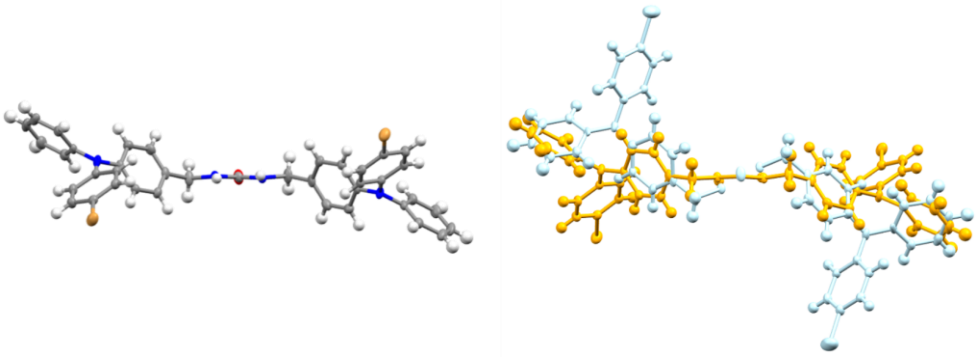

Figure 3.14. Thermal ellipsoid view of **3** at 50% probability (above) and disordered structure of molecule (below). For the disordered structure, two orientations are present on the C_2 axis with the CO on the two-fold axis in common with both. The orange structure is the major component at 91% vs. 9% for the other.

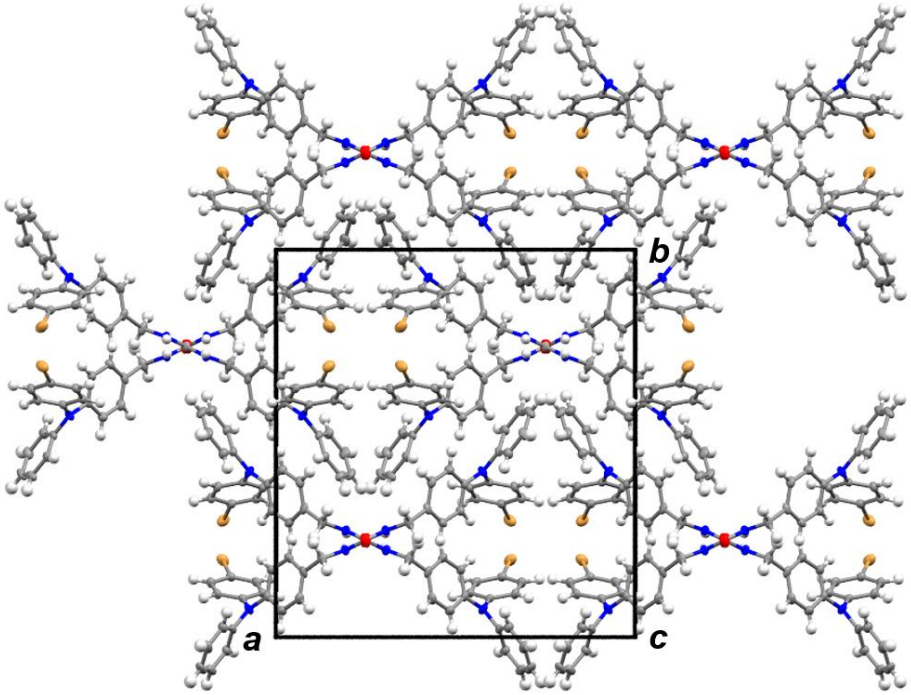

Figure 3.15. Crystal packing of **3** looking down the c-axis. Disorder was omitted for clarity.

3.4.4 Powder X-ray Diffraction (PXRD)

PXRD data was collected on a Rigaku D/Max-2100 powder X-ray diffractometer using Cu Kα radiation. The step can covered an angular range of 10-50˚ 2Θ in steps of 0.02˚.

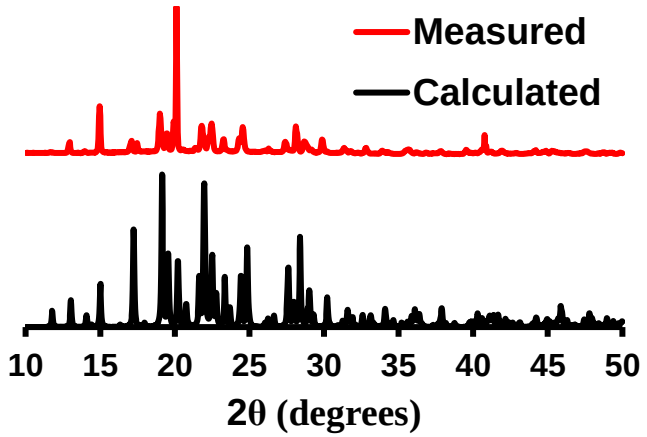

Figure 3.16. PXRD of **3**.

3.4.5 Absorbance Measurements

UV/Vis data was collected on either a Perkin Elmer Lambda 35 UV/vis spectrometer with UV Winlab software or a SoftMax M2 spectrometer (solid and solution, respectively). Spectra were recorded from 270-550 nm at 1 nm steps at room temperature. 10 μM concentrations were used for solution samples, unless otherwise noted. For solid samples, diffuse reflectance data was gathered initially and sequentially converted into absorbance data.

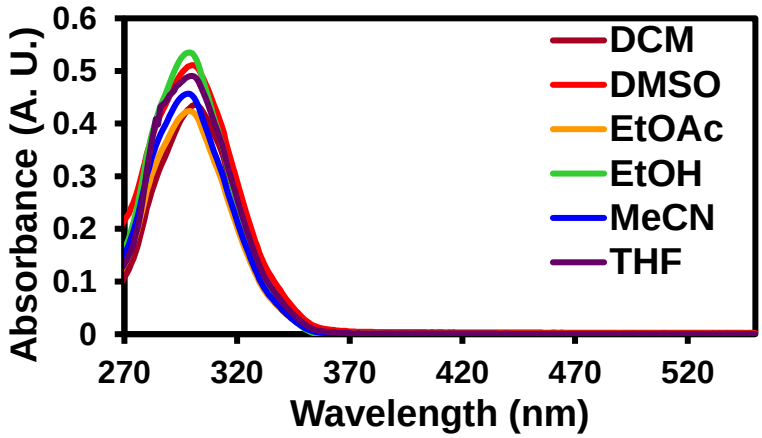

Figure 3.17. UV/Vis absorption spectrum of 1 in different solvents. Concentrations of 20 μM were used.

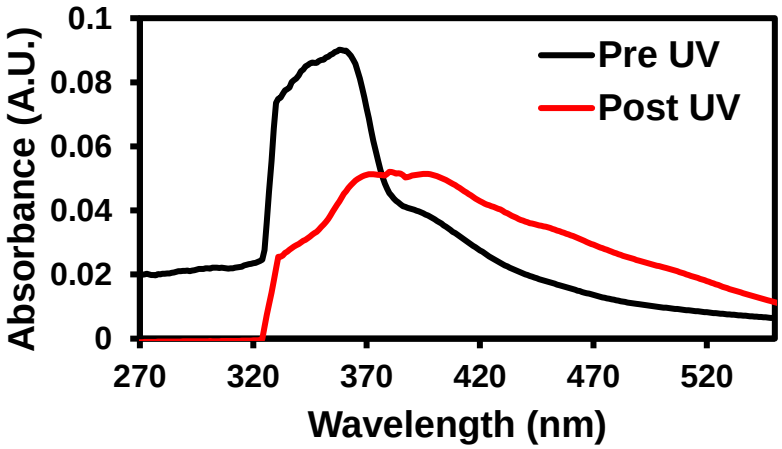

Figure 3.18. Absorbance for **3** pre and post UV for the solid-state. Sample was irradiated for 4 hours before post measurement.

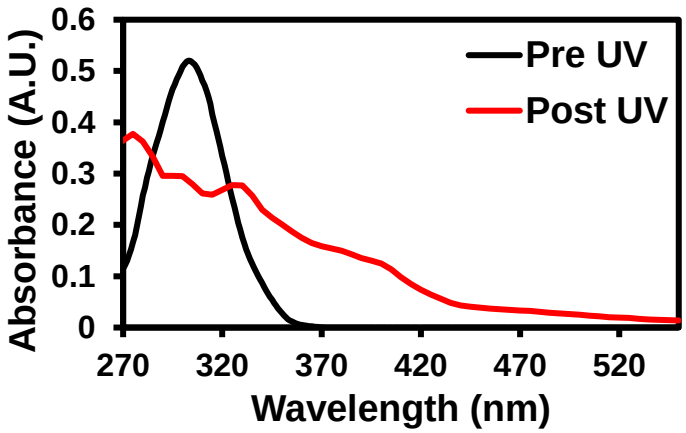

Figure 3.19. Absorbance for **3** pre and post UV in DCM (10 μM). Sample was irradiated for 4 hours before post UV measurement. Pre UV measurement was recorded in 1 nm steps. Post UV measurement was taken in 5 nm steps.

3.4.6 Emission Measurements

Emission data was collected on an Edinburgh FS5 instrument equipped with a 150 W continuous wave xenon lamp source for excitation. Excitations were performed at the λ_{max} of absorbance. Spectra were gathered from X-800 nm at 1 nm steps and are an average of three measurements (X = 25 nm red-shifted from excitation wavelength). Measurements were performed at room temperature.

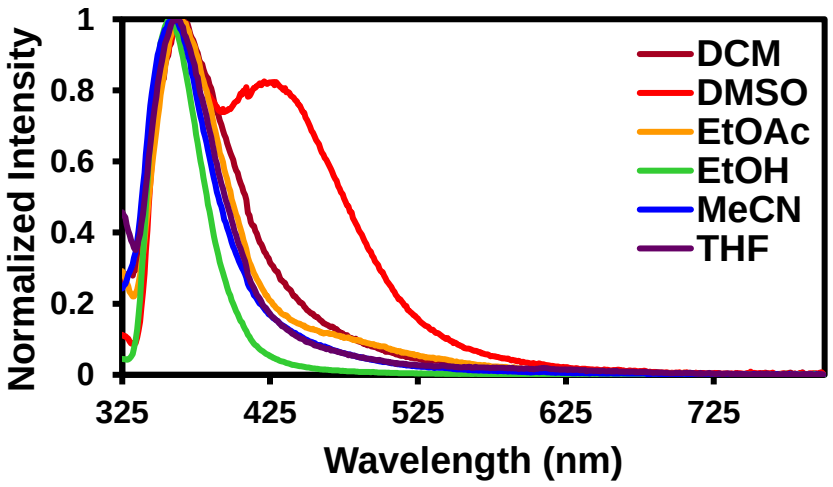

Figure 3.20. Emission spectrum of **1** (20 μM) in different solvents.

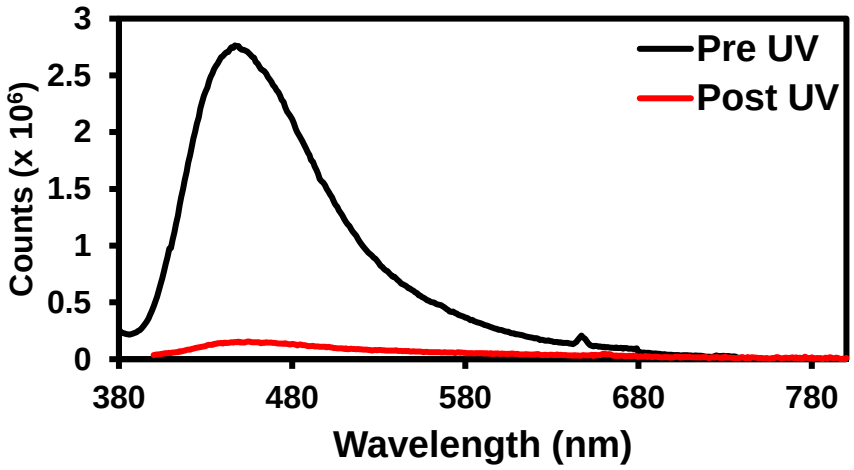

Figure 3.21. Emission for **3** pre and post UV for the solid-state. Sample was irradiated for 4 hours before post measurement.

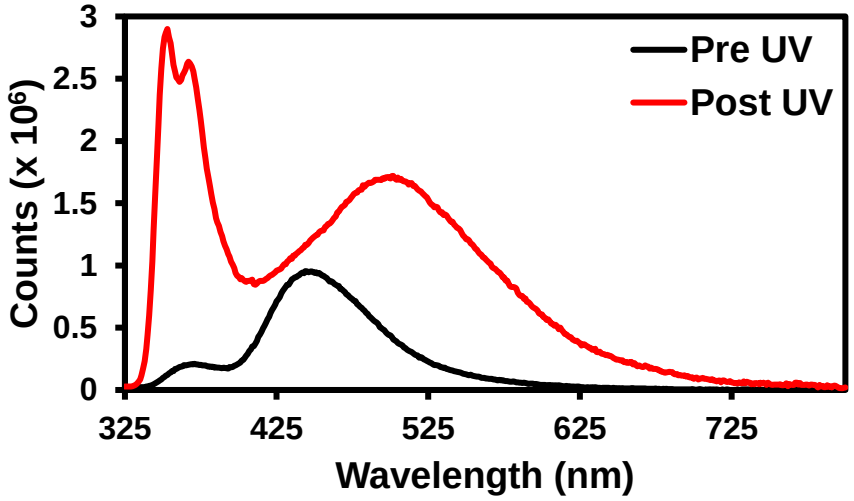

Figure 3.22. Emission for **3** pre and post UV in DCM (10 μM). Sample was irradiated for 4 hours before post UV measurement. Post UV measurement was irradiated at same λ_{max} as pre-UV since no clear λ_{max} was shown in post UV absorbance.

Table 3.3. Photophysical data for **1-3.**

Compound	Solvent	$\lambda_{abs.}$[a]	ε (× 10^4)[b]	$\lambda_{ems.}$[c]	Stoke's Shift[d]
1	DCM	301	2.18	365	64
	THF	300	2.45	360	60

	EtOH	299	2.68	359	60
	EtOAc	299	2.12	365	66
	MeCN	298	2.28	358	60
	DMSO	300	2.56	365*, 427	65
2	DCM	304	5.11	365, 435*	131
	THF	302	5.47	366*, 444	64
	EtOH	301	4.95	361	60
	EtOAc	301	5.34	365	64
	MeCN	300	4.70	371, 451*	151
	DMSO	302	5.42	451	149
3	DCM	303	5.20	366, 449*	146
	THF	302	5.22	367*, 457	65
	EtOH	300	5.45	362*, 437	62
	EtOAc	301	5.53	364*, 453	63
	MeCN	300	5.01	497	197
	DMSO	302	5.41	369, 452*	150
	Solid State	358	--	447	89

[a] Peak position at largest absorption band. [b] Molar absorptivity ($M^{-1} \times cm^{-1}$). [c] Peak positions at largest emission bands in nm (largest denoted with * if applicable, excited at λ_{abs}). [d] Stoke's shift in nm.

3.4.7 Diffused Ordered SpectroscopY (DOSY) NMR

Diffusion measurements were performed on a Bruker Avance IIIHD 400 MHz spectrometer using the vendor-supplied BPPE-LED[56] pulse sequence. 1 mM and 100 μM solutions of **3** in CD_3CN were prepared beforehand and spectra were recorded with a 25 ms diffusion delay and a 2.2 ms diffusion gradient.

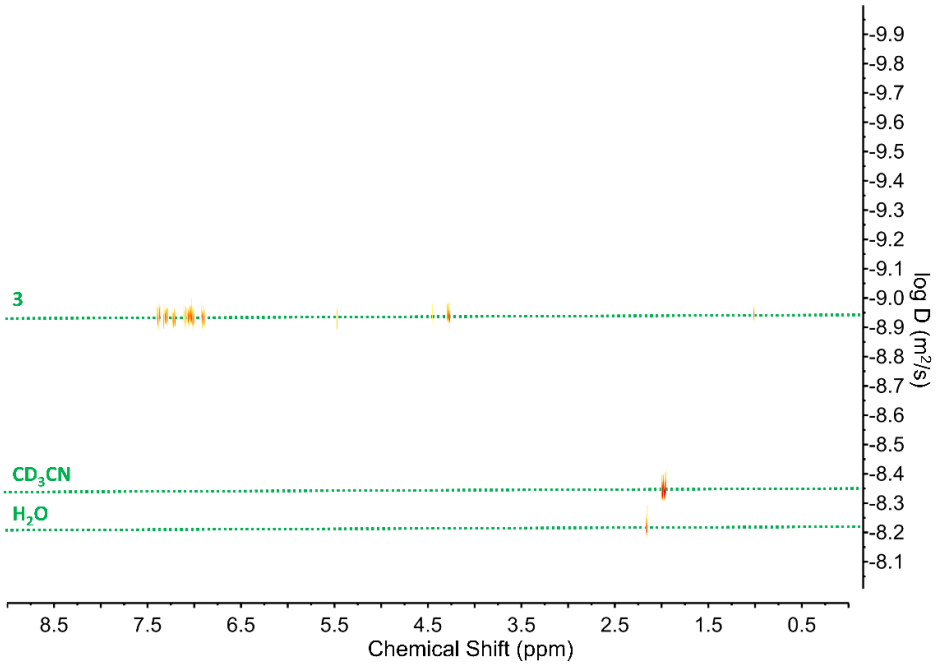

Figure 3.23. DOSY spectra of **3** as a 1 mM solution in CD_3CN.

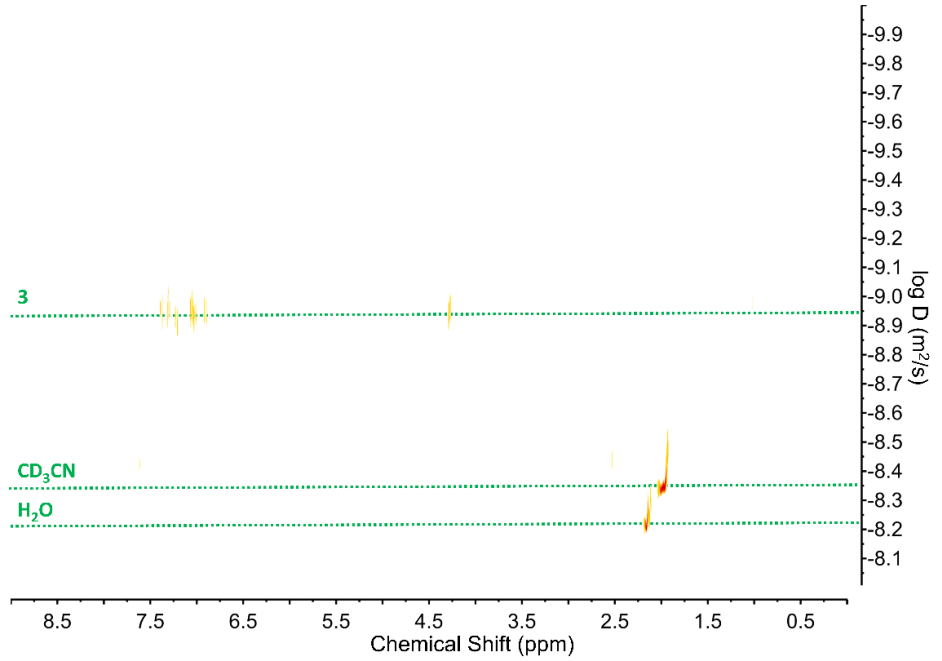

Figure 3.24. DOSY spectra of **3** as a 100 μM solution in CD_3CN.

$$r_{\text{solute}} = \frac{D_{\text{MeCN}}\, r_{\text{MeCN}}}{D_{\text{solute}}}$$

Equation 3.1. Modified Stokes-Einstein equation to solve for the hydrodynamic radius of a solute. D_{MeCN} and D_{solute} are determined experimentally while r_{MeCN} is from a reference value.

Table 3.4. DOSY values for **3.**

Measurement	Compound	Diffusion Coefficient ($\times 10^{-9}$ m^2/s)	Hydrodynamic Radius (Å)
1 mM	CD_3CN	4.57	2.05[57]
	3	1.17	8.01[a]
100 μM	CD_3CN	4.47	2.05[57]
	3	1.12	8.18[a]
Crystal	**3**	N/A	5.83[b]

[a] Values calculated from Equation 3.1. [b] Radius of **3** calculated from crystal structure.

3.4.8 Lifetime Measurements

Lifetimes were measured using a Mini-τ lifetime spectrometer from Edinburgh Instruments equipped with either a 300 nm picosecond-pulsed-light-emitting diode (EPLED 300) or an EPLED 365 on 10 μM solutions. The lifetimes were recorded for the largest emission peak given in Table 3.1 and were recorded at room temperature. The decays for **2** and **3** were fit according to Equation 3.2 as either a bi- or triexponential function where τ and *B* are the lifetime and amplitude, respectively.

$$\mathrm{I(t)} = \int_{-\infty}^{t} \mathrm{IRF}(t') \sum_{\mathrm{i}=1}^{\mathrm{n}} B_{\mathrm{i}} e^{-\frac{t-t'}{\tau_i}}\, dt'$$

Equation 3.2. Fitting equation for fluorescence decay.

The amplitude-weighted average luminescent lifetimes τ_{av} were calculated using Equation 3.2. B_3 and τ_3 were only used for triexponential fits.

$$\langle \tau_{av} \rangle = \frac{B_1\tau_1 + B_2\tau_2 + B_3\tau_3}{B_1 + B_2 + B_3}$$

Equation 3.3. Equation for amplitude-weighted average lifetime.

Table 3.5. Lifetimes for **1**-**3.**

Compound	Solvent	B_1	τ_1 (ns)	B_2	τ_2 (ns)	B_3	τ_3 (ns)	τ_{av} (ns)	X^2
	DCM	0.1390	0.236	0.0310	1.727	0.0112	4.991	0.8	1.252
	DMSO	0.0253	3.084	0.0344	6.617			5.1	1.472
	EtOAc	0.6173	0.101	0.0037	1.180	0.0004	4.914	0.1	1.010
2									
	EtOH	0.7673	0.087	0.0033	1.427	0.0004	6.443	0.1	1.098
	MeCN	0.0489	1.957	0.0289	4.855			3.0	1.302
	THF	0.8936	0.076	0.0041	1.283	0.0007	5.750	<0.1	1.112
	DCM	0.0447	0.828	0.0355	3.281	0.0061	6.480	2.2	1.164
	DMSO	0.0512	2.090	0.0379	6.719			4.1	1.445
	EtOAc	0.7800	0.082	0.0046	1.698	0.0017	3.914	0.1	1.045
3	**EtOH**	0.6104	0.104	0.0048	1.236	0.0007	4.500	0.1	1.117
	MeCN	0.0648	2.748	0.0033	4.480			2.8	1.307
	THF	1.3075	0.059	0.0020	1.534	0.0005	5.491	<0.1	1.064
	Solid State	0.0728	0.392	0.0423	1.427	0.0086	3.282	1.0	1.168

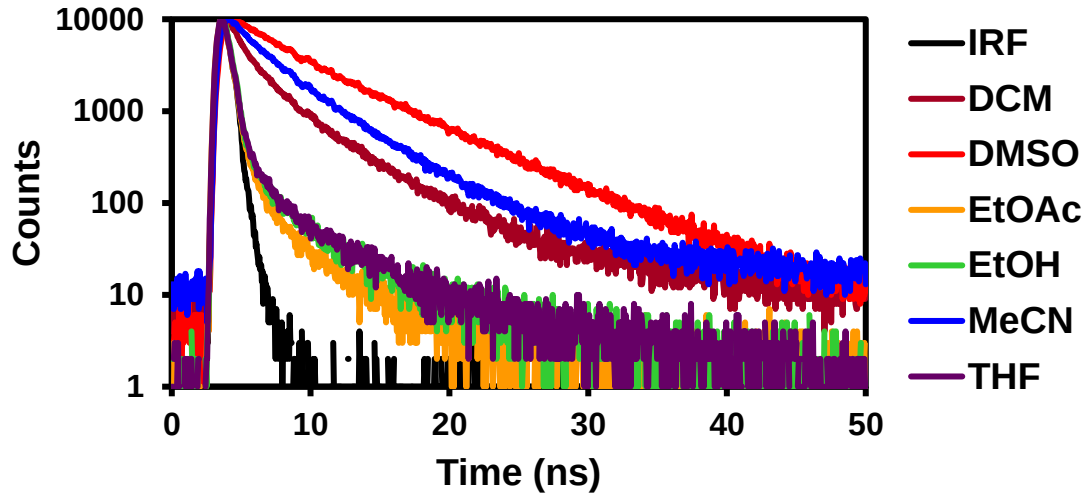

Figure 3.25. Lifetime data for **2** in different solvents.

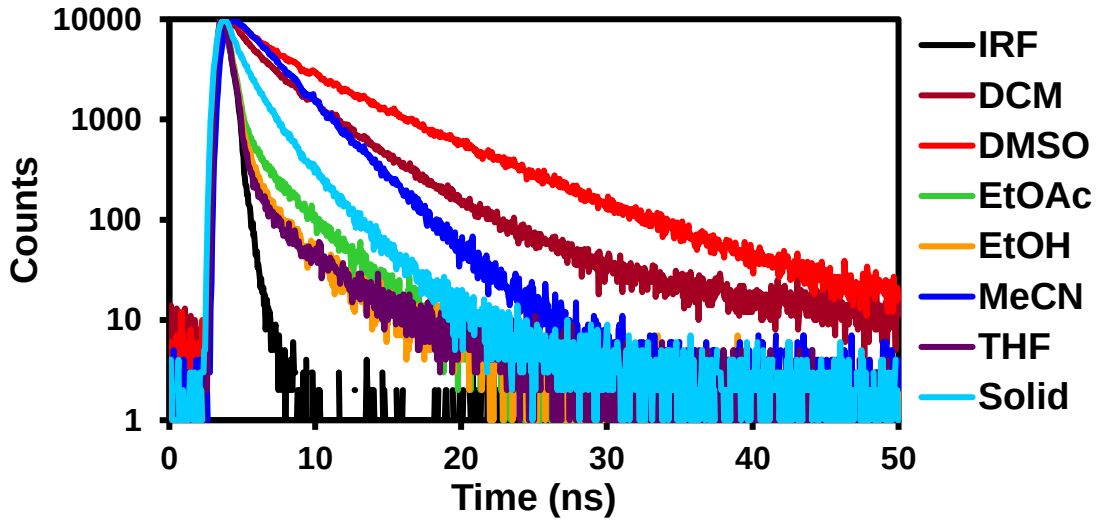

Figure 3.26. Lifetime data for **3** in different solvents and the solid-state.

3.4.9 EPR Measurements

EPR measurements were carried out on a Bruker EMX plus equipped with a Bruker X-band microwave bridgehead and Xenon software (v 1.1b.66). All spectra were recorded at room temperature unless specified. All spectra were recorded at a power of 1.589 mW with a modulation amplitude of 2.0 G. The double integration to obtain peak areas was

performed in the Xenon software. Samples were sealed under argon and UV-irradiated in Norell Suprasil Quartz EPR tubes.

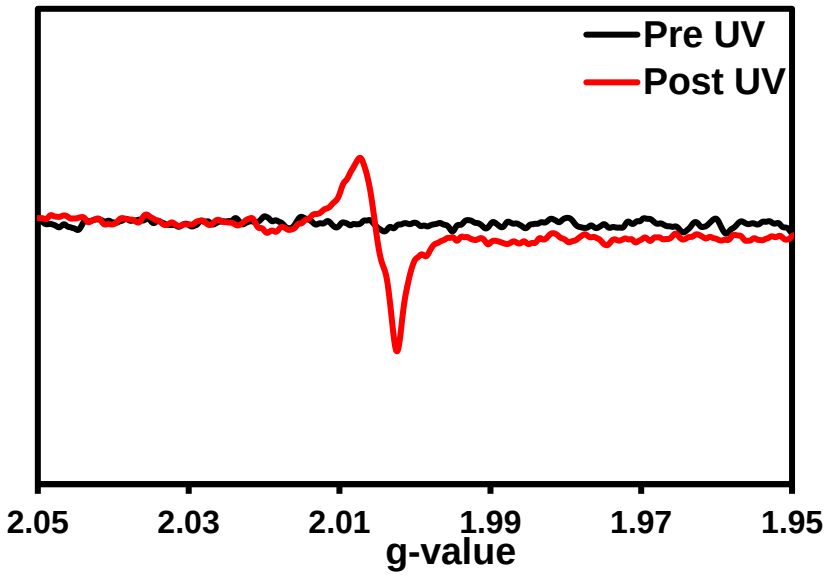

Figure 3.27. EPR spectra of **3** as a 1.09 mM solution in DCM. Sample was irradiated for 6 hours before measurement.

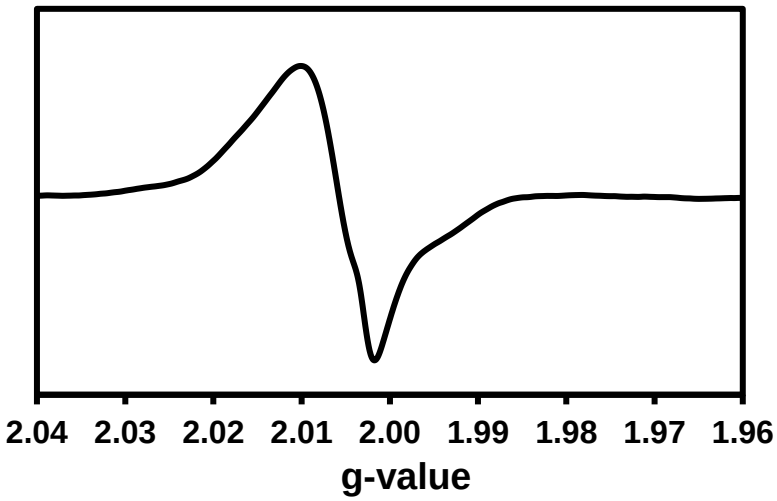

Figure 3.28. EPR spectra of triply recrystallized **3**. Sample was irradiated for 6 hours before measurement.

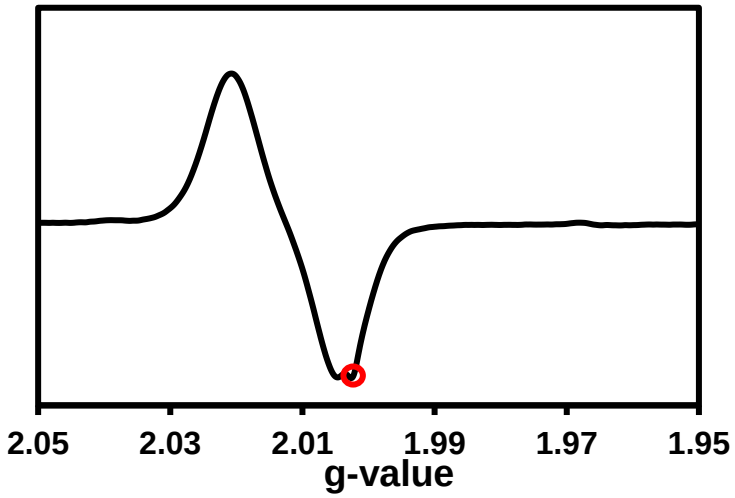

Figure 3.29. EPR spectra of 1 mM solution of *tris*(4-bromophenyl)ammoniumyl hexachloroantimonate (Magic Blue) in DCM. Quartz impurity from EPR tube at g = 2.002 is marked by red circle.

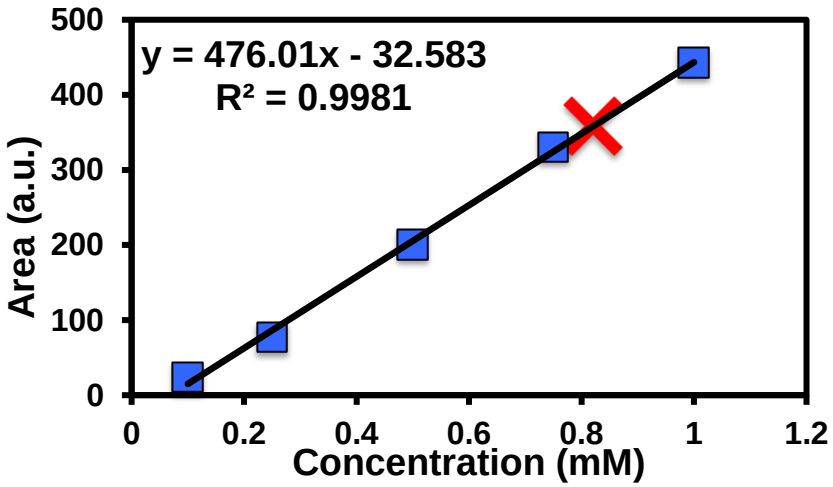

Figure 3.30. Radical concentration determination. The Magic Blue calibration curve is plotted and overlaid with the area and determined concentration of **3** in the solid-state (labeled as a red X). The solid-state measurement was taken as the average of the last four data point from Figure 3.4D from the max radical concentration determination experiment.

3.4.10 NMR Spectra Pre and Post UV

NMR spectra were taken on a Bruker Avance III-HD 300 MHz spectrometer. Samples were UV-irradiated 6 hours before measurement unless otherwise indicated.

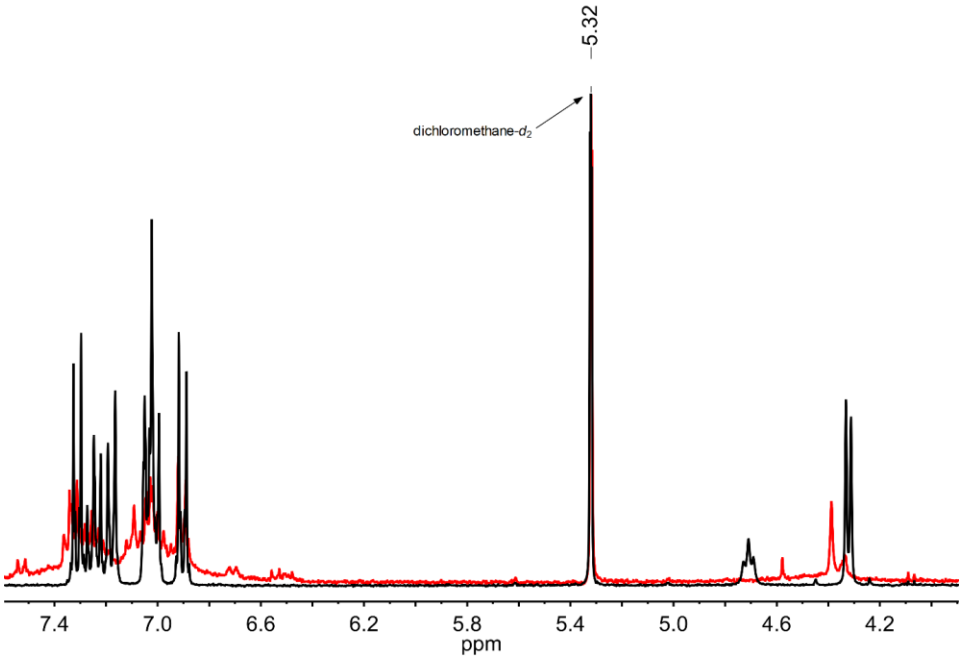

Figure 3.31. ^{1}H NMR of **3** (CD_2Cl_2, 300 MHz) as a solution in DCM pre (black) and post (red) UV irradiation. Significant changes were observed after irradiation.

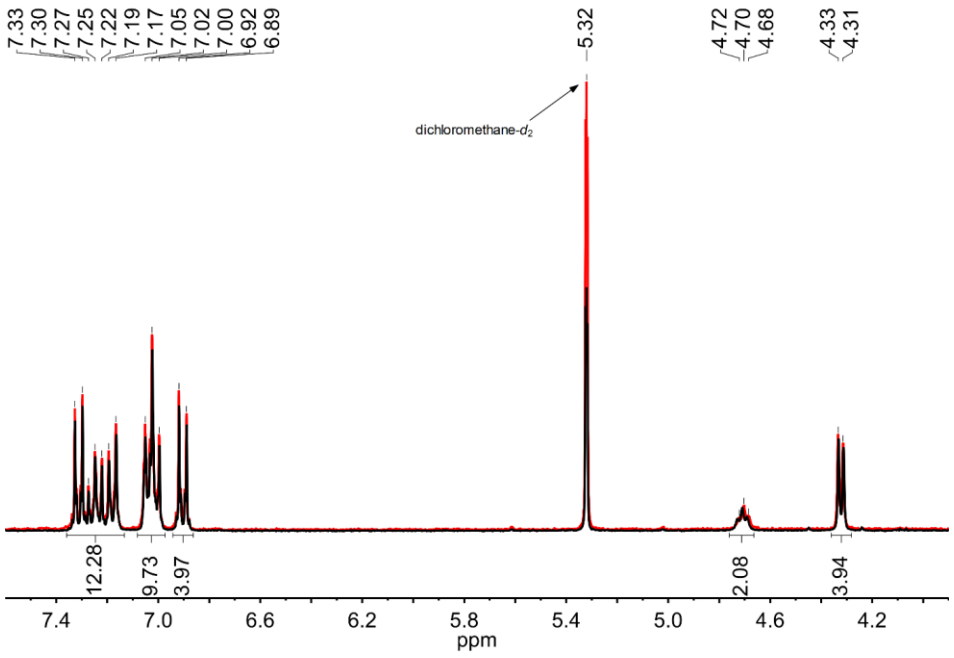

Figure 3.32. ^{1}H NMR of **3** (CD_2Cl_2, 300 MHz) for solid sample after decay of radical signal. Original radical was made from 1 hour of UV-irradiation. Sample was redissolved before measurement. No changes were observed upon dissolution. Peaks and integrals are for the redissolved sample (red). Black is for comparison represents an unirradiated sample.

3.4.11 Infrared Measurements (FT-IR)

All IR analysis were performed using a Perkin Elmer 100 IR Spectrometer. Spectra were taken from 650-4000 cm^{-1}.

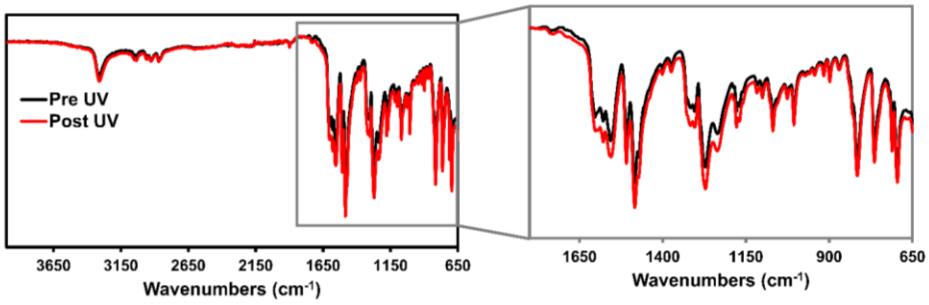

Figure 3.33. IR spectra for **3** pre and post UV for the solid-state. Sample was irradiated for 4 hours before post measurement.

3.4.12 Cyclic Voltammetry (CV)

Measurements were carried out in dichloromethane using a WaveDriver 20 Bipotentiostat combined with Aftermath software. Solutions contained 100 mM (*n*-Bu)$_4N^+PF_6^-$ and 1 mM solute. Measurements were done in an H cell equipped with a SCE reference, platinum wire counter, and glassy carbon working electrodes. Measurements were conducted at a potential rate of 100 mV/s unless otherwise noted.

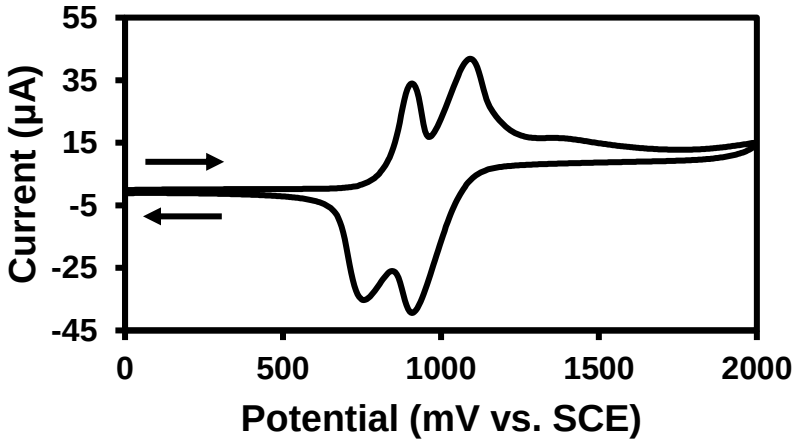

Figure 3.34. Oxidative cyclic voltammetry for **2**. Scanning rate was 40 mV/s instead of 100 mV/s.

3.4.13 Bulk Electrolysis

Measurements were carried out in dichloromethane using a WaveDriver 20 Bipotentiostat combined with Aftermath software. Cell was set up inside a nitrogen filled glovebox in a divided cell that contained an anode in a secondary container separated from the cathodic area by a glass frit. High surface RVC electrodes were used as both the working and counter electrodes while an SCE was used as the reference. The solution of **3** contained 10 mL of a 100 mM $(n\text{-Bu})_4N^+PF_6^-$ and 1 mM solute unless otherwise noted. The solution was continuously stirred at 400 rpm during the experiment.[58]

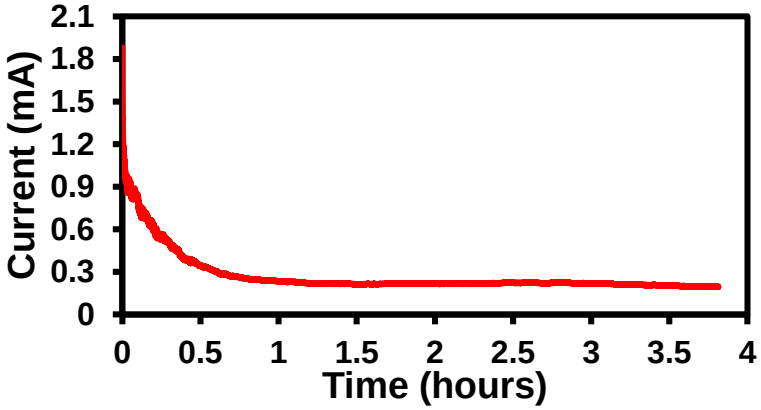

Figure 3.35. Electrolysis of **3** over time. 5 mL of a 0.5 mM solution of **3** was used instead of the standard conditions. Current was allowed to run down to 1% of its initial value. Potential was held at 1.25 V versus SCE. Total area under the curve was found to be 977.2 mC which amounts to 4 total electrons for **3** according to Equation 3.4.

$$n = \frac{Q}{Fz}$$

Equation 3.4. Faraday's law of electrolysis where n is the amount of 3 in mols, Q is the amount of charge in columbs, F is Faraday's constant in C/mol, and z is the number of electrons.

3.4.14 Emission Quenching

Emission data was collected on an Edinburgh FS5 instrument equipped with a 150 W continuous wave xenon lamp source for excitation. Excitations were performed at the

λ_{max} of absorbance (303 nm). Spectra were gathered from 325-800 nm at 1 nm steps and are an average of three measurements. Measurements were performed at room temperature.

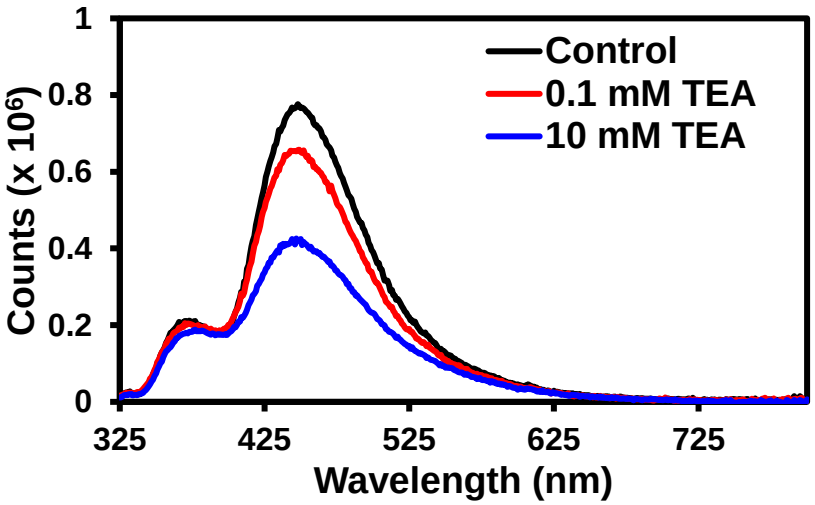

Figure 3.36. Emission for **3** (10 μM in dichloromethane) with different concentrations of triethylamine (TEA).

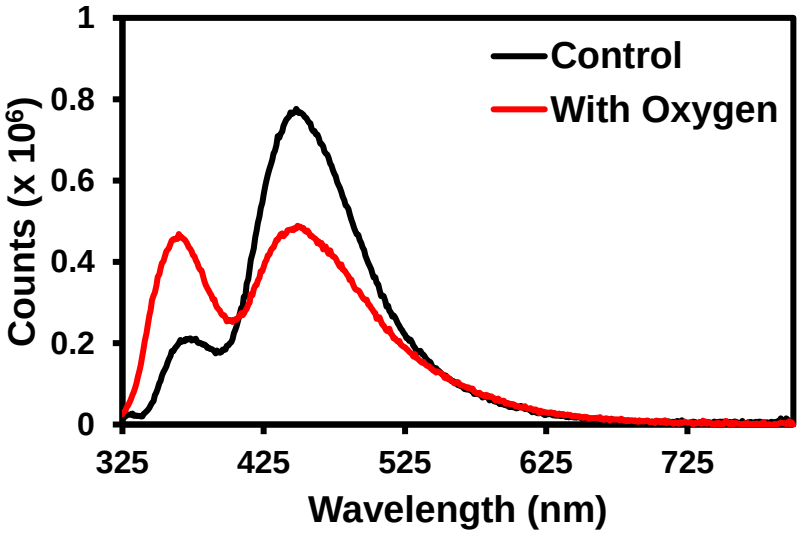

Figure 3.37. Emission for **3** (10 μM) in degassed dichloromethane (control) and oxygenated dichloromethane (with oxygen).

3.5 REFERENCES

1. Mattia, E.; Otto, S. *Nat. Nanotechnol.* **2015**, *10*, 111-119.

2. Mahadevi, A. S.; Sastry, G. N. *Chem. Rev.* **2016**, *116*, 2775-2825.

3. Adachi, T.; Ward, M. D. *Acc. Chem. Res.* **2016**, *49*, 2669-2679.
4. Mei, J.; Leung, N. L. C.; Kwok, R. T. K.; Lam, J. W. Y.; Tang, B. Z. *Chem. Rev.* **2015**, *115*, 11718-11940.
5. He, Z.; Ke, C.; Tang, B. Z. *ACS Omega* **2018**, *3*, 3267-3277.
6. Würthner, F.; Saha-Möller, C. R.; Fimmel, B.; Ogi, S.; Leowanawat, P.; Schmidt, D. *Chem. Rev.* **2016** *116*, 962-1052.
7. Casalini, S.; Bortolotti, C. A.; Leonardi, F.; Biscarini, F. *Chem. Soc. Rev.* **2017**, *46*, 40-71.
8. Liu, M.; Zhang, L.; Wang, T. *Chem. Rev.* **2015**, *115*, 7304-7397.
9. Forrester, A. R.; Hay, J. M.; Thompson, R. H. *Organic Chemistry of Stable Free Radicals*. Academic Press: New York, 1968.
10. Bill, N. L.; Trukhina, O.; Sessler, J. L.; Torres, T. *Chem. Commun.* **2015**, *51*, 7781-7794.
11. Fukui, N.; Cha, W.; Shimizu, D.; Oh, J.; Furukawa, K.; Yorimitsu, H.; Kim, D.; Osuka, A. *Chem. Sci.* **2017**, *8*, 189-199.
12. Murata, H.; Miyajima, D.; Nishide, H. *Macromolecules* **2006**, *39*, 6331-6335.
13. Michinobu, T.; Inui, J.; Nishide, H. *Org. Lett.* **2003**, *5*, 2165-2168.
14. Quinton, C.; Alain-Rizzo, V.; Dumas-Verdes, C.; Miomandre, F.; Clavier, G.; Audebert, P. *RSC Adv.* **2014**, *4*, 34332-34342.
15. Quinton, C.; Alain-Rizzo, V.; Dumas-Verdes, C.; Miomandre, F.; Clavier, G.; Audebert, P. *Chem. Eur. J.* **2015**, *21*, 2230-2240.
16. Ito, A.; Ino, H.; Tanaka, K.; Kanemoto, K.; Kato, T. *J. Org. Chem.* **2002**, *67*, 491-498.

17. Yano, M.; Sato, K.; Shiomi, D.; Ichimura, A.; Abe, K.; Takui, T.; Itoh, K. *Tetrahedron Lett.* **1996**, *37*, 9207-9210.

18. Noh, S. B.; Kim, R. H.; Kim, W. J.; Kim, S.; Lee, K.-S.; Cho, N. S.; Shim, H.-K.; Pudavar, H. E.; Prasad, P. N. *J. Mater. Chem.* **2010**, *20*, 7422-7429.

19. Lee, H. J.; Sohn, J.; Hwang, J.; Park, S. Y.; Choi, H.; Cha, M. *Chem. Mater.* **2004**, *16*, 456-465.

20. Hu, J.; Zhang, X.; Zhang, D.; Cao, X.; Jiang, T.; Zhang, X.; Tao, Y. *Dyes Pigm.* **2017**, *137*, 480-489.

21. Kuramoto, Y.; Nakagiri, T.; Matsui, Y.; Ohta, E.; Ogaki, T.; Ideka, H. *Photochem. Photobiol. Sci.* **2018**, *17*, 1157-1168.

22. Jiang, M.; Gu, X.; Lam, J. W. L.; Zhang, Y.; Kwok, R. T. K.; Wong, K. S.; Tang, B. Z. *Chem. Sci.* **2017**, *8*, 5440-5446.

23. Wang, D.; Su, H.; Kwok, R. T. K.; Hu, X.; Zou, H.; Luo, Q.; Lee, M. S. S.; Xu, W.; Lam, J. W. Y.; Tang, B. Z. *Chem. Sci.* **2018**, *9*, 3685-3693.

24. Shimizu, L. S.; Salpage, S. R.; Korous, A. A. *Acc. Chem. Res.* **2014**, *47*, 2116-2127.

25. Geer, M. F.; Walla, M. D.; Solntsev, K. M.; Strassert, C. A.; Shimizu, L. S. *J. Org. Chem.* **2013**, *78*, 5568-5578.

26. DeHaven, B. A.; Goodlett, D. W.; Sindt, A. J.; Noll, N.; De Vetta, M.; Smith, M. D.; Martin, C. R.; González, L.; Shimizu, L. S. *J. Am. Chem. Soc.* **2018**, *140*, 13064-13070.

27. Turro, N. J.; Ramamurthy, V.; Scaiano, J. C. *Modern Molecular Photochemistry of Organic Molecules*. Viva Books: New Delhi, 2017.

28. Saha, A.; Chen, M.; Lederer, M.; Kahnt, A.; Lu, X.; Guldi, D. M. *Chem. Sci.* **2017**, *8*, 1360-1368.

29. Nyrkova, I.; Moulin, E.; Armao, J. J.; Maaloum, M.; Heinrich, B.; Rawiso, M.; Niess, F.; Cid, J.-J.; Jouault, N.; Buhler, E.; Semenov, A. N.; Giuseppone, N. *ACS Nano* **2014**, *8*, 10111-10124.

30. Li, Z.; Dong, Q.; Xu, B.; Li, H.; Wen, S.; Pei, J.; Yao, S.; Lu, H.; Li, P.; Tian, W. *Sol. Energy Mater. Sol. Cells* **2011**, *95*, 2272-2280.

31. Tian, H.; Yang, X.; Chen, R.; Zhang, R.; Hagfeldt, A.; Sun, L. *J. Phys. Chem. C* **2008**, *112*, 11023-11033.

32. Dubinina, G. G.; Price, R. S.; Abboud, K. A.; Wicks, G.; Wnuk, P.; Stepaneko, Y.; Drobizhev, M.; Rebane, A.; Schanze, K. S. *J. Am. Chem. Soc.* **2012**, *134*, 19346-19349.

33. Groom, C. R.; Bruno, I. J.; Lightfoot, M. P.; Ward, S. C. *Acta Crystallogr. B* **2016**, *72*, 171-179.

34. Yang, M.; Xu, D.; Xi, W.; Wang, L.; Zheng, J.; Huang, J.; Zhang, J.; Zhou, H.; Wu, J. Tian, Y. *J. Org. Chem.* **2013**, *78*, 10344-10359.

35. Würthner, F. *Chem. Commun.* **2004**, 1564-1579.

36. Li, Y.; Liu, T.; Liu, H.; Tian, M.-Z.; Li, Y. *Acc. Chem. Res.* **2014**, *47*, 1186-1198.

37. Li, G.; Chen, Y.; Qiao, Y.; Lu, Y.; Zhou, G. *J. Org. Chem.* **2018**, *83*, 5577-5587.

38. Hu, R.; Gómez-Durán, C. F. A.; Lam, J. Y. L.; Belmonte-Vázquez, J. L.; Deng, C.; Chen, S.; Ye, R.; Peña-Cabrera, E.; Zhong, Y.; Wong, K. S.; Tang, B. Z. *Chem. Commun.* **2012**, *48*, 10099-10101.

39. Steed, J. W. *Chem. Soc. Rev.* **2010**, *39*, 3686-3699.

40. Bagnich, S. A.; Athanasopoulos, S.; Rudnick, A.; Schroegel, P.; Bauer, I.; Greenham, N. C.; Strohriegl, P.; Köhler, A. *J. Phys. Chem. C* **2015**, *119*, 2380-2387.

41. Jiang, Z.; Chen, Y.; Yang, C.; Cao, Y.; Tao, Y.; Qin, J.; Ma, D. *Org. Lett.* **2009**, *11*, 1503-1506.

42. Koziar, J. C.; Cowan, D. O. *Acc. Chem. Res.* **1978**, *11*, 334-341.

43. Turro, N. J.; Kavarnos, G. J.; Cole, T.; Scribe, P.; Dalton, J. C. *J. Am. Chem. Soc.* **1971**, *93*, 1032-1034.

44. Cheng, S.; Song, P.; Yang, S.; Yin, H.; Han, K. *Phys. Chem. Chem. Phys.* **2010**, *12*, 9067-9074.

45. Balasaravanan, R.; Duraimurugan, K.; Sivamani, J.; Thiagaraian, V.; Siva, A. *New J. Chem.* **2015**, *39*, 7472-7480.

46. Kong, L.; Yang, J.-X.; Zhou, H.-P.; Li, S.-L.; Hao, F.-Y.; Zhang, Q.; Tu, Y.-L.; Wu, J.-Y.; Xue, Z.-M.; Tian, Y.-P. *Sci. China Chem.* **2013**, *56*, 106-116.

47. Miller, J. C.; Meek, J. S.; Strickler, S. J. *J. Am. Chem. Soc.* **1977**, *99*, 8175-8179.

48. Le Floch, F.; Simonato, J.-P.; Bidan, G. *Electrochim. Acta* **2009**, *54*, 3078-3085.

49. APEX3 Version 2016.5−0, SAINT+ Version 8.37A; Bruker AXS, Inc.: Madison, WI, 2016.

50. Krause, L.; Herbst-Irmer, R.; Sheldrick, G. M.; Stalke, D. *J. Appl. Cryst.* **2015**, *48*, 3-10.

51. Sheldrick, G. M. *Acta Crystallogr. A* **2015**, *71*, 3-8.

52. Sheldrick, G. M. *Acta Crystallogr. C* **2015**, *71*, 3-8.

53. Dolomanov, O. V., Bourhis, L. J., Gildea, R. J., Howard J. A. K.; Puschmann, H. J. *Appl. Cryst.* **2009**, *42*, 339-341.

54. Spek, A. L. *Acta Crystallogr. D* **2009**, *65*, 148-155.

55. Platon Homepage. www.cryst.chem.uu.nl/platon/ (accessed Jul 26, 2018).

56. Wu, D.; Chen, A.; Johnson, C. S.; *J. Magn. Reson.* **1995**, *115*, 260-264.

57. Zhang, J.; Jonas, J. *J. Phys. Chem.* **1993**, *97*, 8812-8815.

58. Dissanayake, D. M. M. M.; Vannucci, A. K. *ACS Substainable Chem. Eng.* **2018**, *6*, 690-695.

CHAPTER 4

SINGLE-CRYSTAL-TO-SINGLE-CRYSTAL GUEST EXCHANGE IN COLUMNAR ASSEMBLED BROMINATED TRIPHENYLAMINE BIS-UREA MACROCYCLES*

* **Sindt, A. J.**; Smith, M. D.; Berens, S.; Vasenkov, S.; Bowers, C. R.; Shimizu, L. S. *Chem. Commun.* **2019**, *55*, 5619-5622. Reproduced by permission of The Royal Society of Chemistry.

4.0 ABSTRACT

Self-assembly of brominated triphenylamine *bis*-urea macrocycles affords robust porous materials. Urea hydrogen bonds organize these building blocks into 1-dimensional columns, which pack via halogen–aryl interactions. The crystals are stable when emptied, present two distinct absorption sites for Xe with restricted Xe diffusion, and exhibit single-crystal-to-single-crystal guest exchange.

4.1 INTRODUCTION

Porous materials are advantageous for catalysis,[1,2] as nanoreactors,[3] and for the confinement of photoluminescent compounds[4] as well as for storage,[5-7] sensing,[8-10] and separations[11-13] of small molecules. Key to these processes is how the host and guest influence and interact with each other to afford synergetic properties. Single-crystal-to-single-crystal (SC–SC) transformations can follow these molecular processes by providing atomic details to elucidate the factors that guide the molecular interactions. SC–SC transformations can be triggered under a number of conditions including: temperature,[14,15] photoirradiation,[16,17] guest inclusion,[18-20] pressure,[21,22] and mechanoresponses.[23,24] Here, we investigate SC–SC guest exchange in porous organic crystals of triphenylamine *bis*-urea macrocycles.

Typically, hosts for these studies are assembled from rigid materials. Examples include metal organic frameworks (MOFs),[25,26] hydrogen bonded organic frameworks (HOFs),[27,28] and porous organic materials.[29,30] The latter can be beneficial due to the structural versatility organic molecules provide and the ease of forming porous materials simply through crystallization. However, it can be challenging to predict how molecules will assemble in the solid-state. Close-packing principles are often at odds with forming permeable materials. Therefore, molecular families that reliably form porous materials

upon crystallization are highly sought after since they offer tunability within their host framework.[31] The Shimizu group employs simple bis-urea building blocks that stack into pillars and columns to form nanoporous molecular crystals that can be used as containers for photochemical reactions.[32] While experimental evidence suggests these frameworks remain intact during the process of guest exchange and subsequent photoreactions, this is our first demonstration of SC–SC transformations. We report a porous organic material made from a triphenylamine (TPA) *bis*-urea macrocycle **1**, which contains two bromo-TPA units (Figure 4.1). This macrocycle crystallizes into columnar structures through urea–urea interactions with columns packing together with π–π and halogen–π interactions forming large crystals (35 × 265 mm) that are robust and suitable for SC transformations. Simple heating removes the guest affording homogeneous nanochannels. Immersion of the material into an organic solvent results in a SC–SC transformation to afford a new host-guest complex (Figure 4.1b). These complexes organize guests near photoactive TPA units and should consequently enable us to study the effects of closely oriented guests on the optoelectronic properties.

4.2 RESULTS AND DISCUSSION

Macrocycle **1** was synthesized by a strategy similar to its linear counterpart.[33] First, commercial bromotriphenylamine was converted to the dialdehyde using a Vilsmeier–Haack reaction followed by hydride reduction resulting in the diol. Once the alcohols were brominated, two TPA units were connected with two triazinanone spacers under basic conditions, resulting in the protected macrocycle. These macrocycles crystallized in chloroform solutions as colorless blocks as a 1:8 macrocycle:$CHCl_3$ solvate, enabling their

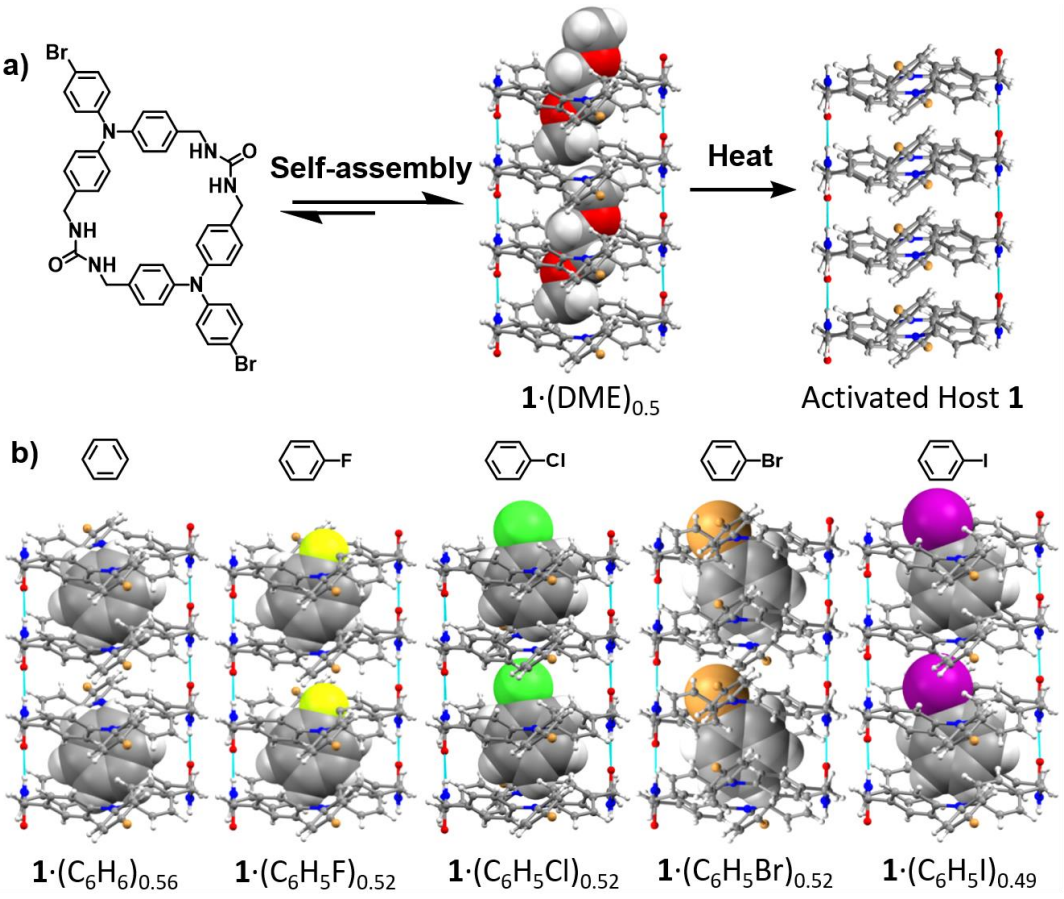

Figure 4.1. (a) Self-assembly of macrocycle **1** from the vapor diffusion of DME into DMSO leads to 1D channels. Subsequent heating activates the channels for the loading of different guests. (b) SC-SC transformations observed upon soaking activated host **1** crystals in guest liquids.

purification (Figure 4.14). Subsequent urea deprotection with diethanolamine under acidic conditions afforded 1 as a beige powder.

Vapor diffusion of 1,2-dimethoxyethane (DME) into a dimethylsulfoxide (DMSO) solution of 1 (~2.5 mg mL^{-1}) produced large colorless needles (0.6 × 0.08 × 0.04 mm^3) crystallizing in the space group $P2_1/c$ of the monoclinic system. In this structure, the macrocycle adopts an anti-conformation with encapsulated, disordered DME solvent in a 2:1 ratio (Figure 4.2a). Both the macrocycle and DME solvent were found on crystallographic inversion centers with the solvent being situated across an additional

inversion center leading to its disorder within the channels. Individual macrocycles assemble into columnar structures organized by the characteristic three centered urea hydrogen bond, with N(H)···O distances of 2.848(4) and 2.929(4) Å. This creates infinite hydrogen bonded tubes along the crystallographic *b* axis with a macrocycle to macrocycle repeat distance of 4.620(2) Å. π-stacking between neighboring TPAs provides additional stabilization within the columns (Figure 4.22).

Individual columns assemble into pseudo-hexagonal rod-packing arrays, similar to other *bis*-urea structures. However, crystals of **1** are on average ten times larger in width (35 × 265 μm versus 3 × 250 μm, Figure 4.15) than any other previously obtained *bis*-urea macrocycle derivative.[32] Hirshfeld analysis was used to identify key interactions that guide assembly and subsequent packing of the columns of **1** to facilitate the growth of larger crystals.[34-37] Figure 4.2b and c shows the d_{norm} surface and highlights the key urea motif driving individual column formation as well as close intercolumnar contacts occurring

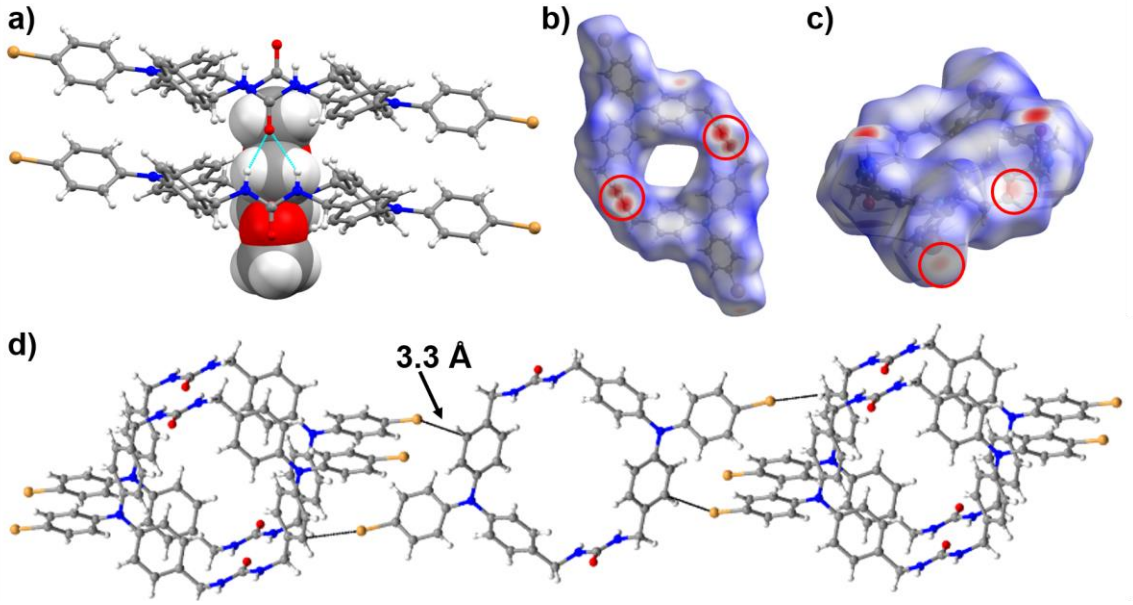

Figure 4.2. (a) View along a single column illustrating the 2 : 1 host : guest ratio and the three-centred urea hydrogen bonding motif. (b) d_{norm} surface showing urea interactions (circled in red). (c) d_{norm} surface showing halogen–π interactions (circled in red). (D) Crystal packing showing select close contacts between columns.

between the bromine substituents and aryl rings. The halogen–π interactions illustrated in Figure 4.2c display a Br···C_{aryl} distance of 3.303(3) Å, which is shorter the sum of the vdW radii (3.5 Å) suggesting that the *p*-bromophenyl groups significantly increases intercolumnar interactions in *1*versus the more cylindrical *bis*-urea macrocycles.[38,39]

Figure 4.3 compares a series of *bis*-urea macrocycles that assembled into similar 1-dimensional columns. Host **1**, phenyl ether (**2**), and benzophenone (**3**) have similar cavity sizes and topographies (Table 4.3). The cavities are roughly elliptical, displaying cross sectional diameters of ∼4 Å × 7 Å (Figure 4.3a). The walls of these channels are held together by urea hydrogen bonds, with further stabilization coming from aryl stacking interactions. In **2** and **3**, these are edge-to-face π-stacking interactions while the extra phenyl groups in **1** lead to offset π-stacking. The alternative edge-to-face aryl stacking interactions in **2** and **3** give the channels a curvature highlighted in blue in Figure 4.3b, which oscillates back and forth along the length of the columns. These oscillations are also pronounced in the offset-aryl stacked structure of host **1**. The channels of hosts **2** proved to be an ideal substrate for monitoring single file diffusion of xenon.[40] Therefore, we sought to test if the framework of **1** was stable in the absence of guests to see if it could be used for a similar application.

To monitor guest removal, thermogravimetric analysis (TGA) was applied. Host **1**·DME crystals displayed a one-step desorption curve with a weight loss of 5.3% between 20 to 90°C (Figure 4.23). Higher temperatures (>90 °C) caused degradation of the material, which was readily detected by NMR. From the percent weight loss, we calculated the macrocycle : guest stoichiometry as 1 : 0.5. On average a host : guest ratio of 1 : 0.55 was found over three batches of crystals. The larger crystal size and heavy bromine atoms in **1**

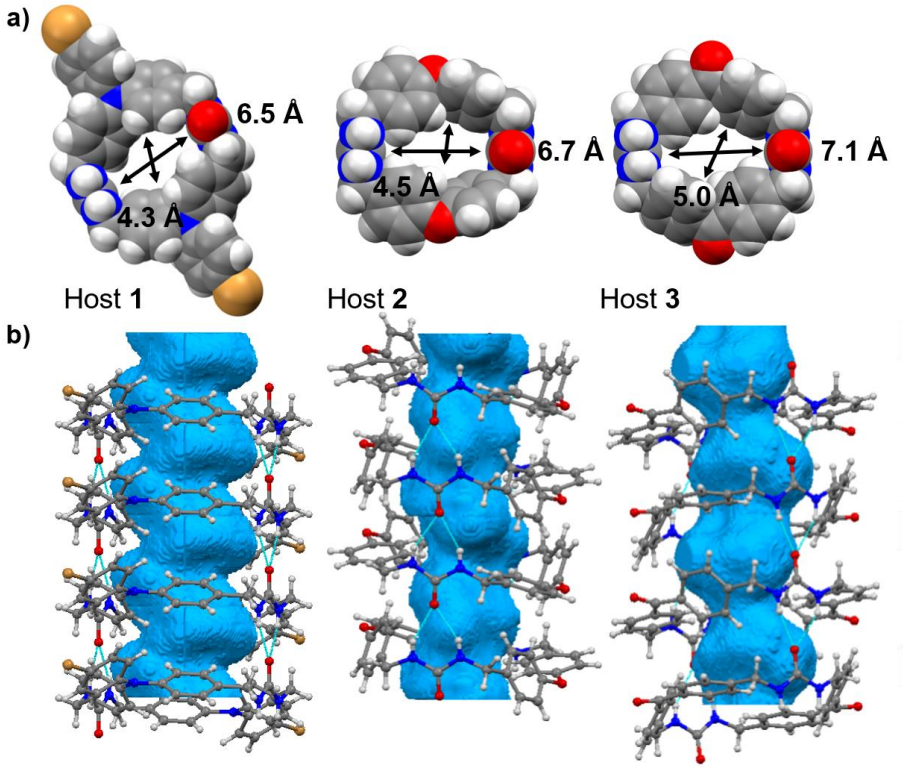

Figure 4.3. (a) Pore sizes of different *bis*-urea macrocycles subtracting the vdW radii. From left to right the urea spacers are 4-bromotriphenylamine, phenyl ether, and benzophenone. (b) Comparison of their corresponding 1-dimensional columns of **1**–**3** with their void space highlighted in blue.

facilitated rapid monitoring of the empty host framework by SC-XRD. To ascertain if the host framework would be maintained, one freshly activated crystal was examined immediately after TGA completion and a second crystal after three days on the lab bench in ambient air. Remarkably, the structures, including the columnar framework and packing, were nearly identical to the **1**·DME crystals except that the electron density of the DME was absent (Figure 4.1a, activated host). The largest electron density maxima found inside the channels within either data set was 0.21 $e^{-}/Å^{3}$, i.e. essentially background noise. These results demonstrate the stability of this assembled material under ambient conditions in the absence of guests.

To further characterize the pore space architecture of host **1**, freshly evacuated crystals were pressurized to 9.5 bar (at 298 K) with isotopically enriched Xe gas and examined by ^{129}Xe NMR. ^{129}Xe NMR has previously been used to study 1D channels[41,42] since the ^{129}Xe NMR chemical shift tensor is highly sensitive to the pore-space structure and shows dependence on de-shielding due to Xe–Xe interactions, especially at higher Xe loadings in single-file nanotubular pores, where cross-sectional dimensions are comparable to the vdW diameter of the Xe atom (0.44 nm).[43-45] Figure 4.4a and b show the NMR spectra for ^{129}Xe·**1** at 295 and 243 K referenced to gas phase ^{129}Xe at 0 ppm. A well-defined axially symmetric chemical shift anisotropy (CSA) powder pattern with δ_{iso} = 217 ppm emerges upon cooling the sample to 243 K. This ^{129}Xe CSA tensor is consistent with a high Xe loading in channels with the dimensions of host **1**.[45] The symmetric peak centered near 310 ppm is attributed to highly confined Xe atoms residing in pores with (dynamically averaged) cubic symmetry in host **1**, tentatively identified as the inter-columnar pores (Figure 4.25). The ratio of the areas of the adsorbed Xe peaks are close to 3 : 1 at both temperatures. In the spectrum recorded at 295 K, the small peak that appears near 260 ppm (indicated by the arrow in Figure 4.4a) suggests that Xe is in fast chemical exchange between the two types of pore spaces.

^{129}Xe PFG NMR experiments were performed at 298 K to investigate the diffusion of Xe atoms adsorbed inside the 1-D channels. Unfortunately, short T_2 NMR relaxation times prevented us from using sufficiently large gradient pulse durations and amplitudes to measure intra-channel diffusion. However, these diffusion studies allowed us to qualitatively examine the exchange of Xe atoms between the channels and the surrounding gas phase on the time scale of the diffusion observation (5–100 ms). It was found that a

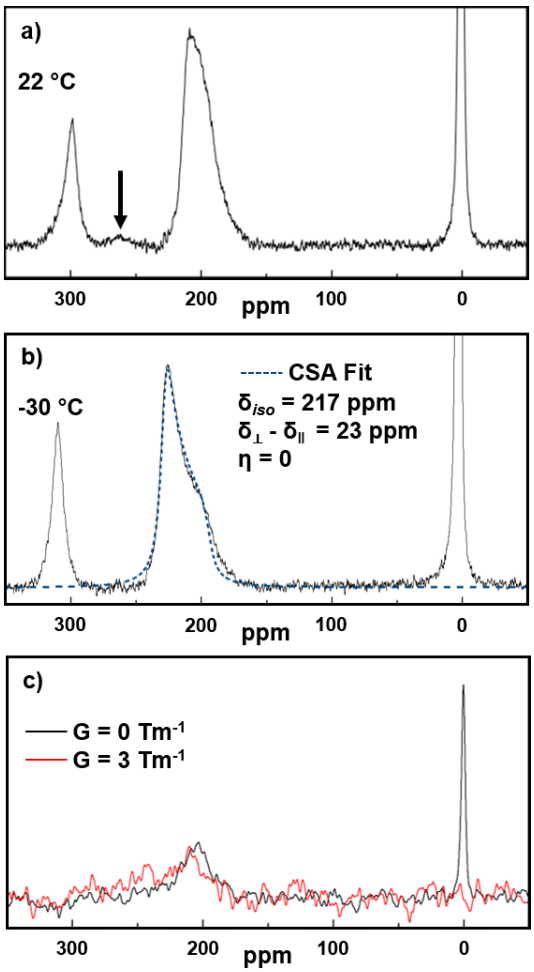

Figure 4.4. ^{129}Xe NMR spectra of **1** acquired at 138.45 MHz (11.756 T) at (a) 295 K and (b) 243 K by accumulating 1920 and 960 transients respectively, with a recycle delay of 40 × and pulse length of 10 μs. The dashed blue trace is the least-squares fit[46] to an axially symmetric chemical shift anisotropy powder pattern. (c) ^{129}Xe NMR spectra measured using a stimulated echo PFG NMR sequence at 298 K and diffusion time 5 ms.

complete diffusion attenuation of the gas-phase line could be achieved with an expected gas-phase diffusivity of 6.7×10^{-7} m^2 s^{-1} at 298 K. However, there was no noticeable diffusion attenuation of the line corresponding to Xe atoms adsorbed in the channels (Figure 4.4c). This was seen for all diffusion times used. The observed lack of the diffusion attenuation for the Xe line at 206 ppm allows us to estimate a lower limit of 100 ms on the

exchange time. Therefore, we can conclude that there are no defects in the channel walls that might lead to such an exchange.

To investigate the ability of this host to absorb and store small molecules, we treated the activated crystals with a series of halogenated benzenes. Host **1**·DME crystals were consistently activated for SC–SC exchange by heating at 90 °C for ~2.5 h until no further weight loss was detected via TGA (Figure 4.23). Freshly activated crystals (5 mg) were then immersed in a liquid guest (1 mL) for 1 day followed by examination with SC-XRD. SC–SC transformations were observed giving five host **1**·guest structures that displayed 1 : 0.5 host guest stoichiometry including **1**·C_6H_6, **1**·C_6H_5F, **1**·C_6H_5Cl, **1**·C_6H_5Br, and **1**·C_6H_5I. All the inclusion crystals were found to be isoskeletal with one another, the original DME solvate, and the activated host. Figure 4.1b highlights the similarity between these host-guest complexes.

In all cases, the guests showed a moderate amount of disorder within the columns. Fortunately, the halogen-substituted guests permitted more reliable determination despite this disorder due to the larger X-ray scattering factors (especially for Cl, Br and I). The guests aligned in a planar tape-like manner within the channels with guests being crystallographically modelled on two independent sites, one having the halogen–benzene bond more perpendicular to the macrocycle, shown for iodobenzene in Figure 4.5a (red structure) with the other in a slightly tilted orientation (Figure 4.5a, orange). Both of these sites were located near inversion centers (Figure 4.5a, blue and green) giving a total of four possible sites for the guest location, with each having similar occupancies. This disorder was quite similar across all structures. The alignment of the guests in all of these structures

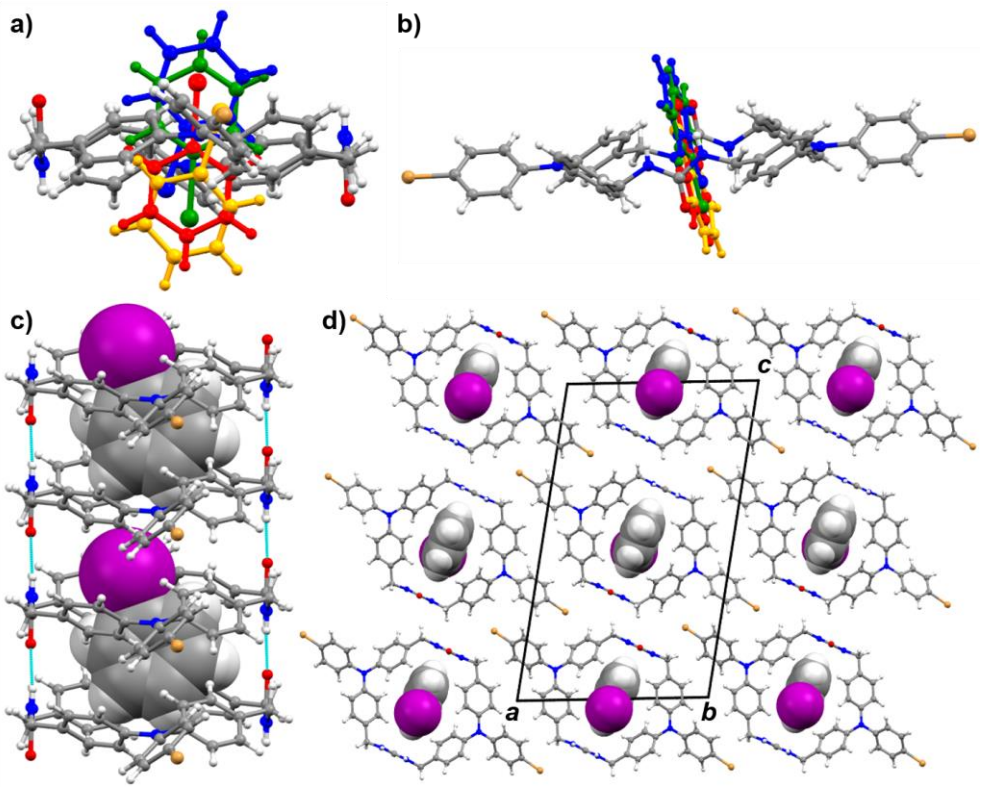

Figure 4.5. Crystal views of **1**·C_6H_5I. (a) View of disorder of guest inside the host **1**. Four sites are found. (b) Another view of guest disorder. (c) Space-filled guests inside host **1**. (d) Crystal packing of host **1** with guests. For (c) and (d), disorder was removed for clarity.

may arise from C–H···halogen and/or C–H···π interactions; however, these details are obscured by the crystallographic disorder.

4.3 CONCLUSIONS

In summary, a brominated TPA *bis*-urea macrocycle assembled to form robust crystals with accessible columnar channels suitable for SC–SC guest exchange. The host is stable when emptied and exhibits confined ^{129}Xe NMR signals when pressurized under xenon. ^{129}Xe PFG NMR measurements suggest these channels are homogeneous. Most intriguingly, assembly of this macrocycle orients the individual TPAs close in space to potential guests and enforces close contacts between the two units. Since TPAs are known to undergo chemical or electrochemical oxidation to generate radical cations, these

crystalline materials offer potential models for the investigation of electron transfer between organic molecules within confinement. Indeed, linear analogues of host **1** showed stable and regenerable radical formation upon UV-irradiation in the solid-state.[17] Currently, we are evaluating guests that can undergo electron transfer with the TPA units and hope to report on these in due time.

4.4 EXPERIMENTAL

4.4.1 General Experimental

NMR spectra were recorded on Bruker 300 or 400 MHz spectrometers. Chemical shifts are reported in ppm (δ) and were internally referenced with the solvent peak. All chemicals were purchased from chemical suppliers and were used as received unless otherwise noted. High-resolution mass spectrum data were recorded using a direct exposure probe (DEP) in electron ionization mode on a Waters QTOF-I quadrupole time-of-flight mass spectrometer. All other instrument protocols are described in their own sections hereafter.

4.4.2 Synthesis and characterization of macrocycles

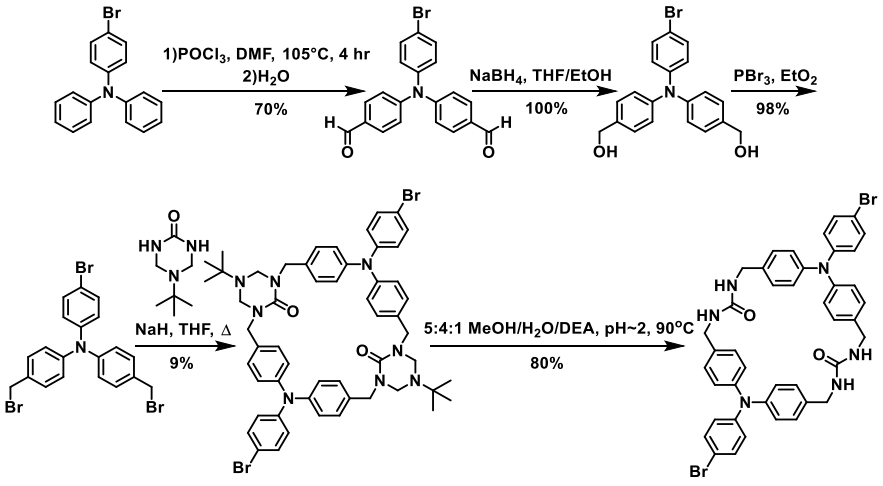

Scheme 4.1. Overview of synthesis.

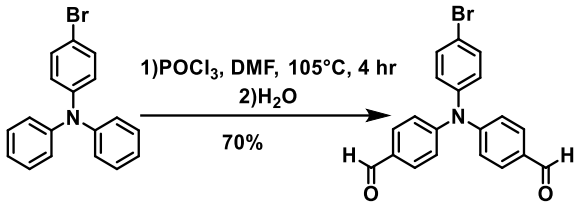

4,4'-((4-Bromophenyl)azanediyl)dibenzaldehyde: Phosphoryl chloride (10.00 mL, 107.3 mmol) was added dropwise to dry *N, N*-dimethylformamide (10.80 mL, 139.4 mmol) under nitrogen and the mixture was stirred at room temperature for one hour. Then 4-bromo-*N, N*-diphenylaniline (3.48 g, 10.7 mmol) was added, and this mixture stirred for 4 hours at 105 ˚C. After the mixture cooled to room temperature, 110 mL of ice-cold water was added to the mixture and it was filtered. The crude product was purified by column chromatography (Hexanes/Diethyl Ether = 3:1) to yield the product as a yellow solid (70%). Spectra matched that as previously reported.[47] ^{1}H NMR (300 MHz, $CDCl_3$): δ (ppm) 9.90 (s, 2H), 7.79 (d, *J* = 8.6 Hz, 4H), 7.50 (d, *J* = 8.9 Hz, 2H), 7.18 (d, *J* = 8.6 Hz, 4H), 7.05 (d, *J* = 8.6 Hz, 2H).

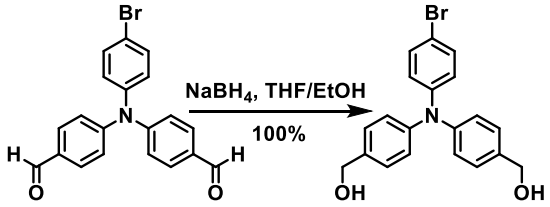

(((4-Bromophenyl)azanediyl)*bis*(4,1-phenylene))dimethanol: The previous aldehyde (1.724 g, 4.5 mmol) and sodium borohydride (0.378 g, 10.0 mmol) were suspended in 120 mL of a 2:1 mixture of dry tetrahydrofuran and ethanol and was heated at 40 ˚C overnight in the dark. Then the reaction was cooled to room temperature and 120 mL of water was added to quench the reaction. The mixture was extracted with chloroform (3 × 120 mL) and dried with $NaSO_4$. The solvent was removed under rotary evaporation

yielding the product as a white solid (100%). ^{1}H NMR (300 MHz, $(CD_3)_2SO$): δ (ppm) 7.40 (d, *J* = 8.8 Hz, 2H), 7.26 (d, *J* = 8.3 Hz, 4H), 6.98 (d, *J* = 8.6 Hz, 4H), 6.84 (d, *J* = 9 Hz, 2H), 5.13 (t, *J* = 5.8 Hz, 2H), 4.44 (d, *J* = 5.7 Hz, 4H). ^{13}C NMR (75 MHz, $(CD_3)_2SO$): δ (ppm) 147.01, 145.41, 137.92, 132.04, 127.94, 124.21, 123.81, 113.14, 62.53. HRMS (DEP): [M+] calculated, 384.0594; found, 384.0593.

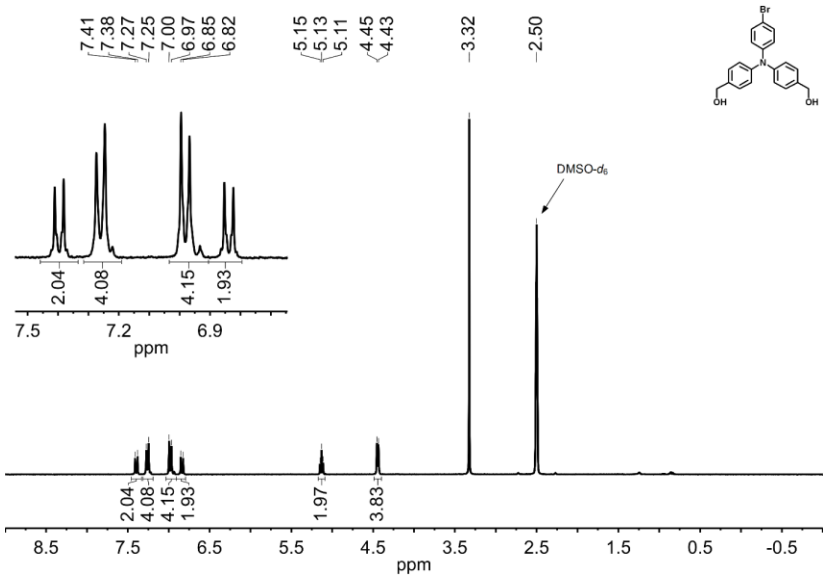

Figure 4.6. ^{1}H NMR of diol **1** ($(CD_3)_2SO$, 300 MHz).

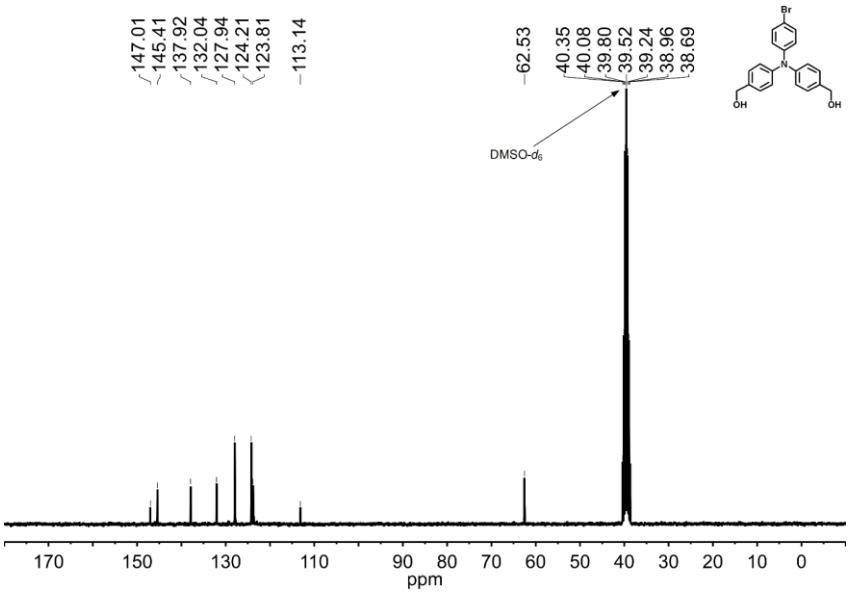

Figure 4.7. ^{13}C NMR of diol **1** ($(CD_3)_2SO$, 75 MHz).

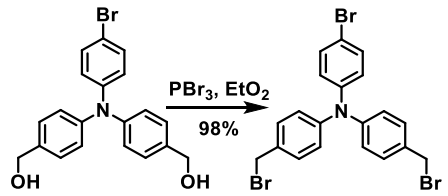

4-Bromo-*N*,*N*-*bis*(4-(bromomethyl)phenyl)aniline: The previous alcohol (1.733 g, 4.5 mmol) was suspended in 50 mL of dry diethyl ether and was cooled to 0 ˚C. Then a solution of phosphorus tribromide (514 μL, 5.4 mmol) in 10 mL dry diethyl ether was added dropwise over 5 minutes. The reaction stirred at room temperature overnight in the dark. In the morning, 60 and 30 mL of ice cold water and saturated $NaHCO_{3(aq)}$ was added to quench the reaction. The mixture was extracted with 60 mL of dichloromethane and the organics were washed with brine (3 × 60 mL) and dried with $MgSO_4$. The solvent was removed under rotary evaporation to yield the bromide as a sticky solid (98%). ^{1}H NMR (300 MHz, CD_2Cl_2): δ (ppm) 7.38 (d, *J* = 8.6 Hz, 2H), 7.29 (d, *J* = 8.6 Hz, 4H), 7.02 (d, *J* = 8.6 Hz, 4H), 6.97 (d, *J* = 8.6 Hz, 2H), 4.51 (s, 4H). ^{13}C NMR (75 MHz, CD_2Cl_2): δ (ppm) 147.55, 146.68, 133.03, 132.80, 130.68, 126.65, 124.36, 116.38, 34.25. HRMS (DEP): [M+] calculated, 506.8833; found, 506.8837.

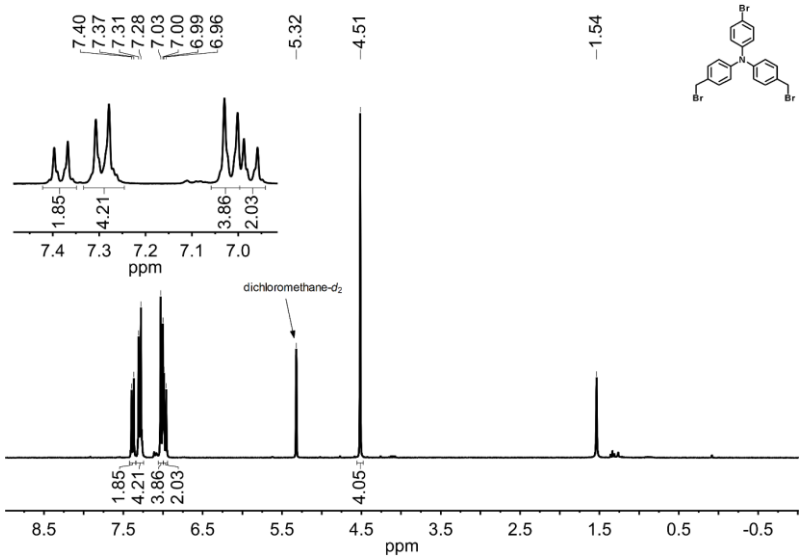

Figure 4.8. ^{1}H NMR of dibromide **1** (CD_2Cl_2, 300 MHz).

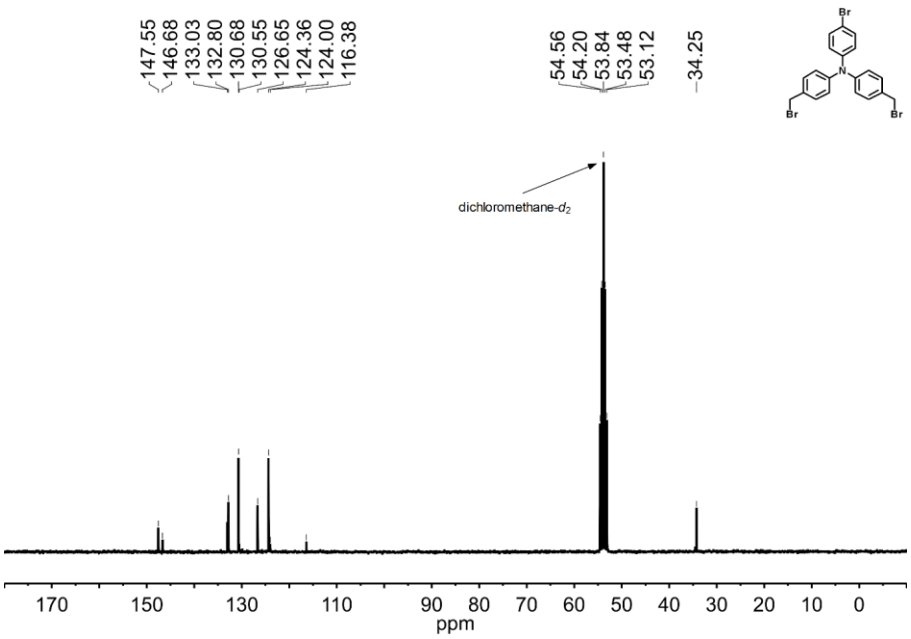

Figure 4.9. ^{13}C NMR of dibromide **1** (CD_2Cl_2, 75 MHz).

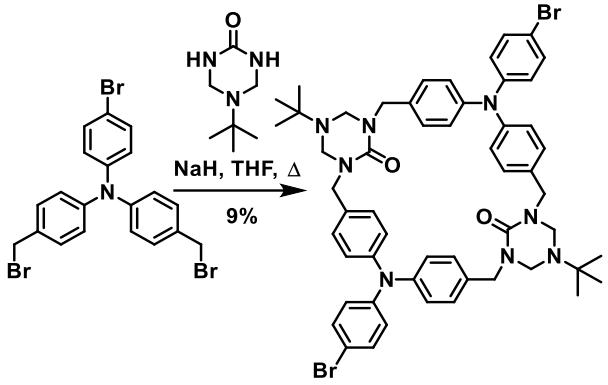

4,10-*bis*(4-Bromophenyl)-1^5,7^5-di-*tert*-butyl-4,10-diaza-1,7(1,3)-ditriazinana3,5,-9,11(1,4)-tetr-abenzenacyclododecaphane-1^2,7^2-dione: *tert*-Butyl triazinanone (1.321 g, 8.4 mmol) and sodium hydride (60% suspension in paraffin oil, 1.344 g, 33.6 mmol) were suspended in 330 mL of dry tetrahydrofuran and was stirred for 2 hours at reflux. After cooling to room temperature, the previous bromide (4.285 g, 8.4 mmol) was added as a solution in 330 mL of dry tetrahydrofuran. The reaction stirred at reflux in the dark for 2 days. Upon completion, the reaction was quenched with 17 and 61 mL of 1N $HCl_{(aq)}$ and

water then reduced *in vacuo* to 330 mL. An additional 44 and 218 mL of 1N $HCl_{(aq)}$ and water were added to the solution before it was extracted with dichloromethane (3 × 440 mL). The combined organic layers were washed with brine (1 × 440 mL) and dried with $MgSO_4$. The solvent was removed via rotary evaporation, and then the material was recrystallized from chloroform. Vacuum drying the crystals yielded the product as a white powder (9%). ^{1}H NMR (400 MHz, TCE-d_2, 90˚C): δ (ppm) 7.39 (d, J = 8.7 Hz, 4H), 7.25 (d, 8.1 Hz, 8H), 7.03 (m, 12H), 4.46 (br, 8H), 4.29 (s, 8H), 0.83 (s, 18H). ^{13}C NMR (75 MHz, $CDCl_3$): δ (ppm) 155.59, 147.03, 146.70, 133.02, 132.35, 130.58, 125.34, 124.23, 115.14, 60.29, 54.46, 47.07, 28.30. HRMS (DEP): [M+] calculated, 1009.3122; found, 1009.3136.

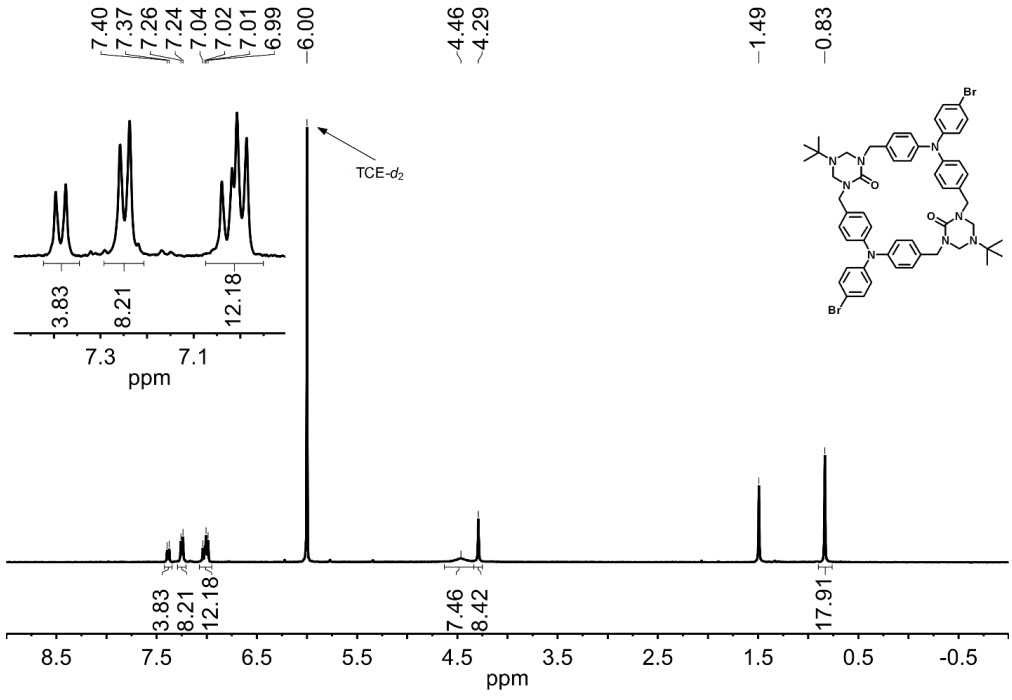

Figure 4.10. ^{1}H NMR of protected **1** (TCE-d_2, 90°C, 400 MHz).

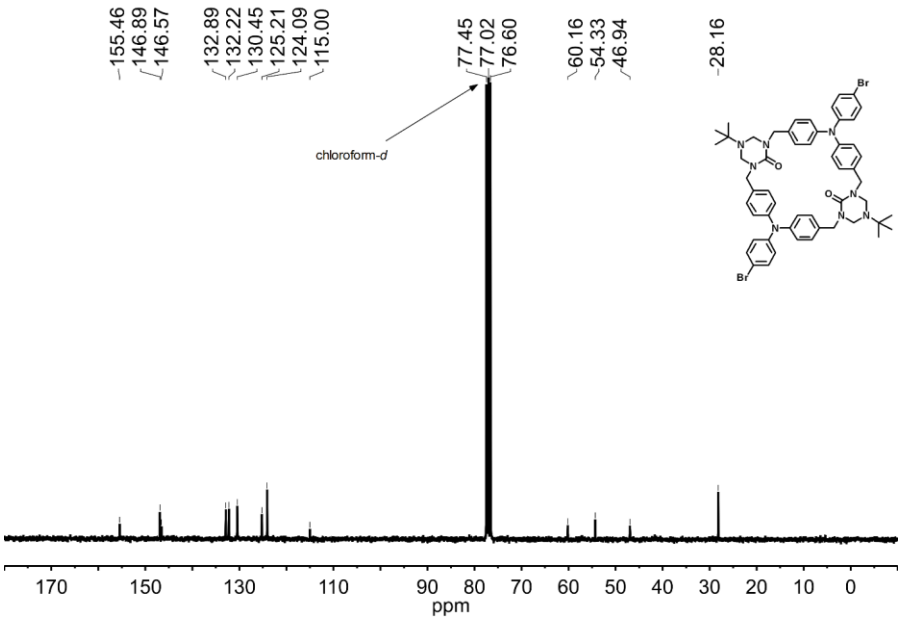

Figure 4.11. ^{13}C NMR of protected **1** ($CDCl_3$, 75 MHz).

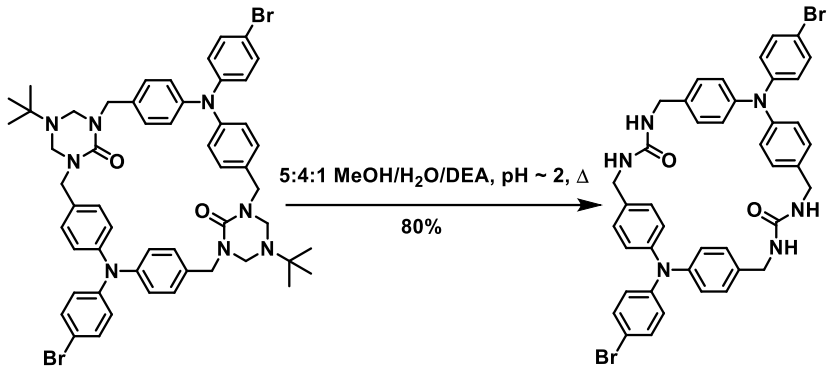

2,10-*bis*(4-Bromophenyl)-2,5,7,10,13,15-hexaaza-1,3,9,11(1,4)tetrabenzenacyclo-hexadecaphane-6,14-dione: The previous protected urea (0.240 g, 0.2 mmol) was suspended in 225 mL of a 5:4:1 solution of methanol, water, and diethanol amine and the pH was adjusted to 2 using 12 M HCl. This mixture was heated at reflux for one week in the dark. During this time the pH was recalibrated to 2 every 12 hours. After cooling to room temperature, the reaction was filtered and the residue was washed with 100 mL of 1 N $HCl_{(aq)}$ then 100 mL water leaving behind the product as a beige solid (80%).^1H NMR (300 MHz, $(CD_3)_2SO$): δ (ppm) 7.39 (d, J = 8.8 Hz, 4H), 7.15 (d, J = 8.3 Hz, 8H), 6.93 (d,

J = 8.3 Hz, 8H), 6.82 (d, *J* = 8.7 Hz, 4H), 6.52 (t, *J* = 6.0 Hz, 4H), 4.18 (d, *J* = 6.0 Hz, 8H). ^{13}C NMR (75 MHz, $(CD_3)_2SO$): δ (ppm) 157.80, 146.93, 145.23, 136.61, 132.07, 128.12, 124.28, 124.02, 113.40, 42.08.

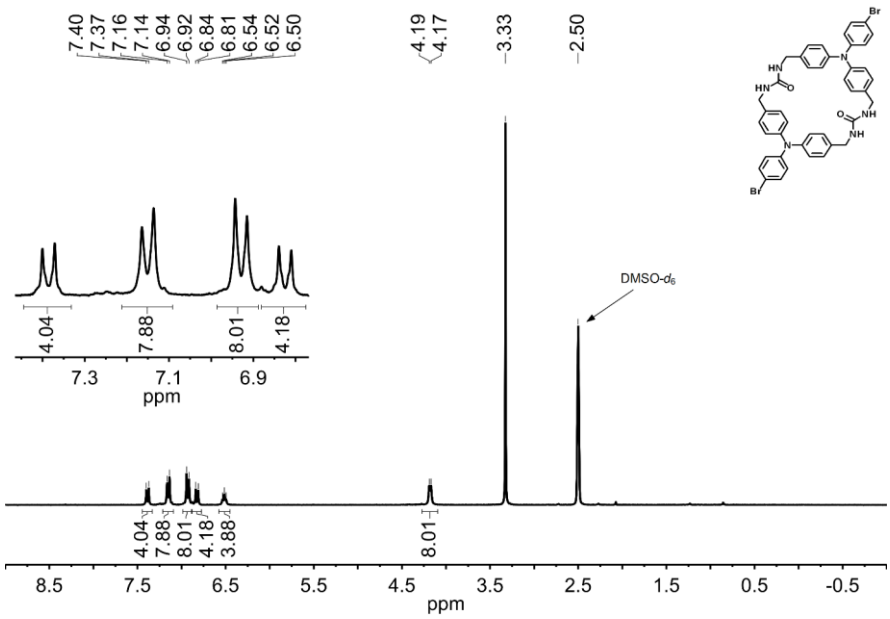

Figure 4.12. ^{1}H NMR of **1** ($(CD_3)_2SO$, 300 MHz).

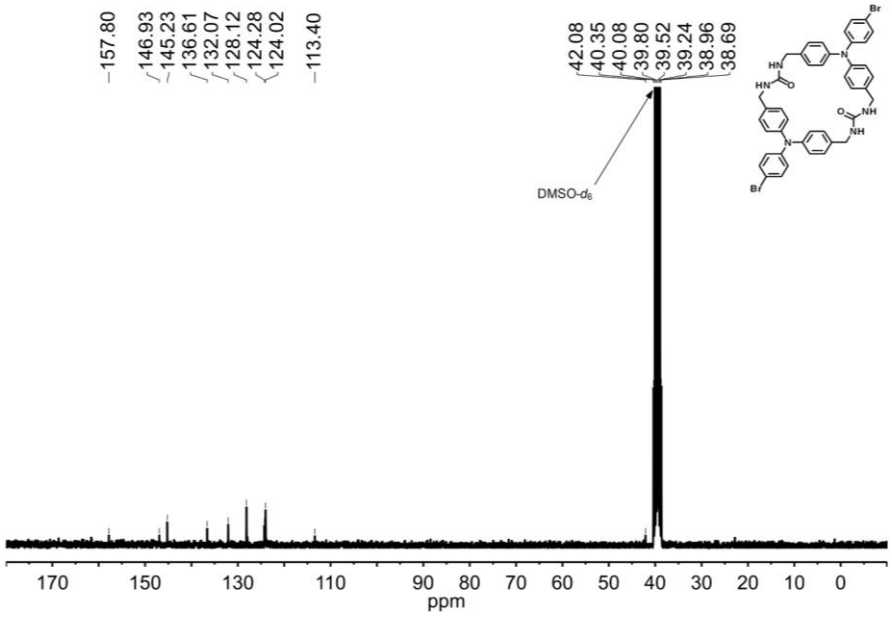

Figure 4.13. ^{13}C NMR of **1** ($(CD_3)_2SO$, 75 MHz).

4.4.3 Crystal Data and Structure Refinement

Table 4.1. Data Collection and Refinement for Non-Benzene Related Crystals.

Identification Code	(Protected 1)·$(CHCl_3)_8$	1·$(DME)_{0.5}$	1
CCDC	1899526	1899527	1899528
Color of Crystal	$C_{62}H_{66}Br_2Cl_{24}N_8O_2$	$C_{44}H_{41}Br_2N_6O_3$	$C_{42}H_{36}Br_2N_6O_2$
Empirical formula	1965.84	861.65	816.59
Formula weight	173(2)	100(2)	100(2)
Temperature/K	triclinic	monoclinic	monoclinic
Crystal system	P-1	$P2_1/c$	$P2_1/c$
Space group	12.3182(5)	15.8633(11)	15.8204(7)
a/Å	12.4639(5)	4.6200(4)	4.6117(2)
b/Å	14.2206(5)	26.788(2)	26.8694(12)
c/Å	91.288(2)	90	90
α/deg	105.248(2)	100.128(2)	100.316(2)
β/deg	95.864(2)	90	90
γ/deg	2092.67(14)	1932.6(3)	1928.67(15)
Volume/$Å^3$	1	2	2
Z	1.560	1.481	1.406
$\rho_{calc}g/cm^3$	1.780	2.147	2.145
μ/mm^{-1}	988.0	882.0	832.0
F(000)	0.48 × 0.35 × 0.24	0.6 × 0.08 × 0.04	0.4 × 0.04 × 0.03
Crystal size/mm^3	MoKα (λ = 0.71073)	MoKα (λ = 0.71073)	MoKα (λ = 0.71073)
Radiation	4.318 to 50.05	4.38 to 50.164	5.234 to 55.178
2Θ range for data collection/deg	-14 ≤ h ≤ 14, -14 ≤ k ≤ 14, -16 ≤ l ≤ 16	-18 ≤ h ≤ 18, -5 ≤ k ≤ 5, -30 ≤ l ≤ 31	-20 ≤ h ≤ 20, -6 ≤ k ≤ 6, -34 ≤ l ≤ 33
Index ranges	66320	16686	28652
Reflections collected	7388 [R_{int} = 0.0348, R_{sigma} = 0.0204]	3424 [R_{int} = 0.0613, R_{sigma} = 0.0489]	4436 [R_{int} = 0.0610, R_{sigma} = 0.0358]
Independent reflections	7388/146/634	3424/16/269	4436/2/242
Data/restraints/parameters	1.034	1.065	1.038
Goodness-of-fit on F^2	R_1 = 0.0624, wR_2 = 0.1705	R_1 = 0.0403, wR_2 = 0.0920	R_1 = 0.0310, wR_2 = 0.0729
Final R indexes [I ≥ 2σ (I)]	R_1 = 0.0799, wR_2 = 0.1859	R_1 = 0.0605, wR_2 = 0.1001	R_1 = 0.0426, wR_2 = 0.0775
Final R indexes [all data]	0.95/-1.09	0.59/-0.55	0.51/-0.47

Table 4.2. Data Collection and Refinement for Lighter Benzene Derivative Loaded Hosts.

Identification Code	$1\cdot(C_6H_6)_{0.56}$	$1\cdot(C_6H_5F)_{0.52}$	$1\cdot(C_6H_5Cl)_{0.52}$
CCDC	1899529	1899530	1899531
Color of Crystal	$C_{45.38}H_{39.38}Br_2N_6O_2$	$C_{45}H_{38.5}Br_2F_{0.5}N_6O_2$	$C_{45.14}H_{38.62}Br_2Cl_{0.52}N_6O_2$
Empirical formula	860.52	864.64	875.54
Formula weight	100(2)	100(2)	100(2)
Temperature/K	monoclinic	monoclinic	monoclinic
Crystal system	$P2_1/c$	$P2_1/c$	$P2_1/c$
Space group	15.8777(5)	15.8857(6)	15.8533(6)
a/Å	4.6345(2)	4.6310(2)	4.6332(2)
b/Å	26.7173(8)	26.7350(10)	26.7661(10)
c/Å	90	90	90
α/deg	99.975(2)	99.910(2)	100.069(2)
β/deg	90	90	90
γ/deg	1936.28(12)	1937.46(13)	1935.73(13)
Volume/$Å^3$	2	2	2
Z	1.476	1.482	1.502
$\rho_{calc}g/cm^3$	2.141	2.142	2.178
μ/mm^{-1}	879.0	882.0	893.0
F(000)	0.28 × 0.04 × 0.03	0.14 × 0.06 × 0.03	0.1 × 0.06 × 0.02
Crystal size/mm^3	MoKα (λ = 0.71073)	MoKα (λ = 0.71073)	MoKα (λ = 0.71073)
Radiation	3.684 to 50.148	4.372 to 50.098	3.68 to 50.104
2Θ range for data collection/deg	-18 ≤ h ≤ 18, -4 ≤ k ≤ 5, -31 ≤ l ≤ 31	-18 ≤ h ≤ 18, -5 ≤ k ≤ 5, -31 ≤ l ≤ 31	-18 ≤ h ≤ 18, -5 ≤ k ≤ 5, -31 ≤ l ≤ 31
Index ranges	22892	19628	18624
Reflections collected	3428 [R_{int} = 0.0644, R_{sigma} = 0.0354]	3422 [R_{int} = 0.0611, R_{sigma} = 0.0369]	3419 [R_{int} = 0.0665, R_{sigma} = 0.0414]
Independent reflections	3428/21/281	3422/4/259	3419/7/274
Data/restraints/parameters	1.067	1.058	1.063
Goodness-of-fit on F^2	R_1 = 0.0395, wR_2 = 0.0882	R_1 = 0.0461, wR_2 = 0.1076	R_1 = 0.0417, wR_2 = 0.0905
Final R indexes [I ≥ 2σ (I)]	R_1 = 0.0547, wR_2 = 0.0944	R_1 = 0.0651, wR_2 = 0.1163	R_1 = 0.0597, wR_2 = 0.0982
Final R indexes [all data]	0.59/-0.44	1.09/-0.65	0.67/-0.44

Table 4.3. Data Collection and Refinement for Heavier Benzene Derivative Loaded Hosts.

Identification Code	$1\cdot(C_6H_5Br)_{0.52}$	$1\cdot(C_6H_5I)_{0.49}$
CCDC	1899532	1899533
Color of Crystal	$C_{45.09}H_{38.58}Br_{2.52}N_6O_2$	$C_{44.98}H_{38.48}Br_2I_{0.5}N_6O_2$
Empirical formula	897.51	917.63
Formula weight	100(2)	100(2)
Temperature/K	monoclinic	monoclinic
Crystal system	$P2_1/c$	$P2_1/c$
Space group	15.8509(6)	15.8680(5)
a/Å	4.6392(2)	4.6477(2)
b/Å	26.7433(9)	26.6829(9)
c/Å	90	90
α/deg	100.019(2)	100.071(2)
β/deg	90	90
γ/deg	1936.59(13)	1937.53(12)
Volume/$Å^3$	2	2
Z	1.539	1.573
$\rho_{calc}g/cm^3$	2.672	2.534
μ/mm^{-1}	910.0	925.0
F(000)	0.12 × 0.04 × 0.03	0.22 × 0.05 × 0.03
Crystal size/mm^3	MoKα (λ = 0.71073)	MoKα (λ = 0.71073)
Radiation	2.61 to 48.61	2.606 to 52.768
2Θ range for data collection/deg	-18 ≤ h ≤ 18, -4 ≤ k ≤ 5, -30 ≤ l ≤ 30	-19 ≤ h ≤ 19, -5 ≤ k ≤ 5, -33 ≤ l ≤ 33
Index ranges	16210	37894
Reflections collected	3149 [R_{int} = 0.0861, R_{sigma} = 0.0548]	3962 [R_{int} = 0.0607, R_{sigma} = 0.0270]
Independent reflections	3149/6/276	3962/90/281
Data/restraints/parameters	1.032	1.050
Goodness-of-fit on F^2	R_1 = 0.0452, wR_2 = 0.0971	R_1 = 0.0369, wR_2 = 0.0840
Final R indexes [I ≥ 2σ (I)]	R_1 = 0.0729, wR_2 = 0.1081	R_1 = 0.0473, wR_2 = 0.0889
Final R indexes [all data]	0.66/-0.42	0.67/-0.46

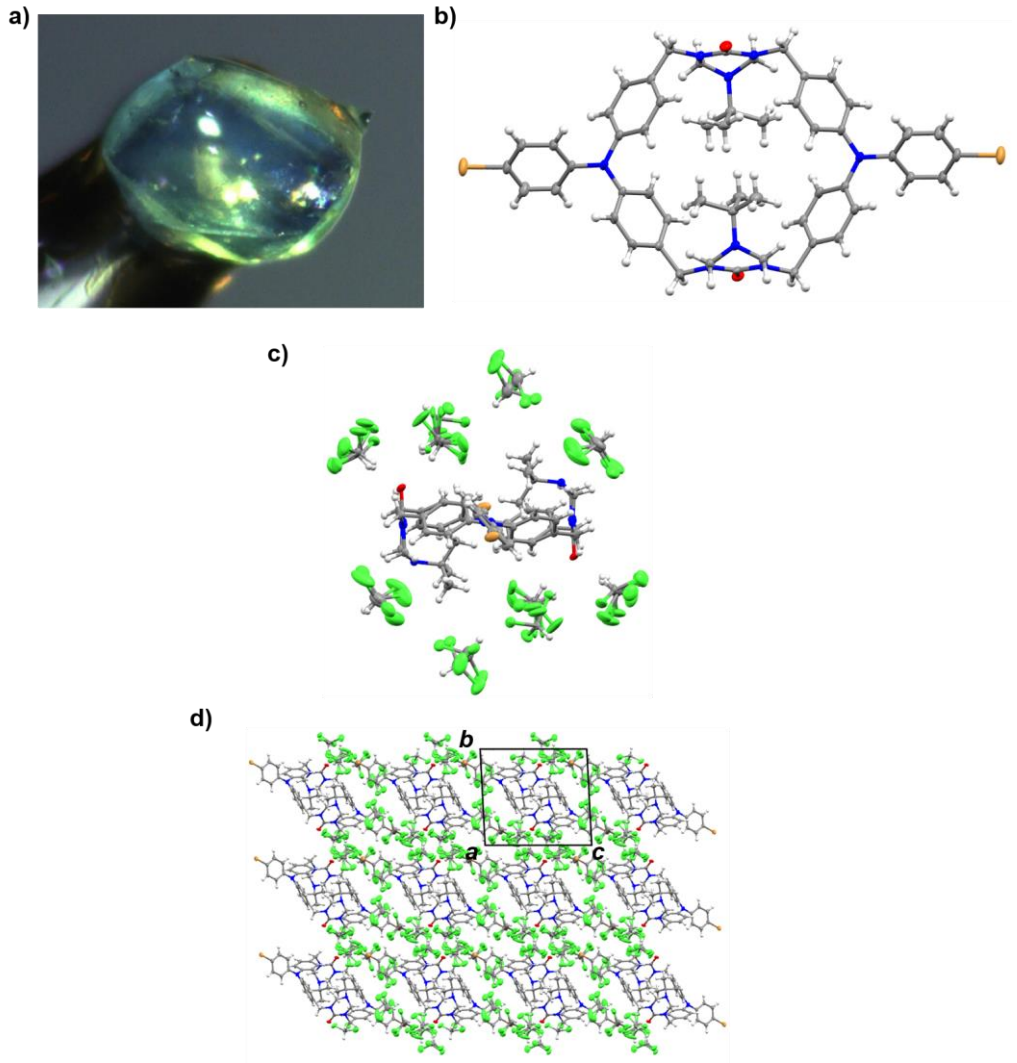

Figure 4.14. Crystal views of (Protected **1**)·$(CHCl_3)_8$. (a) Data crystal coated with oil and mounted on the diffractometer at T = 173(2) K. (b) Molecular structure of protected **1**, (c) one unit cell, and (d) crystal packing along the *a* axis. Thermal ellipsoids were drawn at the 30% probability level.

Crystals formed as visually perfect colorless blocks. They are extremely unstable with respect to solvent loss and crumble to a powder within seconds of removal from the mother liquor. If transferred rapidly from the mother liquor into a drop of oil (*e.g* paratone-N), they can be handled for minutes before decomposition. They were also observed to fracture and suffer degraded crystallinity when flash-cooled at temperatures below *ca*. 150 K. X-ray intensity data were collected at 173(2) K using a Bruker D8 QUEST

diffractometer equipped with a PHOTON-100 CMOS area detector and an Incoatec microfocus source (Mo Kα radiation, λ = 0.71073 Å). The raw area detector data frames were reduced and corrected for absorption effects using the Bruker APEX3, SAINT+ and SADABS programs.[48,49] Final unit cell parameters were determined by least-squares refinement of 9408 reflections taken from the data set. The structure was solved with SHELXT.[50,51] Subsequent difference Fourier calculations and full-matrix least-squares refinement against F^2 were performed with SHELXL-2018[50,51] using OLEX2.[52]

The compound crystallizes in the triclinic system. The space group *P*-1 (No. 2) was confirmed by structure solution. The asymmetric unit consists of half of one $C_{54}H_{58}Br_2N_8O_2$ molecule, which is located on a crystallographic inversion center, and four independent chloroform molecules. All four $CHCl_3$ molecules are disordered and were modeled with two, three or four components. The total site occupancy for each molecule was constrained to sum to one. C-Cl distances were restrained to 1.75(2) Å, and all Cl-Cl distances were restrained to be similar. All non-hydrogen atoms were refined with anisotropic displacement parameters. Anisotropic displacement parameters for nearly overlapped atoms of the disordered chloroform molecules were held equal. Hydrogen were placed in geometrically idealized positions and included as riding atoms with *d*(C-H) = 1.00 Å and *U*iso(H) = 1.2*U*eq(C) for methine hydrogen atoms, *d*(C-H) = 0.95 Å and *U*iso(H) = 1.2*U*eq(C) for aromatic hydrogen atoms, *d*(C-H) = 0.99 Å and *U*iso(H) = 1.2*U*eq(C) for methylene hydrogen atoms, and *d*(C-H) = 0.98 Å and *U*iso(H) = 1.5*U*eq(C) for methyl hydrogens. The methyl hydrogens were allowed to rotate as a rigid group to the orientation of maximum observed electron density. The largest residual electron density peak in the final difference map is 0.95 $e^-/Å^3$, located 1.95 Å from Cl29.

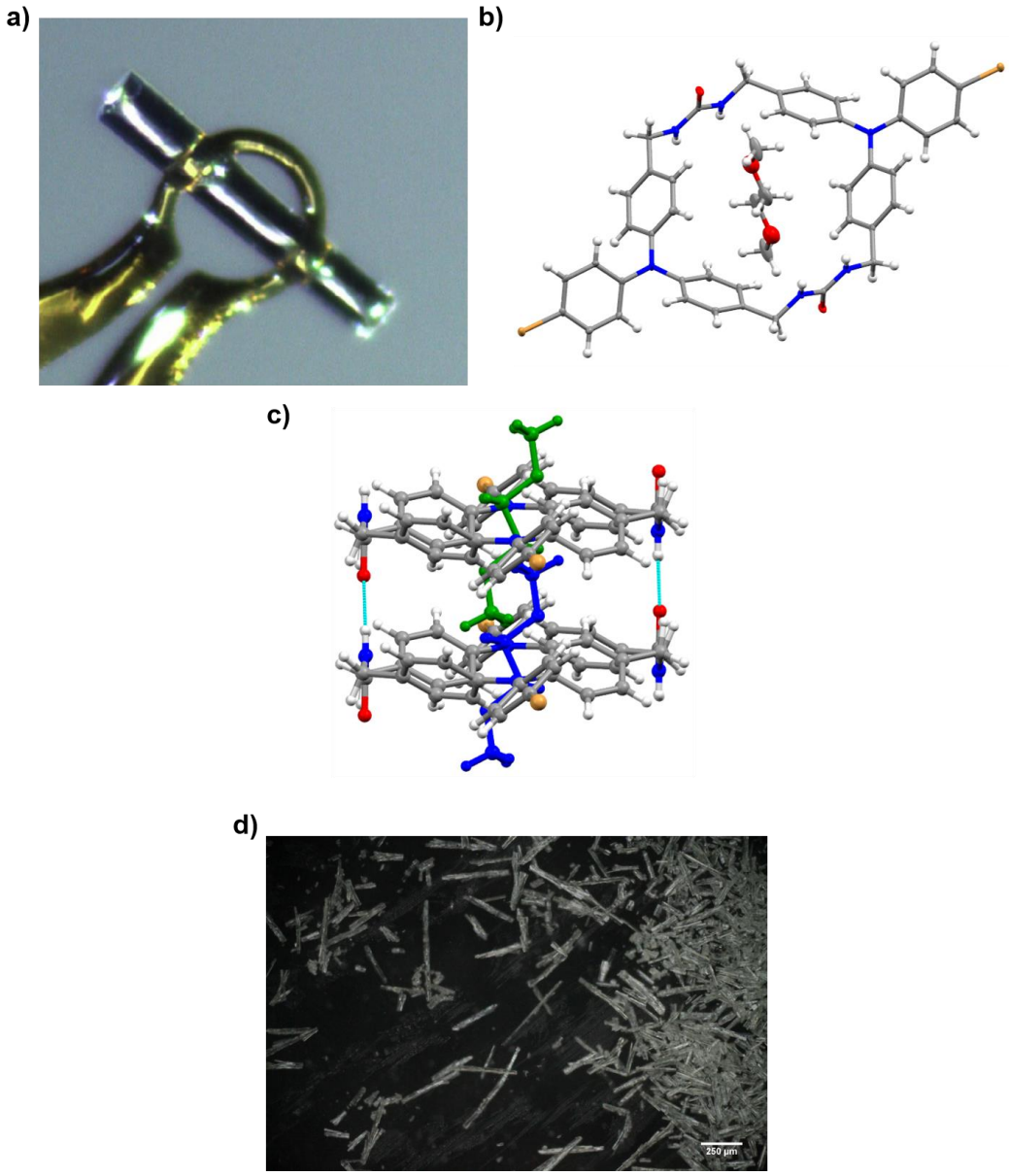

Figure 4.15. Crystal views of **1**·$(DME)_{0.5}$. (a) Data crystal. (b) Components of structure. Thermal ellipsoids were drawn at the 30% probability level. (c) View of DME disorder inside the host **1**. (d) Picture of crystals using an Olympus BX-51 epifluorescence microscope using a 5× objective lens in dark field mode. Image was collected with a color digital CMOS camera (Canon EOS REBEL T3/1100D). Scale bar is set at 250 µm. An average crystal size of 35 × 265 µm was found by measuring multiple crystals.

X-ray intensity data from a colorless needle were collected at 100(2) K using a Bruker D8 QUEST diffractometer equipped with a PHOTON-100 CMOS area detector

and an Incoatec microfocus source (Mo Kα radiation, λ = 0.71073 Å). The raw area detector data frames were reduced and corrected for absorption effects with the Bruker APEX3, SAINT+ and SADABS programs.[48,49] The structure was solved with SHELXT.[50,51] Subsequent difference Fourier calculations and full-matrix least-squares refinement against F^2 were performed with SHELXL-2018[50,51] using OLEX2.[52]

The compound crystallizes in the monoclinic system. The pattern of systematic absences in the intensity data was uniquely consistent with the space group $P2_1/c$, which was confirmed by structure solution. The asymmetric unit consists of half of one $C_{42}H_{36}Br_2N_6O_2$ cycle and (formally) ¼ of one glyme (1,2-dimethoxyethane) molecule. The glyme molecule is located on a crystallographic inversion center and is further disordered over another inversion center. The three symmetry-independent atoms of this molecule were refined with fixed occupancies of 0.5. Appropriate C-C and C-O distance restraints were applied. All non-hydrogen atoms were refined with anisotropic displacement parameters. Enhanced rigid-bond restraints (SHELX RIGU) was applied to the U_{ij} coefficients of the disordered glyme atom displacement parameters. Hydrogen atoms bonded to carbon were placed in geometrically idealized positions and included as riding atoms with *d*(C-H) = 0.95 Å and *U*iso(H) = 1.2*U*eq(C) for aromatic hydrogen atoms, *d*(C-H) = 0.99 Å and *U*iso(H) = 1.2*U*eq(C) for methylene hydrogen atoms, and *d*(C-H) = 0.98 Å and *U*iso(H) = 1.5*U*eq(C) for methyl hydrogens. The methyl hydrogens were allowed to rotate as a rigid group to the orientation of maximum observed electron density. N-H hydrogen atoms were located in a difference maps and refined with *d*(N-H) = 0.84(2) Å distance restraints and *U*iso(H) = 1.2*U*eq(N). The largest residual electron density peak in the final difference map is 0.59 $e^-/Å^3$, located 0.34 Å from H1SA.

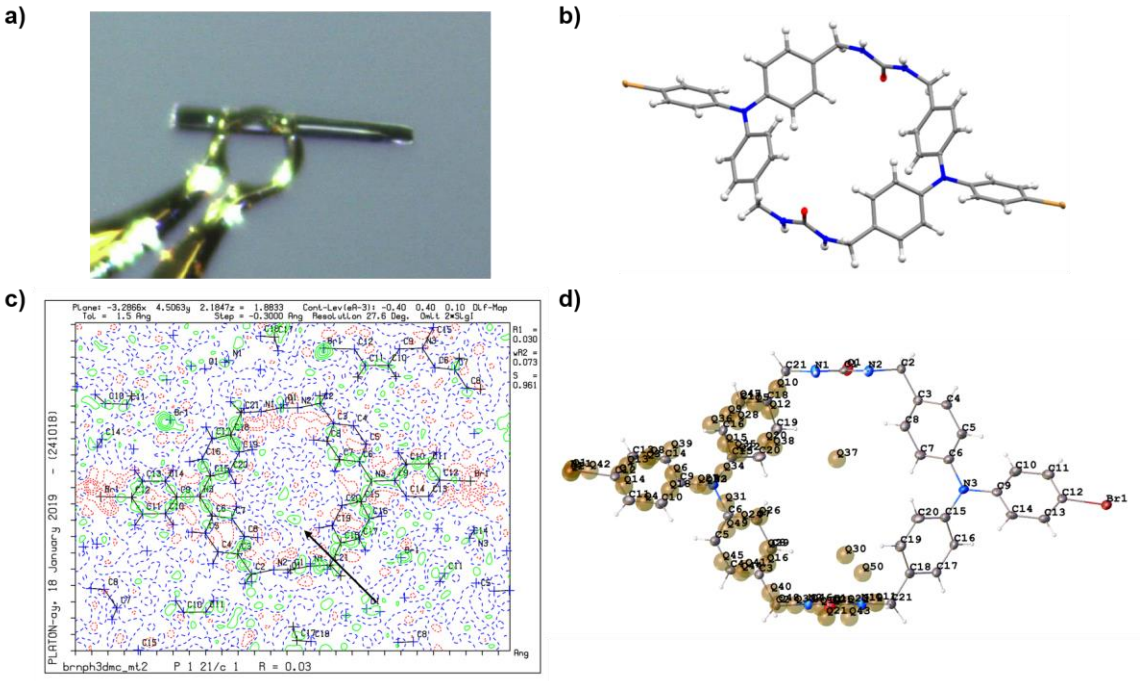

Figure 4.16. Crystal views of **1**. (a) Data crystal for second data set. (b) Molecular structure. Thermal ellipsoids were drawn at the 30% probability level. (c) Difference electron density contour map. Solid green contours represent positive electron density, red dashed lines negative electron density, and blue dashed lines zero e-/Å^3 contours. The maximum observed electron density of 0.19 e-/Å^3 inside the cycle column is marked with an arrow. (d) Difference electron density shown as SHELXL "Q-peaks". Q30 has magnitude of 0.20 e-/Å^3; Q37 is 0.19 e-/Å^3.

X-ray intensity data from colorless needles were collected at 100(2) K using a Bruker D8 QUEST diffractometer equipped with a PHOTON-100 CMOS area detector and an Incoatec microfocus source (Mo Kα radiation, λ = 0.71073 Å). The raw area detector data frames were reduced and corrected for absorption effects using the Bruker APEX3, SAINT+ and SADABS programs.[48,49] The structure was solved with SHELXT.[50,51] Subsequent difference Fourier calculations and full-matrix least-squares refinement against F^2 were performed with SHELXL-2018[50,51] using OLEX2.[52]

The compound crystallizes in the monoclinic system. The pattern of systematic absences in the intensity data was consistent with the space group $P2_1/c$, which was

confirmed by structure solution. The asymmetric unit consists of half of one $C_{42}H_{36}Br_2N_6O_2$ molecule, which is located on a crystallographic inversion center. All non-hydrogen atoms were refined with anisotropic displacement parameters. Hydrogen atoms bonded to carbon were located in difference Fourier maps before being placed in geometrically idealized positions and included as riding atoms with *d*(C-H) = 0.95 Å and *U*iso(H) = 1.2*U*eq(C) for aromatic hydrogen atoms and *d*(C-H) = 0.99 Å and *U*iso(H) = 1.2*U*eq(C) for methylene hydrogen atoms. Hydrogen atoms bonded to the urea nitrogen atoms were located and refined with a common isotropic displacement parameter and *d*(N-H) = 0.85(2) Å. The largest residual electron density peak and hole in the final difference map are +0.50 $e^-/Å^3$ and -0.47 $e^-/Å^3$, located 1.02 Å and 0.91 Å from Br1, respectively.

The difference electron density map was inspected carefully for residual electron density in the interior of the columns formed by the $C_{42}H_{36}Br_2N_6O_2$ cycle, where solvent molecules were located before heating. Datasets were collected from two separate single crystals. The first dataset (crystal 1) came from a specimen selected immediately after removing the sample from the heating apparatus (TGA) used to remove the solvent guests. The second dataset (crystal 2) was from a crystal which had been exposed to air for three days. The results from the two datasets were essentially identical. No significant electron density was observed in interior of the columns formed by the cycles. The largest residual peaks inside the columns had magnitudes of 0.21 e-/$Å^3$ (crystal no. 1, Q-peak #40 in the SHELXL list) and 0.19 $e^-/Å^3$ (crystal no. 2, SHELXL Q-peak #37). Trial refinements of this peak as a partially occupied carbon atom resulted in an occupancy value of 0.03(2), within experimental error of zero (crystal 1). No change in *R*-values or difference map features was observed upon including this peak in the refinement. It is concluded then, that

the peak is simply background noise and does not arise from atomic electron density, and further, that the column interior is effectively empty to within the detection limit of the single crystal X-ray diffraction technique.

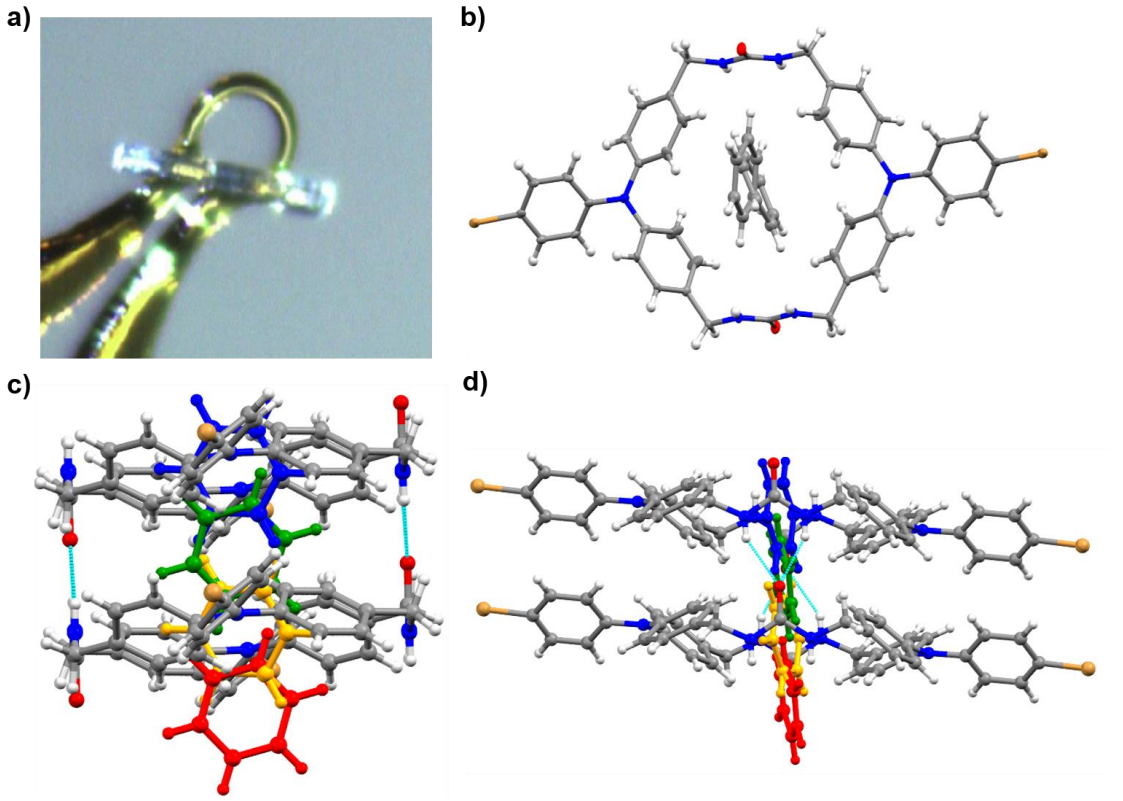

Figure 4.17. Crystal views of **1**·$(C_6H_6)_{0.56}$. (a) Data crystal. (b) Components of structure. Thermal ellipsoids were drawn at the 30% probability level. (c) View of C_6H_6 disorder inside the host **1**. (d) Another view of the disorder.

X-ray intensity data from a colorless needle were collected at 100(2) K using a Bruker D8 QUEST diffractometer equipped with a PHOTON-100 CMOS area detector and an Incoatec microfocus source (Mo Kα radiation, λ = 0.71073 Å). The raw area detector data frames were reduced and corrected for absorption effects using the Bruker APEX3, SAINT+ and SADABS programs.[48,49] The structure was solved with SHELXT.[50,51] Subsequent difference Fourier calculations and full-matrix least-squares refinement against F^2 were performed with SHELXL-2018[50,51] using OLEX2.[52]

The compound crystallizes in the space group $P2_1/c$ of the monoclinic system. The asymmetric unit consists of half of one $C_{42}H_{36}Br_2N_6O_2$ cycle located on a crystallographic inversion center and several electron density peaks inside the tubular channels created by the cycle columns. The residual difference electron density in the channel region is disordered, but arranged in a tapelike fashion along the crystallographic *b* axis direction. If assigned as carbon atoms, all peaks refined to less than full occupancy. The peaks could be reasonably fitted to half each (3 carbon atoms) of two crystallographically independent benzene molecules, both located on crystallographic inversion centers. All 1,2-C-C distances in the benzene guests were restrained to d = 1.40(2) Å. 1,4-C-C (opposite) distances were restrained to be similar to each other (SHELX SADI), and the minor component (C4S-C6S) was further restrained to be flat (SHELX FLAT). Occupancies refined to: C1S-C3S = 0.437(5) and C4S-C6S = 0.126(9), generating a C_6H_6 composition per cycle of 0.56(1). The benzene group occupancies were linked so that the sum of occupancies of benzene molecules within van der Waals radii of other benzenes was not greater than one. All non-hydrogen atoms were refined with anisotropic displacement parameters, except for atoms of the minor benzene component, which were assigned a common isotropic displacement parameter. Hydrogen atoms bonded to carbon were placed in geometrically idealized positions and included as riding atoms with d(C-H) = 0.95 Å and Uiso(H) = 1.2Ueq(C) for aromatic hydrogen atoms and d(C-H) = 0.99 Å and Uiso(H) = 1.2Ueq(C) for methylene hydrogen atoms. The two urea hydrogen atoms were located and refined with d(N-H) = 0.85(2) Å distance restraints and Uiso(H) = 1.2Ueq(N). The largest residual electron density peak in the final difference map is 0.59 $e^-/Å^3$, located 1.08 Å from Br1.

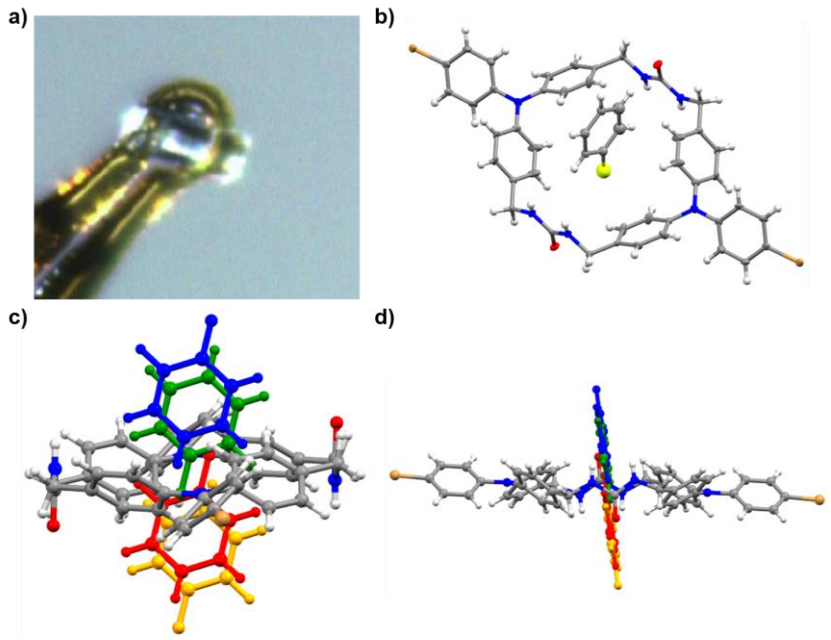

Figure 4.18. Crystal views of **1**·$(C_6H_5F)_{0.52}$. (a) Data crystal. (b) Components of structure. Thermal ellipsoids were drawn at the 30% probability level. (c) View of C_6H_5F disorder inside the host **1**. (d) Another view of the disorder.

X-ray intensity data from a colorless needle were collected at 100(2) K using a Bruker D8 QUEST diffractometer equipped with a PHOTON-100 CMOS area detector and an Incoatec microfocus source (Mo Kα radiation, λ = 0.71073 Å). The raw area detector data frames were reduced and corrected for absorption effects using the Bruker APEX3, SAINT+ and SADABS programs.[48,49] The structure was solved with SHELXT.[50,51] Subsequent difference Fourier calculations and full-matrix least-squares refinement against F^2 were performed with SHELXL-2018[50,51] using OLEX2.[52]

The compound crystallizes in the space group $P2_1/c$ of the monoclinic system. The asymmetric unit consists of half of one $C_{42}H_{36}Br_2N_6O_2$ cycle located on a crystallographic inversion center and disordered fluorobenzene molecules located in channels created by the cycle packing. The fluorobenzene molecules are disordered within planar 'tapes' running along the crystallographic *b* axis direction. One crystallographically independent

C_6H_5F was modeled, which is disordered over two sites about a crystallographic inversion center. Translational symmetry brings two additional symmetry-related C_6H_5F molecules in close proximity, and therefore the maximum crystallographic occupancy for each C_6H_5F disorder component is 0.25. Free refinement of the C_6H_5F occupancy yielded 0.26(1), but was fixed at 0.25 for the final model. The phenyl rings was fitted to a regular hexagonal with *d*(C-C) = 1.39 Å, and appropriate C-F distance restraints were applied. All non-hydrogen atoms were refined with anisotropic displacement parameters except for disordered fluorobenzene atoms (isotropic). Hydrogen atoms bonded to carbon were located in difference Fourier maps before being placed in geometrically idealized positions and included as riding atoms with *d*(C-H) = 0.95 Å and *U*iso(H) = 1.2*U*eq(C) for aromatic hydrogen atoms and *d*(C-H) = 0.99 Å and *U*iso(H) = 1.2*U*eq(C) for methylene hydrogen atoms. The two urea hydrogen atoms were located in difference Fourier maps and refined isotropically with *d*(N-H) = 0.84(2) distance restraints. The largest residual electron density peak in the final difference map is 1.09 $e^-/Å^3$, located 1.11 Å from C3S.

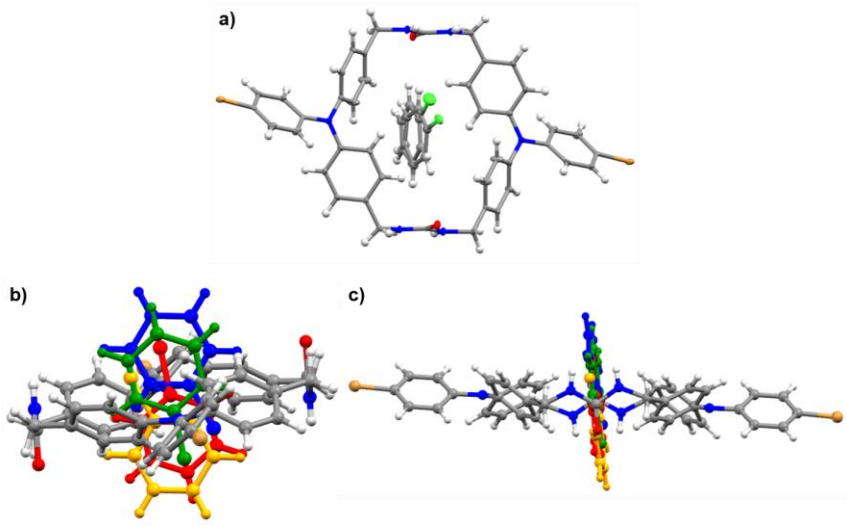

Figure 4.19. Crystal views of **1**·$(C_6H_5Cl)_{0.52}$. (a) Data crystal. (b) Components of structure. Thermal ellipsoids were drawn at the 30% probability level. (c) View of C_6H_5Cl disorder inside the host **1**. (d) Another view of the disorder.

X-ray intensity data from a colorless needle were collected at 100(2) K using a Bruker D8 QUEST diffractometer equipped with a PHOTON-100 CMOS area detector and an Incoatec microfocus source (Mo Kα radiation, λ = 0.71073 Å). The raw area detector data frames were reduced and corrected for absorption effects using the Bruker APEX3, SAINT+ and SADABS programs.[48,49] The structure was solved with SHELXT.[50,51] Subsequent difference Fourier calculations and full-matrix least-squares refinement against F^2 were performed with SHELXL-2018[50,51] using OLEX2.[52]

The compound crystallizes in the space group $P2_1/c$ of the monoclinic system. The asymmetric unit consists of half of one $C_{42}H_{36}Br_2N_6O_2$ cycle located on a crystallographic inversion center and several electron density peaks inside the tubular channels created by the cycle columns. The residual difference electron density in the channel region is highly disordered, but arranged in a tapelike planar fashion along the crystallographic *b* axis direction. If assigned as carbon atoms, most peaks refined to less than full occupancy. Two peaks refined to significantly greater than or near 100% carbon occupancy. These were assumed to be chlorine atoms from the crystal soaking agent chlorobenzene. Two independent, partially occupied C_6H_5Cl molecules were modeled. Both are further disordered about a crystallographic inversion center. The phenyl rings of each were fitted to rigid hexagons, and both bonded C-Cl distances were restrained to 1.74(2) Å. 1,3-C-Cl distances were restrained to be similar to each other (SHELX SADI). Occupancies refined to: Cl1S/C1S-C6S = 0.187(3) and Cl2S/C7S-C12S = 0.074(3), generating a C_6H_5Cl composition per cycle of 0.523(6). All non-hydrogen atoms were refined with anisotropic displacement parameters. All carbon atoms of the chlorobenzene C_6 rings were assigned a common isotropic displacement parameter. Hydrogen atoms bonded to carbon were placed

in geometrically idealized positions and included as riding atoms with *d*(C-H) = 0.95 Å and *U*iso(H) = 1.2*U*eq(C) for aromatic hydrogen atoms and *d*(C-H) = 0.99 Å and *U*iso(H) = 1.2*U*eq(C) for methylene hydrogen atoms. The two urea hydrogen atoms were located and refined with *d*(N-H) = 0.84(2) Å distance restraints and *U*iso(H) = 1.2*U*eq(N). The largest residual electron density peak in the final difference map is 0.67 $e^-/Å^3$, located 0.56 Å from C1S.

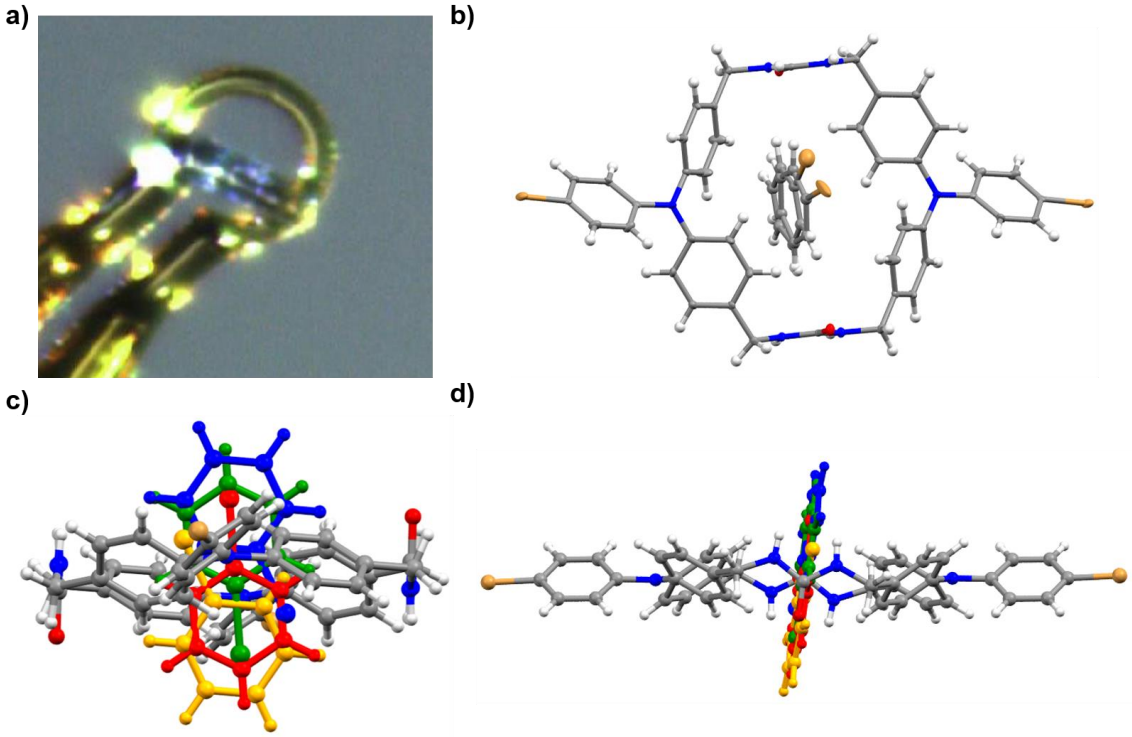

Figure 4.20. Crystal views of **1**·$(C_6H_5Br)_{0.52}$. (a) Data crystal. (b) Components of structure. Thermal ellipsoids were drawn at the 30% probability level. (c) View of C_6H_5Br disorder inside the host **1**. (d) Another view of the disorder.

X-ray intensity data from a colorless needle were collected at 100(2) K using a Bruker D8 QUEST diffractometer equipped with a PHOTON-100 CMOS area detector and an Incoatec microfocus source (Mo Kα radiation, λ = 0.71073 Å). The raw area detector data frames were reduced and corrected for absorption effects using the Bruker

APEX3, SAINT+ and SADABS programs.[48,49] The structure was solved with SHELXT.[50,51] Subsequent difference Fourier calculations and full-matrix least-squares refinement against F^2 were performed with SHELXL-2018[50,51] using OLEX2.[52]

The compound crystallizes in the space group $P2_1/c$ of the monoclinic system. The asymmetric unit consists of half of one $C_{42}H_{36}Br_2N_6O_2$ cycle located on a crystallographic inversion center and several electron density peaks inside the tubular channels created by the cycle columns. The residual difference electron density in the channel region is highly disordered, but arranged in a tapelike planar fashion along the crystallographic *b* axis direction. If assigned as carbon atoms, most peaks refined to less than full occupancy. Two peaks refined to significantly greater than or near 100% carbon occupancy. These were assumed to be bromine atoms from the crystal soaking agent bromobenzene. Two independent, partially occupied C_6H_5Br molecules were modeled. Both are further disordered about a crystallographic inversion center. The phenyl rings of each were fitted to rigid hexagons, and both bonded C-Br distances were restrained to 1.90(2) Å. 1,3-C-Br distances were restrained to be similar to each other (SHELX SADI). Occupancies refined to: Br1S/C1S-C6S = 0.187(2) and Br2S/C7S-C12S = 0.071(2), generating a C_6H_5Br composition per cycle of 0.516(6). All non-hydrogen atoms were refined with anisotropic displacement parameters. All carbon atoms of the bromobenzene C_6 rings were assigned a common isotropic displacement parameter. Hydrogen atoms bonded to carbon were placed in geometrically idealized positions and included as riding atoms with *d*(C-H) = 0.95 Å and *U*iso(H) = 1.2*U*eq(C) for aromatic hydrogen atoms and *d*(C-H) = 0.99 Å and *U*iso(H) = 1.2*U*eq(C) for methylene hydrogen atoms. The two urea hydrogen atoms were refined

isotropically with *d*(N-H) = 0.84(2) Å distance restraints. The largest residual electron density peak in the final difference map is 0.66 $e^-/Å^3$, located 0.52 Å from H4S.

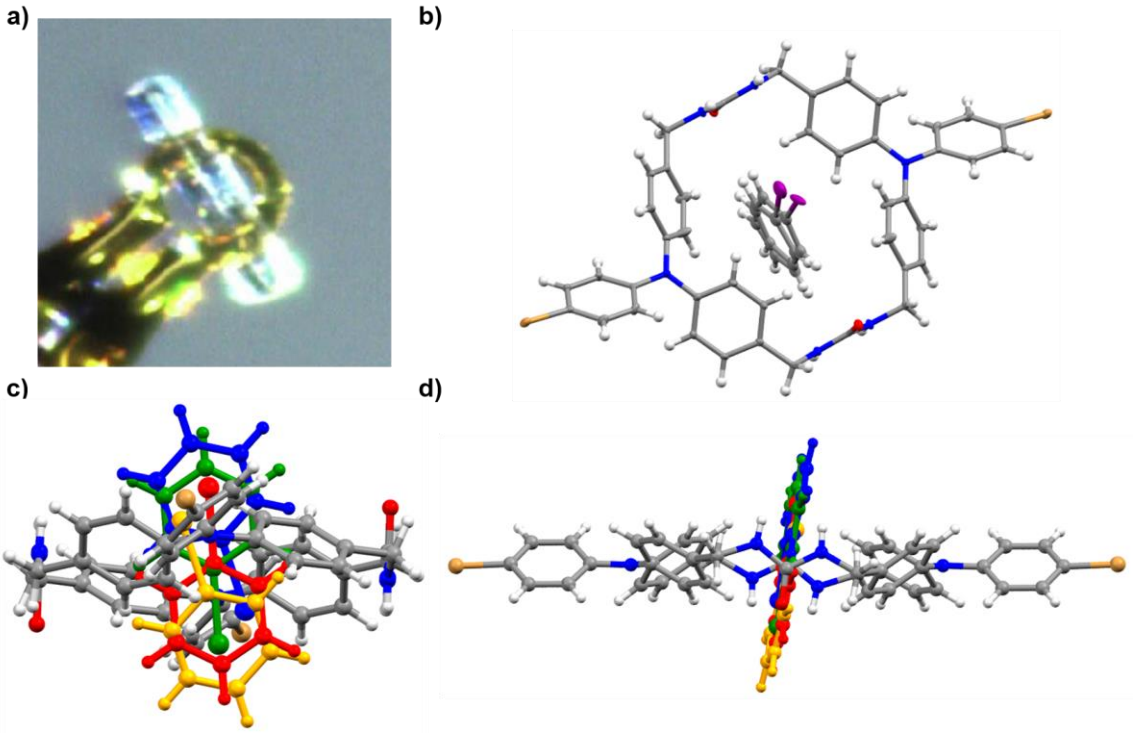

Figure 4.21. Crystal views of **1**·$(C_6H_5I)_{0.49}$. (a) Data crystal. (b) Components of structure. Thermal ellipsoids were drawn at the 30% probability level. (c) View of C_6H_5I disorder inside the host **1**. (d) Another view of the disorder.

X-ray intensity data from a colorless needle were collected at 100(2) K using a Bruker D8 QUEST diffractometer equipped with a PHOTON-100 CMOS area detector and an Incoatec microfocus source (Mo Kα radiation, λ = 0.71073 Å). The raw area detector data frames were reduced and corrected for absorption effects using the Bruker APEX3, SAINT+ and SADABS programs.[48,49] The structure was solved with SHELXT.[50,51] Subsequent difference Fourier calculations and full-matrix least-squares refinement against F^2 were performed with SHELXL-2018[50,51] using OLEX2.[52]

The compound crystallizes in the space group $P2_1/c$ of the monoclinic system. The asymmetric unit consists of half of one $C_{42}H_{36}Br_2N_6O_2$ cycle located on a crystallographic inversion center and several electron density peaks inside the tubular channels created by the cycle columns. The residual difference electron density in the channel region is highly disordered, but arranged in a tapelike planar fashion along the crystallographic *b* axis direction. If assigned as carbon atoms, most peaks refined to less than full occupancy. Two peaks refined to significantly greater than or near 100% carbon occupancy. These were assumed to be iodine atoms from the crystal soaking agent iodobenzene. Two independent, partially occupied C_6H_5I molecules were modeled. Both are further disordered about a crystallographic inversion center. The phenyl rings of each were fitted to rigid hexagons, and both bonded C-I distances were restrained to 2.10(1) Å. 1,3-C-I distances were restrained to be similar to each other (SHELX SADI). Occupancies refined to: I1S/C1S-C6S = 0.156(2) and I2S/C7S-C12S = 0.091(2), generating a C_6H_5I composition per cycle of 0.494(6). All non-hydrogen atoms were refined with anisotropic displacement parameters. All carbon atoms of the iodobenzene C_6 rings were assigned a common anisotropic displacement parameter. They were further restrained to approximate an isotropic shape (SHELX ISOR). Hydrogen atoms bonded to carbon were placed in geometrically idealized positions and included as riding atoms with *d*(C-H) = 0.95 Å and *U*iso(H) = 1.2*U*eq(C) for aromatic hydrogen atoms and *d*(C-H) = 0.99 Å and *U*iso(H) = 1.2*U*eq(C) for methylene hydrogen atoms. The two urea hydrogen atoms were refined isotropically with *d*(N-H) = 0.84(2) Å distance restraints. The largest residual electron density peak in the final difference map is 0.61 $e^-/Å^3$, located 0.71 Å from C1S.

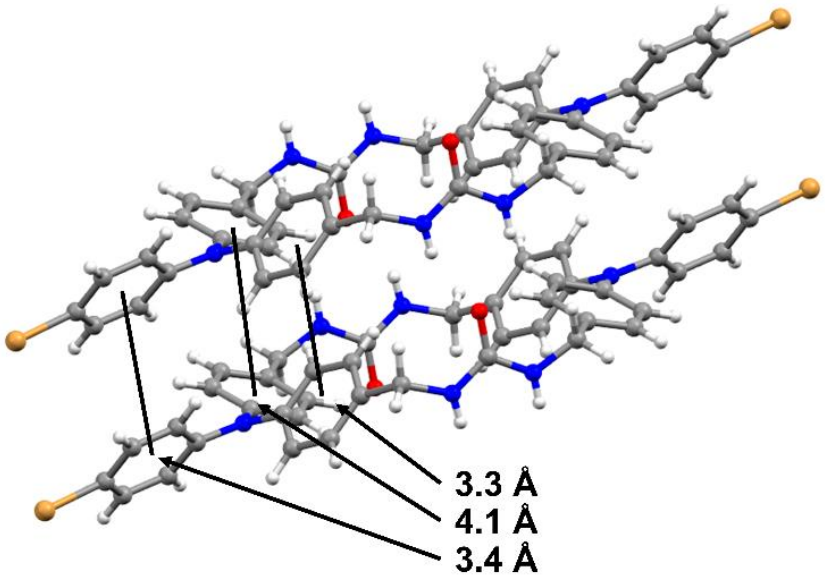

Figure 4.22. Crystal view of **1**·(DME)$_{0.5}$ showing the π-stacking in-between macrocycles. The three phenyl rings of the TPA unit align in an offset π-stacking arrangement with perpendicular distances of 3.2536(14), 3.4086(14), and 4.1013(15) Å.

Table 4.4. Comparison of between different *bis*-urea macrocycles**.**

Macrocycle Spacer	Approximate Pore Size (Å)[a]	Void Space (% per unit cell)[b]	Urea Repeat Distance (Å)	Inter-columnar π-stacking
Benzene[53]	1.0 × 1.4	0	4.62	Offset π-stacking
Phenyl Ether[38]	4.5 × 6.7	14.5	4.65	Edge-to-face
Benzophenone[39]	5.0 × 7.1	14.9	4.72	Edge-to-face
4-Bromotriphenylamine	4.3 × 6.5	10.1	4.62	Offset π-stacking
m-di(phenylethynyl)benzene[54]	8.4 × 13.0	22.2	4.69	Alkyne phenyl stacking

[a]Calculated by measuring distance between diagonal hydrogens and opposing carbonyls and subtracting the *vdw* radii (See Figure 4.3A). [b]Calculated by removing initial guest in channels and performing a contact surface void space calculation in Mercury (probe radius 1.2 Å, grid spacing 0.1 Å).[55]

4.4.4 Thermal Gravimetric Analysis (TGA)

TGA was carried out using TA instruments SDT-Q600 simultaneous DTA/TGA at a rate of 3˚/min from 25-90˚C with a 5-minute isotherm before temperature increase and 150 minute isotherm after.

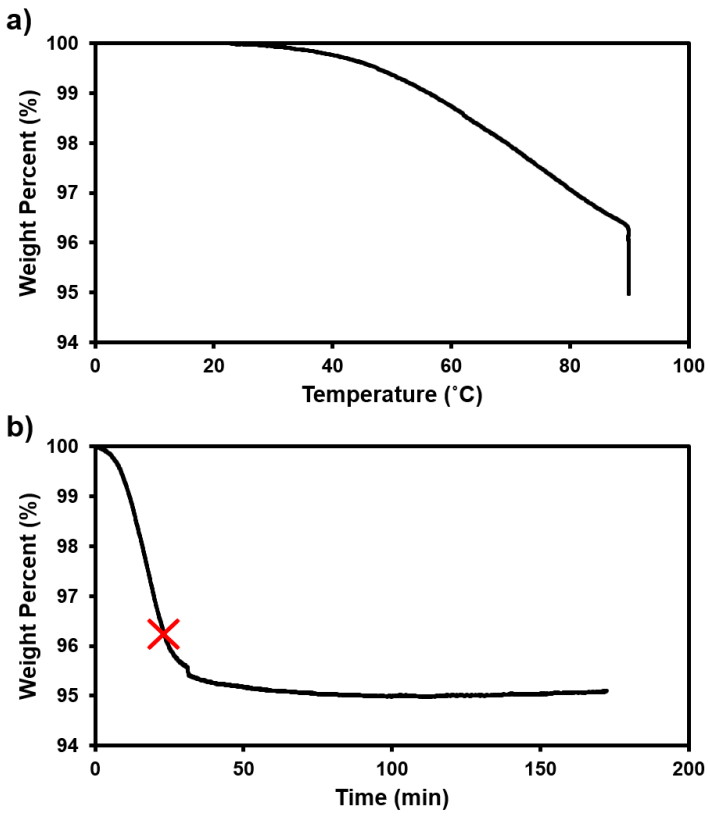

Figure 4.23. TGA graphs showing a one-step desorption of DME from **1**·(DME)$_{0.5}$. (a) Shows X-axis temperature and (b) shows x-axis as time (better indicator to ensure complete guest removal). Red X indicates where 150-minute isotherm at 90˚C began. Host: guest ratio calculated to be 1:0.5. An average of 1:0.55 was found from an average of three trials.

4.4.5 Hirshfeld Calculations

The molecular Hirshfeld surface for **1** was constructed using Crystal Explorer 17.5.[34-37,56] The crystallographic information file (.cif) of **1**·(DME)$_{0.5}$ was imported into Crystal Explorer, and the guest (DME) was removed. Then a high resolution Hirshfeld surface was mapped with the d_{norm} function. A two-dimensional fingerprint map was obtained by calculating the distances from the Hirshfeld surface to the nearest interior nucleus (d_i) to the outside surface (d_e) to measure interactions to neighboring molecules. The Hirshfeld surface was generated over a d_{norm} range of -0.5 to 1.5.

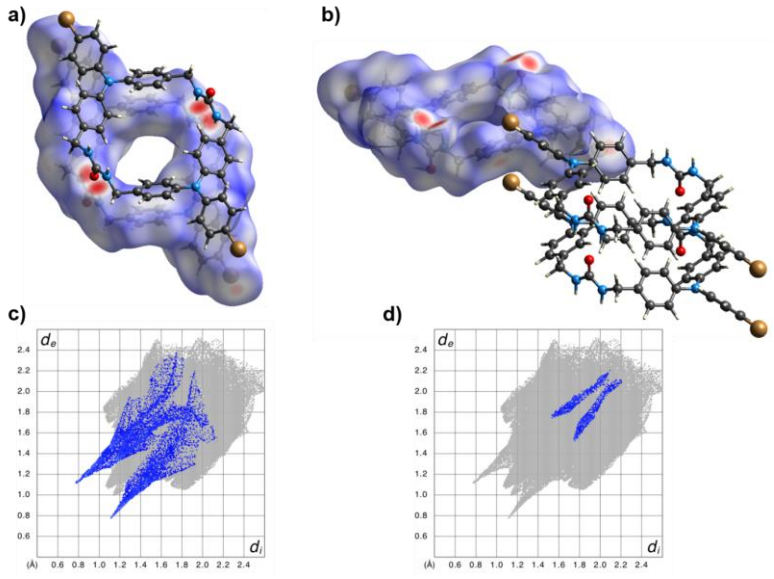

Figure 4.24. Hirshfeld surface analysis of macrocycle **1**. (a) Bifurcated hydrogen bonding between macrocycles. Red areas represent distances shorter than sum of the *vdw* radii while blue regions are longer. (b) Br···C_{aryl} interactions between neighboring macrocycles. (c) Fingerprint plot resolved for O···H/H···O contacts. (d) Fingerprint plot resolved for Br···C/C···Br contacts.

4.4.6 Sample preparation for ^{129}Xe NMR measurements

A medium wall 5 mm NMR tube (Wilmad-Labglass) was loaded with around 100 mg of Br-TPA macrocycle and attached to a custom-built vacuum system. The sample was made sorbate free by exposing it to a high vacuum (< 10^{-4} bar) at 298 K for at least 10 hours. A desired quantity of ^{129}Xe gas (99% enrichment, Sigma-Aldrich) was cryogenically loaded into the tube using liquid nitrogen to achieve a loading pressure of 9.5 bar at 298 K. After loading, the tube was flame sealed and left to equilibrate at 298 K for at least 12 hours before NMR measurements.

4.4.7 ^{129}Xe PFG NMR and relaxation measurements

^{129}Xe pulsed field gradient (PFG) NMR and ^{129}Xe NMR relaxation measurements were performed at 298 K using a wide-bore Avance III HD 17.6 T spectrometer (Bruker

Biospin) operating at 208.6 MHz. The magnetic field gradients were generated using Diff50 diffusion probe and GREAT 60 gradient amplifier (Bruker Biospin). A standard stimulated echo PFG NMR sequence with the sine-shaped gradient pulses was used. The duration between the first and second radiofrequency pulses was 0.68 ms, and the diffusion time was varied between 5 and 100 ms. The gradient duration and maximum amplitude were equal to around 0.20 ms and 3 T/m, respectively. Using larger durations and amplitudes of the gradient pulses was not possible due to a relatively short transverse (T_2) NMR relaxation time of the strongest line of the adsorbed ^{129}Xe (around 0.4 ms). This short T_2 time also prevented an application of PFG NMR sequences with bipolar gradients, such as a 13-interval PFG NMR sequence.[57] The T_2 time was estimated using the stimulated echo sequence by changing the time intervals during which the T_2 NMR relaxation takes place. Longitudinal (T_1) NMR relaxation measurements of the adsorbed Xe were performed using a standard inversion recovery sequence. The T_1 time of the strongest line of the adsorbed ^{129}Xe was found to be around 7 s.

In the case of normal self-diffusion with a single diffusion coefficient (D), PFG NMR attenuation curves measured by the stimulated echo PFG NMR sequence can be presented as follows.[58]

$$\Psi = \frac{S(g)}{S(g{\sim}0)} = e^{-Dq^2t}$$

Equation 4.1. Equation for PFG NMR signal attenuation.

Here, Ψ is the PFG NMR signal attenuation, S is the PFG NMR signal intensity, t is the time of observation of diffusion process (i.e., diffusion time) and $q = \gamma g \delta$, where γ is the gyromagnetic ratio and δ is the effective gradient pulse length. This equation is

expected to hold for the diffusion of Xe in the voids between porous particles as well as for long-range diffusion, i.e. diffusion under the conditions of fast exchange of Xe atoms between porous particles and the surrounding gas phase. In the complete analogy with gas diffusion in zeolite beds, the long-range diffusivity (D_{lr}) in the studied sample can be presented as follows.[58]

$$D_{Ir} = p_{int} D_{int}$$

Equation 4.2. Equation for long-range diffusivity.

Here, p_{int} is a fraction of Xe atoms, which at any particular time are located in the voids between the porous particles, calculated with respect to all Xe atoms in a particle bed, and D_{int} is the diffusivity of Xe in the voids between porous particles. This equation is expected to provide a good approximation for the studied sample because the diffusion process in microporous particles is many orders of magnitude slower than that in the gas phase between the particles. The value of p_{int} was estimated to be ≥ 0.37 from the area under the ^{129}Xe NMR lines corresponding to the adsorbed and gas-phase Xe. Hence, $D_{lr} \geq 0.37\ D_{int}$. Using the measured value of D_{int} for Xe in the studied sample (6.7×10^{-7} m^2/s at 298 K) we estimate that the attenuation (Eq. 1) of the ^{129}Xe PFG NMR signal for the case of the long-range diffusion at the largest gradient used in this work should be ≤ 0.09. It is important to note that this is only an estimate. A complete analysis of the diffusion attenuation in the case of chemical exchange is provided, for example, in ref.[59] We observe that $\Psi = 1.0$ with the uncertainty of 20% in all cases for the line at 206 ppm, which is attributed to Xe adsorbed in the channels. This observation rules out fast exchange of Xe atoms between the channels and the surrounding gas phase on the time scale used in the measurements (5-100 ms).

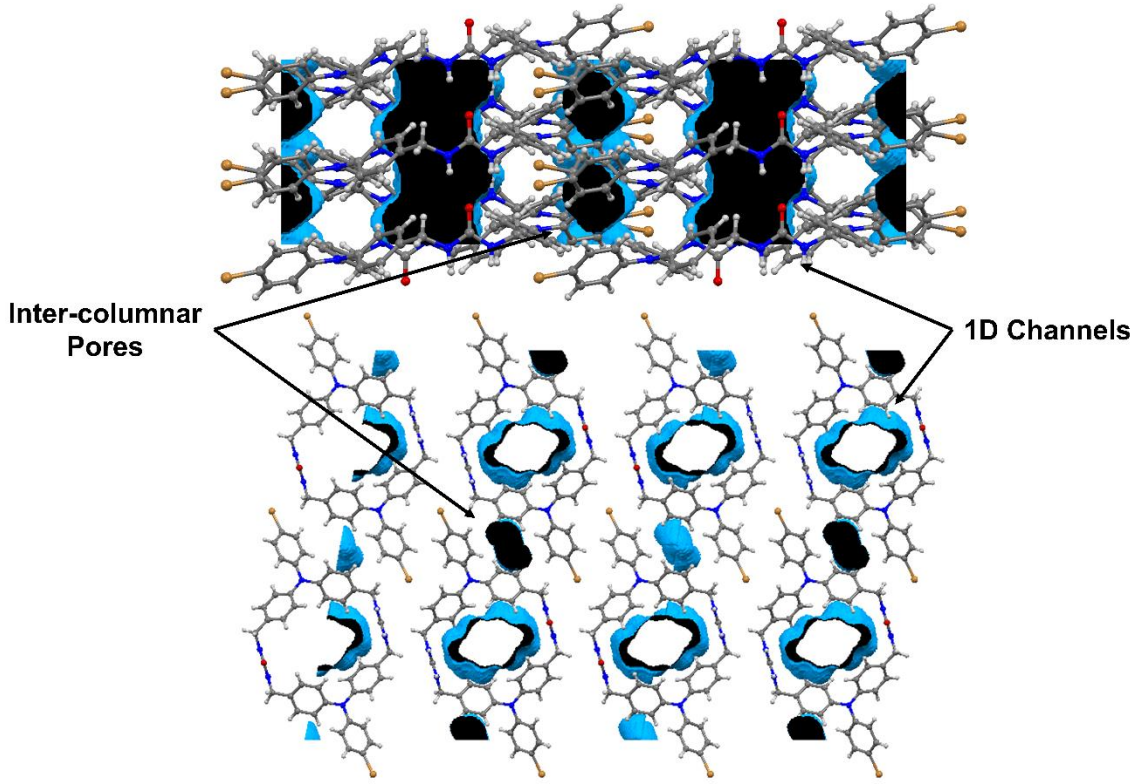

Figure 4.25. Views of **1** showing void space within columns. Top view is looking down *c* axis and bottom view is looking down *b* axis. Calculated by performing a contact surface void space calculation in Mercury (probe radius 0.9 Å, grid spacing 0.1 Å).[55]

4.5 REFERENCES

1. Dhakhinamoorthy, A.; Alvaro, M.; Garcia, H. *Chem. Commun.* **2012**, *48*, 11275-11288.
2. Ding, S.-Y.; Gao, J.; Wang, Q.; Zhang, Y.; Song, W.-G.; Su, C.-Y.; Wang, W. *J. Am. Chem. Soc*. **2011**, *133*, 19816-19822.
3. Ramamurthy, V.; Sivaguru, J. *Chem. Rev*. **2016**, *116*, 9914-9993.
4. Tabacchi, G. *ChemPhysChem* **2018**, *19*, 1249-1297.
5. Kitagawa, S.; Kitaura, R.; Noro, S. *Angew. Chem., Int. Ed.* **2004**, *43*, 2334-2375.
6. Sozzani, P.; Bracco, S.; Comotti, A.; Ferretti, L.; Simonutti, R. *Angew. Chem., Int. Ed.* **2005**, *44*, 1816-1820.

7. Kane, C. M.; Banisafar, A.; Dougherty, T. P.; Barbour, L. J.; Holman, K. T. *J. Am. Chem. Soc.* **2016**, *138*, 4377-4392.
8. Kreno, L. E.; Leong, K.; Farha, O. K.; Allendorf, M.; Van Duyne, R. P.; Hupp, J. T. *Chem. Rev.* **2012**, *112*, 1105-1125.
9. Wales, D. J.; Grand, J.; Ting, V. P.; Burke, R. D.; Edler, K. J.; Bowen, C. R.; Mintova, S.; Burrows, A. D. *Chem. Soc. Rev.* **2015**, *44*, 4290-4321.
10. Mastalerz, M. *Acc. Chem. Res.* **2018**, *51*, 2411-2422.
11. Sumida, K.; Rogow, D. L.; Mason, J. A.; McDonald, T. M.; Bloch, E. D.; Herm, Z. R.; Bae, T.-H.; Long, J. R. *Chem. Rev.* **2012**, *112*, 724-781.
12. Li, J.-R.; Sculley, J.; Zhou, H.-C. *Chem. Rev.* **2012**, *112*, 869-932.
13. Lü, J.; Cao, R. *Angew. Chem., Int. Ed.* **2016**, *55*, 9474-9480.
14. Lee, S.; Hwang, S. Y.; Lee, H.; Jung, O.-S. *Cryst. Growth Des.* **2018**, *18*, 1278-1282.
15. Zhuang, C.-F.; Zhang, J.; Wang, Q.; Chu, Z.-H.; Fenske, D.; Su, C.-Y. *Chem.-Eur. J.* **2009**, *15*, 7578-7585.
16. Huang, S.-L.; Hor, T. S. A.; Jin, G.-X. *Coord. Chem. Rev.* **2017**, *346*, 112-122.
17. Seki, T.; Sakurada, K.; Muromoto, M.; Ito, H. *Chem. Sci.* **2015**, *6*, 1491-1497.
18. Nikolayenko, V. I.; Castell, D. C.; van Heerden, D. P.; Barbour, L. J. *Angew. Chem., Int. Ed.* **2018**, *57*, 12086-12091.
19. Nikolayenko, V. I.; van Wyk, L. M.; Munro, O. Q.; Barbour, L. J. *Chem. Commun.* **2018**, 54, 6975-6978.
20. O'Brien, E. S.; Trinh, M. T.; Kann, R. L.; Chen, J.; Elbaz, G. A.; Masurkar, A.; Atallah, T. L.; Paley, M. V.; Patel, N.; Paley, D. W.; Kymissis, I.; Crowther, A. C.; Millis, A. J.; Reichman, D. R.; Zhu, X.-Y.; Roy, X. *Nat. Chem.* **2017**, *9*, 1170-1174.

21. Zakharov, B. A.; Marchuk, A. S.; Boldyreva, E. V. *CrystEngComm* **2015**, *17*, 8812-8816.

22. Zakharov, B. A.; Boldyreva, E. V. *Acta Crystallogr. B* **2013**, *69*, 271-280.

23. Liu, G.; Liu, J.; Liu, Y.; Tao, X. *J. Am. Chem. Soc.* **2014**, *136*, 590-593.

24. Jin, M.; Sumitani, T.; Sato, H.; Seki, T.; Ito, H. *J. Am. Chem. Soc.* **2018**, *140*, 2875-2879.

25. Alhamami, M.; Doan, H.; Cheng, C.-H. *Materials* **2014**, *7*, 3198-3250.

26. Yan, K.; Dubey, R.; Arai, T.; Inokuma, Y.; Fujita, M. *J. Am. Chem. Soc.* **2017**, *139*, 11341-11344.

27. Wahl, H.; Haynes, D. A.; le Roex, T. *Cryst. Growth Des.* **2017**, *17*, 4377-4383.

28. Li, Y.; Handke, M.; Chen, Y.-S.; Shtukenberg, A. U.; Hu, C. T.; Ward, M. D. *J. Am. Chem. Soc.* **2018**, *140*, 12915-12921.

29. Jones, J. T. A.; Holden, D.; Mitra, T.; Hasell, T.; Adams, D. J.; Jelfs, K. E.; Trewin, A.; Willock, D. J.; Day, G. M.; Bacsa, J.; Steiner. A.; Cooper, A. I. *Angew. Chem., Int. Ed.* **2011**, *50*, 749-753.

30. Sanna, E.; Escudero-Adán, E. C.; Bauzá, A.; Ballester, P.; Frontera, A.; Rotger C.; Costa, A. *Chem. Sci.* **2015**, *6*, 5466-5472.

31. Natarajan, R.; Bridgland, L.; Sirikulkajorn, A.; Lee, J.-H.; Haddow, M. F.; Magro, G.; Ali, B.; Narayanan, S.; Strickland, P.; Charmant, J. P. H.; Orpen, A. G.; McKeown, N. B.; Bezzu, C. G.; Davis, A. P. *J. Am. Chem. Soc.* **2013**, *135*, 16912-16925.

32. Shimizu, L. S.; Salpage, S. R.; Korous, A. A. *Acc. Chem. Res.* **2014**, *47*, 2116-2127.

33. Sindt, A. J.; DeHaven, B. A.; McEachern, D. F.; Dissanayake, D. M. M. M.; Smith, M. D.; Vannucci, A. K.; Shimizu, L. S. *Chem. Sci.* **2019**, *10*, 2670-2677.

34. Hirshfeld, F. L. *Theor. Chim. Acta* **1977**, *44*, 129-138.

35. Spackman, M. A.; Jayatilaka, D. *CrystEngComm* **2009**, *11*, 19-32.

36. McKinnon, J. J.; Jayatilaka, D.; Spackman, M. A. *Chem. Commun.* **2007**, 3814-3816.

37. Wolff, S. K.; Grimwood, D. J.; McKinnon, J. J.; Turner, M. J.; Jayatilaka, D.; Spackman, M. A. CrystalExplorer Version 3.1, University of Western Australia, 2012.

38. Shimizu, L. S.; Hughes, A. D.; Smith, M. D.; Davis, M. J.; Zhang, B. P.; zur Loye, H.-C.; Shimizu, K. D. *J. Am. Chem. Soc.* **2003**, *125*, 14972-14973.

39. Dewal, M. B.; Xu, Y.; Yang, J.; Mohammed, F.; Smith, M. D.; Shimizu, L. S.; *Chem. Commun.* **2008**, 3909-3911.

40. Bowers, C. R.; Dvoyashkin, M.; Salpage, S. R.; Akel, C.; Bhase, H.; Geer, M. F.; Shimizu, L. S. *ACS Nano* **2015**, *9*, 6343-6353.

41. Sozzani, P.; Comotti, A.; Simonutti, R.; Meersmann, T.; Logan, J. W.; Pines, A. *Angew. Chem., Int. Ed.* **2000**, *39*, 2695-2699.

42. Soldatov, D. V.; Moudrakovski, I. L.; Grachev, E. V.; Ripmeester, J. A. *J. Am. Chem. Soc.* **2006**, *128*, 6737-6744.

43. Bonardet, J.-L.; Fraissard, J.; Gédéon, A.; Springuel-Huet, M.-A. *Catal. Rev. Sci. Eng.* **1999**, *41*, 115-225.

44. Cheng, C.-Y.; Bowers, C. R. *ChemPhysChem* **2007**, *8*, 2077-2081.

45. Weiland, E.; Springuel-Huet, M.-A.; Nossov, A.; Gédéon, A. *Microporous Mesoporous Mater.* **2016**, *225*, 41-65.

46. Massiot, D.; Fayon, F.; Capron, M.; King, I.; Le Calvé, S.; Alonso, B.; Durand, J.-O.; Bujoli, B.; Gan, Z.; Hoatson, G. *Magn. Reson. Chem.* **2002**, *40*, 70-76.

47. Paul, G. K.; Mwauru, J.; Argun, A. A.; Taranekar, P.; Reynolds, J. R. *Macromolecules* **2006**, *39*, 7789-7792.

48. APEX3 Version 2016.5−0, SAINT+ Version 8.37A; Bruker AXS, Inc.: Madison, WI, 2016.

49. Krause, L.; Herbst-Irmer, Sheldrick, G. M.; Stalke, D. *J. Appl. Cryst.* **2015**, *48*, 3-10.

50. Sheldrick, G. M. *Acta Crystallogr. A* **2015**, *71*, 3.8.

51. Sheldrick, G. M. *Acta Crystallogr. C* **2015**, *71*, 3-8.

52. Dolomanov, O. V.; Bourhis, L. J.; Gildea, R. J.; Howard, J. A. K.; Puschmann, H. *J. Appl. Cryst.* **2009**, *42*, 339-341.

53. Shimizu, L. S.; Smith, M. D.; Hughes, A. D.; Shimizu, K. D. *Chem. Commun.* **2001**, 1592-1593.

54. Dawn, S.; Dewal, M. B.; Sobransingh, D.; Paderes, M. C.; Wilbowo, A. C.; Smith, M. D.; Krause, J. A.; Pellechia, P. J.; Shimizu, L. S. *J. Am. Chem. Soc.* **2011**, *133*, 7025-7032.

55. Macrae, C. F.; Bruno, I. J.; Chisholm, J. A.; Edgington, P. R.; McCabe, P.; Pidcock, L.; Rodriguez-Monge, L.; Taylor, R.; van der Streek, J.; Wood, P. A. *J. Appl. Crystallogr.* **2008**, *41*, 466-470.

56. Spackman, M. A.; McKinnon, J. J. *CrystEngComm* **2002**, *4*, 378-392.

57. Cotts, R. M.; Hoch, M. J. R.; Sun, T.; Markert, J. T. *J. Magn. Reson.* **1989**, *83*, 252-266.

58. Kärger, J.; Ruthven, D. M.; Theodorou, D. N. *Diffusion in Nanoporous Materials*. Wiley-VCH: Weinheim, 2012.

59. Hazelbarker, E. D.; Budhathoki, S.; Wang, H.; Shah, J.; Maginn, E. J.; Vasenkov, S. *J. Phys. Chem. Lett.* **2014**, *5*, 1766-1770.

CHAPTER 5

GUEST INCLUSION MODULATES CONCENTRATION AND PERSISTENCE OF PHOTOGENERATED RADICALS IN ASSEMBLED TRIPHENYLAMINE MACROCYCLES*

* **Sindt, A. J.**; DeHaven, B. A.; Goodlett, D. W.; Hartel, J. O.; Ayare, P. J.; Du, Y.; Smith, M. D.; Mehta, A. K.; Brugh, A. M.; Forbes, M. D. E.; Bowers, C. R.; Vannucci, A. K.; Shimizu, L. S. *Submitted to J. Am. Chem. Soc.* October 25, 2019. ja-2019-115189.

5.0 ABSTRACT

Substituted triphenylamine (TPA) radical cations show great potential as oxidants and as spin containing units in polymer magnets. Their properties can be further tuned by supramolecular assembly. Here, we examine how the properties of photo-generated radical cations, intrinsic to TPA macrocycles, are altered upon their self-assembly into 1D columns. These macrocycles consist of two TPAs and two methylene ureas which drive the assembly into porous organic materials. Advantageously, upon activation the crystals can undergo guest exchange in a single-crystal-to-single-crystal transformation generating a series of isoskeletal host-guest complexes whose properties can be directly compared. Photoinduced electron transfer, initiated using 365 nm LED's, affords radicals at room temperature as observed by EPR spectroscopy. The line shape of the EPR spectra and the quantity of radicals can be modulated by both polarity and heavy atom inclusion of the encapsulated guest. These photo-generated radicals are persistent, with half-lives between 1-7 days and display no degradation upon radical decay. Re-irradiation of the samples can restore the radical concentration back to a similar maximum concentration, a feature that is re-producible over several cycles. EPR simulations of a representative spectrum indicate two species, one containing two N hyper-fine interactions and an additional broad signal with no resolvable hyperfine interaction. Intriguingly, TPA analogs without bromine substitution also exhibit similar quantities of photogenerated radicals, suggesting that supramolecular strategies can enable more flexibility in stable TPA radical structures. These studies will help guide the development of new photoactive materials.

5.1 INTRODUCTION

Construction of hierarchical materials through supramolecular assembly of small molecules is an expedient method for crafting materials with useful properties.[1-4] These properties range from conductivity,[5] magnetism,[6] to dichromism.[7] In addition, supramolecular assembly can also be used to make porous materials that encapsulate small guests.[8,9] This leads to materials of use in catalysis,[10,11] storage,[12,13] confinement,[14] separation,[15,16] and sensing.[17,18] Furthermore, bound guests may alter the chemical and physical properties of the host itself, for example, modulating the rotational speed of host-bound molecular rotors[19] or expanding/contracting the host framework.[20,21] Here, we investigate how different guests encapsulated within a triphenylamine (TPA) host affect its ability to form radicals in the solid-state upon UV irradiation (Figure 5.1). The host is robust and exchanges guests via single-crystal-to-single-crystal (SC-SC) transformations while retaining its original framework. This affords a series of isoskeletal host-guest structures whose properties can be directly compared. Upon UV irradiation of the host, long-lived radicals are generated. Encapsulated guests within the host modulate the line shape of their EPR spectra and the concentration of radicals observed during irradiation. Additionally, after decay of the photogenerated radicals, samples can be re-irradiated to regenerate the observed radicals without harming or degrading the TPA host. Understanding how guest inclusion affects these radical properties will be useful for designing the next generation of conductive and magnetic materials.

Organic radicals have many uses, ranging from MRI contrasting agents[22] to multifunctional magnetic materials.[23] One class of these radicals are TPA radical cations, which have undergone a single electron oxidation from their neutral state.[24] Key to their

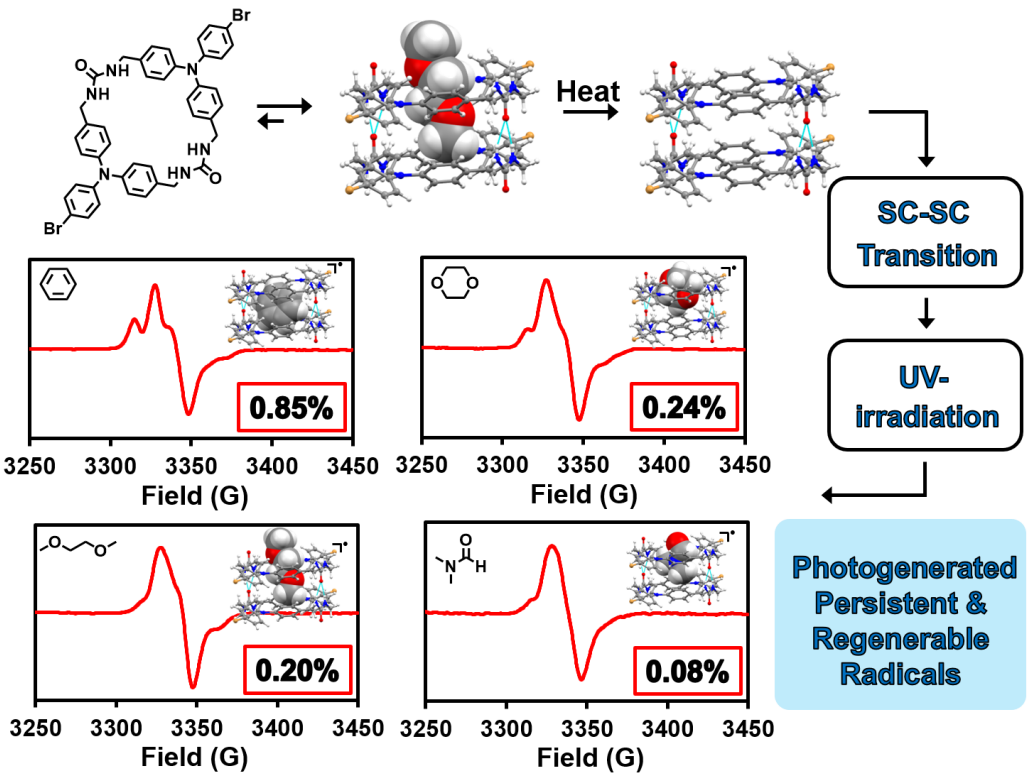

Figure 5.1. Self-assembly of TPA macrocycles results in the formation of a columnar assembled host. Activation of this host by heating allows for the introduction of new guests via SC-SC transformations. Each complex generates radicals upon irradiation with 365 nm LEDs, affording EPR spectra with different line shapes and intensities. A comparison of four of these EPR is shown above (benzene, 1,4-dioxanes, DME, and DMF). The insets for each graph show structure of the guest, SC-XRD of the host-guest complex, and the percentage of radicals formed upon UV-irradiation.

stability is the presence of *para* substitution on all three phenyl rings of the TPA system, which slows degradation reactions such as benzidine formation.[25,26] This is seen for Magic Blue, a commercial one-electron oxidant,[27,28] as it has bromine substitution on all three *para* sites of the TPA. When stabilized, TPAs find use as high-spin polymers,[29,30] cathodes in batteries,[31,32] and as hole-transport layers in solar cells.[33] Typically, these radicals are formed through chemical or electrochemical oxidation pathways,[34] but they may also be generated by UV-irradiation when an electron acceptor is present.[35,36]

Our group employs the three-centered urea hydrogen bonding interaction to organize linear and macrocyclic compounds in high fidelity. This affords nanoporous materials that are typically used as nanoreactors for photochemical reactions.[37] In addition to forming nanochambers, these structures also exhibit markedly different photophysical properties when compared to their unassembled monomers in solution. For example, assembly of benzophenone containing urea macrocycles and linear analogs display surprisingly stable radical formation upon UV-irradiation; this behavior is not observed in solution.[38] Similarly, brominated TPA **2a** (Figure 5.2) also shows enhanced stability of photogenerated radicals within its assembled structure, while radical formation in solution results in complete degradation of the TPAs.[39] Thus, demonstrating the importance of supramolecular assembly on the overall stability of the photogenerated radicals. Here, we investigate if TPA containing macrocycle system, **1a**, also exhibits enhanced photogenerated radical stability upon self-assembly.

TPA **1a** self-assembles to form a porous host that can facilitate guest inclusion and removal via SC-SC crystal transformations.[40] By irradiating this host we can probe if macrocycle **1a** exhibits similar radical formation as its linear analog counterpart **2a** and if

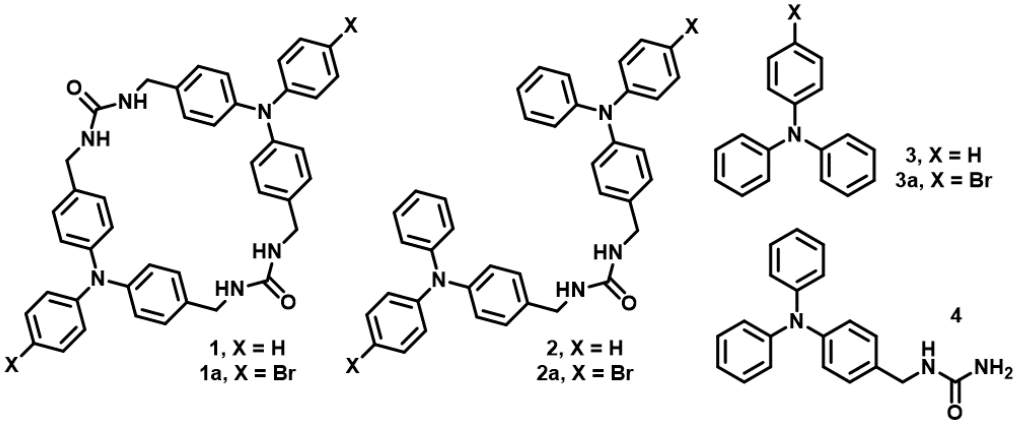

Figure 5.2. Comparison of TPA structures investigated. Macrocycles **1** and **1a**, linear analogs **2** and **2a**, and control compounds **3**, **3a,** and **4** are shown.

guest inclusion alters the process of radical generation within the host. Thus, the photophysical properties and photogenerated radical formation of this host were investigated. The guests in these studies were selected to cover a range of polarities as well as heavy atom inclusion. Control compounds **1**, **2**, and **3-4** were prepared to elucidate the structure of the photogenerated radicals and to identify the features of these assembled TPA systems that allow for stable radical formation. Our goal is to understand the effects different guests have on radical formation and to determine what characteristics are necessary for TPA-containing compounds to exhibit these properties.

5.2 RESULTS AND DISCUSSION

Macrocycles (**1** and **1a**) and linear analogs (**2** and **2a**) were synthesized in five steps following established methods (Scheme 5.1).[39,40] For macrocycle **1**, its dibromide and protected macrocycle precursor were structurally characterized. Control compounds **3** and **3a** were purchased from commercial suppliers, while control **4** was synthesized in two steps using a Vilsmeier–Haack reaction to yield the aldehyde,[41] followed by a reductive alkylation of urea to give the desired product.[42] Host-guest crystals of **1** and **1a** were obtained from vapor diffusion of either water or 1,2-dimethoxyethane (DME), respectively, into DMSO solutions. Solvent free crystals for **2-4** were grown via slow evaporation of acetonitrile (**2** and **3a**), ethyl acetate (**2a**), or ethanol (**3**); or by vapor diffusion of water into a DMF solution (**4**).

For TPA **1**, the X-ray structure revealed the desired macrocycle in the space group $P2_1/n$ of the monoclinic system. The macrocycles were found in the *syn* conformation organized into tubular columns encapsulating disordered DMSO in a 1:1 host-guest ratio. The *syn* conformation was surprising as previous *bis*-urea macrocycles crystallize in the

anti-conformation, where the urea groups in a single macrocycle are oppositely aligned to minimize dipole interactions.[37] Despite this, the macrocycles still organize into columns through the characteristic three-centered urea hydrogen bond (d(N···O) = 3.090(5), 3.078(5), 3.147(5), and 3.063(5) Å). Additional stabilization occurs through intracolumnar edge-to-face π-stacking of the TPA groups (Figure 5.32). This stacking affords individual nanotubes with a pore aperture of 6.4 × 4.3 Å after accounting for the van der Waals (vdW) radii of the participating atoms (Figure 5.3a, top). The resulting nanotubes pack together to form robust hexagonal arrays as seen in Figure 5.26.

For comparison, the brominated macrocycle, **1a**, crystallizes as colorless needles in the space group $P2_1/c$ of the monoclinic system.[40] This macrocycle adopts the typical *anti* conformation and organizes into columnar tubes. The channels display an interior cross-section diameter of 6.5 × 4.3 Å and contain encapsulated, disordered DME (Figure 5.3b,

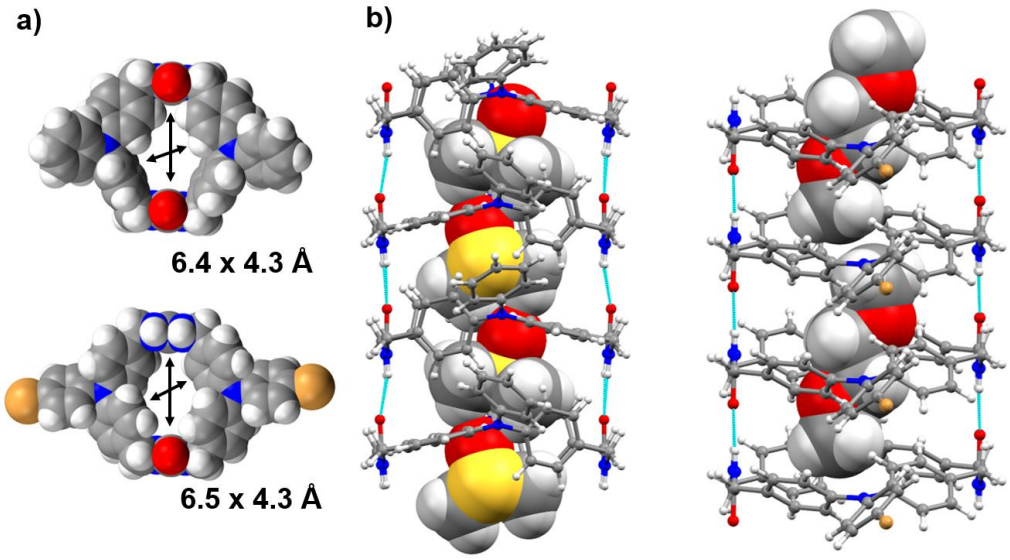

Figure 5.3. Comparison of TPA hosts **1**·DMSO and **1a**·DME. (a) Comparison of cross-sectional areas with **1** on top and **1a** on bottom (subtracting vdW radii). (b) Comparison of columnar structures with guests included with **1**·DMSO on the left and **1a**·DME. Disorder in the guests has been omitted for clarity.

right) in a host-guest ratio of 2:1. The tubes form along the crystallographic *b* axis and are held together via hydrogen bonds between the ureas (d(N···O) = 2.848(4) and 2.929(4) Å) and π-stacking between neighboring TPAs. Individual columns are held together with π-π and halogen-π stacking interactions forming a hexagonal array similar to **1**·DMSO.

To generate different host-guest complexes of host **1a**, crystals of **1a**·DME were activated and loaded with new guests via SC-SC transformations.[40] Crystals of **1a**·DME were activated by heating under vacuum at 90 °C for 2.5 h to remove the DME. Next, a series of host-guest complexes (Figure 5.4) were prepared by immersing the activated crystals in a guest solution for 24 h. Afterwards, the crystals were filtered and air dried affording the new host-guest complex. The activated host and benzene derivative loaded hosts of **1a** have been previously characterized via SC-XRD and are all isoskeletal in regard to the macrocycle framework of **1**·DME. New to this work, DMF and 1,4-dioxanes were also loaded into the nanotubes. Again, the host framework remained isoskeletal.

In the benzene derivative loaded hosts of **1a**, (Figure 5.4), the guests were arranged in a planar tape-like manner inside the channels and were modeled on two crystallographic independent sites.[40] These sites were located near inversion centers giving four possible sites for guest location. Each of these sites had similar occupancy giving an approximate host-guest ratio of 1:0.5. The 1,4-dioxane and DMF-loaded **1a** complexes exhibited a very similar guest disorder, although 1,4-dioxane was modeled on three independent crystallographic sites instead of two. Overall, the 1,4-dioxanes and DMF guests exhibited host-guest ratios of 1:0.58(2) and 1:0.65(1), respectively. These loading ratios were higher compared to all the other modeled complexes, likely a result of the smaller size of these guests.

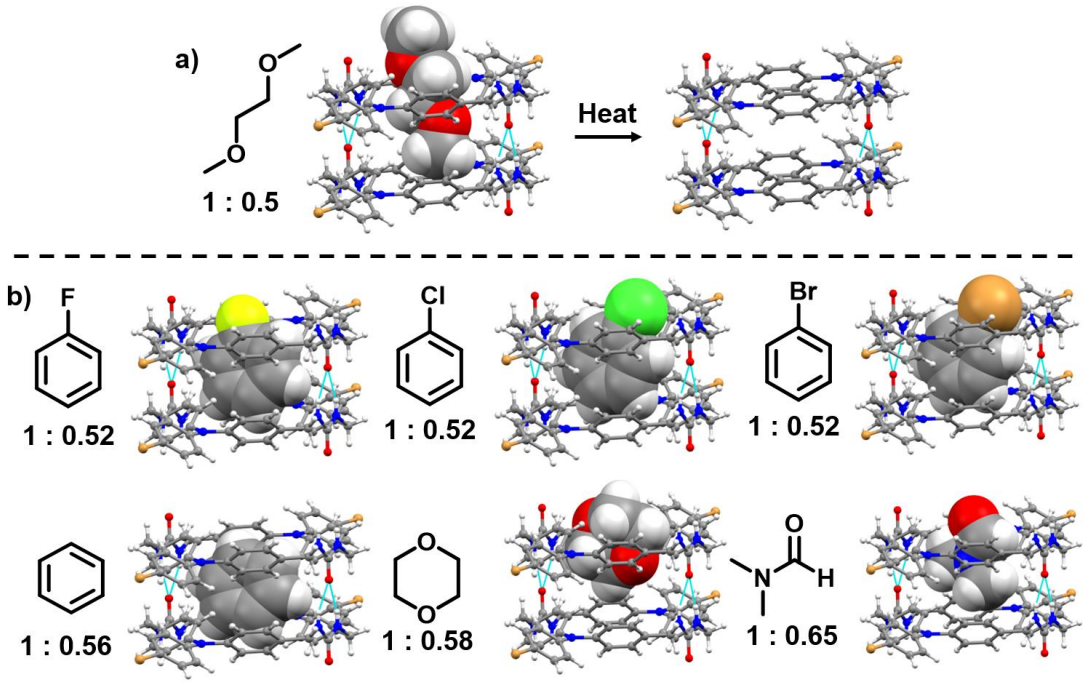

Figure 5.4. Guest inclusion complexes of **1a** with their host-guest ratios. (A) Heating of **1a**·DME results in an activated host. (B) Guests can then be added upon submersion of the activated crystals into a liquid of the new desired guest, resulting in SC-SC transformation to afford a new host-guest complex. The DME complex, activated host, and four benzene derivative guest complexes have been previously reported,[40] while the DMF and 1,4-dioxane structures are new to these studies.

For comparison to the macrocycles, linear analog **2** crystallized in the orthorhombic system in the centrosymmetric space group *Pbcn*. In this structure, both TPA groups extend to either side of a disordered methylene urea tether in a linear *trans-trans* arrangement (Figure 5.5). The disorder in the urea tether is oriented either up (50%) or down (50%) relative to the *c* axis, forming three-centered urea hydrogen bonded chains (d(N···O) = 2.749(8) and 2.716(8) Å). The TPA groups, which are not disordered, organize in a cruciform pattern in relation to the urea chain with edge-to-face π-stacking from the TPAs holding alternating chains together (Figure 5.33).

The brominated derivative **2a** was similarly organized in the orthorhombic system in the *Pccn* space group.[39] TPA **2a** was also found in a linear *trans-trans* arrangement with

both TPA groups extended out on either side of the methylene urea tether (Figure 5.5). The TPA units show minor disorder in this structure (5% to 9% depending on the chosen crystal) resulting from an opposite TPA rotation relative to the urea group. Overall, the urea groups still organize **2a** into chains along the crystallo-graphic *c* axis (*d*(N···O) = 2.823(3) and 2.70(2) Å), resulting in an X-shape pattern in projection along the chain direction instead of the cruciform pattern observed for TPA **2**.

Triphenylamines (**3** and **3a**) and urea derivative **4** were also crystallized. Together with the linear analogs and macrocycle **1**, this provides a series of control compounds for photophysical studies of macrocycle **1a**. The structure of TPA **3** has been previously

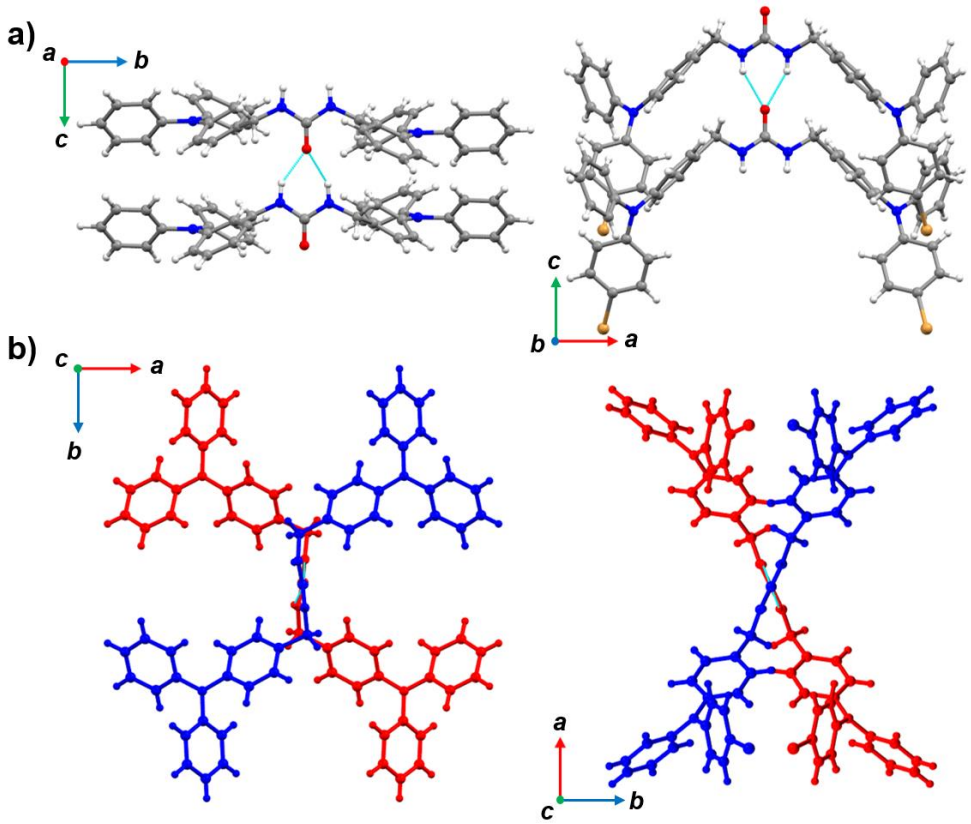

Figure 5.5. Comparison of triphenylamine linear analogs **2** (left) and **2a** (right). (A) Three-center urea hydrogen bonding interactions stack the triphenyl amine groups on top of one another forming urea tape motifs. (B) Top-down view of the urea tapes showing either a cruciform pattern (left) or X-shaped pattern (right).

reported (CCDC# 1319035), and it crystallized in the monoclinic system in the *Bb* space group with multiple edge-to-face π-stacking interactions driving the assembly.[43] For TPA **3a**, two different polymorphs were found, crystallizing either as colorless needles (triclinic system, *P*-1 (No.2) space group) or as colorless blocks (monoclinic system, $P2_1/c$ space group). The packing in both polymorphs was primarily driven through edge-to-face π stacking interactions (Figures 5.34 and 5.35); however, the bromines stacked much closer to each other in the monoclinic polymorph (4.473 Å vs 6.230 Å). According to powder X-ray diffraction results, the bulk sample most similarly matched the monoclinic polymorph (Figure 5.40). Lastly, TPA **4** crystallized in the monoclinic space group $P2_1/c$ as colorless flakes. Assembly was organized through the three-centered urea hydrogen bond forming twisted chains along the crystallographic *c* axis similar to **2a** (d(N···O) = 3.069(3) and 3.028(2) Å) with additional stabilization coming via edge-to-face π stacking interactions (Figure 5.36).

To probe how structure, self-assembly, and guest encapsulation effects the photophysics of macrocycle **1a**, the absorption, emission, and lifetimes for solution and solid-state samples were measured. Table 5.1 compares the photophysics of macrocycle **1a** and linear analog **2a** as 10 μM solutions in nitrogen purged DMSO to the assembled crystals of **1**-**2a** and some guest inclusion complexes of host **1a**. In solution, macrocycle **1a** exhibits only one band in its absorption spectra with a λ_{max} at 303 nm and molar absorptivity of $\sim 5 \times 10^4$ M^{-1} cm^{-1} which is similar to its linear analog counterpart **2a** under comparable conditions.[39] In the emission spectra, macrocycle **1a** shows two bands, with a smaller one at 378 nm and the larger at 450 nm, also quite similar to linear analog **2a**. Prior work suggests that for linear analog **2a** these bands arise from fluorescence and

phosphorescence with the band intensities being modulated by the polarity or hydrogen bonding capability of the solvent. However, the low solubility of macrocycle **1a** precluded similar solvent effect studies. The phosphorescent lifetime of macrocycle **1a** was quite short and approximately half of what was observed for linear analog **2a** (2.3 ns versus 4.1 ns). Both lifetimes are short for phosphorescence and are likely due to the Br substituents. The heavy atom effect is known to increase phosphorescent intensity through spin-orbit coupling,[44] but it can result in a shortened lifetime.[45]

Table 5.1. Measured photophysical properties for compounds **1**, **1a**, **2**, and **2a** with different conditions.

Compound	λ_{abs} (nm)[a]	ε ($\times 10^4$ M^{-1} $\times$ cm^{-1})	λ_{ems} (nm)[b]	$\tau_{<avg>}$ (ns)[c]
1	369, 414	--	478	1.6
10 **1a** μM in DMSO	303	4.65	378, 450*	2.3
1a	366	--	465	1.1
1a·DME	377	--	456	1.4
1a·C_6H_6	370	--	455	1.2
1a·DMF	372	--	456	1.3
2	366	--	487	1.5
10 **2a** μM in DMSO	302[d]	5.41[d]	369, 452*[d]	4.1[d]
2a	358[d]	--	447[d]	1.0[d]

[a] Peak position at largest absorption band. [b] Peak positions at largest emission bands in nm (largest denoted with * if applicable, excited at λ_{abs}.). [c] Average lifetime of the most intense emission peak. [d] Values taken from reference.[39]

In the solid-state, activated host **1a** showed a 60 nm red-shift of the absorption maxima versus dissolution in DMSO going from 303 to 366 nm (Figure 5.48). The formation of an additional broad absorption band at ~400 nm was also observed. The shift in absorption is more typical for J-aggregation in planar dyes.[46] However, Yang et al. observed such shifts in a crystalline styrene derivatized TPAs[47] and we also observed a similar shift for the related linear analog **2a**.[39] Similar absorption spectra were also

observed for **1a**·DME, **1a**·C_6H_6, and **1a**·DMF. These host-guest complexes were chosen because of their polarity differences since polarity played a large role in determining the photophysical properties of linear analog **2a** in solution. Interestingly, the non-brominated TPAs of macrocycle **1** and linear analog **2** also exhibited a red-shift in absorption, although their broad band at ~400 nm is comparatively more intense.

Assembly had less influence on the emission spectra and photoluminescent lifetimes for macrocycle **1a**. Indeed, activated host **1a** and its complexes (**1a**·DME, **1a**·C_6H_6, and **1a**·DMF) exhibited similar λ_{max} of emissions at ~460 nm upon excitation at the λ_{max} of absorption with similar lifetimes of ~1.2 ns. For comparison, activated **1**, **2**, and **2a**[39] show similar behavior with the non-halogen containing compounds exhibiting marginally longer lifetimes (1.5 ns) likely due to the lack of a heavy atom. Our hypothesis is that these shortened lifetimes are a result of non-irradiative pathways which may include radical formation.

Previously, we reported that UV-irradiation of linear analog **2a** generated radicals, which were unstable in solution resulting in degradation of the material.[39] Intriguingly, the radicals were found to be stable and persistent when generated within the assembled structures. Thus, we irradiated the activated host of **1a** to see if similar radicals would be observed. For this, freshly activated **1a** was sealed under Argon and was examined by X-band EPR spectroscopy pre and post irradiation. For UV-irradiation, 365 nm LEDs were employed instead of the previously employed medium pressure Hg lamp,[38,39] since the 365 nm LEDs are close to the λ_{max} of absorbance for these materials and have the advantage that quartz impurities are not generated during the irradiation period (see experimental section). Figure 5.6a compares the EPR signal of **1a** after 4 h of irradiation versus the pre-

UV sample. After exhibiting very little signal pre irradiation, the EPR signal exhibits a broad, axial powder pattern shape with a *g*-value of 2.008 post irradiation.

Next, we measured the EPR signal of activated **1a** (9.8 mg) under increasing irradiation time (1 to 24 h) to see if more radicals would be generated with longer irradiation times. To monitor the formation of radicals, we plotted the double integration of the EPR spectra over time. To estimate the number of radicals generated, the double integration of the EPR spectra were compared to a calibration of Magic Blue standard solutions in dichloromethane (Figure 5.78). A comparison of these can give an approximate concentration of the number of radicals generated in the solid-state. As seen in Figure 5.6d, the concentration of radicals grows with increasing irradiation time until it plateaus around 20 h. At this point, ~ 0.69% of the molecules generated a radical (or ~ 1 in 150 molecules)

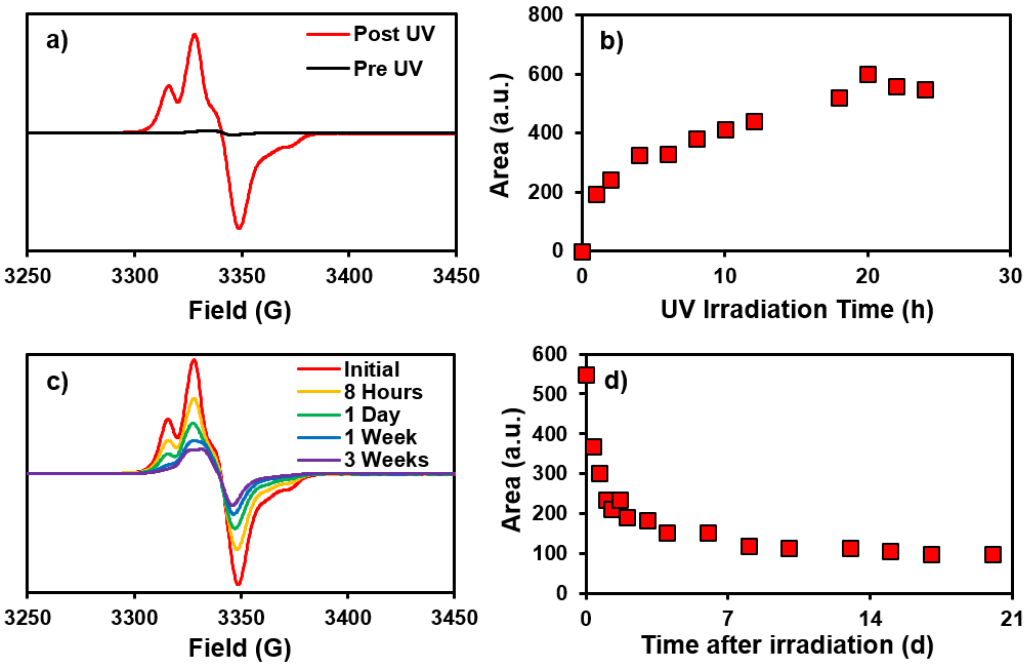

Figure 5.6. EPR studies for activated **1a**. (A) EPR signal pre and post UV irradiation. (B) Double integration over time of UV irradiation. (C) Dark decay spectra for activated **1a** after it was irradiated to its maximum radical concentration. (D) Double integration versus time after irradiation.

which estimates to the same number of radicals seen in 100 μL of a 0.83 mM solution of Magic Blue.

Next, seven host-guest complexes of **1a** were systematically investigated to quantify the maximum amount of radical they could generate upon irradiation. These complexes were chosen as to vary the polarity and heavy atom substitution of the guests to see if they had any effects on radical formation. As seen in Figures 5.71-5.77, most of these complexes reached their maximum EPR signals after ~ 20-24 h, apart from **1a**·C_6H_5F and **1a**·C_6H_5Cl which reached a maximum after 12 h. Interestingly, the presence of encapsulated guests altered both the line shape of the signal as well as the quantity of radicals formed as seen in Figures 5.1 and 5.7; and Table 5.2, respectively. This was quite surprising since guest encapsulation had little effect on the absorption, emission and lifetimes of host **1a**. For the line shapes, the least polar and least heavy atom substituted complex, **1a**·C_6H_6, showed the line shape most similar to the empty structure, activated **1a**, while the more polar, heavy atom complexes of **1a**·DMF and **1a**·C_6H_5Br showed a narrowing of the line shape. Similarly, the least polar and least heavy atom substituted complex, **1a**·C_6H_6, generated the most radicals (0.78%) while the more polar, heavy atom substituted complexes of **1a**·DMF and **1a**·C_6H_5Br exhibited the least number of radicals (0.15% and 0.23%, respectively). In fact, trends were observed along these lines with polarity (**1a**·C_6H_6 > **1a**·1,4-dioxanes > **1a**·DME > **1a**·DMF) and heavy atom incorporation (**1a**·C_6H_6 > **1a**·C_6H_5F > **1a**·C_6H_5Cl > **1a**·C_6H_5Br) clearly affecting the amount of radical observed. Intriguingly, encapsulation of benzene within host **1a** afforded an even higher radical concentration than activated **1a**. This may be due to a stabilization of the framework, or because the filled channel slows down oxygen quenching processes.

Table 5.2. Approximate number of radicals generated during UV-irradiation from 365 LEDs.

Compound	4 Hours	Max
1	0.69%	--
1a	0.42%	0.69%
1a·DME	0.20%	0.28%
1a·C_6H_6	0.55%[a]	0.85%[a]
1a·C_6H_5F	0.33%	0.45%
1a·C_6H_5Cl	0.19%	0.24%
1a·C_6H_5Br	0.13%	0.23%
1a·1,4-dioxanes	0.24%	0.38%
1a·DMF	0.08%	0.15%
2	0.16%	--
2a	0.16%	--
3	~ 0%	--
3a	Very Small[b]	--
4	Very Small[b]	--

[a] Average of four trials. [b] Concentration below values of calibration curve given in Figure 5.78.

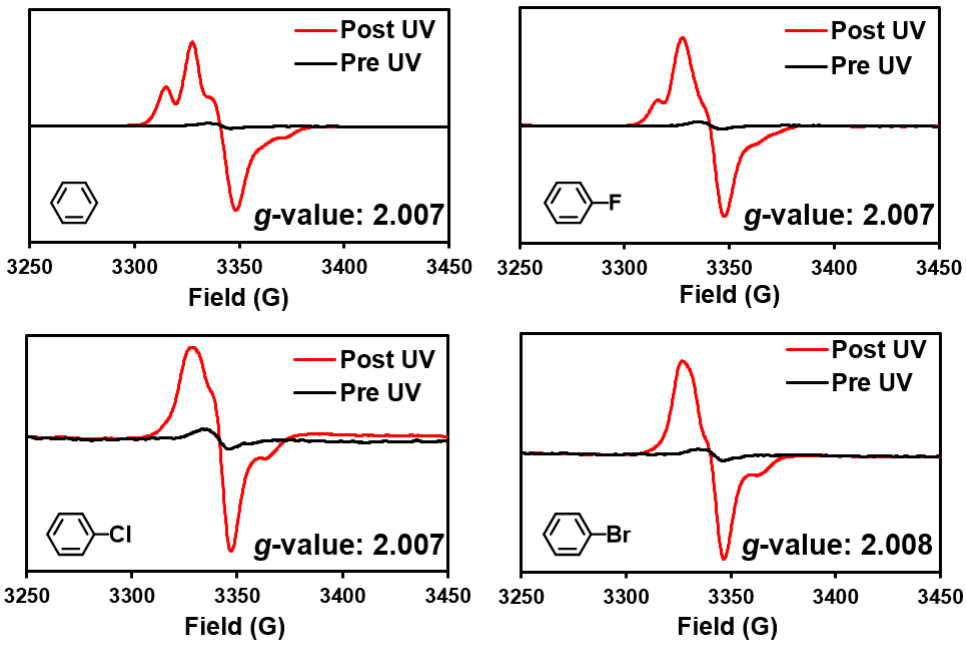

Figure 5.7. EPR studies for guest inclusion complexes of **1a**. EPR signal pre and post UV irradiation is given for each complex. Additionally, the *g*-values are given.

To further estimate the error of these measurements, we repeated the **1a**·C_6H_6 experiment three more times, by irradiating the sample until radical formation plateaued

(Figure 5.71). On average 0.85% of the molecules generated a radical at maximum concentration (or 1 in 120 molecules) with a standard deviation of 0.06%. This demonstrates the reproducibility of radical concentrations between samples.

Next, the persistence of the photogenerated radicals were examined with dark decay studies. For this, samples which were irradiated to their maximum concentration, were stored in the dark at room temperature. Then EPR spectra were taken periodically afterwards to assess the stabilities of the radicals. Figures 5.6c and 5.6d show the EPR signal and the double integration of the EPR signal, respectively, over time for the activated **1a** host over three weeks. Figure 5.6d shows that the number of radicals decays to about 20% of the maximum concentration after one week, with an estimated half-life of ~ 24 h. The remaining radical species display more stability, with their concentration remaining somewhat constant up to three weeks later. These results in combination with the different line shapes shown in the latter spectra (Figure 5.6c), suggest that at least two types of radical decay processes are occurring. Simulations of the EPR spectra (see below) also support this suggestion.

For the host-guest complexes, dark decay studies were performed on complexes **1a**·C_6H_6, **1a**·DME and **1a**·DMF as these guests afforded the greatest difference in radical concentrations (Table 5.2). Similar behavior and half-lives were observed for **1a**·C_6H_6 and **1a**·DMF crystals when compared to activated **1a** (Figures 5.71 and 5.73). A longer half-life of ~ 1 week was estimated for the **1a**·DME complex (Figure 5.72). Additionally, the radical concentration only dipped to about 40% of its maximum after 3 weeks instead of 20% which was observed for all the other cases for host **1a**. This may be a result of minimal processing on this sample of crystals, as every other sample had to be evacuated and, in

some cases, reloaded with another guest. Complex **1a**·DME is formed from the initial crystallization conditions for macrocycle **1a**, so activation and guest loading to form the complex was unnecessary. Complex **1a**·DME showed similar behavior to linear analog **2a**, which also had a half-life of ~ 1 week and decayed to ~ 40% of its initial signal.[39] There is therefore significant similarity between freshly crystallized samples. Overall, the line shapes of the EPR spectra for each case involving macrocycle **1a** decayed to very similar signal levels, suggesting that the longer-lived radical species among these samples is similar.

Usually with chemical or electrochemical radical generation methods, the sample must be resynthesized once the TPA radicals have decayed due to degradation. However, no degradation was detected by NMR for linear analog **2a** after radical generation.[39] Moreover, after radical decay, re-exposure of linear analog **2a** to UV-light led to regeneration of the radical species. This led us to test four samples of host **1a** (activated **1a**, **1a**·DME, **1a**·C_6H_6, **1a**·DMF) to determine if similar stable and regenerable radicals would be observed. For these experiments, each sample (5-10 mg) was irradiated to its maximum concentration, its EPR spectrum measured, followed by storage in the dark for two days. EPR signals were recorded at t = 8, 24, and 48 h. Then the samples were re-irradiated (12 – 14 h) so the cycle could be repeated. Figure 5.8 plots the area of the EPR signal versus time over four cycles of this photo-regeneration process for each sample. Remarkably, in all four cases, the radical signal could be fully restored in both intensity and line shape (Figures 5.70-5.73). For complex **1a**·C_6H_6, the maximum radical concentration slightly increased over each cycle. This unexpected result may be a consequence of some charge equilibria during radical decay, allowing for more charge to

be introduced during later irradiation, since this is suspected to be a charge separation-based process.[39] Overall, in each case radicals could be formed, decay, and then formed again over multiple 2-day cycles, in a reproducible manner.

After seeing that the radicals could be repeatably lost and regenerated, we wanted to monitor if the host material could survive this process similar to linear analog **2a**.[39] For this, each sample used from the regeneration studies (activated **1a**, **1a**·DME, **1a**·C_6H_6, **1a**·DMF) were dissolved in DMSO-d_6 and their ^{1}H NMR recorded and compared to a freshly synthesized sample of **1a**. As seen in Figures 5.79-5.82, no degradation was observed for any of the samples. Comparing these spectra, the only difference is the presence of guests in the NMR spectra (as is the case with benzene). These studies suggest that radical formation of host **1a** is reversible and does not lead to the degradation of the material as a whole.

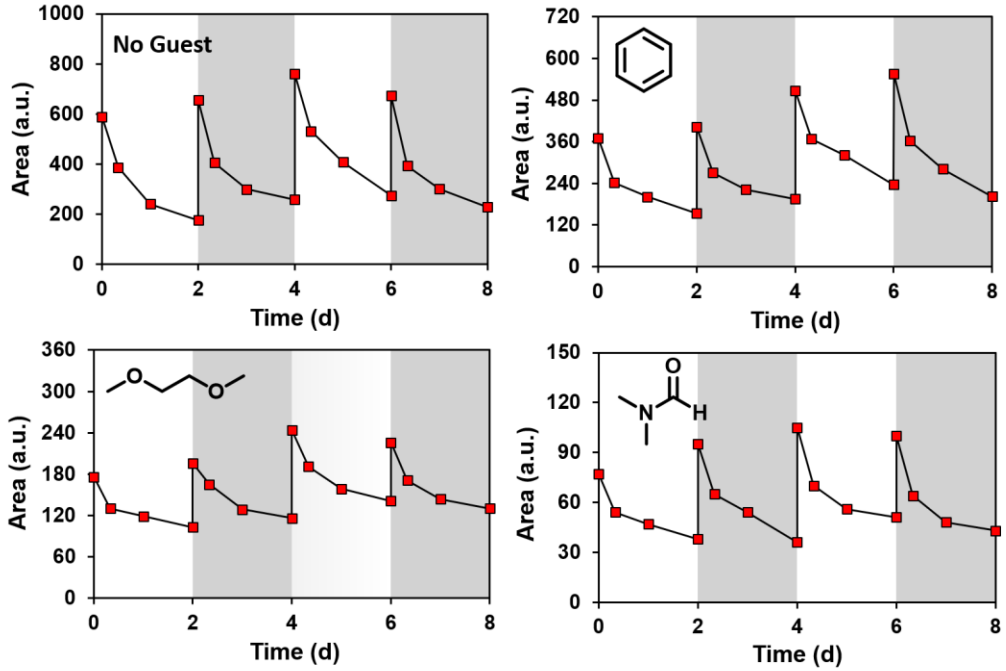

Figure 5.8. Regeneration of radical signals for activated **1a**, **1a**·C_6H_6, **1a**·DME, and **1a**·DMF. After initial irradiation to maximum concentration, each sample was allowed to decay for two days. Then they were re-irradiated overnight to restore radical signal.

Next, we compared the EPR spectra for control compounds **1** and **2-4** before and after irradiation (4 h, 365 nm LEDs) to investigate the chemical structure that contributes to radical formation (Figure 5.9 and Table 5.2). The first of these, TPA **3**, which has no substitution on the TPA group, displayed no significant radical formation after irradiation, suggesting that at least some substitution on the TPA moiety is needed for radical formation in the solid-state. The mono-brominated equivalent of TPA **3**, compound **3a**, showed a very small signal after irradiation. This signal was so small that it was below the detection limits of our calibration curve to quantify the radical concentration. This suggests that the signal from TPA **3a** does not arise from the same process as macrocycle **1a** as many more radicals were produced for macrocycle **1a**. The radicals generated from TPA **3a** may just be the result of photolysis of the C-Br, bond which can be expected for halogenated aromatics.[48] Control **4**, which has one methylene urea connected to the TPA group, also exhibited a very small signal similar to the singly brominated TPA of **3a** suggesting that it may also be susceptible to a small amount of photolysis.

Given these controls, we suspected that closely organizing two TPA units in a linear or macrocyclic system is important for generating significant radical concentrations in the solid-state. Therefore, we tested the non-brominated analogs of macrocycle **1a** and linear analog **2a** to see if they afforded significant amounts of radical. Indeed, non-brominated linear analog **2** forms a similar number of radicals as its brominated counterpart, **2a**, after 4 h of irradiation (both ~ 0.16%). Surprisingly, the non-brominated macrocycle **1** exhibited the highest efficiency of radical generation after four hours of irradiation (0.69% for the non-brominated macrocycle **1** versus 0.42% for the brominated macrocycle of **1a**) and showed more hyperfine interactions than its linear counterpart, **2**. Considering that

macrocycle **1a** also had more hyperfine splitting than its linear analog counterpart **2a**, this suggests that the additional tether between the TPAs (macrocycles having two and linear analogs having one) increases the hyperfine splitting in the EPR spectra.

To investigate how UV-induced radical formation affected the TPA materials and to probe insight into a possible mechanism of radical formation, both linear analog **2a** and the activated host of **1a** were further investigated by Cross-Polarized Magic Angle Spinning (CP-MAS) ^{13}C NMR. Overlays of the NMR spectra of the pre- and post-

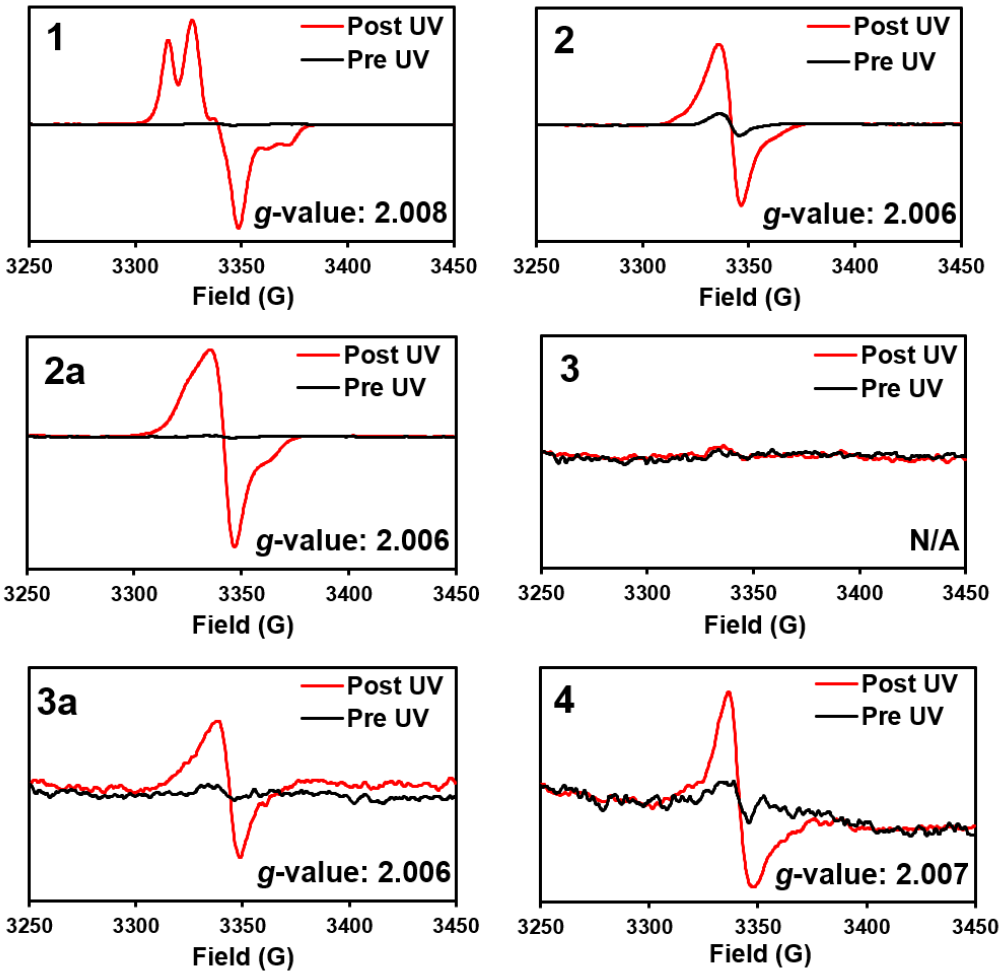

Figure 5.9. EPR signals pre and post irradiation for control samples **1**, **2**, **2a**, **3**, **3a**, and **4**. Each sample was irradiated for four hours before the post-irradiation EPR spectra were taken.

irradiated solids are shown in Figure 5.83. While the methylene carbon resonances of the urea linker (ca. 43 ppm) were minimally affected, the overlays reveal significant UV-induced broadening of the aromatic and carbonyl ^{13}C lines, particularly for linear analog **2a**. Thus, the proton spin-lattice relaxation times at different sites in crystals of the UV-irradiated linear analog **2a** were probed by application of the inversion-recovery pulse sequence to the protons prior to cross-polarization and detection on ^{13}C (Figure 5.84). The longest spin relaxation times were observed for protons attached to the urea linker carbons, consistent with the minimal line-broadening observed at these sites. In contrast, the T_1 relaxation time of the protons in the vicinity of the carbonyl carbon were among the shortest in the sample, where the recovery null occurs at approximately 3.5 s. The proton T_1 of the protons on the aromatic rings varied and was shortest for broad resonance at ~120 ppm and increased with increasing chemical de-shielding, consistent with the observed variations in the line broadening. The CP-MAS NMR results suggest localization of unpaired electron density in the $BrNPh_3$ moiety. Significant line broadening on the carbonyl carbon but not the methylene carbon suggests radical formation impacts the urea network more strongly than the methylene bridge. To probe if the structure of the radicals changes with time, the stability of the UV-induced radicals were monitored over the course of 16 h by acquiring a series of ^{13}C CP-MAS spectra every 53 minutes. As seen in the overlay of these spectra in Figure 5.75, the spectra are all identical (within the noise), demonstrating the stability of the photoinduced radicals on the timescale of this experiment.

To gain more insight into structure of the photogenerated radicals we next investigated the more soluble TPAs **2-4** via electrochemical methods. Prior electrochemical studies with linear analog **2a** demonstrated oxidation at 1.0 V versus a

saturated calomel electrode (SCE) as a 1 mM solution in dichloromethane. This resulted in a dication with both TPA groups containing a radical cation.[39] Bulk electrolysis at this potential exhibited a very similar EPR spectrum to the photogenerated radicals of linear analog **2a** in the solid-state indicating that a similar radical species (radical cation) was present in both samples.

For this study, a cathodic investigation of TPA and its related derivatives were investigated with cyclic voltammetry. Voltammograms of TPAs **2**-**4**, Figures 5.86-5.90, all exhibit irreversible reductions occurring between -1.2 and -1.5 V versus SCE as 1 mM dichloromethane solutions. Reduction of TPA **3** occurred with an $E_{p,c}$ = -1.28 V under the standard experimental conditions. Reduction of the brominated TPA, **3a**, occurred at a less negative potential of $E_{p,c}$ = -1.18 V. This shift can be attributed to the electron withdrawing Br moiety on TPA **3a**. In addition, reduction of methylene urea substituted TPA **4** occurred with a negative potential shift relative to TPA **3** likely due to the electron donating behavior of the methylene urea substituent on the TPA core. These redox trends are consistent with previously reported redox behavior for related TPA derivatives.[49] Furthermore, linear analogs **2** and **2a** exhibit two closely spaced 1e$^-$ reductions. These reductions are attributed to reduction of the individual TPA units tethered by the urea linkers and illustrates an ability to generate closely spaced radicals.

Using the EPR, NMR, and electrochemical data, we next set out to simulate the EPR spectra of the UV-irradiated activated **1a**. Figure 5.10 shows our best effort to simulate the EPR spectrum with the most fine structure. The fact that two independent radicals are needed to get this reasonable fit, with all lines accounted for, supports that two radical decay processes may be at play. The discrepancies in intensity on the high field side

of the spectrum are almost certainly due to anisotropy in this solid-state spectrum. Furthermore, the presence of a signal carrier with two N hyperfine interactions and one without strongly supports the suggestion above that more than one redox pathway is available to these structures and that both mono-cations and di-cations may be present. Future isotopic substitutions and *in situ* electrochemical EPR experiments are planned in order to explore this further.

Overall, UV-irradiation of self-assembled methylene urea tethered TPA macrocycles gives rise to persistent organic radicals. Guests loaded within the TPA hosts can modulate the concentration of radicals generated with concentrations ranging from 0.15-0.85% of the molecules generating a radical at maximum concentration. These

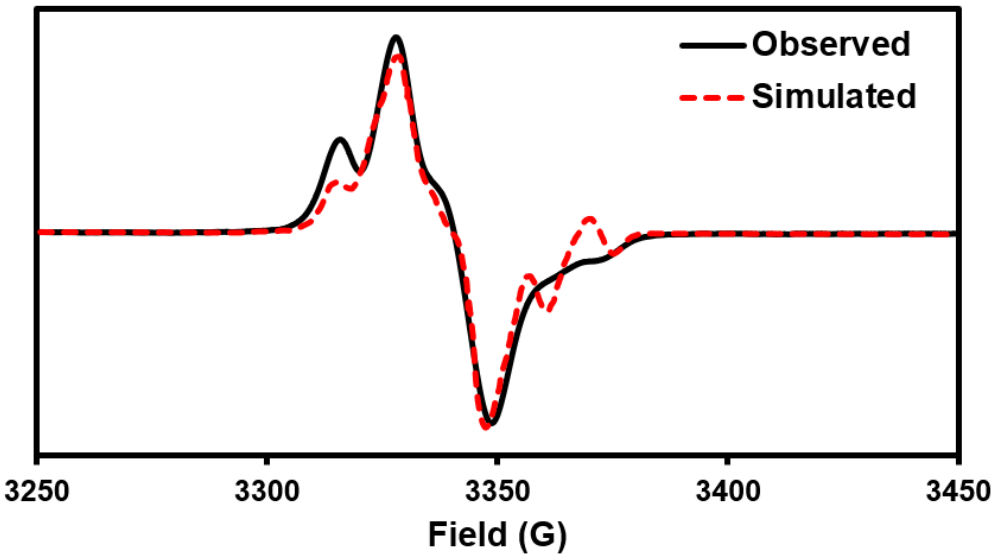

Figure 5.10. Experimental steady–state X-band EPR spectrum (solid black line) of activated host **1a** post UV-irradiation, overlaid onto a best fit simulation (dashed red line) using EasySpin.[50] The simulation was performed using parameters for two independent radicals. The first has two nitrogen hyperfine interactions with g = 2.0049, a_N = 39 Gauss for two equivalent nitrogens, line width (peak to peak) 5 Gauss, and a relative weighting of 0.1. The second radical has g = 2.0087, contains no hyperfine interactions, line width = 20 G, and a relative weighting of 1.1.

radicals display a half-life of about 24 hours, persist an upwards of 3 weeks, and can be regenerated with additional UV-irradiation to their original maximum concentration without causing degradation to the TPA host. Future work with these TPA hosts could include investigating how different electron accepting guests affect the radical formation of the TPA host and if it leads to any new conductive properties of the material.

5.3 CONCLUSIONS

In summary, several TPA derivatives were synthesized and were organized in the solid-state via crystalline assemblies. One of these derivatives, brominated macrocycle **1a**, organizes into robust columnar needles and displays 1D porosity through small nanochannels. Inside these channels, small guests can be exchanged via SC-SC transformations without changing the host framework. This creates a series of isoskeletal complexes whose properties can be directly compared. We have monitored how the photophysics and photo-induced radical formation change with the inclusion of different guest molecules. Although the absorption, emission, and photoluminescent lifetime properties of each complex were somewhat similar, the amount of photogenerated radicals produced by each complex varied considerably. It was found that an increase in polarity or heavy atom substitution decreases the number of radicals observed. This is highlighted in the complexes of **1a**·C_6H_6, **1a**·DMF, and **1a**·C_6H_5Br, with the first of these displaying the most radical formation after 24 h of irradiation with 0.78% of the molecules generating a radical. The latter two complexes are more polar or contain heavy atoms and show less radical formation after a similar amount of UV-irradiation, 0.15% and 0.23%, respectively. Overall, the complexes show similar radical half-lives of 24 hours and persist up to 3 weeks. Intriguingly, reirradiation of these materials with more UV-light can regenerate

radical quantities to similar amounts to their pre-radical decays. In fact, this radical formation/decay process can continue over several cycles with reproducible results and occurs without degradation of the host material.

The key to forming these robust materials with regenerative radical properties is connecting two TPAs together through a methylene urea bridge. Although UV-irradiation of simple bromine or methylene urea substituted TPAs resulted in a small amount of radical signal, significant amounts of photogenerated radicals were not observed until the two TPAs were connected. Currently, we are planning Q-band EPR, ENDOR, ESEEM, and SQUID experiments to try and pinpoint the mechanism of radical formation upon UV-irradiation for these materials.

5.4 EXPERIMENTAL

5.4.1 General Experimental

NMR spectra were recorded on Bruker Avance 300 or 400 MHz spectrometers. Chemical shifts are reported in ppm (δ) and were internally referenced with the solvent peak. All chemicals were purchased from chemical suppliers and were used as received unless otherwise noted. High-resolution mass spectrum data were recorded using a direct exposure probe (DEP) in electron ionization mode on a Waters QTOF-I quadrupole time-of-flight mass spectrometer. UV-irradiation of all materials were carried out with Waveform Lighting realUV LED strips (365 nm, 4.5 W/ft, 3.2 ft). Samples were purged with argon before irradiation. Hosts **1** and **1a** were activated by placing them under vacuum at 90°C either for 2.5 hours (**1a**) or overnight (**1**). Higher temperatures were found to degrade these materials. The host-guest complexes of **1a** with lower volatility guests (**1a**·C_6H_5Cl, **1a**·C_6H_5Br, and **1a**·DMF) were allowed to air dry on the balance until no more

weight loss was detected (~ 1-2 h). In addition, TGAs were also measured on samples upon completion of the radical studies (Figures 5.43-5.45) for comparison. PXRDs (Figures 5.37-5.41) were measured to monitor the phase purity of the samples. Figures 5.46 and 4.48-4.55 compare the solid-state absorption spectra. All other instrument protocols and sample preparations are described in their own sections hereafter.

5.4.2 Synthesis and Characterization of Compounds

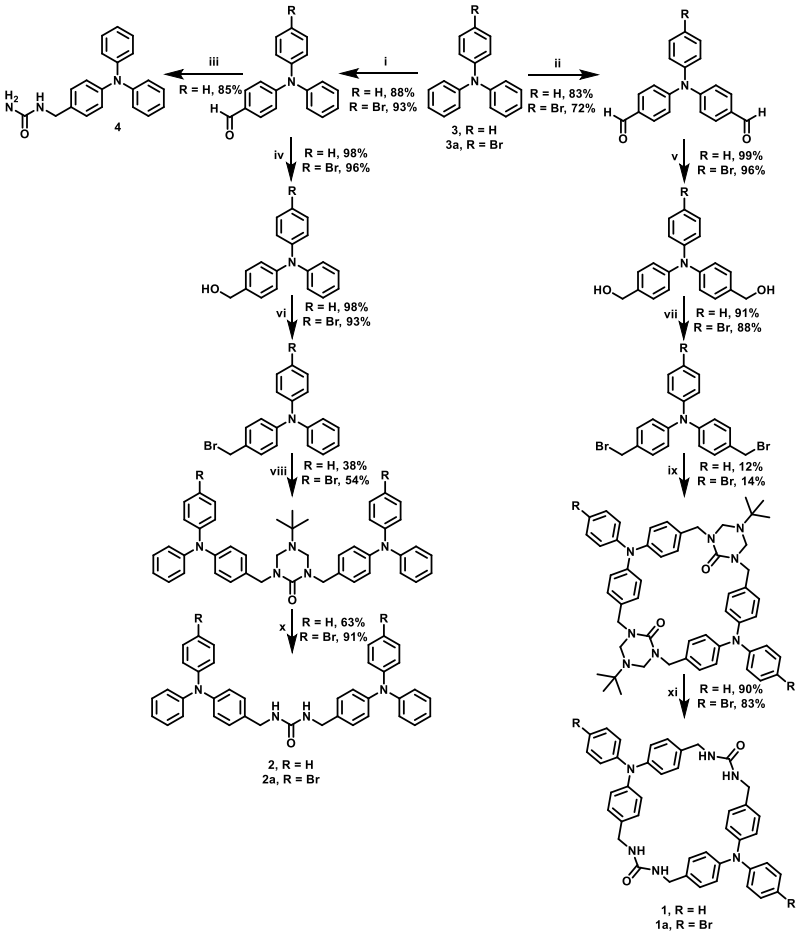

Scheme 5.1. Synthesis of compounds. i) $POCl_3$, DMF, 40 °C (R = H) or 60 °C (R = Br), 12h (R = H) or 2h (R = Br). ii) $POCl_3$, DMF, 105 °C, 4 h. iii) 1) Urea, TMSCl, CH_3CO_2H 2) $NaBH_4$. iv) $NaBH_4$, DCM/EtOH. v) $NaBH_4$, THF/EtOH. vi) PBr_3 (0.7 eq.), Et_2O vii) PBr_3 (1.2 eq.), Et_2O. viii) NaH, triazinone (0.5 eq.), THF, Δ, 12 h. ix) NaH, triazinone (1 eq.), THF, Δ, 48 h. x) 9:1 DMF/DEA (0.5 mL/mg), pH~2, 90 °C, 48 h. xi) 9:1 DMF/DEA (1 mL/mg), pH~2, 90 °C, 48 h.

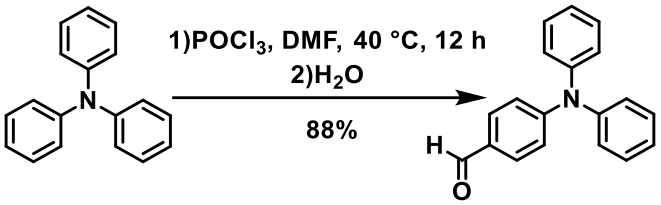

4-(Diphenylamino)benzaldehyde: Compound was made according to previous procedures.[41] Phosphoryl chloride (1.0 mL, 11.4 mmol) was added dropwise to dry *N*, *N*-dimethylformamide (875 μL, 11.4 mmol) and the mixture was stirred at room temperature for 20 min. Then a solution of triphenylamine (1.000 g, 4.1 mmol) in 10 mL of *N*, *N*-dimethylformamide was added, and this mixture was heated at 40 ˚ C overnight. After cooling to room temperature, 35 mL of ice-cold water was added to the mixture and the solution was filtered. The resulting residue was recrystallized in ethanol giving a yellow crystalline product (0.980 g, 88%). Spectra matched that as previously reported.[41] ^{1}H NMR (300 MHz, $CDCl_3$): δ (ppm) 9.83 (s, 1H), 7.70 (d, *J* = 8.7 Hz, 2H), 7.37 (t, *J* = 7.7 Hz, 4H), 7.24-7.15 (m, 6H), 7.04 (d, *J* = 8.7 Hz, 2H).

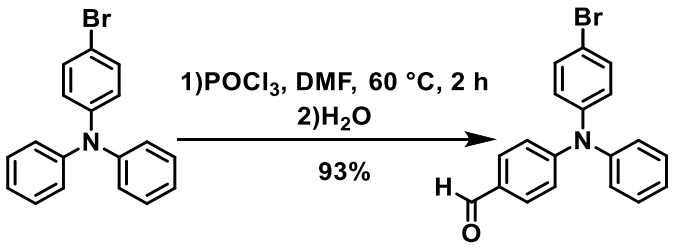

4-((4-Bromophenyl)(phenyl)amino)benzaldehyde: Compound was made according to previous procedures.[51] Phosphoryl chloride (840 μL, 9.0 mmol) was added dropwise to dry *N, N*-dimethylformamide (830 μL, 10.8 mmol) in an ice bath and the mixture was stirred for 20 min. Then 4-bromo-*N, N*-diphenylaniline (2.590 g, 8.0 mmol) was added, and this mixture was heated to 110 ˚C for 5 min then cooled to 60 ˚C for 2 h

with stirring. After cooling to room temperature, 50 mL of ice water was added, and the solution was neutralized with saturated aqueous $NaHCO_3$. Then the mixture was extracted with chloroform (3 × 50 mL) and washed with water (1 × 50 mL), then brine (1 × 50 mL), and dried with $MgSO_4$. The solvent was removed under reduced pressure and the crude material was further purified by column chromatography (Hexanes/Ethyl Acetate = 3:1) to yield the product as a yellow solid (2.616 g, 93%). Spectra matched that as previously reported.[51] ^{1}H NMR (300 MHz, $CDCl_3$): δ (ppm) 9.82 (s, 1H), 7.69 (d, *J* = 8.7 Hz, 2H), 7.44 (t, *J* = 8.7 Hz, 2H), 7.35 (t, *J* = 7.7 Hz, 2H), 7.22-7.11 (m, 3H), 7.08-6.99 (m, 4H).

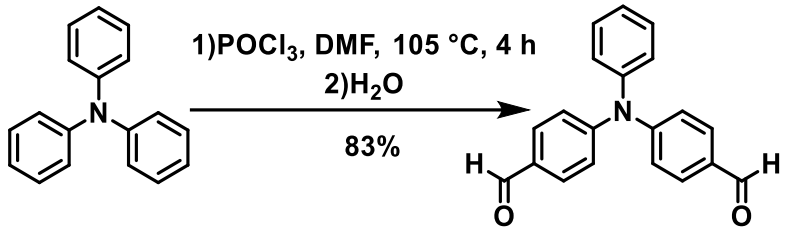

4,4'-(Phenylazanediyl)dibenzaldehyde: Compound was made by modifying previous procedures.[52] Phosphoryl chloride (7.17 mL, 76.9 mmol) was added dropwise to dry *N*, *N*-dimethylformamide (7.71 mL, 100.0 mmol) under nitrogen at 0 ˚C and the mixture was stirred at room temperature for one hour. Then triphenylamine (1.890 g, 7.7 mmol) was added, and this mixture stirred for 4 h at 105 ˚C. After the mixture cooled to room temperature, 80 mL of ice-cold H_2O was added to the mixture and it was neutralized with sodium bicarbonate. This mixture was extracted with chloroform (3 × 80 mL) and the organics were washed with water (3 × 80 mL) and brine (1 × 80). After drying with $MgSO_4$, the solvent was removed with rotary evaporation. The crude product was purified by column chromatography (Hexanes/Diethyl Ether = 3:1) to yield the product as a yellow solid (1.926 g, 83%). Spectra matched that as previously reported.[53] ^{1}H NMR (300 MHz,

$CDCl_3$): δ (ppm) 9.90 (s, 2H), 7.78 (d, *J* = 8.7 Hz, 4H), 7.40 (t, *J* = 7.2 Hz, 2H), 7.29 (t, *J* = 7.3 Hz, 1H), 7.18 (m, 6H).

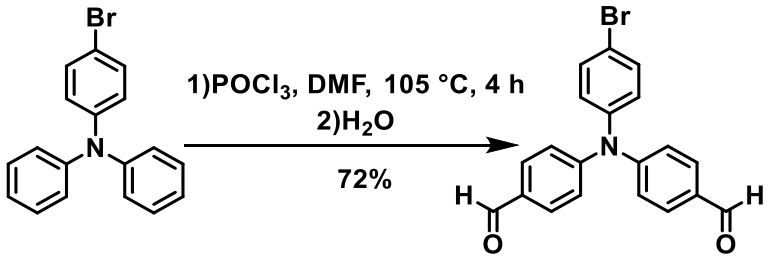

4,4'-((4-Bromophenyl)azanediyl)dibenzaldehyde: Compound was made according to previous procedures.[40] Phosphoryl chloride (9.12 mL, 97.8 mmol) was added dropwise to dry *N*, *N*-dimethylformamide (10.00 mL, 129.7 mmol) under nitrogen and the mixture was stirred at room temperature for one hour. Then 4-bromo-*N*, *N*-diphenylaniline (3.17 g, 9.78 mmol) was added, and this mixture stirred for 4 h at 105 ˚C. After the mixture cooled to room temperature, 100 mL of ice-cold water was added followed by further dilution to 1 L with water. Then the suspension was filtered, and the crude product was purified by column chromatography (Hexanes/Diethyl Ether = 3:1) to yield the product as a yellow solid (2.677 g, 72%). Spectra matched that as previously reported.[54] ^{1}H NMR (300 MHz, $CDCl_3$): δ (ppm) 10.03 (s, 2H), 7.79 (d, *J* = 8.6 Hz, 4H), 7.50 (d, *J* = 8.7 Hz, 2H), 7.18 (d, *J* = 8.4 Hz, 4H), 7.05 (d, *J* = 8.8 Hz, 2H).

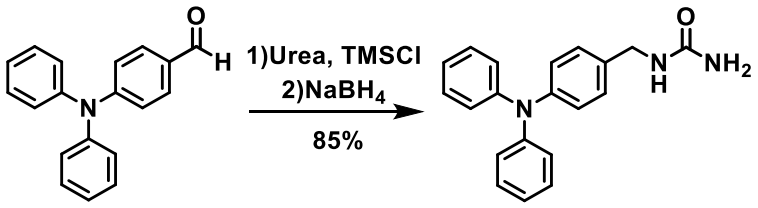

1-(4-(diphenylamino)benzyl)urea: The previous aldehyde (0.460 g, 1.7 mmol), urea (1.000 g, 16.8 mmol), and trimethylsilyl chloride (0.315 mL, 2.52 mmol) were dissolved

in 30 mL of acetic acid and stirred at room temperature overnight. Then sodium borohydride (0.095 g, 2.52 mmol) was added and the mixture stirred for an additional two h. After reaction completion, 500 mL of water was added, and the precipitate was filtered and washed with plenty of water. Then column chromatography (Dichloromethane/Ethyl Acetate = 1:1) was used to purify the product as a beige solid (0.454 g, 85%). ^{1}H NMR (300 MHz, CD_3OD): δ (ppm) 7.28-7.15 (m, 6H), 7.04-6.94 (m, 8H), 4.25 (s, 2H). HRMS (DEP): [M+] calculated, 317.1528; found, 317.1524.

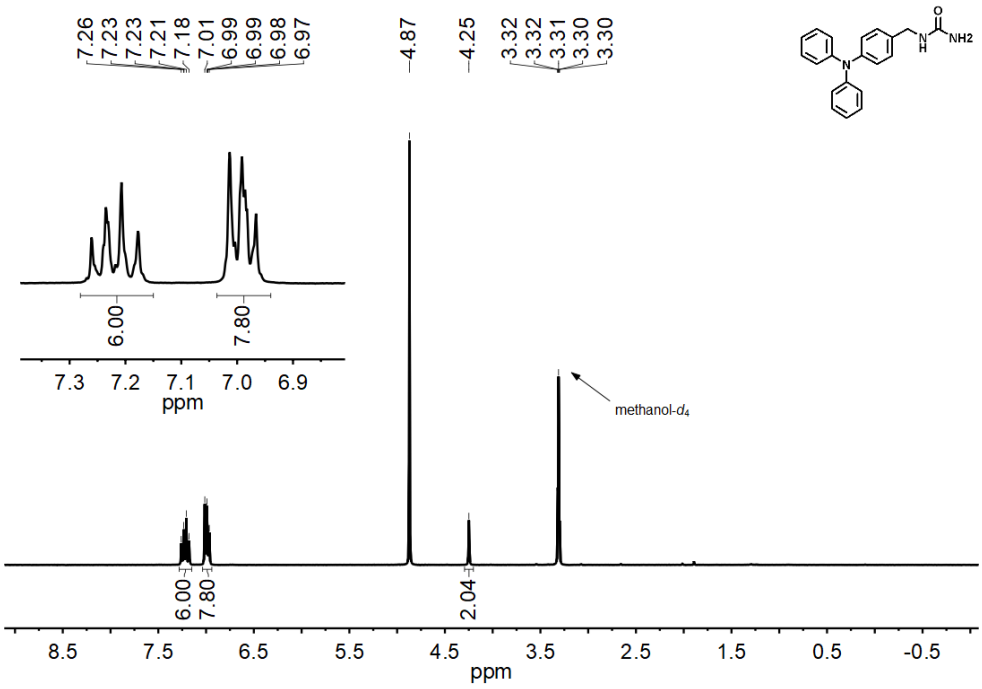

Figure 5.11. ^{1}H NMR of TPA **4** ((CD_3OD, 300 MHz).

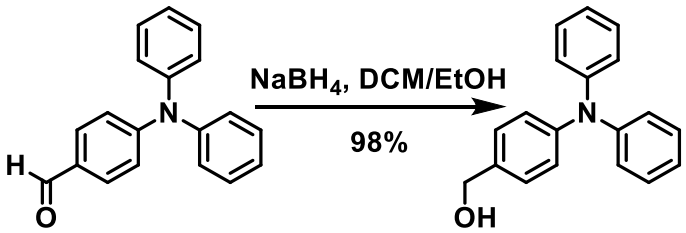

(4-(Diphenylamino)phenyl)methanol: Compound was made according to previous procedures.[55] The previous aldehyde (0.4885 g, 1.8 mmol) was dissolved in 28 mL of a 3:1

mixture of dry dichloromethane and ethanol. Sodium borohydride (0.074 g, 2.0 mmol) was added after and the mixture stirred at room temperature for 2 h in the dark. Then 40 mL of water was added, and the mixture was extracted with dichloromethane (3 × 15 mL) and dried with $MgSO_4$. Solvent was removed *via* rotary evaporation leaving behind the alcohol as a sticky solid (0.482 g, 98%). Spectra matched that as previously reported.[52] ^{1}H NMR (300 MHz, $(CD_3)_2SO$): δ (ppm) 7.33-7.21 (m, 6H), 7.06-6.92 (m, 8H), 5.12 (t, *J* = 5.7 Hz, 1H), 4.44 (d, *J* = 5.6 Hz, 2H).

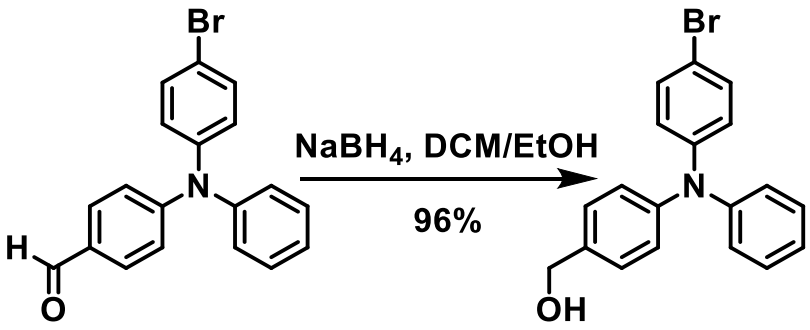

(4-((4-Bromophenyl)(phenyl)amino)phenyl)methanol: Compound was made according to previous procedures.[39] The previous aldehyde (1.0466 g, 3.0 mmol) was dissolved in 50 mL of a 3:1 mixture of dry dichloromethane and ethanol. Sodium borohydride (0.124 g, 3.3 mmol) was added after and the mixture stirred at room temperature for 12 h in the dark. Then 70 mL of water was added, and the mixture was extracted with dichloromethane (3 × 70 mL) and dried with $MgSO_4$. Solvent was removed *via* rotary evaporation leaving behind the alcohol as a sticky solid (1.011 g, 96%). Spectra matched that as previously reported.[39] ^{1}H NMR (300 MHz, $(CD_3)_2SO$): δ (ppm) 7.41 (d, *J* = 8.8 Hz, 2H), 7.35-7.23 (m, 4H), 7.09-6.96 (m, 5H), 6.86 (d, *J* = 8.9 Hz, 2H), 5.14 (t, *J* = 5.7 Hz, 1H), 4.45 (d, *J* = 5.7 Hz, 2H).

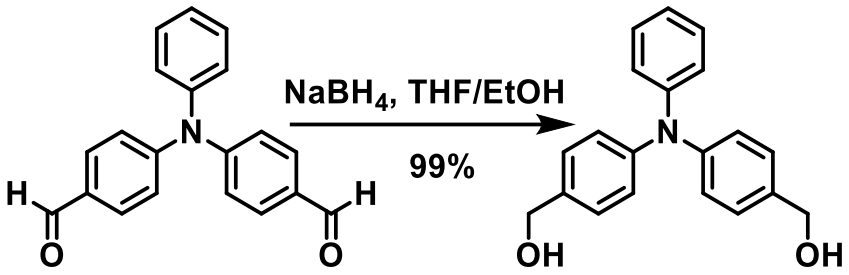

((Phenylazanediyl)*bis*(4,1-phenylene))dimethanol: Compound was made according to previous procedures.[56] The previous aldehyde (2.439 g, 8.1 mmol) and sodium borohydride (0.674 g, 17.8 mmol) were suspended in 180 mL of a 2:1 mixture of dry tetrahydrofuran and ethanol and heated at 40 ˚C overnight in the dark. Then the reaction was cooled to room temperature and 180 mL of water was added to quench the reaction. The mixture was extracted with chloroform (3 × 180 mL) and dried with $MgSO_4$. Then the solvent was removed under rotary evaporation to yield the alcohol as a white solid (2.446 g, 99%). Spectra matched that as previously reported.[56] ^{1}H NMR (300 MHz, $CDCl_3$): δ (ppm) 7.24-7.20 (m, 5H), 7.11-6.98 (m, 8H), 4.64 (s, 4H).

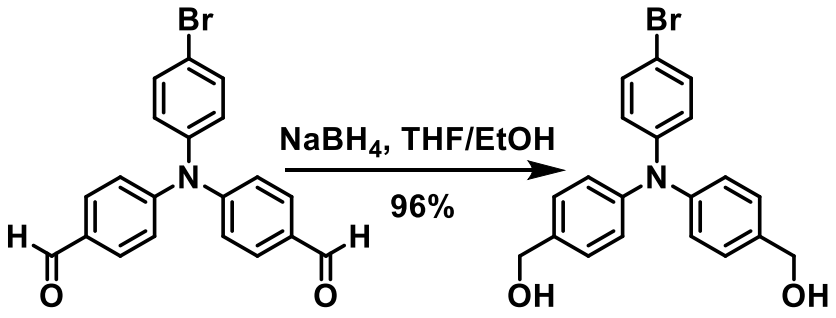

(((4-Bromophenyl)azanediyl)*bis*(4,1-phenylene))dimethanol: Compound was made according to previous procedures.[40] The previous aldehyde (2.6574 g, 7.0 mmol) and sodium borohydride (0.582 g, 15.4 mmol) were suspended in 180 mL of a 2:1 mixture of dry tetrahydrofuran and ethanol and was heated at 40 ˚C overnight in the dark. Then the

reaction was cooled to room temperature and 180 mL of water was added to quench the reaction. The mixture was extracted with chloroform (3 × 180 mL) and dried with $NaSO_4$. The solvent was removed under rotary evaporation yielding the product as a white solid (2.579 g, 96%). Spectra was similar to that as previously recorded.[40] ^{1}H NMR (300 MHz, $CDCl_3$): δ (ppm) 7.32 (d, *J* = 8.7 Hz, 2H), 7.26 (d, *J* = 8.3 Hz, 4H), 7.05 (d, *J* = 8.4 Hz, 4H), 6.93 (d, *J* = 8.8 Hz, 2H), 4.65 (s, 4H), 1.64 (s, 2H).

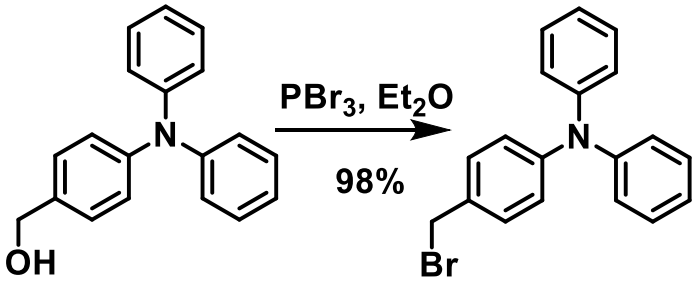

4-(Bromomethyl)-N,N-diphenylaniline: Compound was made according to previous procedures.[57] The previous alcohol (0.482 g, 1.8 mmol) was suspended in 20 mL of dry diethyl ether and was cooled to 0 ˚C. Then a solution of phosphorus tribromide (120 μL, 1.2 mmol) in 10 mL dry diethyl ether was added dropwise over 5 minutes. The reaction stirred at room temperature overnight in the dark. In the morning, ice cold water (20 mL) and saturated aqueous $NaHCO_3$ (10 mL) was added to quench the reaction. The mixture was extracted with (1 × 20 mL) of dichloromethane and the organics were washed with brine (3 × 20 mL) and dried with $MgSO_4$. The solvent was removed under rotary evaporation to yield the bromide as a sticky solid (0.580 g, 98%). Spectra was similar to that as previously recorded.[57] ^{1}H NMR (300 MHz, CD_2Cl_2): δ (ppm) 7.31-7.22 (m, 6H), 7.12-6.95 (m, 8H), 4.52 (s, 2H).

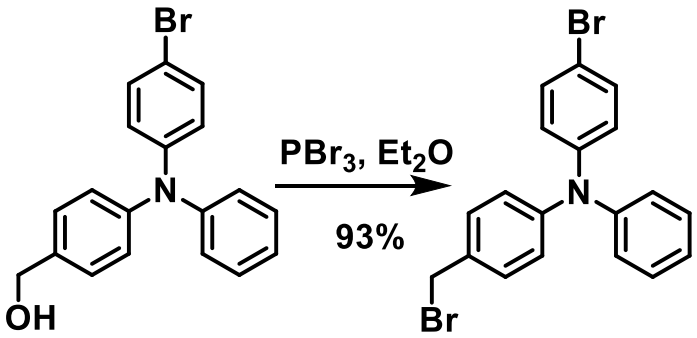

4-Bromo-*N*-(4-(bromomethyl)phenyl)-*N*-phenylaniline: Compound was made according to previous procedures.[39] The previous alcohol (1.013 g, 2.9 mmol) was suspended in 35 mL of dry diethyl ether and was cooled to 0 ˚C. Then a solution of phosphorus tribromide (163 μL, 1.7 mmol) in 10 mL dry diethyl ether was added dropwise over 5 minutes. The reaction stirred at room temperature overnight in the dark. In the morning, ice cold water (45 mL) and saturated aqueous $NaHCO_3$ (22.5 mL) was added to quench the reaction. The mixture was extracted with (1 × 45 mL) of dichloromethane and the organics were washed with brine (3 × 22.5 mL) and dried with $MgSO_4$. The solvent was removed under rotary evaporation to yield the bromide as a sticky solid (1.110 g, 93%). Spectra was similar to that as previously recorded.[39] ^{1}H NMR (300 MHz, CD_3Cl): δ (ppm) 7.30-7.14 (m, 6H), 7.04-6.95 (m, 3H), 6.95-6.84 (m, 4H), 4.41 (s, 2H).

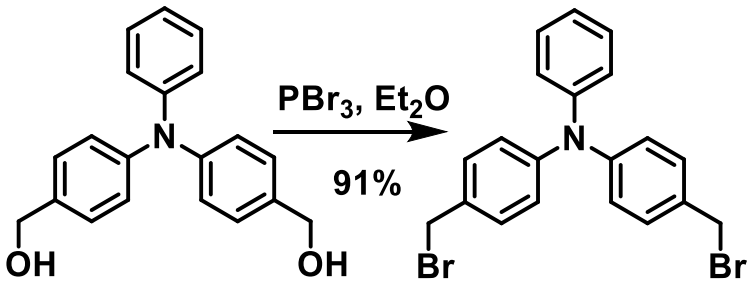

4-(Bromomethyl)-*N*-(4-(bromomethyl)phenyl)-*N*-phenylaniline: The previous alcohol (1.828 g, 6.0 mmol) was suspended in 62 mL of dry diethyl ether and was cooled

to 0 ˚C. Then a solution of phosphorus tribromide (682 μL, 7.2 mmol) in 10 mL dry diethyl ether was added dropwise over 5 minutes. The reaction stirred at room temperature overnight in the dark. In the morning, ice cold water (72 mL) and saturated aqueous $NaHCO_3$ (36 mL) was added to quench the reaction. The mixture was extracted with 72 mL of dichloromethane and the organics were washed with brine (3 × 72 mL) and dried with $MgSO_4$. The solvent was removed under rotary evaporation to yield the bromide as colorless plates which were suitable for SC-XRD (2.349 g, 91%). ^{1}H NMR (300 MHz, CD_2Cl_2): δ (ppm) 7.34-7.23 (m, 6H), 7.13-7.05 (m, 3H), 7.01 (d, J = 8.4 Hz, 4H), 4.52 (s, 4H). ^{13}C NMR (75 MHz, CD_2Cl_2): δ (ppm) 148.03, 147.41, 132.40, 130.55, 129.88, 125.72, 124.34, 124.00, 34.49.

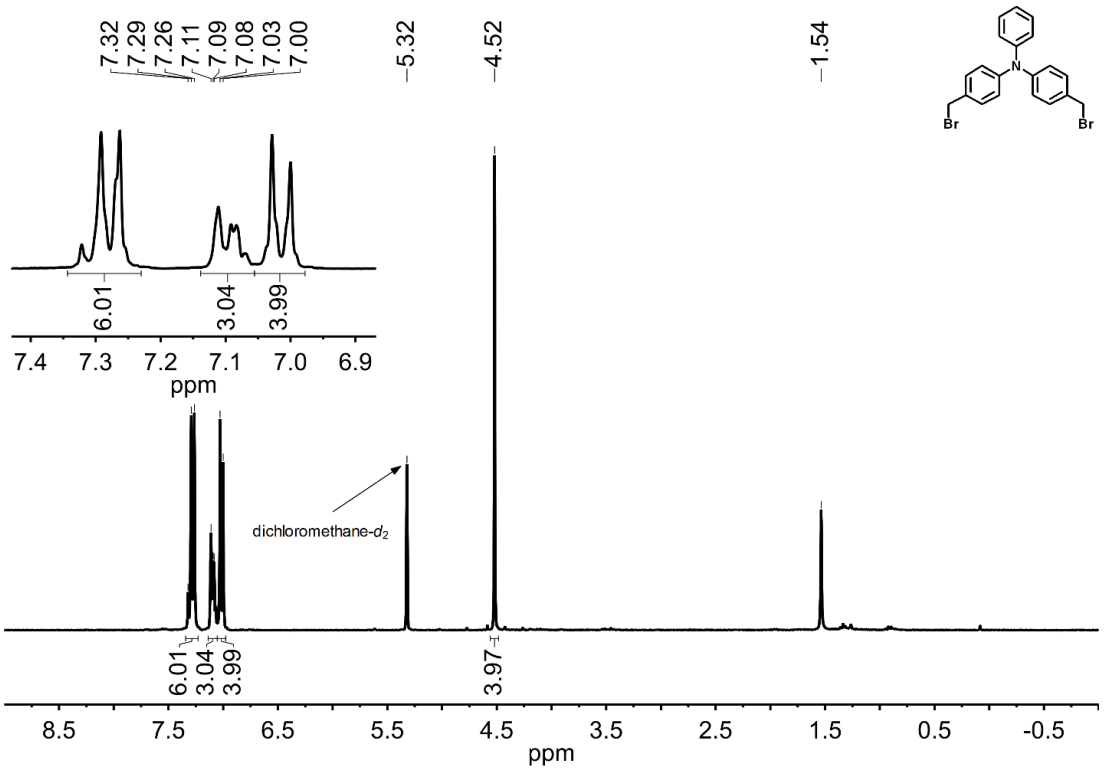

Figure 5.12. ^{1}H NMR of dibromide **1** (CD_2Cl_2, 300 MHz).

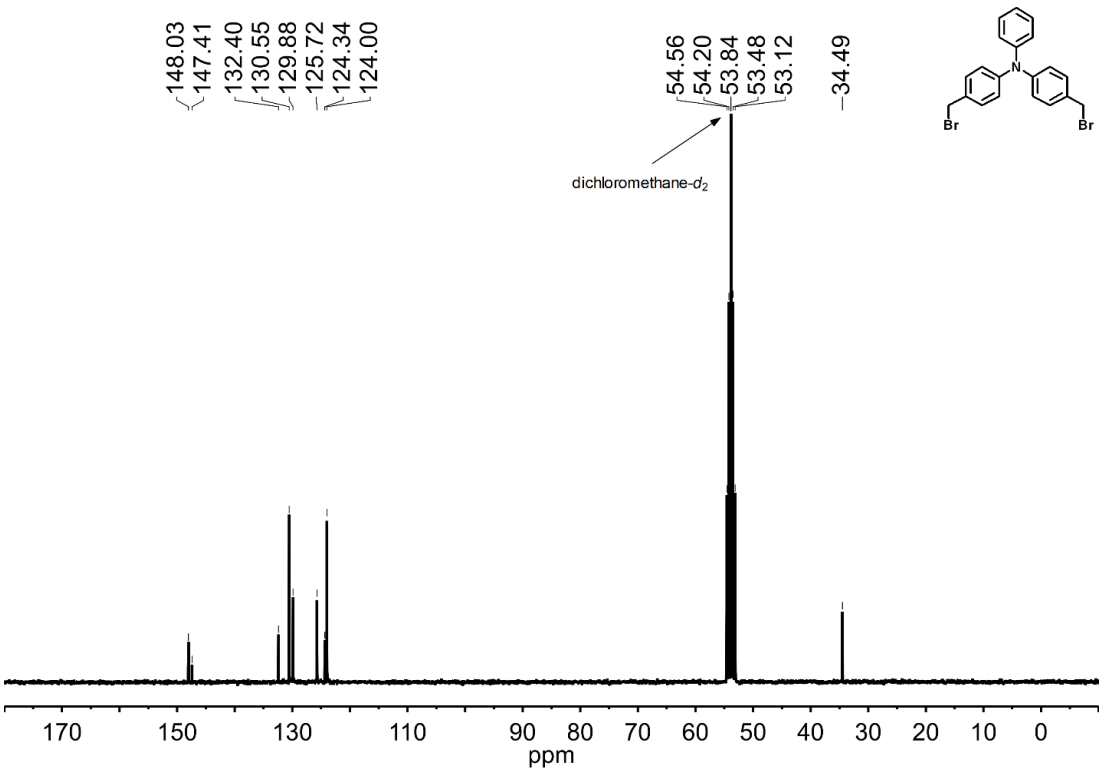

Figure 5.13. ^{13}C NMR of dibromide **1** (CD_2Cl_2, 75 MHz).

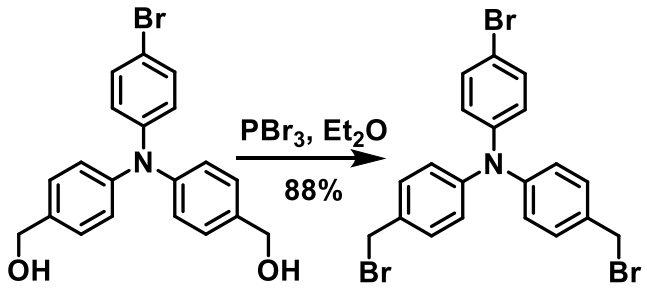

4-Bromo-*N*,*N*-*bis*(4-(bromomethyl)phenyl)aniline: Compound was made according to previous procedures.[40] The previous alcohol (2.568 g, 6.7 mmol) was suspended in 70 mL of dry diethyl ether and was cooled to 0 ˚C. Then a solution of phosphorus tribromide (761 μL, 8.0 mmol) in 10 mL dry diethyl ether was added dropwise over 5 minutes. The reaction stirred at room temperature overnight in the dark. In the morning, 80 mL ice cold water and 40 mL saturated aqueous $NaHCO_3$ were added to quench the reaction. The mixture was extracted with 80 mL of dichloromethane and the

organics were washed with brine (3 × 40 mL) and dried with $MgSO_4$. The solvent was removed under rotary evaporation to yield the bromide as a sticky solid (2.999 g, 88%). Spectra matched that as previously recorded.[40] ^{1}H NMR (300 MHz, CD_2Cl_2): δ (ppm) 7.38 (d, *J* = 8.7 Hz, 2H), 7.29 (d, *J* = 8.5 Hz, 4H), 7.02 (d, *J* = 8.5 Hz, 4H), 6.97 (d, *J* = 8.7 Hz, 2H), 4.51 (s, 4H).

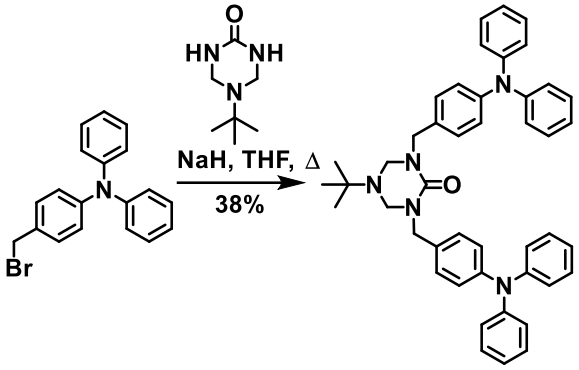

5-(*tert*-butyl)-1,3-*bis*(4-(diphenylamino)benzyl)-1,3,5-triazinan-2-one: *tert*-Butyl triazinanone (0.135 g, 0.9 mmol) and sodium hydride (60% suspension in paraffin oil, 0.103 g, 2.6 mmol) were suspended in 12 mL of dry tetrahydrofuran and was stirred for 5 minutes. Then the previous bromide (0.5778 g, 1.7 mmol) was added as a solution in 12 mL of dry tetrahydrofuran. The reaction stirred at reflux in the dark overnight. After cooling to room temperature, 4 mL of 1 N aqueous HCl and 4 mL of water were added to quench the reaction. This solution was extracted with dichloromethane (3 × 40 mL). The organics were washed with brine (1 × 40 mL) and dried with $MgSO_4$. The solvents were removed under rotary evaporation, and the product was isolated using column chromatography (Hexanes/Ethyl Acetate = 1:1) to yield the product as a sticky solid (0.218 g, 38%). ^{1}H NMR (300 MHz, $(CD_3)_2CO$): δ (ppm) 7.38-7.22 (m, 12H), 7.07-6.97 (m, 16H), 4.50 (s, 4H), 4.34 (s, 4H), 1.02 (s, 9H). ^{13}C NMR (75 MHz, $(CD_3)_2CO$): δ (ppm) 156.68,

148.83, 147.73, 134.77, 130.48, 130.16, 125.19, 124.63, 123.56, 62.34, 54.86, 48.37, 28.75. HRMS (DEP): [M+] calculated, 672.3697; found, 672.3699.

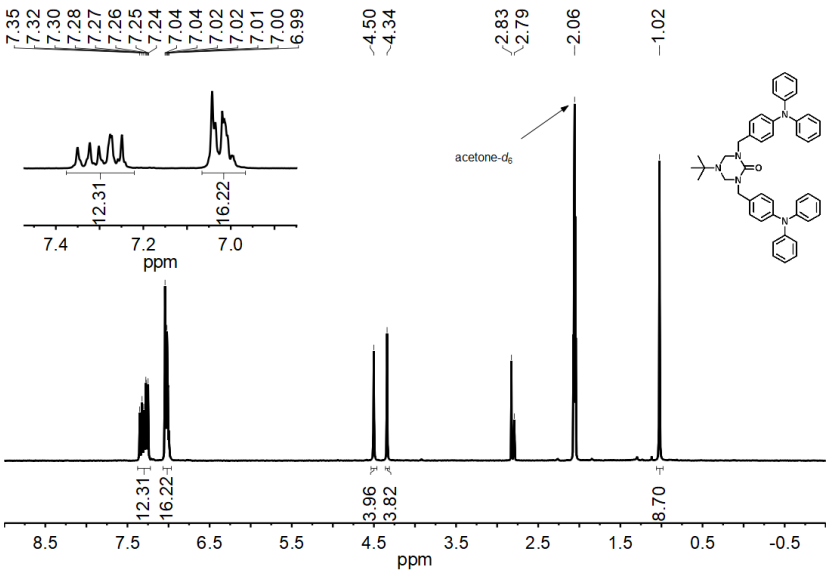

Figure 5.14. ^{1}H NMR protected **2** ($(CD_3)_2CO$, 300 MHz).

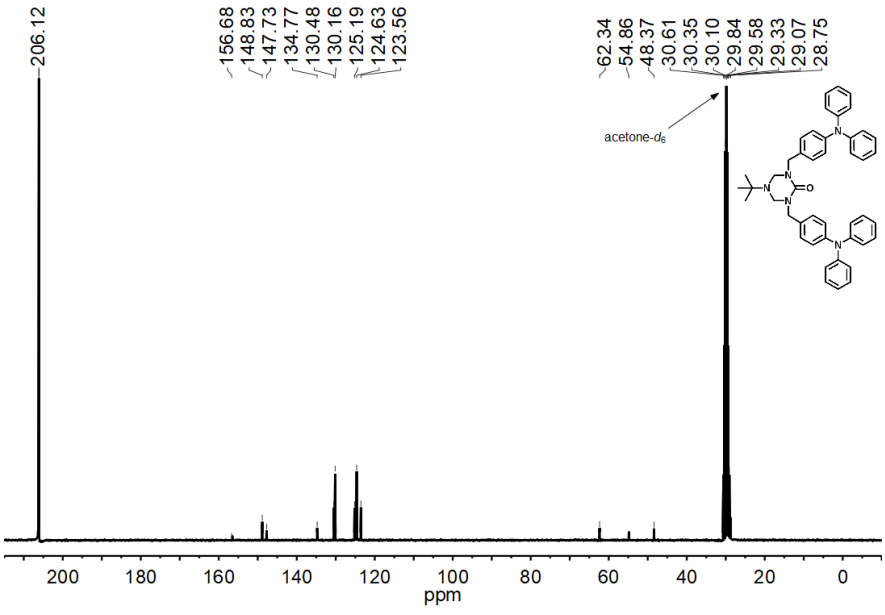

Figure 5.15. ^{13}C NMR protected **2** ($(CD_3)_2CO$, 75 MHz).

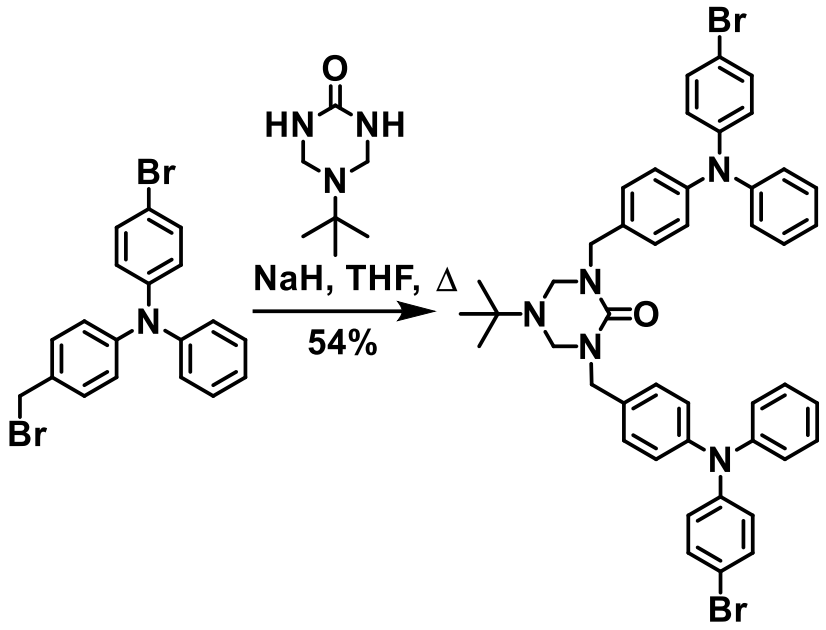

1,3-*bis*(4-((4-bromophenyl)(phenyl)amino)benzyl)-5-(*tert*-butyl)-1,3,5-triazinan-2-one: Compound was made according to previous procedures.[39] *tert*-Butyl triazinanone (0.209 g, 1.3 mmol) and sodium hydride (60% suspension in paraffin oil, 0.160 g, 4.0 mmol) were suspended in 20 mL of dry tetrahydrofuran and was stirred for 10 minutes. Then the previous bromide (1.111 g, 2.7 mmol) was added as a solution in 20 mL of dry tetrahydrofuran. The reaction stirred at reflux in the dark overnight. After cooling to room temperature, 6 mL of 1 N aqueous HCl and 6 mL of water were added to quench the reaction. This solution was extracted with dichloromethane (3 × 60 mL). The organics were washed with brine (1 × 60 mL) and dried with $MgSO_4$. The solvents were removed under rotary evaporation, and the product was isolated using column chromatography (Hexanes/Ethyl Acetate = 2:1) to yield the product as a sticky solid (0.596 g, 54%). Spectra was similar to that as previously recorded.[39] ^{1}H NMR (300 MHz, $CDCl_3$): δ (ppm) 7.35-7.19 (m, 12H), 7.09-6.99 (m, 10H), 6.92 (d, *J* = 8.9 Hz, 4H), 4.50 (s, 4H), 4.26 (s, 4H), 1.03 (s, 9H).

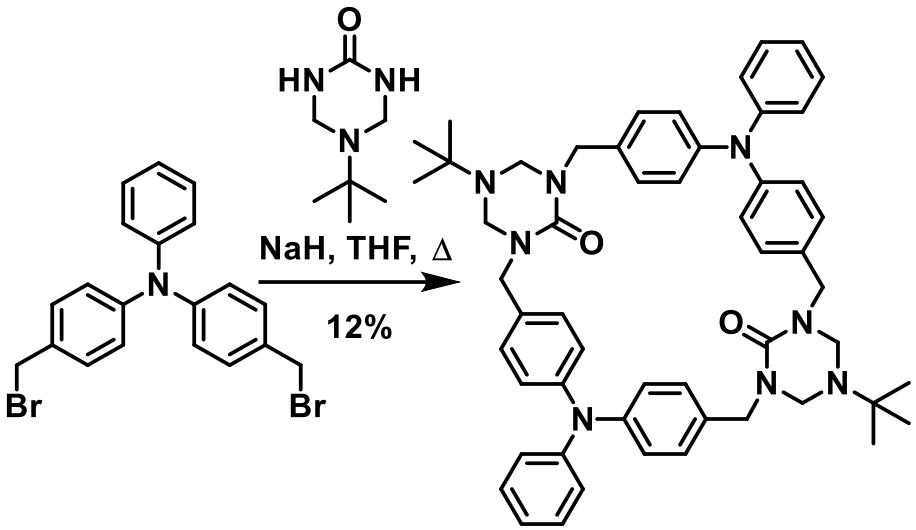

$1^5,7^5$-Di-*tert*-butyl-4,10-diphenyl-4,10-diaza-1,7(1,3)-ditriazinana3,5,9,11(1,4)-tetrabenzenacy-c-lododecaphane-$1^2,7^2$-dione: *tert*-Butyl triazinanone (1.148 g, 7.3 mmol) and sodium hydride (60% suspension in paraffin oil, 1.168 g, 7.3 mmol) were suspended in 285 mL of dry tetrahydrofuran and was stirred for 2 h at reflux. After cooling to room temperature, the previous bromide (3.149 g, 7.3 mmol) was added as a solution in 285 mL of dry tetrahydrofuran. The reaction stirred at reflux in the dark for 2 days. Upon completion, the reaction was quenched with 13 and 53 mL of 1N aqueous HCl and water then reduced *in vacuo* to 285 mL. An additional 40 mL 1N $HCl_{(aq)}$ and 173 mL of and water were added to the solution before it was extracted with dichloromethane (3 × 370 mL). The combined organic layers were washed with brine (1 × 370 mL) and dried with $MgSO_4$. The solvent was removed via rotary evaporation, and the material was recrystallized from chloroform. Vacuum drying the crystals yielded the product as a white powder (0.374 g, 12%). ^{1}H NMR (400 MHz, TCE-d_2, 90 ˚C): δ (ppm) 7.29 (t, J = 7.5 Hz, 4H), 7.23 (d, J = 8.0 Hz), 7.16 (d, J = 8.0 Hz, 4H), 7.06 (t, J = 7.1 Hz, 2H), 7.01 (d, J = 8.0 Hz, 8H) 4.47 (br, 8H), 4.29 (s, 8H), 0.85 (s, 18H). ^{13}C NMR (100 MHz, TCE-d_2, 90 ˚C): δ

(ppm) 155.33, 147.34, 147.18, 132.41, 129.68, 129.03, 124.15, 123.74, 122.75, 60.53, 54.07, 47.19, 27.99. HRMS (DEP): [M+] calculated, 853.4912; found, 853.4935.

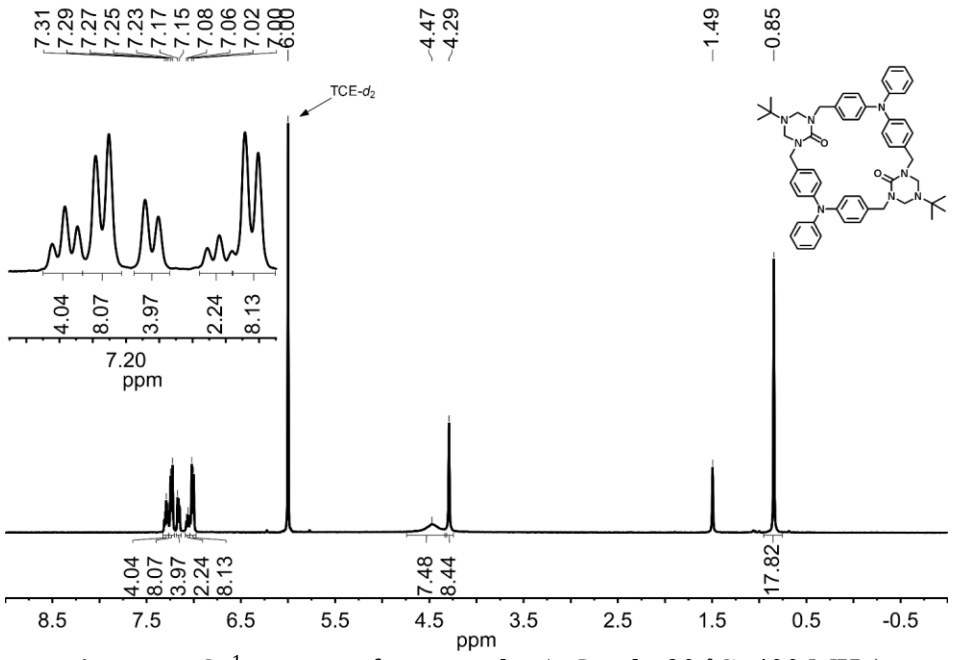

Figure 5.16. ^{1}H NMR of protected **1** (TCE-d_2, 90 ˚C, 400 MHz).

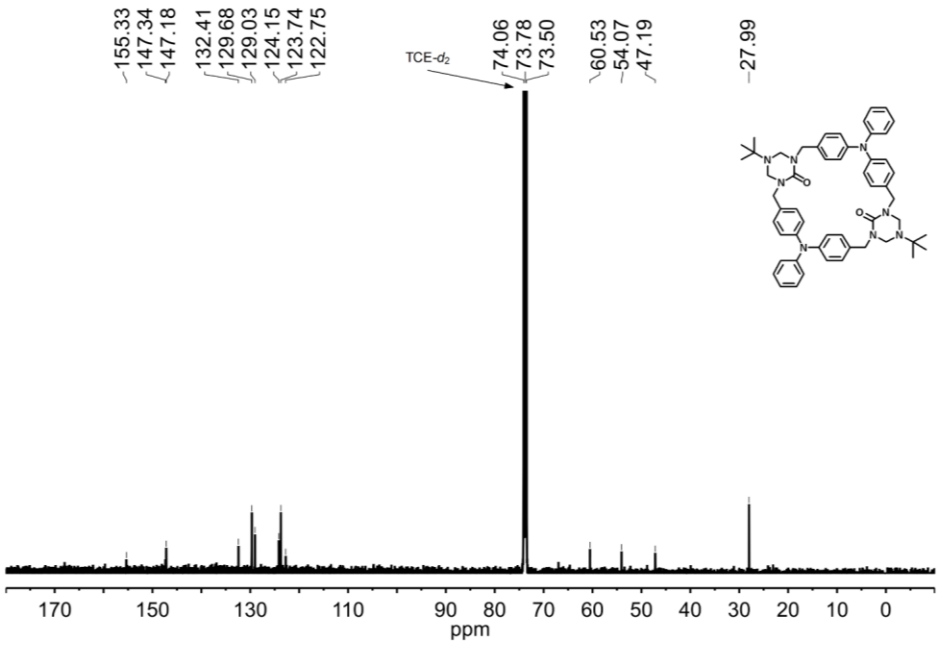

Figure 5.17. ^{13}C NMR of protected **1** (TCE-d_2, 90 ˚C, 100 MHz).

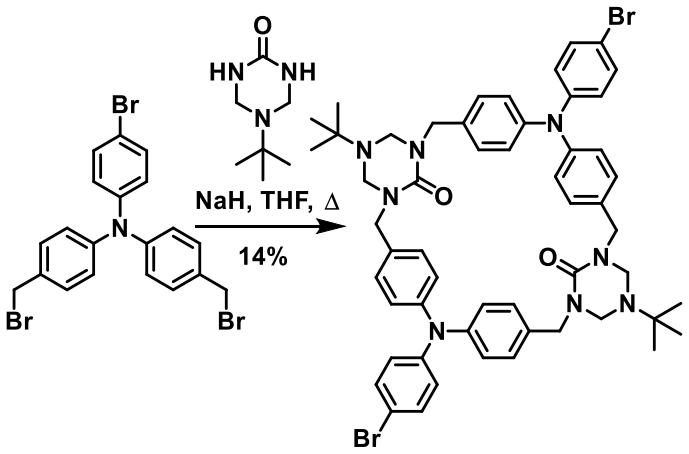

4,10-*bis*(4-Bromophenyl)-1^5,7^5-di-*tert*-butyl-4,10-diaza-1,7(1,3)-ditriazinana-3,5,-9,11(1,4)-tetr-abenzenacyclododecaphane-1^2,7^2-dione: Compound was made according to previous procedure.[40] *tert*-Butyl triazinanone (3.13 g, 6.1 mmol) and sodium hydride (60% suspension in paraffin oil, 0.983 g, 24.6 mmol) were suspended in 250 mL of dry tetrahydrofuran and was stirred for 2 h at reflux. After cooling to room temperature, the previous bromide (3.134 g, 6.1 mmol) was added as a solution in 250 mL of dry tetrahydrofuran. The reaction stirred at reflux in the dark for 2 days. Upon completion, the reaction was quenched with 12 mL of 1N aqueous HCl and 45 mL of water and was then reduced *in vacuo* to 330 mL. An additional 30 mL of 1N aqueous HCl and 140 mL of water were added to the solution before it was extracted with dichloromethane (3 × 300 mL). The combined organic layers were washed with brine (1 × 300 mL) and dried with $MgSO_4$. The solvent was removed via rotary evaporation, and then the material was recrystallized from chloroform. Vacuum drying the crystals yielded the product as a white powder (0.435 g, 14%). Spectra was similar to that as previously recorded.[40] ^{1}H NMR (300 MHz, CD_2Cl_2): δ (ppm) 7.33 (d, *J* = 8.7 Hz, 4H), 7.22 (d, 8.2 Hz, 8H), 7.02-6.91 (m, 12H), 4.44 (br, 8H), 4.22 (s, 8H), 0.73 (s, 18H).

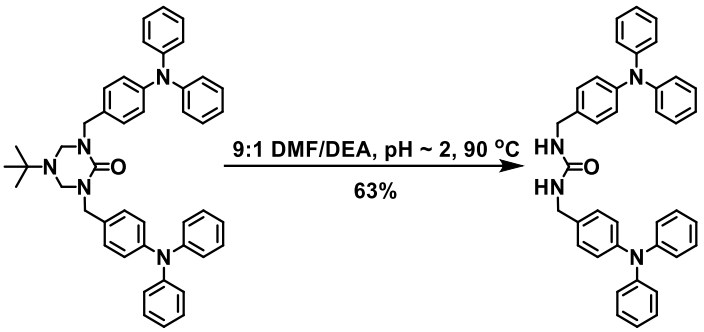

1,3-*bis*(4-(Diphenylamino)benzyl)urea: The previous protected urea (0.211 g, 0.4 mmol) was suspended in 100 mL of a 9:1 solution of *N*, *N*-dimethylformamide and diethanol amine and the pH was adjusted to 2 using 12 M aqueous HCl. This mixture was heated at 90 ˚C for 2 days in the dark. The pH was readjusted to 2 using 12 M aqueous HCl every 12 h until completion. After cooling to room temperature, 400 mL of water was added and the reaction was filtered. The residue was washed with 50 mL of water leaving behind the product as a beige solid (0.114 g, 63%). ^{1}H NMR (300 MHz, CD_2Cl_2): δ (ppm) 7.26-7.13 (m, 12H), 7.06-6.96 (m, 16H), 4.69 (t, *J* = 5.6 Hz, 2H), 4.31 (d, *J* = 5.8 Hz, 4H). ^{13}C NMR (75 MHz, $CDCl_3$): δ (ppm) 158.04, 147.85, 147.29, 133.19, 129.38, 128.54, 124.32, 124.24, 122.94, 44.48. HRMS (DEP): [M+] calculated, 575.2805 found, 575.2801.

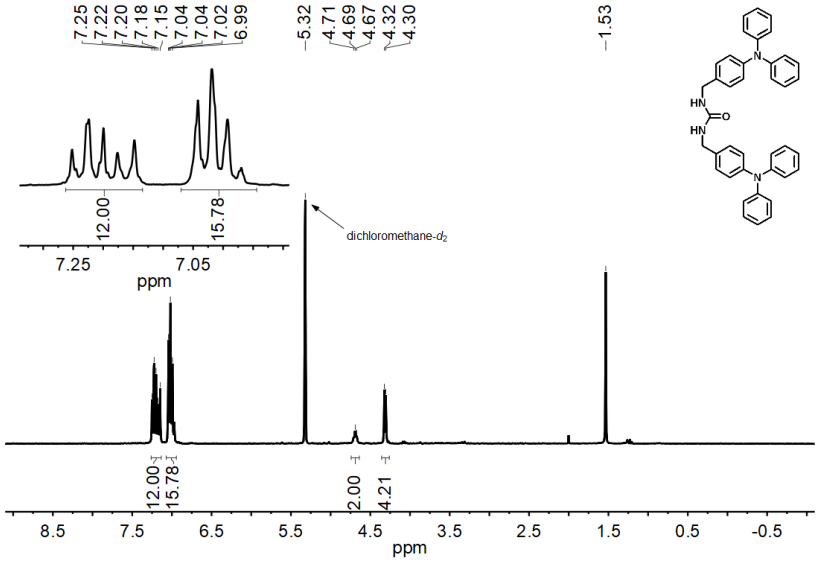

Figure 5.18. ^{1}H NMR linear analog **2** (CD_2Cl_2, 300 MHz).

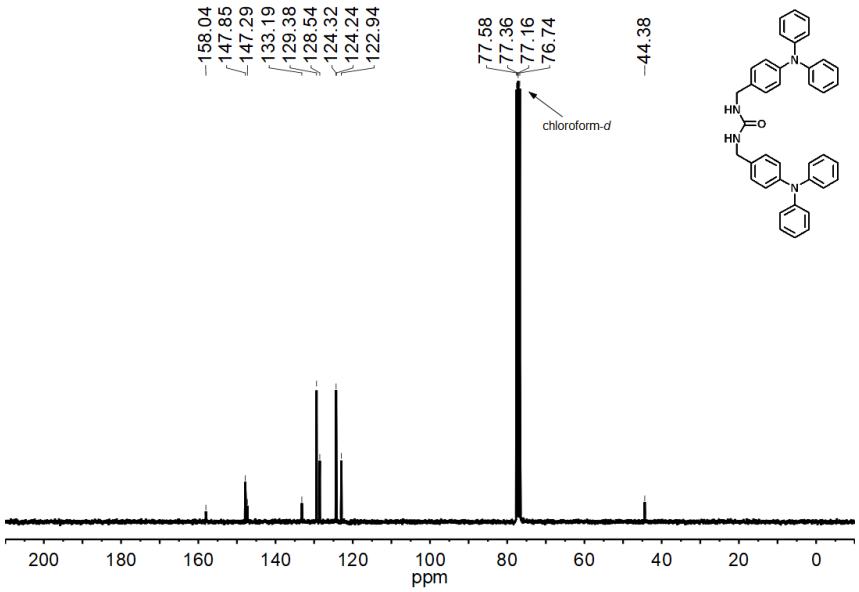

Figure 5.19. ^{13}C NMR linear analog **2** ($CDCl_3$, 75 MHz).

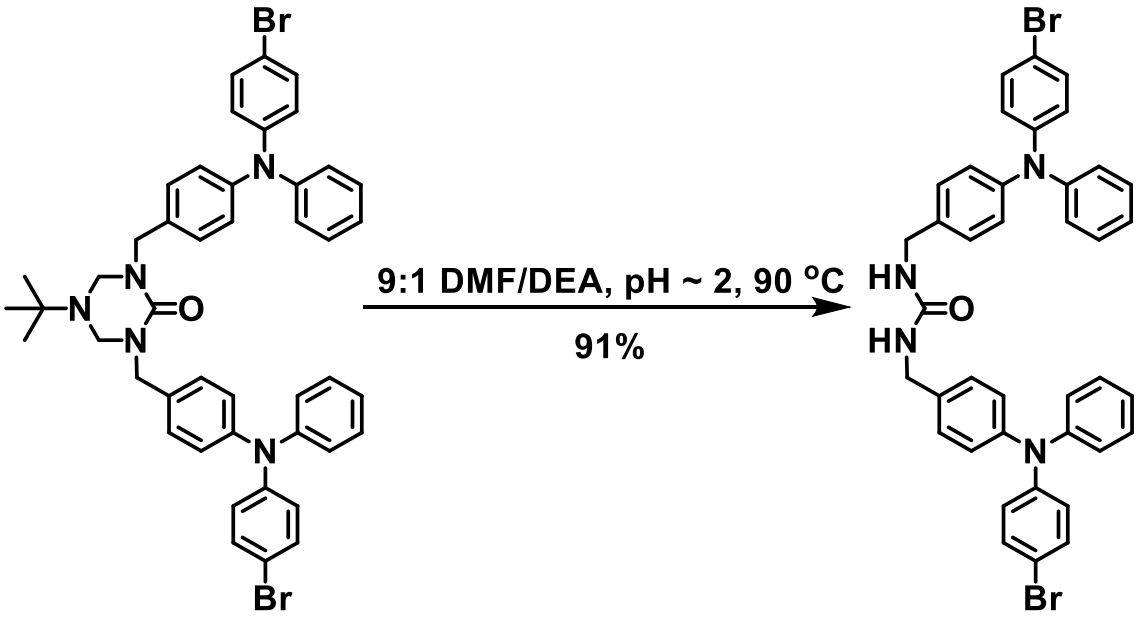

1,3-*bis*(4-((4-bromophenyl)(phenyl)amino)benzyl)urea: Compound was made according to previous procedure.[39] The previous protected urea (0.100 g, 0.1 mmol) was suspended in 50 mL of a 9:1 solution of *N, N*-dimethylformamide and diethanol amine and the pH was adjusted to 2 using 12 M aqueous HCl. This mixture was heated at 90 ˚C for 2 days in the dark. The pH was readjusted to 2 using 12 M aqueous HCl every 12 h until

completion. After cooling to room temperature, the solution was neutralized with aqueous $NaHCO_3$, and was diluted to 500 mL with water. The resulting suspension was filtered, and the residue was washed with 50 mL of water leaving behind the product as a beige solid (0.080 g, 91%). The spectra was similar to that as previously recorded.[39] ^{1}H NMR (300 MHz, $(CD_3)SO_2$): δ (ppm) 7.40 (d, *J* = 8.8 Hz, 4H), 7.29 (t, *J* = 7.8 Hz, 4H), 7.20 (d, *J* = 8.4 Hz, 4H), 7.09-6.95 (m, 10H), 6.85 (d, 8.8 Hz, 4H), 6.43 (t, *J* = 5.9 Hz, 2H), 4.19 (d, *J* = 5.8 Hz, 4H).

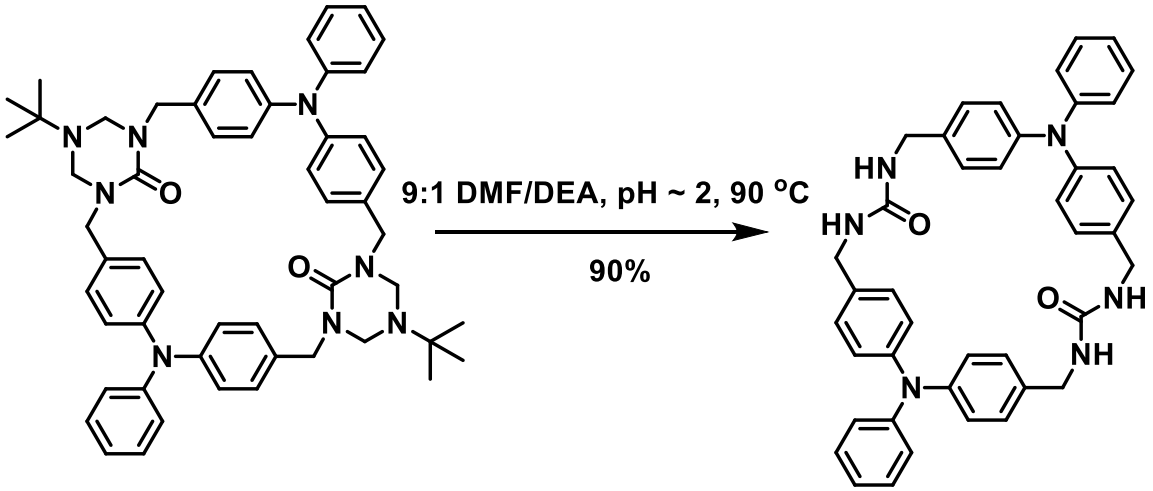

2,10-Diphenyl-2,5,7,10,13,15-hexaaza-1,3,9,11(1,4)-tetrabenzenacyclohexadeca-phane-6,14-dione: The previous protected urea (0.026 g, 0.03 mmol) was dissolved in 30 mL of a 9:1 solution of DMF and diethanol amine the pH was adjusted to 2 using 12 M aqueous HCl. This mixture was heated at reflux for three days in the dark. During this time the pH was recalibrated to 2 every 12 h. After cooling to room temperature, the reaction was neutralized with saturated aqueous $NaHCO_3$ and diluted to 210 mL using water. The solution was filtered washed with 50 mL of water then acetonitrile leaving behind the product as a beige solid (0.018 g, 90%). ^{1}H NMR (300 MHz, $(CD_3)_2SO$): δ (ppm) 7.25 (t, *J* = 7.7 Hz, 4H), 7.13 (d, *J* = 8.4 Hz, 8H), 7.03-6.86 (m, 14H) 6.50 (t, *J* = 6.2 Hz, 4H), 4.18

(d, J = 6.1 Hz, 8H). ^{13}C NMR (75 MHz, $(CD_3)_2SO$): δ (ppm) 157.83, 147.48, 145.79, 135.90, 129.39, 127.95, 123.50, 123.37, 122.52, 42.08.

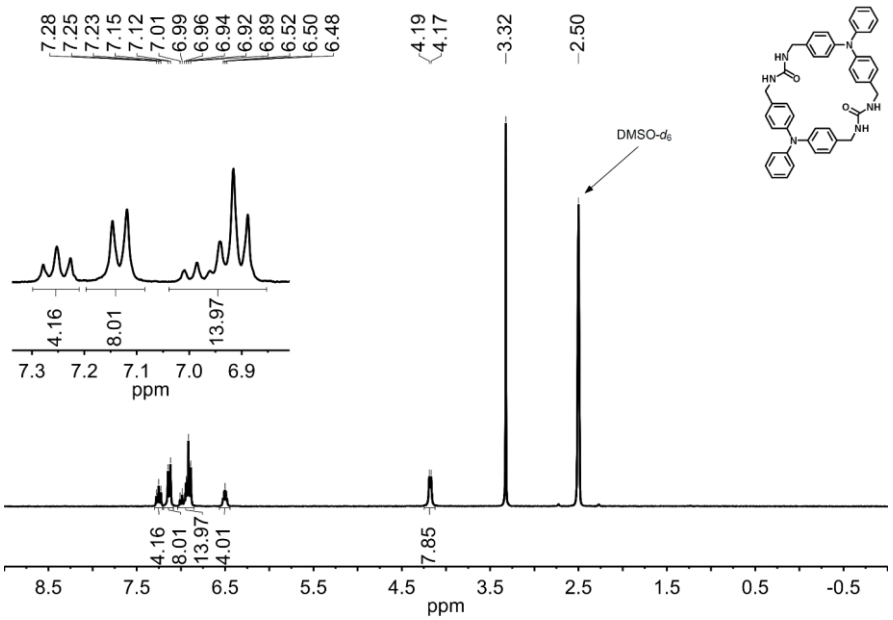

Figure 5.20. ^{1}H NMR of macrocycle **1** ($(CD_3)_2SO$, 300 MHz).

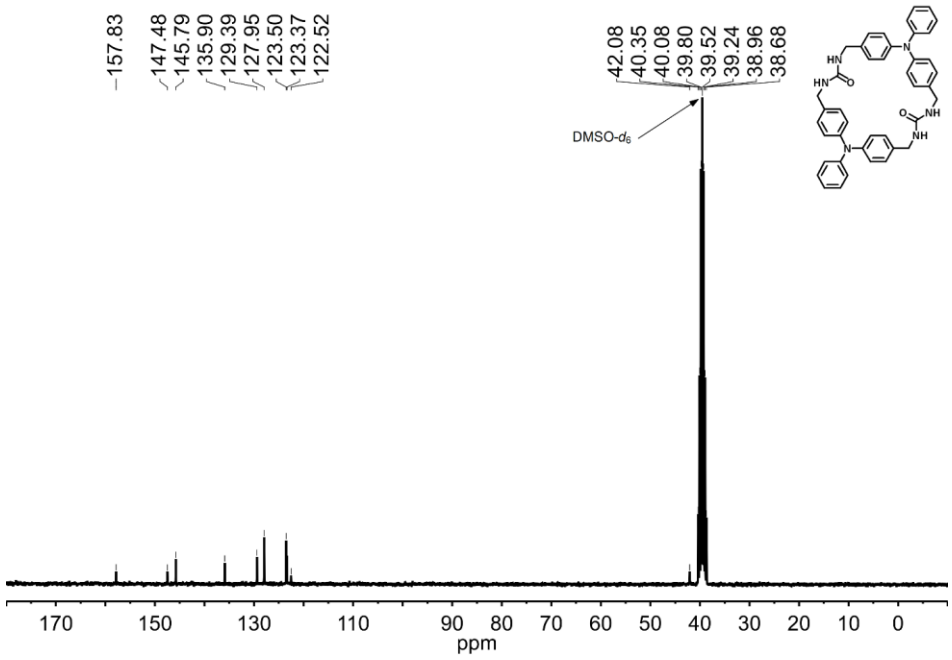

Figure 5.21. ^{13}C NMR of macrocycle **1** ($(CD_3)_2SO$, 75 MHz).

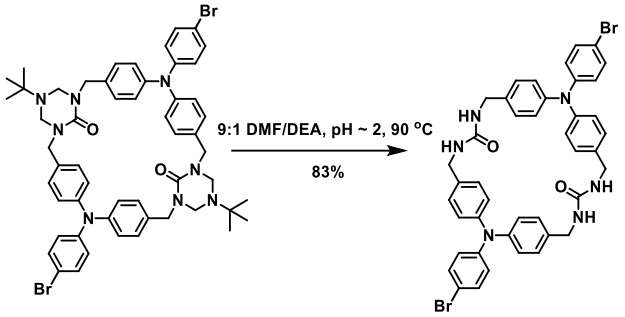

2,10-*bis*(4-Bromophenyl)-2,5,7,10,13,15-hexaaza-1,3,9,11(1,4)tetrabenzenacyclo-hexadecaph-ane-6,14-dione: The previous protected urea (0.225 g, 0.22 mmol) was dissolved in 225 mL of a 9:1 solution of DMF and diethanol amine the pH was adjusted to 2 using 12 M aqueous HCl. This mixture was heated at reflux for three days in the dark. During this time the pH was recalibrated to 2 every 12 h. After cooling to room temperature, the reaction was neutralized with saturated aqueous $NaHCO_3$ and diluted to 1 L using water. The solution was filtered washed with water leaving behind the product as a beige solid (0.151 g, 83%). Spectra matched that as previously recorded.[40] ^{1}H NMR (300 MHz, $(CD_3)_2SO$): δ (ppm) 7.38 (d, *J* = 8.8 Hz, 4H), 7.15 (d, *J* = 8.3 Hz, 8H), 6.93 (d, *J* = 8.4 Hz, 8H), 6.82 (d, *J* = 8.7 Hz, 4H), 6.53 (t, *J* = 6.2 Hz, 4H), 4.18 (d, *J* = 5.9 Hz, 8H).

5.4.3 Crystal Data and Structure Refinement

Table 5.3. Data Collection and Refinement for Macrocycle **1** Related Compounds.

Identification Code	Dibromide 1	Protected 1·$(CHCl_3)_4$	Protected 1·$(MeOH)_2$	1·DMSO
CCDC	1961251	1961244	1961245	1961246
Color of Crystal	$C_{20}H_{17}NBr_2$	$C_{58}H_{64}Cl_{12}N_8O_2$	$C_{56}H_{68}N_8O_4$	$C_{44}H_{44}N_6O_3S$
Empirical formula	431.17	1330.57	917.18	736.91
Formula weight	100(2)	100(2)	100(2)	100(2)
Temperature/K	monoclinic	triclinic	triclinic	monoclinic
Crystal system	$P2_1/c$	P-1	P-1	$P2_1/n$
Space group	8.1537(4)	10.0428(5)	9.4489(11)	13.2794(5)
a/Å	12.3944(6)	12.0048(7)	12.1817(13)	9.6773(4)

b/Å	17.4953(8)	13.6585(8)	12.3451(14)	28.5236(11)
c/Å	90	76.855(2)	63.821(4)	90
α/deg	102.0490(10)	83.018(2)	76.099(5)	93.197(2)
β/deg	90	79.682(2)	87.623(5)	90
γ/deg	1729.13(14)	1571.99(15)	1234.5(2)	3659.8(2)
Volume/Å^3	4	1	1	4
Z	1.656	1.406	1.234	1.337
ρ_{calc}g/cm^3	4.687	0.577	0.079	0.140
μ/mm^{-1}	856.0	688.0	492.0	1560.0
F(000)	0.18 × 0.16 × 0.06	0.52 × 0.46 × 0.36	0.56 × 0.48 × 0.42	0.2 × 0.08 × 0.06
Crystal size/mm^3	MoKα (λ = 0.71073)	MoKα (λ = 0.71073)	MoKα (λ = 0.71073)	MoKα (λ = 0.71073)
Radiation	4.762 to 52.324	4.942 to 56.63	4.454 to 56.718	4.446 to 48.592
2Θ range for data collection/deg	-10 ≤ h ≤ 10, -15 ≤ k ≤ 15, -21 ≤ l ≤ 21	-13 ≤ h ≤ 13, -15 ≤ k ≤ 15, -18 ≤ l ≤ 18	-12 ≤ h ≤ 12, -16 ≤ k ≤ 16, -16 ≤ l ≤ 16	-15 ≤ h ≤ 15, 0 ≤ k ≤ 11, 0 ≤ l ≤ 33
Index ranges	41775	61229	34422	9387
Reflections collected	3442 [R_{int} = 0.0481, R_{sigma} = 0.0251]	7782 [R_{int} = 0.0366, R_{sigma} = 0.0250]	6165 [R_{int} = 0.0432, R_{sigma} = 0.0373]	9387 [R_{int} = 0.0466, R_{sigma} = 0.0827]
Independent reflections	3442/0/208	7782/15/389	6165/4/343	9387/6/512
Data/restraints/parameters	1.058	1.033	1.026	1.046
Goodness-of-fit on F^2	R_1 = 0.0441, wR_2 = 0.1086	R_1 = 0.0460, wR_2 = 0.1227	R_1 = 0.0419, wR_2 = 0.0926	R_1 = 0.0629, wR_2 = 0.1259
Final R indexes [I ≥ 2σ (I)]	R_1 = 0.0579, wR_2 = 0.1146	R_1 = 0.0613, wR_2 = 0.1319	R_1 = 0.0664, wR_2 = 0.1026	R_1 = 0.1213, wR_2 = 0.1456
Final R indexes [all data]	2.45/-0.85	1.06/-0.68	0.27/-0.22	0.31/-0.30

Table 5.4. Data Collection and Refinement for Macrocycle **2** Related Compounds.

Identification Code	**1a·(1,4-dioxanes)$_{0.58}$**	**1a·(DMF)$_{0.65}$**
CCDC	1961243	1961242
Color of Crystal	$C_{44.34}H_{40.66}Br_2N_6O_{3.17}$	$C_{43.95}H_{40.56}Br_2N_{6.65}O_{2.65}$
Empirical formula	867.97	864.16
Formula weight	100(2)	100(2)
Temperature/K	monoclinic	monoclinic
Crystal system	$P2_1/c$	$P2_1/c$
Space group	15.838(2)	15.8837(16)
a/Å	4.6056(6)	4.6117(5)
b/Å	26.637(3)	26.786(3)
c/Å	90	90
α/deg	99.746(3)	100.216(2)
β/deg	90	90
γ/deg	1915.0(4)	1931.0(3)
Volume/Å^3	2	2

Z	1.505	1.486
ρ_{calc}g/cm^3	2.168	2.149
μ/mm^{-1}	888.0	884.0
F(000)	0.12 × 0.05 × 0.02	0.16 × 0.06 × 0.04
Crystal size/mm^3	MoKα (λ = 0.71073)	MoKα (λ = 0.71073)
Radiation	4.38 to 50.364	4.382 to 50.082
2Θ range for data collection/deg	-18 ≤ h ≤ 18, -5 ≤ k ≤ 5, -31 ≤ l ≤ 31	-18 ≤ h ≤ 18, -5 ≤ k ≤ 5, -31 ≤ l ≤ 31
Index ranges	19443	17340
Reflections collected	3429 [R_{int} = 0.0470, R_{sigma} = 0.0291]	3413 [R_{int} = 0.0617, R_{sigma} = 0.0405]
Independent reflections	3429/35/277	3413/11/261
Data/restraints/parameters	1.102	1.045
Goodness-of-fit on F^2	R_1 = 0.0467, wR_2 = 0.0995	R_1 = 0.0470, wR_2 = 0.0971
Final R indexes [I ≥ 2σ (I)]	R_1 = 0.0617, wR_2 = 0.1079	R_1 = 0.0666, wR_2 = 0.1051
Final R indexes [all data]	0.53/-0.68	0.76/-0.56

Table 5.5. Data Collection and Refinement for Macrocycle **2** Related Compounds.

Identification Code	**2**	**Triclinic Polymorph of 3a**	**Monoclinic Polymorph of 3a**	**4**
CCDC	1961250	1961247	1961248	1961249
Color of Crystal	$C_{39}H_{34}N_4O$	$C_{18}H_{14}BrN$	$C_{18}H_{14}NBr$	$C_{20}H_{19}N_3O$
Empirical formula	574.70	324.21	324.21	317.38
Formula weight	100(2)	100(2)	100(2)	100(2)
Temperature/K	orthorhombic	triclinic	monoclinic	monoclinic
Crystal system	Pbcn	P-1	$P2_1/c$	$P2_1/c$
Space group	35.075(2)	9.9285(5)	7.8591(5)	12.9146(18)
a/Å	9.9908(6)	12.2758(6)	18.1807(11)	13.9280(19)
b/Å	8.8263(6)	12.5370(6)	10.0050(6)	9.4512(13)
c/Å	90	98.954(2)	90	90
α/deg	90	90.731(2)	91.477(2)	110.841(4)
β/deg	90	106.446(2)	90	90
γ/deg	3093.0(3)	1445.03(12)	1429.08(15)	1588.8(4)
Volume/Å^3	4	4	4	4
Z	1.234	1.490	1.507	1.327
ρ_{calc}g/cm^3	0.075	2.833	2.865	0.084
μ/mm^{-1}	1216.0	656.0	656.0	672.0
F(000)	0.28 × 0.14 × 0.05	0.4 × 0.16 × 0.08	0.5 × 0.32 × 0.22	0.8 × 0.46 × 0.01

Crystal size/mm^3	MoKα (λ = 0.71073)	MoKα (λ = 0.71073)	MoKα (λ = 0.71073)	MoKα (λ = 0.71073)
Radiation	4.646 to 48.956	4.286 to 63.35	4.48 to 63.094	4.466 to 50.462
2Θ range for data collection/deg	-40 ≤ h ≤ 40, -11 ≤ k ≤ 11, -10 ≤ l ≤ 10	-14 ≤ h ≤ 14, -18 ≤ k ≤ 18, -18 ≤ l ≤ 18	-11 ≤ h ≤ 11, -26 ≤ k ≤ 26, -14 ≤ l ≤ 14	-15 ≤ h ≤ 15, -15 ≤ k ≤ 16, -11 ≤ l ≤ 11
Index ranges	41755	72155	36454	28771
Reflections collected	2541 [R_{int} = 0.0772, R_{sigma} = 0.0401]	9692 [R_{int} = 0.0341, R_{sigma} = 0.0200]	4785 [R_{int} = 0.0323, R_{sigma} = 0.0181]	2851 [R_{int} = 0.0786, R_{sigma} = 0.0433]
Independent reflections	2541/7/227	9692/0/367	4785/0/182	2851/0/230
Data/restraints/parameters	1.125	1.086	1.018	1.017
Goodness-of-fit on F^2	R_1 = 0.0639, wR_2 = 0.1422	R_1 = 0.0362, wR_2 = 0.0893	R_1 = 0.0245, wR_2 = 0.0604	R_1 = 0.0438, wR_2 = 0.0984
Final R indexes [I ≥ 2σ (I)]	R_1 = 0.0881, wR_2 = 0.1524	R_1 = 0.0430, wR_2 = 0.0922	R_1 = 0.0293, wR_2 = 0.0626	R_1 = 0.0761, wR_2 = 0.1120
Final R indexes [all data]	0.21/-0.17	1.38/-1.29	0.47/-0.51	0.29/-0.20

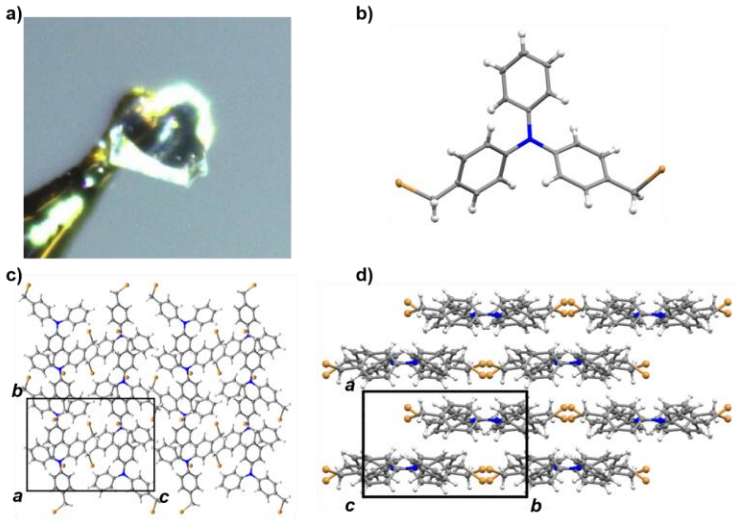

Figure 5.22. Crystal views of dibromide **1**. (a) Data crystal. (b) Molecular structure of the dibromide **1**. Thermal ellipsoids were drawn at the 30% probability level. (c) Crystal packing along the *a* axis. (e) Crystal packing along the *c* axis.

X-ray intensity data from a colorless plate were collected at 100(2) K using a Bruker D8 QUEST diffractometer equipped with a PHOTON-100 CMOS area detector and an Incoatec microfocus source (Mo Kα radiation, λ = 0.71073 Å). The raw area detector data frames were reduced and corrected for absorption effects using the Bruker APEX3, SAINT+ and SADABS programs.[58,59] Final unit cell parameters were determined by least-squares refinement of 9959 reflections taken from the data set. The structure was

solved with SHELXT.[60,61] Subsequent difference Fourier calculations and full-matrix least-squares refinement against F^2 were performed with SHELXL-2017[60,61] using OLEX2.[62]

The compound crystallizes in the monoclinic system. The pattern of systematic absences in the intensity data was consistent with the space group $P2_1/c$, which was confirmed by structure solution. The asymmetric unit consists of one molecule. All non-hydrogen atoms were refined with anisotropic displacement parameters. Hydrogen atoms bonded to carbon were located in Fourier difference maps before being placed in geometrically idealized positions and included as riding atoms with *d*(C-H) = 0.95 Å and *U*iso(H) = 1.2*U*eq(C) for arene hydrogen atoms and *d*(C-H) = 0.99 Å and *U*iso(H) = 1.2*U*eq(C) for methylene hydrogen atoms. The largest residual electron density peak in the final difference map is +2.45 e-/Å^3, located 2.13 Å from H4.

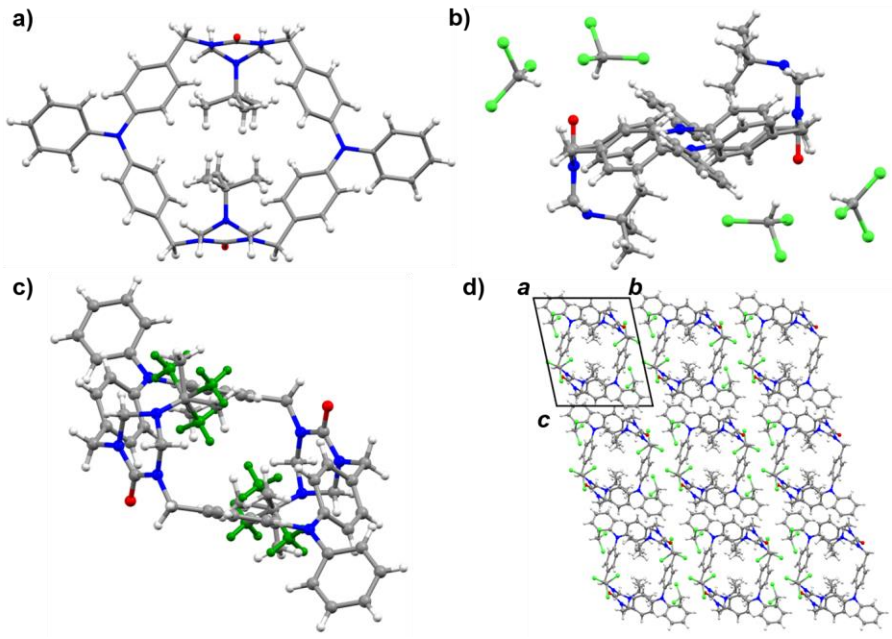

Figure 5.23. Crystal views of (protected macrocycle **1**)·$(CHCl_3)_4$. (a) Molecular structure of protected macrocycle **1** (disorder omitted for clarity). Thermal ellipsoids were drawn at the 30% probability level. (b) One unit cell (disorder omitted for clarity). (c) View showing disorder in the *tert*-butyl groups. The major component population fraction (non-green) was 0.697(6). (d) Crystal packing along the *a* axis.

X-ray intensity data from a colorless block were collected at 100(2) K using a Bruker D8 QUEST diffractometer equipped with a PHOTON-100 CMOS area detector and an Incoatec microfocus source (Mo Kα radiation, λ = 0.71073 Å). The raw area detector data frames were reduced and corrected for absorption effects using the Bruker APEX3, SAINT+ and SADABS programs.[58,59] Final unit cell parameters were determined by least-squares refinement of 9923 reflections taken from the data set. The structure was solved with SHELXT.[60,61] Subsequent difference Fourier calculations and full-matrix least-squares refinement against F^2 were performed with SHELXL-2018[60,61] using OLEX2.[62]

The compound crystallizes in the triclinic system. The space group *P*-1 (No. 2) was confirmed by structure solution. The asymmetric unit consists of half of one $C_{54}H_{60}N_8O_2$ molecule located on a crystallographic inversion center and two independent chloroform molecules. The unique *tert*-butyl substituent of the $C_{54}H_{60}N_8O_2$ molecule is rotationally disordered over two orientations. The major component population fraction is 0.697(6). C-C distances in the disordered *t*-butyl groups were restrained to be similar to one another (SHELX SADI). All non-hydrogen atoms were refined with anisotropic displacement parameters. Hydrogen atoms bonded to carbon were before being placed in geometrically idealized positions and included as riding atoms with *d*(C-H) = 1.00 Å and *U*iso(H) = 1.2*U*eq(C) for methine hydrogen atoms, *d*(C-H) = 0.95 Å and *U*iso(H) = 1.2*U*eq(C) for aromatic hydrogen atoms, *d*(C-H) = 0.99 Å and *U*iso(H) = 1.2*U*eq(C) for methylene hydrogen atoms, and *d*(C-H) = 0.98 Å and *U*iso(H) = 1.5*U*eq(C) for methyl hydrogens. The methyl hydrogens were allowed to rotate as a rigid group to the orientation of maximum observed electron density. The largest residual electron density peak in the final difference map is 1.06 e-/Å^3, located 0.99 Å from Cl6.

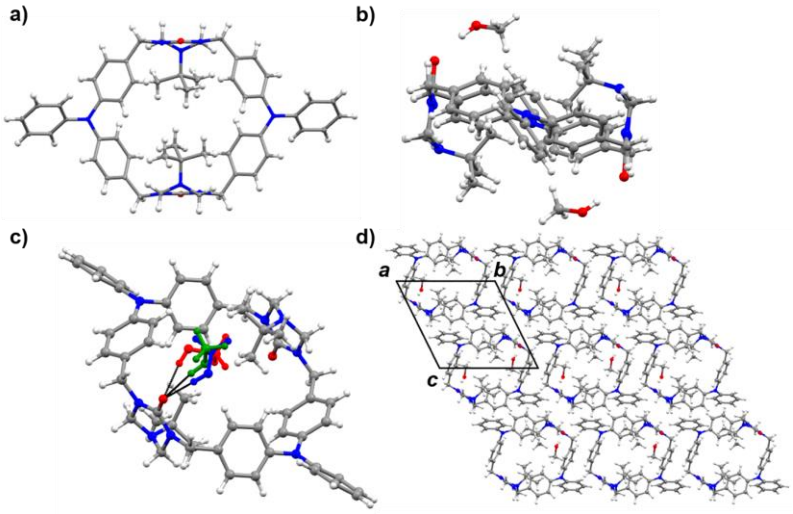

Figure 5.24. Crystal views of (protected macrocycle **1**)·$(MeOH)_2$. (a) Molecular structure of protected macrocycle **1**. Thermal ellipsoids were drawn at the 30% probability level. (b) One formula unit (disorder omitted for clarity). (c) View showing disorder in the methanol solvate. Hydrogen bonds are shown in black. (d) Crystal packing along the *a* axis (disorder omitted for clarity).

X-ray intensity data from an irregular colorless block were collected at 100(2) K using a Bruker D8 QUEST diffractometer equipped with a PHOTON-100 CMOS area detector and an Incoatec microfocus source (Mo Kα radiation, λ = 0.71073 Å). The raw area detector data frames were reduced and corrected for absorption effects using the Bruker APEX3, SAINT+ and SADABS programs.[58,59] Final unit cell parameters were determined by least-squares refinement of 9916 reflections taken from the data set. The structure was solved with SHELXT.[60,61] Subsequent difference Fourier calculations and full-matrix least-squares refinement against F^2 were performed with SHELXL-2018[60,61] using OLEX2.[62]

The compound crystallizes in the triclinic system. The space group *P*-1 (No. 2) was confirmed by structure solution. The asymmetric unit consists of half of one $C_{54}H_{60}N_8O_2$ molecule and one methanol molecule. The $C_{54}H_{60}N_8O_2$ molecule is located on a crystallographic inversion center. The methanol molecule is positionally disordered and

was modeled using three components. Total component occupancy was constrained to sum to one, and refined to O1S/O2S/O3S = 0.577(2)/0.346(2)/0.077(2). Methanol C-O distances were restrained to 1.45(2) Å. All non-hydrogen atoms were refined with anisotropic displacement parameters. Hydrogen atoms were placed in geometrically idealized positions and included as riding atoms with *d*(O-H) = 0.84 Å and *U*iso(H) = 1.5*U*eq(O) for hydrogen atoms bonded to oxygen, *d*(C-H) = 0.95 Å and *U*iso(H) = 1.2*U*eq(C) for aromatic hydrogen atoms, *d*(C-H) = 0.99 Å and *U*iso(H) = 1.2*U*eq(C) for methylene hydrogen atoms, and *d*(C-H) = 0.98 Å and *U*iso(H) = 1.5*U*eq(C) for methyl hydrogens. The methyl hydrogens were allowed to rotate as a rigid group to the orientation of maximum observed electron density. The largest residual electron density peak in the final difference map is 0.27 e-/Å^3, located 0.70 Å from N4.

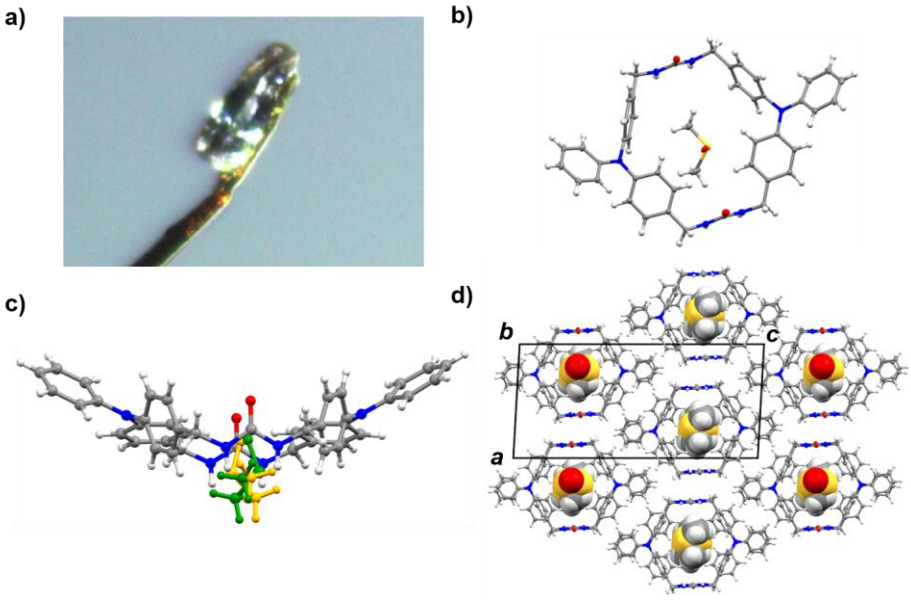

Figure 5.25. Crystal views of **1**·DMSO. (a) Data crystal. (b) Components of structure. Thermal ellipsoids were drawn at the 30% probability level. (c) View of DMSO disorder inside macrocycle **1**. (d) Crystal packing along the *b* axis (disorder omitted for clarity).

Crystals formed as colorless multifaceted rods. Several crystals examined, intact or cleaved and of various sizes, persistently gave doubled or split diffraction spots, along with difficulty in indexing the diffraction pattern to a reasonable unit cell. Eventually crystals of the material were determined to be twinned by non-merohedry. Using the Bruker Cell_Now program,[63] reflections from a set of 199 from the data crystal could be indexed entirely to two domains with the reported primitive monoclinic unit cell parameters. The derived twin law, relating indices of one domain to those of the other, is (-1 0 0 / 0 -1 0 / -0.24 0 -1). The twin law corresponds to a 180° rotation about the real-space [100] axis. X-ray intensity data were collected at 100(2) K using a Bruker D8 QUEST diffractometer equipped with a PHOTON 100 CMOS area detector and an Incoatec microfocus source (Mo Kα radiation, λ = 0.71073 Å). The raw area detector data frames were reduced and corrected for absorption effects using the SAINT+ and TWINABS programs.[63] TWINABS also constructed SHELX HKLF-4 and HKLF-5 format reflection files for solution and refinement, respectively. Final unit cell parameters were determined by least-squares refinement of 9957 reflections in the range $5.136° < 2\theta < 48.445°$ taken from both twin domains of the crystal. The structure was solved by dual-space methods with SHELXT.[60,61] Subsequent difference Fourier calculations and full-matrix least-squares refinement against F^2 were done with SHELXL-2018[60,61] using OLEX2.[62] The major twin domain volume fraction refined to 0.520(1).

The compound crystallizes in the space group $P2_1/n$ of the monoclinic system. The asymmetric unit consists of one $C_{42}H_{38}N_6O_2$ molecular cycle and one DMSO molecule. The DMSO molecule is disordered over two closely spaced orientations with a major component occupancy of 0.516(4). The total DMSO occupancy was constrained to sum to

one. Appropriate S-O and S-C distance restraints were applied. All non-hydrogen atoms were refined with anisotropic displacement parameters. Hydrogen atoms were located in Fourier difference maps before being placed in geometrically idealized positions and included as riding atoms with *d*(C-H) = 0.95 Å and *U*iso(H) = 1.2*U*eq(C) for aromatic hydrogen atoms, *d*(C-H) = 0.99 Å and *U*iso(H) = 1.2*U*eq(C) for methylene hydrogens and *d*(C-H) = 0.98 Å and *U*iso(H) = 1.5*U*eq(C) for methyl hydrogens. The methyl hydrogens were allowed to rotate as a rigid group to the orientation of maximum observed electron density. Hydrogen atoms bonded to urea nitrogen atoms were included with *d*(N-H) = 0.90 Å and *U*iso(H) = 1.2*U*eq(N). The largest residual electron density peak in the final difference map is 0.31 e-/Å^3, located 1.11 Å from N4.

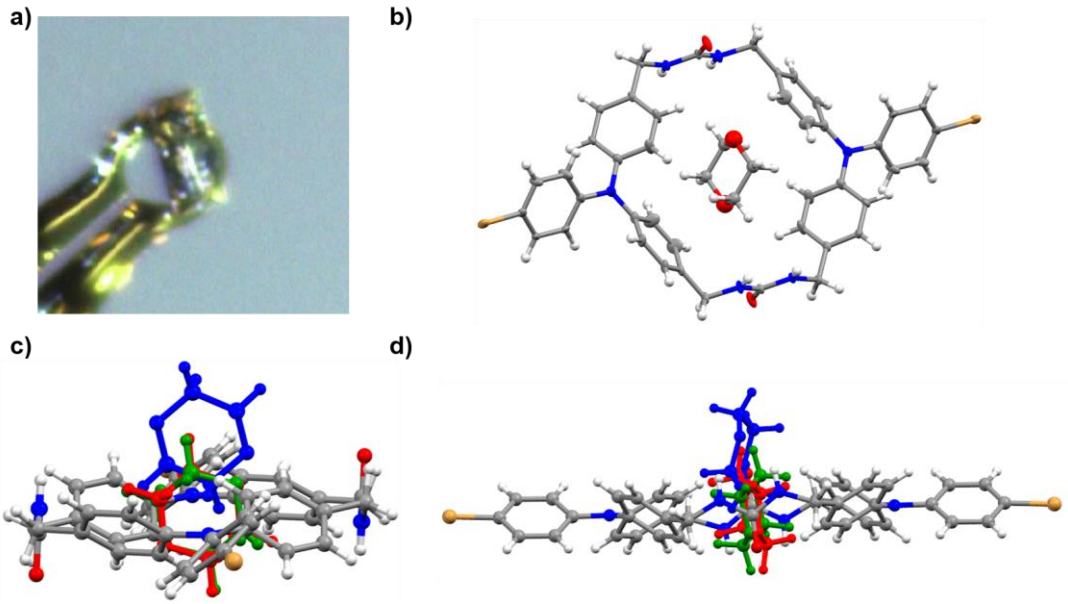

Figure 5.26. Crystal views of **1a**·1,4-dioxanes. (a) Data crystal. (b) Components of structure. Thermal ellipsoids were drawn at the 30% probability level. (c) View of 1,4-dioxanes disorder inside macrocycle **1a**. (d) Another view of the disorder.

X-ray intensity data from a colorless needle were collected at 100(2) K using a Bruker D8 QUEST diffractometer equipped with a PHOTON-100 CMOS area detector

and an Incoatec microfocus source (Mo Kα radiation, λ = 0.71073 Å). The raw area detector data frames were reduced and corrected for absorption effects using the Bruker APEX3, SAINT+ and SADABS programs.[64,59] The structure was solved with SHELXT.[60,61] Subsequent difference Fourier calculations and full-matrix least-squares refinement against F^2 were performed with SHELXL-2018[60,61] using OLEX2.[62]

The compound crystallizes in the space group $P2_1/c$ of the monoclinic system. The asymmetric unit consists of half of one $C_{42}H_{36}Br_2N_6O_2$ cycle located on a crystallographic inversion center and several electron density peaks inside the tubular channels created by the cycle columns. The residual difference electron density in the channel region is disordered but arranged in a tapelike fashion along the crystallographic *b* axis direction. If assigned as carbon atoms, all peaks refined to significantly less than full occupancy. The peaks could be reasonably fitted to half each (two carbon atoms and one oxygen atom) of three crystallographically independent dioxane molecules, all located on crystallographic inversion centers. For the disorder model, all 1,2- and 1,3- and 1,4- C-C and C-O distances in the dioxane guests were restrained to appropriate values. Occupancies of the three components refined to O1S-C2S = 0.22(1), O2S-C4S = 0. 23(1) and O3S-C6S = 0.13(1), generating a dioxane composition per cycle of 0.58(2). All non-hydrogen atoms were refined with anisotropic displacement parameters except for atoms of the disordered dioxane guests, which were refined isotropically. Components O2S-C4S and O3S-C6S were each assigned a separate common isotropic displacement parameter. Hydrogen atoms bonded to carbon were placed in geometrically idealized positions and included as riding atoms with *d*(C-H) = 0.95 Å and *U*iso(H) = 1.2*U*eq(C) for aromatic hydrogen atoms and *d*(C-H) = 0.99 Å and *U*iso(H) = 1.2*U*eq(C) for methylene hydrogen atoms. The two urea

hydrogen atoms were located and refined with *d*(N-H) = 0.85(2) Å distance restraints and a common isotropic displacement parameter. The largest residual electron density peak in the final difference map is 0.53 e-/Å^3, located 0.85 Å from C5S.

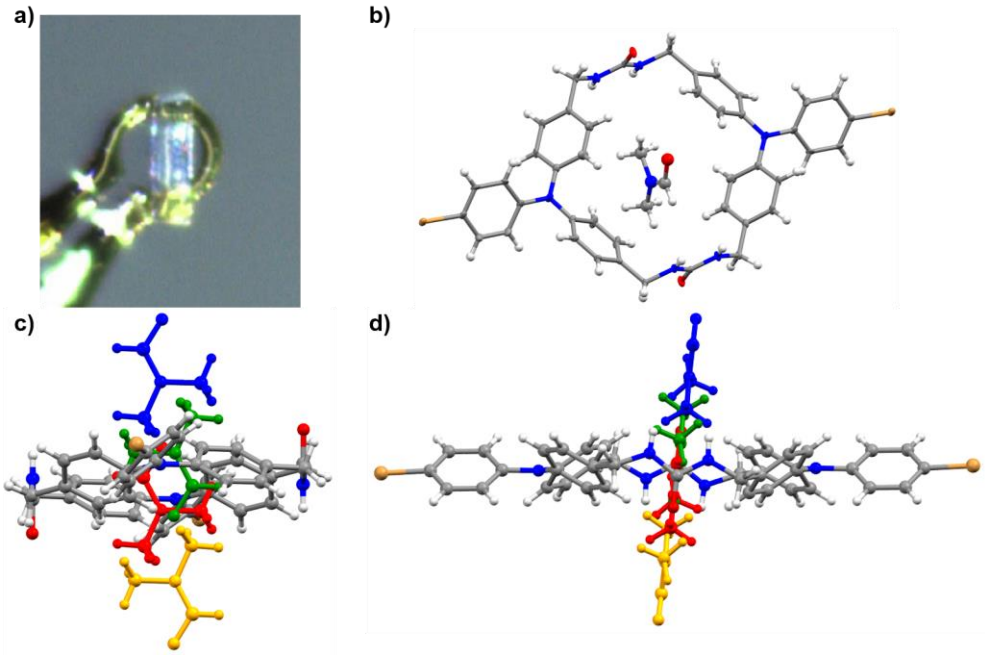

Figure 5.27. Crystal views of **1a**·(DMF)$_{0.65}$. (a) Data crystal. (b) Components of structure. Thermal ellipsoids were drawn at the 30% probability level. (c) View of DMF disorder inside macrocycle **1a**. (d) Another view of the disorder.

X-ray intensity data from colorless needle were collected at 100(2) K using a Bruker D8 QUEST diffractometer equipped with a PHOTON-100 CMOS area detector and an Incoatec microfocus source (Mo Kα radiation, λ = 0.71073 Å). The raw area detector data frames were reduced and corrected for absorption effects using the Bruker APEX3, SAINT+ and SADABS programs.[64,59] The structure was solved with SHELXT. [60,61] Subsequent difference Fourier calculations and full-matrix least-squares refinement against F^2 were performed with SHELXL-2018[60,61] using OLEX2.[62]

The compound crystallizes in the monoclinic system. The pattern of systematic absences in the intensity data was consistent with the space group $P2_1/c$, which was confirmed by structure solution. The asymmetric unit consists of half of one $C_{42}H_{36}Br_2N_6O_2$ cycle located on a crystallographic inversion center and several electron density peaks inside the tubular channels created by the cycle columns. The residual difference electron density in the channel region is disordered, but arranged in a planar, tapelike fashion along the crystallographic *b* axis direction. If assigned as carbon atoms, all peaks refined to significantly less than full occupancy. The peaks could be reasonably fitted to one partially occupied, crystallographically independent DMF molecule, disordered across nearby crystallographic inversion centers. For the disorder model, 1,2-, 1,3- and 1,4- C-C, C-N and C-O distances of the DMF guest were restrained to appropriate values. The guest occupancy refined to 0.325(4), generating a DMF composition per cycle of 0.65(1). All non-hydrogen atoms were refined with anisotropic displacement parameters except for atoms of the disordered DMF guest, which were refined with a common isotropic displacement parameter. Hydrogen atoms bonded to carbon were placed in geometrically idealized positions and included as riding atoms with *d*(C-H) = 0.95 Å and *U*iso(H) = 1.2*U*eq(C) for aromatic hydrogen atoms, *d*(C-H) = 0.99 Å and *U*iso(H) = 1.2*U*eq(C) for methylene hydrogen atoms and *d*(C-H) = 0.98 Å and *U*iso(H) = 1.5*U*eq(C) for methyl hydrogen atoms. The two urea hydrogen atoms were located and refined with *d*(N-H) = 0.85(2) Å distance restraints and a common isotropic displacement parameter. The largest residual electron density peak in the final difference map is 0.76 e-/Å^3, located 0.72 Å from N1S.

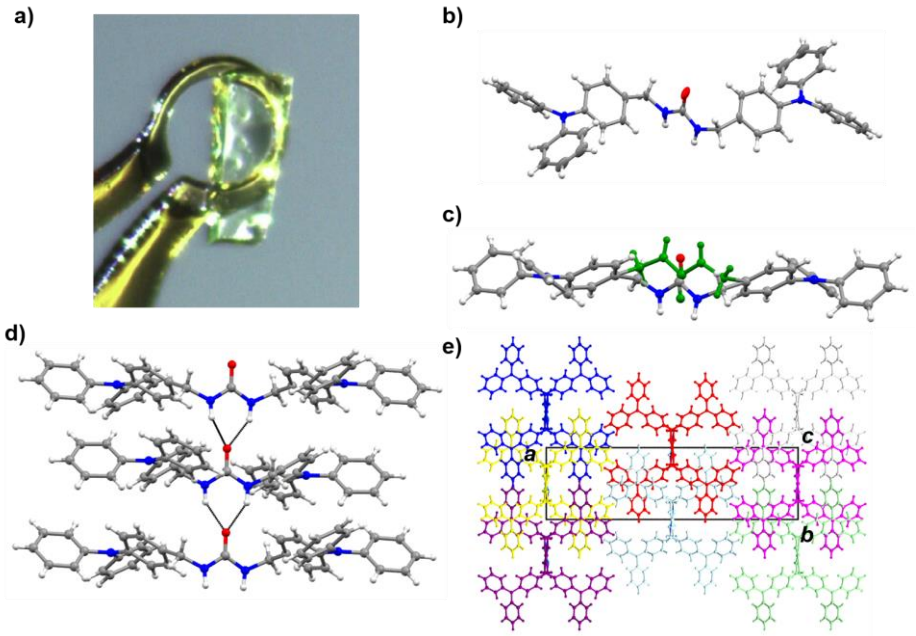

Figure 5.28. Crystal views of linear analog **2**. (a) Data crystal. (b) Molecular structure of linear analog **2**. Thermal ellipsoids were drawn at the 30% probability level. (c) View showing disorder in the methylene urea unit. Both units were found in equal populations resulting in (d) chains of hydrogen bonds going along either direction of the *c* axis. (e) Color coded crystal packing along the *c* axis.

X-ray intensity data from a pale-yellow needle were collected at 100(2) K using a Bruker D8 QUEST diffractometer equipped with a PHOTON-100 CMOS area detector and an Incoatec microfocus source (Mo Kα radiation, λ = 0.71073 Å). The raw area detector data frames were reduced and corrected for absorption effects using the Bruker APEX3, SAINT+ and SADABS programs.[64,59] The structure was solved with SHELXT.[60,61] Subsequent difference Fourier calculations and full-matrix least-squares refinement against F^2 were performed with SHELXL-2018[60,61] using OLEX2.[62]

The compound crystallizes in the orthorhombic system. The best solution was obtained in the centrosymmetric space group *Pbcn*. This space group was also indicated by the pattern of systematic absences in the intensity data, which were uniquely consistent with *Pbcn*. The structure is disordered and required several distance and displacement

parameter restraints to achieve a reasonable and stable refinement. In *Pbcn* there is half of one molecule in the asymmetric unit, located on a crystallographic inversion center. The central urea group (atoms O1, N1, N2, C1) is inconsistent with inversion symmetry and is thus disordered across the center. The disorder extends to the -CH_2- group (C2A/C2B) bonded to the urea. Occupancies of disordered atoms were fixed at 50%. The carbonyl C=O distance was restrained to 1.20(2) Å. Like C-C and C-N distances were restrained to similar values (SHELX SADI). A rigid-bond restraint (RIGU) was applied to atoms C1 and O1 for stability; these atoms are nearly superimposed with symmetry-equivalents. All non-hydrogen atoms were refined with anisotropic displacement parameters. Hydrogen atoms bonded to carbon were placed in geometrically idealized positions and included as riding atoms with *d*(C-H) = 0.95 Å and *U*iso(H) = 1.2*U*eq(C) for aromatic hydrogen atoms and *d*(C-H) = 0.99 Å and *U*iso(H) = 1.2*U*eq(C) for methylene hydrogen atoms. Hydrogen atoms bonded to the urea nitrogen atoms were also idealized with *d*(N-H) = 0.90 Å and *U*iso(H) = 1.2*U*eq(N). The largest residual electron density peak in the final difference map is 0.21 e-/$Å^3$, located 1.49 Å from H12.

Similar disorder issues were observed in the acentric space group *Pca*2_1. In *Pca*2_1, the central -CH_2N(H)CON(H)CH_2- grouping is still disordered, though now over two pseudo-inversion related orientations. In addition, refinement instability was encountered because of strong correlations between inversion-related atoms of the triphenylamine substituent. Solution in monoclinic space groups gave similar results; *i.e*. the disorder is not resolved by lowering crystal symmetry. For these reasons, *Pbcn* was retained as the best description of the structure. The disorder encountered upon solution and refinement was foretold during the crystal screening process. Despite showing excellent extinctions in

polarized light, all of several crystals examined from two separate crystallizations showed diffuse scattering, appearing as relatively faint streaks between strong Bragg diffraction peaks in the area detector frames. This persisted regardless of crystal size and data collection temperature. Several trial specimens were cleaved as thin as mechanically possible to eliminate misaligned crystal domains (twinning) or other defects, and data frames were collected at room temperature and after flash-cooling to 100 K, but the diffuse streaking was still observed in all cases.

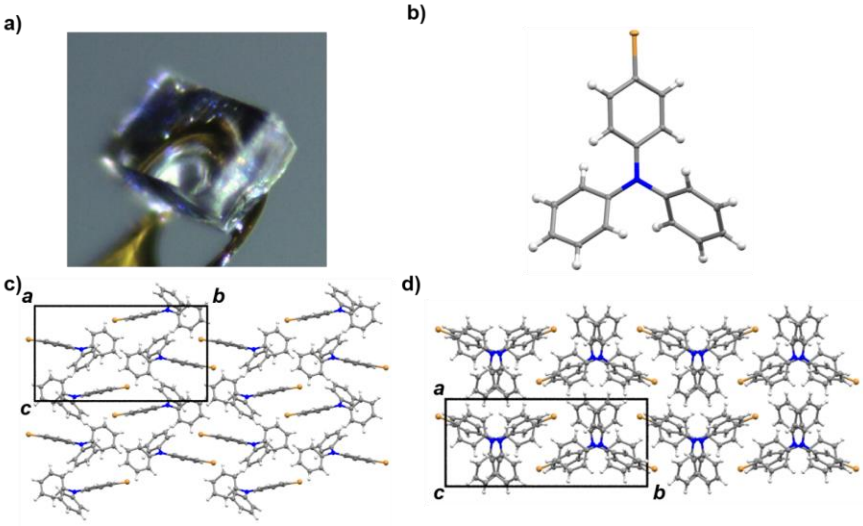

Figure 5.29. Crystal views of the monoclinic polymorph of TPA **3a**. (a) Data crystal. (b) Molecular structure of TPA **3a**. Thermal ellipsoids were drawn at the 30% probability level. (c) Crystal packing along the *a* axis. (d) Crystal packing along the *c* axis.

X-ray intensity data from a colorless block were collected at 100(2) K using a Bruker D8 QUEST diffractometer equipped with a PHOTON-100 CMOS area detector and an Incoatec microfocus source (Mo Kα radiation, λ = 0.71073 Å). The raw area detector data frames were reduced and corrected for absorption effects using the Bruker APEX3, SAINT+ and SADABS programs.[64,59] The structure was solved with SHELXT.[60,61] Subsequent difference Fourier calculations and full-matrix least-squares refinement against F^2 were performed with SHELXL-2018[60,61] using OLEX2.[62]

The compound crystallizes in the monoclinic system. The pattern of systematic absences in the intensity data was consistent with the space group $P2_1/c$, which was confirmed by structure solution. The asymmetric unit consists of one molecule. All non-hydrogen atoms were refined with anisotropic displacement parameters. Hydrogen atoms bonded to carbon were located in difference Fourier maps before being placed in geometrically idealized positions and included as riding atoms with d(C-H) = 0.95 Å and Uiso(H) = 1.2Ueq(C). The largest residual electron density peak in the final difference map is 0.47 e-/Å^3, located 0.68 Å from C18.

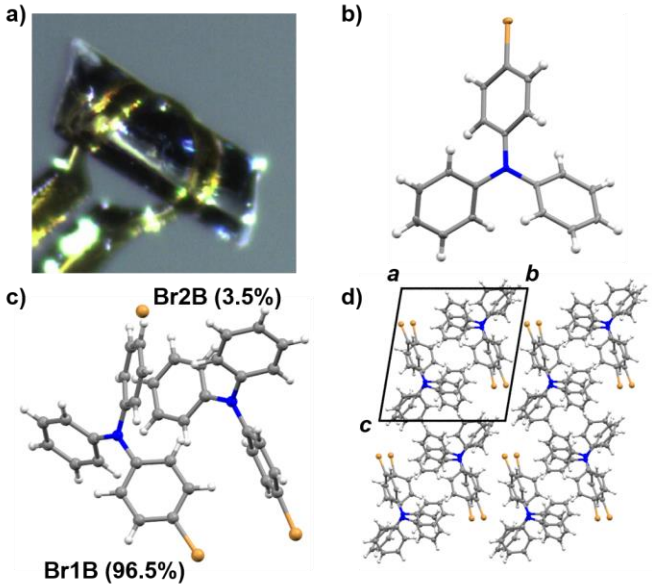

Figure 5.30. Crystal views of the triclinic polymorph of TPA **3a**. (a) Data crystal. (b) Molecular structure of TPA **3a**. Thermal ellipsoids were drawn at the 30% probability level. (c) Asymmetric unit of the crystal. Two crystallographically independent molecules were found. Br2B is a minor disorder component of molecule "B", with an occupancy of 3.5%. Only the Br atom of the minor component was modeled. (d) Crystal packing along the *a* axis (disorder omitted for clarity).

X-ray intensity data from a colorless needle were collected at 100(2) K using a Bruker D8 QUEST diffractometer equipped with a PHOTON-100 CMOS area detector and an Incoatec microfocus source (Mo Kα radiation, λ = 0.71073 Å). The raw area

detector data frames were reduced and corrected for absorption effects using the Bruker APEX3, SAINT+ and SADABS programs.[64,59] The structure was solved with SHELXT.[60,61] Subsequent difference Fourier calculations and full-matrix least-squares refinement against F^2 were performed with SHELXL-2018[60,61] using OLEX2.[62]

The compound crystallizes in the triclinic system. The space group *P*-1 (No. 2) was confirmed by structure solution. The asymmetric unit consists of two crystallographically independent but chemically identical molecules, labeled identically except for atom label suffixes A or B. All non-hydrogen atoms were refined with anisotropic displacement parameters. After normal location and anisotropic refinement of the two independent molecules, a single large residual electron density peak of magnitude +3.78 e-/Å was observed *ca*. 1.7 Å from C16B of molecule "B". The next largest peak was +1.35 e-/Å. The highest peak was interpreted as arising from the bromine atom of a minor disorder component of this molecule. Trial refinements of site occupancy parameters supported this assumption, as free refinement of the occupancies of the major bromine (Br1B) and the likely minor bromine peak (Br2B) resulted in occupancies of 0.965(1) and 0.035(1), respectively, summing to one bromine per molecule. Inspection of the packing shows this minor peak Br2B in the vicinity of a symmetry-equivalent Br1B, *i.e.* they are disordered together in a physically reasonable assembly (Br1B present, Br2B absent and *vice versa*). Omitting this single peak gave $R1 = 0.044$ / $wR2 = 0.118$ and the offending difference map. Instead of a whole-molecule model to account for 3% of one Br atom, Br2B was left isolated (with no minor component triphenylamine), and a fully occupied H atom refined on C16B. Additonally, no H atom was added to C4B, which would have an occupancy of 3% H. Hydrogen atoms were located in difference Fourier maps before being placed in

geometrically idealized positions and included as riding atoms with *d*(C-H) = 0.95 Å and *U*iso(H) = 1.2*U*eq(C). The largest residual electron density peak in the final difference map is 1.38 e-/Å^3, located 0.77 Å from Br1B.

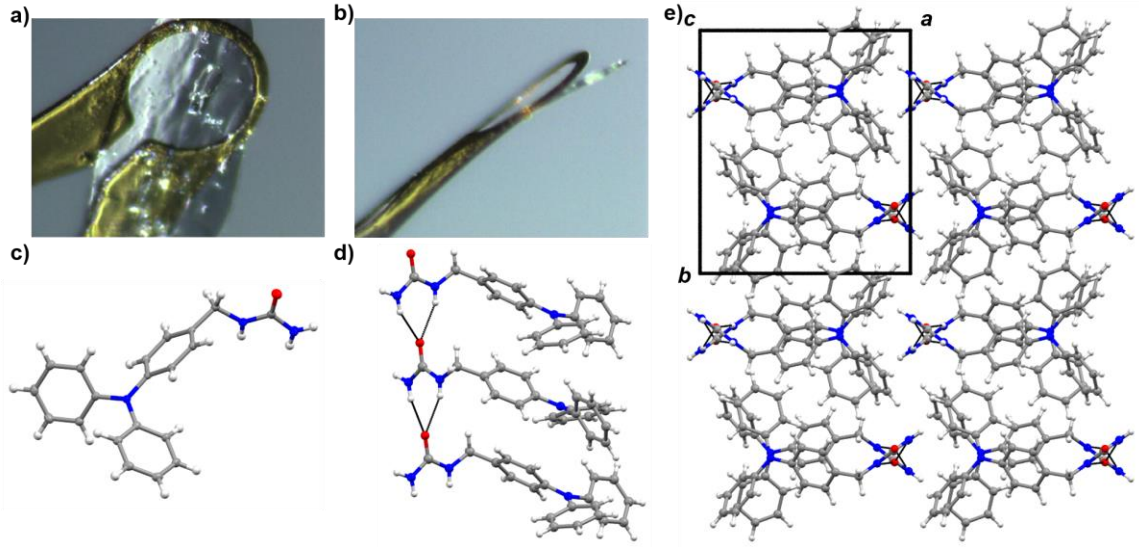

Figure 5.31. Crystal views of TPA **4**. (a) Data crystal. (b) Another view of the crystal. (c) Molecular structure of TPA **4**. Thermal ellipsoids were drawn at the 30% probability level. (d) Hydrogen bonding through the urea groups. Hydrogen bonds are shown in black. (d) Crystal packing along the *c* axis.

Crystals formed as thin colorless flakes with an irregular shape. Because of their extreme brittleness, several attempts were necessary to mount a suitably-sized plate without bending or breaking the crystal. It was necessary to use a crystal much larger than the X-ray beam in order to observe sufficient diffraction intensity and also to provide mechanical stability of the thin plate in the flowing cold stream. X-ray intensity data were collected at 100(2) K using a Bruker D8 QUEST diffractometer equipped with a PHOTON-100 CMOS area detector and an Incoatec microfocus source (Mo Kα radiation, λ = 0.71073 Å). The raw area detector data frames were reduced and corrected for absorption effects using the Bruker APEX3, SAINT+ and SADABS programs.[58,59] Final unit cell parameters were determined by least-squares refinement of 5698 reflections taken from the data set.

The structure was solved with SHELXT.[60,61] Subsequent difference Fourier calculations and full-matrix least-squares refinement against F^2 were performed with SHELXL-2017[60,61] using OLEX2.[62]

The compound crystallizes in the monoclinic system. The pattern of systematic absences in the intensity data was consistent with the space group $P2_1/c$, which was verified by structure solution. The asymmetric unit consists of one molecule. All non-hydrogen atoms were refined with anisotropic displacement parameters. Hydrogen atoms bonded to carbon were located in Fourier difference maps before being placed in geometrically idealized positions and included as riding atoms with *d*(C-H) = 0.95 Å and *U*iso(H) = 1.2*U*eq(C) for aromatic hydrogen atoms and *d*(C-H) = 0.99 Å and *U*iso(H) = 1.2*U*eq(C) for methylene hydrogen atoms. Hydrogen atoms bonded to nitrogen were located in difference maps and refined freely. The largest residual electron density peak in the final difference map is 0.29 e-/Å^3, located 0.86 Å from C5.

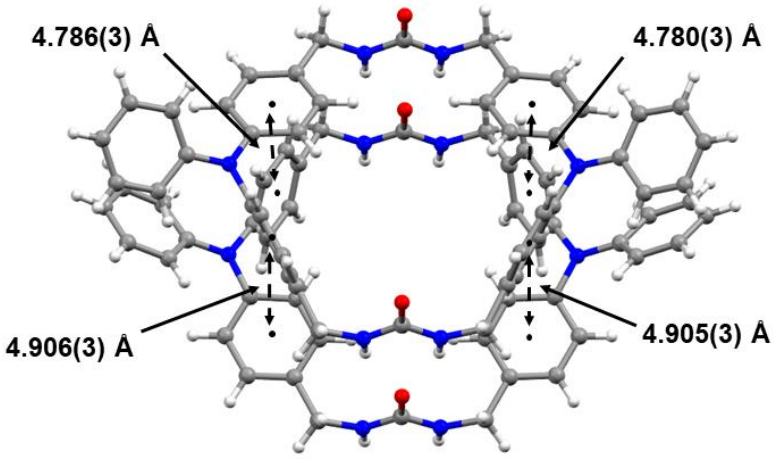

Figure 5.32. Crystal view of complex 1·DMSO showing the edge-to-face π-stacking in-between macrocycles. Distances were measured from centroid to centroid of the phenyl rings. DMSO guests were removed for clarity.

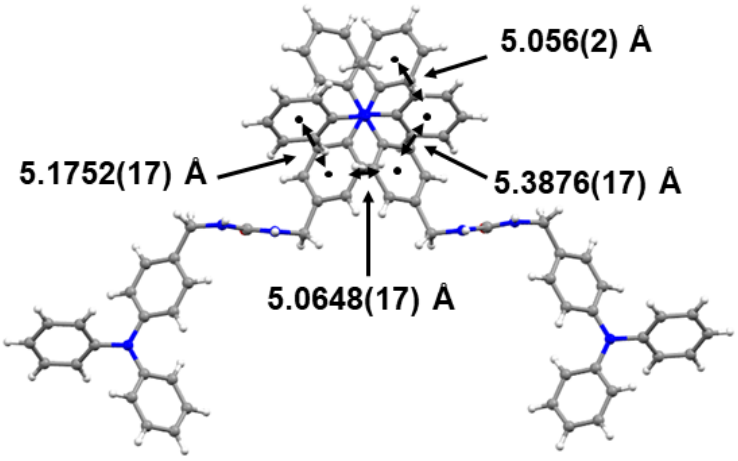

Figure 5.33. Crystal view of linear analog **2** showing the edge-to-face π-stacking in-between macrocycles. Distances were measured from centroid to centroid of the phenyl rings. Disorder in methylene urea bridge was removed for clarity.

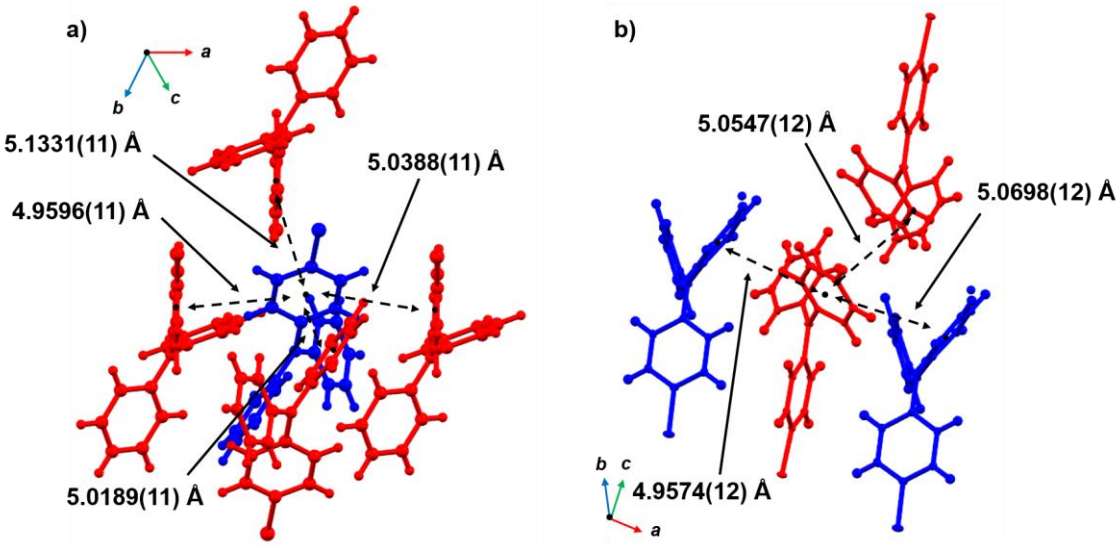

Figure 5.34. Crystal views of the triclinic polymorph of TPA **3a** showing the edge-to-face π-stacking in-between different TPA units. (a) and (b) show different views of this stacking. Distances were measured from centroid to centroid of the phenyl rings. Symmetry equivalent TPAs were colored either red or blue. Disorder was removed for clarity.

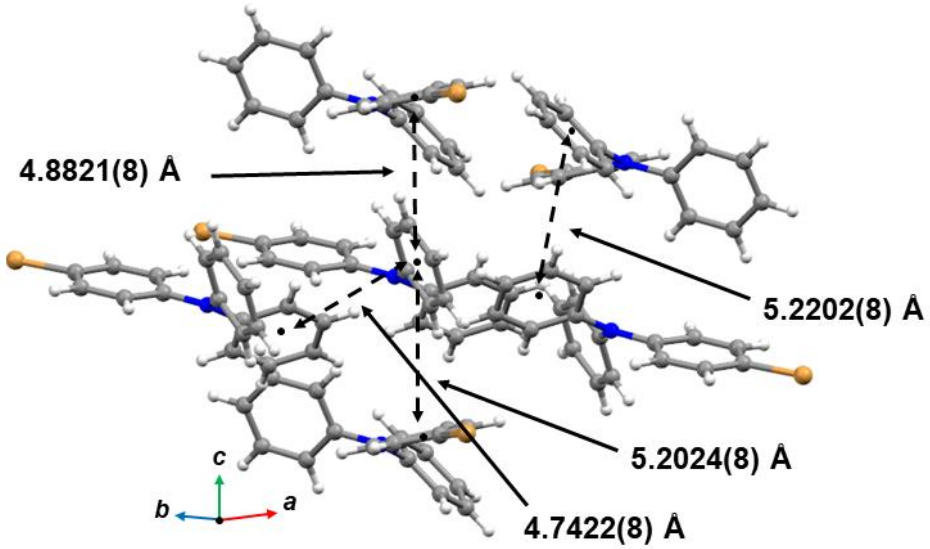

Figure 5.35. Crystal views of the monoclinic polymorph of TPA **3a** showing the edge-to-face π-stacking in-between different TPA units. Distances were measured from centroid to centroid of the phenyl rings.

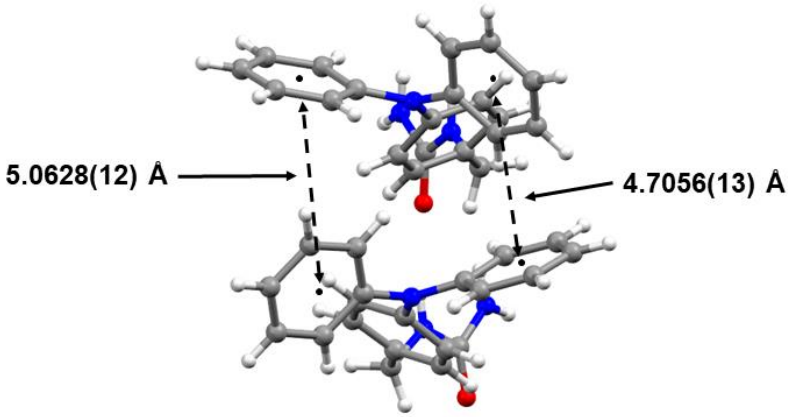

Figure 5.36. Crystal views of TPA **4** showing the edge-to-face π-stacking in-between different TPA units. Distances were measured from centroid to centroid of the phenyl rings.

5.4.4 Powder X-ray Diffraction (PXRD)

PXRD data was collected on a Rigaku D/Max-2100 powder X-ray diffractometer using Cu Kα radiation at room temperature. The step can covered an angular range of 5-50˚ 2Θ in steps of 0.02˚.

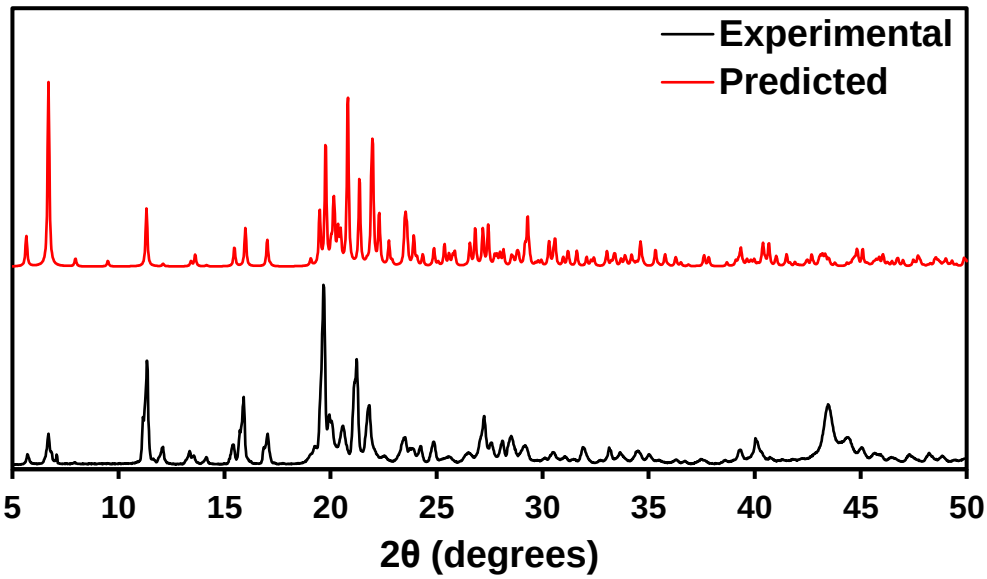

Figure 5.37. PXRD of the complex **1a**·DME.

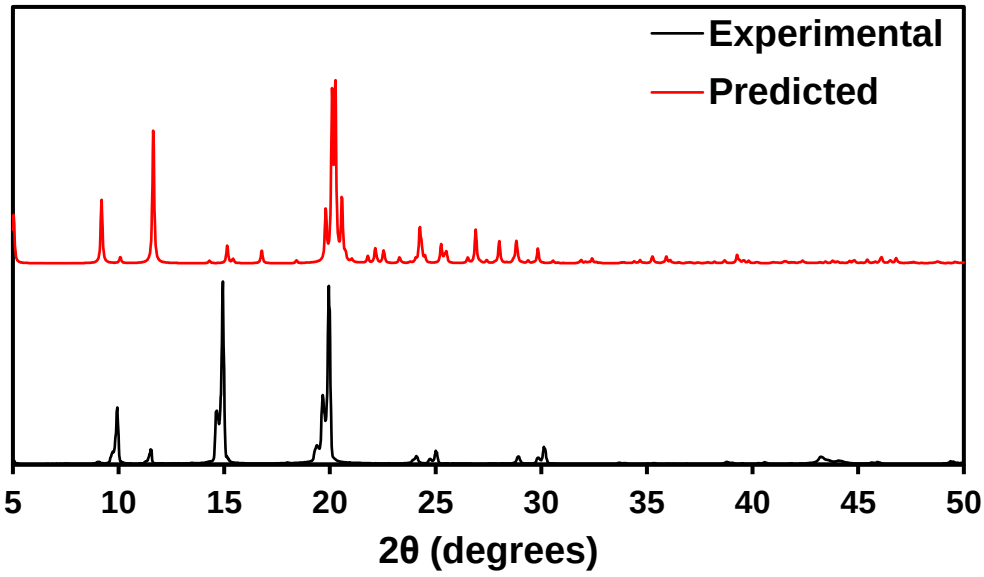

Figure 5.38. PXRD of linear analog **2**.

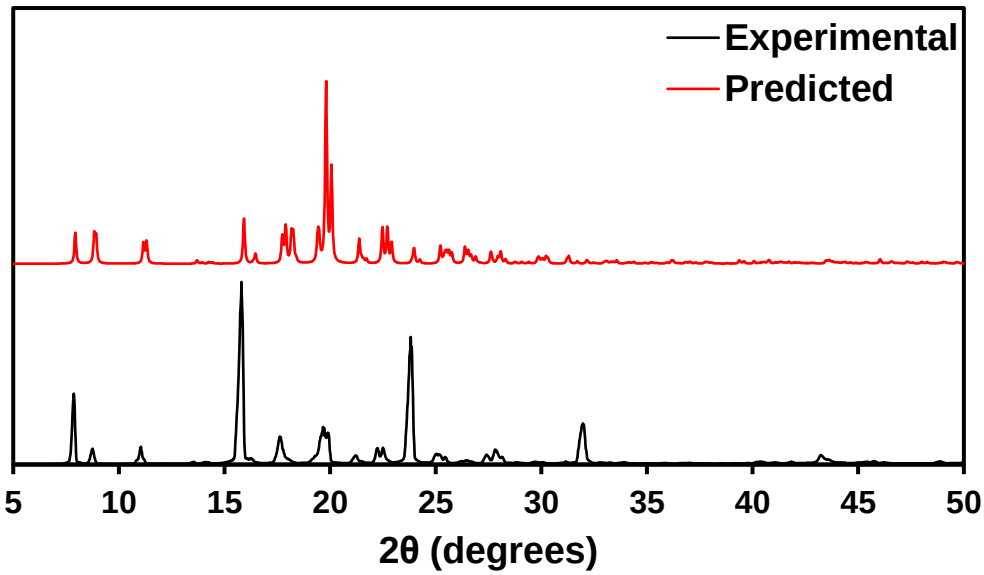

Figure 5.39. PXRD of TPA **3**.

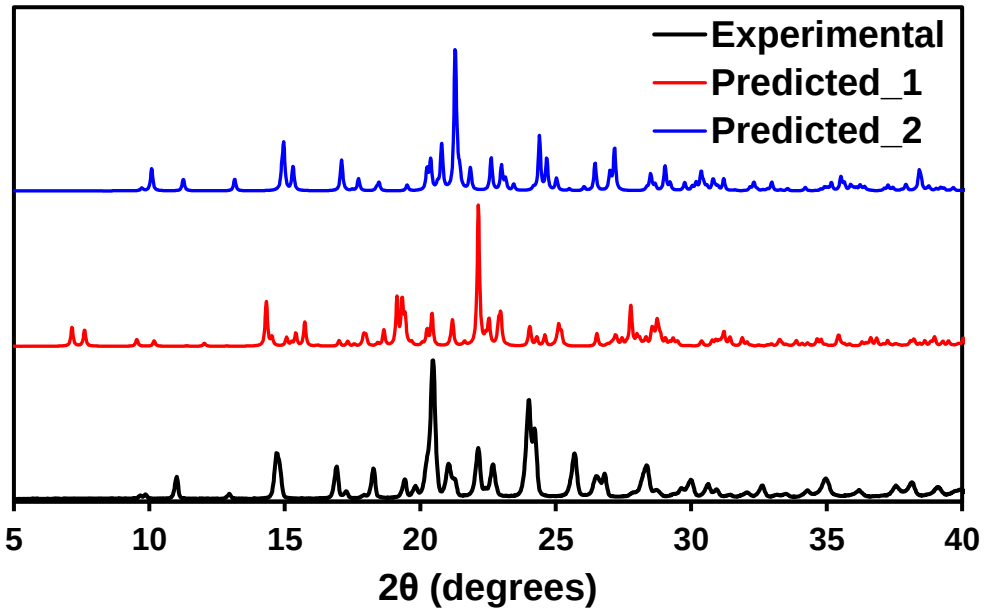

Figure 5.40. PXRD of TPA **3a**. Predicted_1 and Predicted_2 are the calculated patterns for the triclinic and monoclinic polymorphs, respectively.

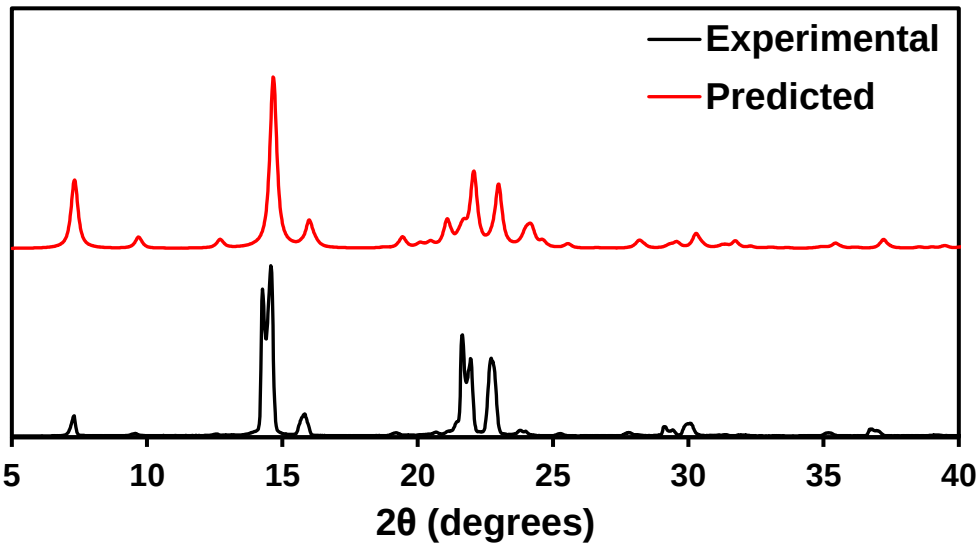

Figure 5.41. PXRD of TPA **4** with preferential orientation along the [100] direction and the full-width at a half-maximum of 0.3 2θ.

5.4.5 Thermal Gravimetric Analysis (TGA)

TGA was carried out using TA instruments SDT-Q600 simultaneous DTA/TGA at a rate of 4 °C/min from 25-180 °C with a 5-minute isotherm before temperature increase and 15 minute isotherm afterwards.

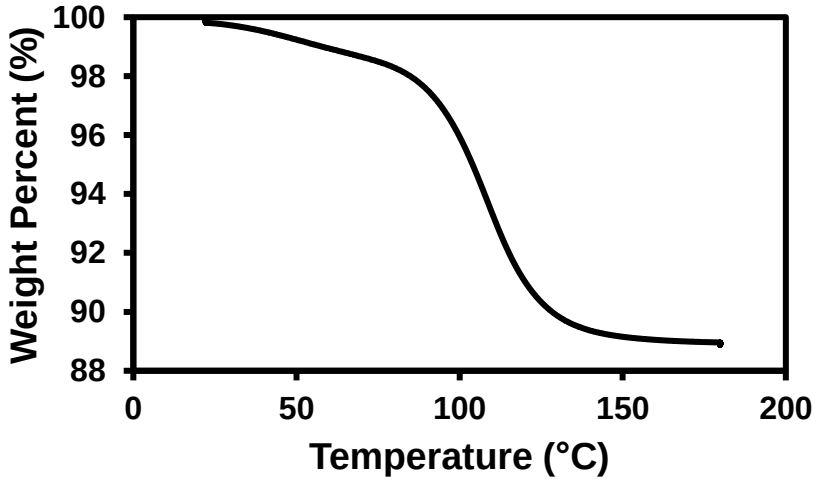

Figure 5.42. TGA graph showing a one-step desorption of DMSO from complex **1**·DMSO. Host-guest ratio was calculated to be 1:1.05.

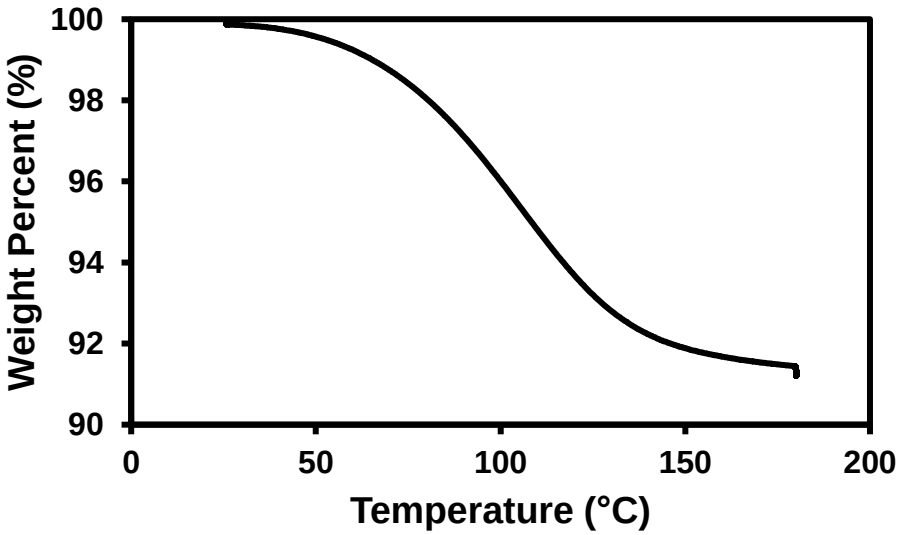

Figure 5.43. TGA graph showing a one-step desorption of C_6H_5Br from complex **1a**·C_6H_5Br after the radical regeneration studies. Host-guest ratio was calculated to be 1:0.50.

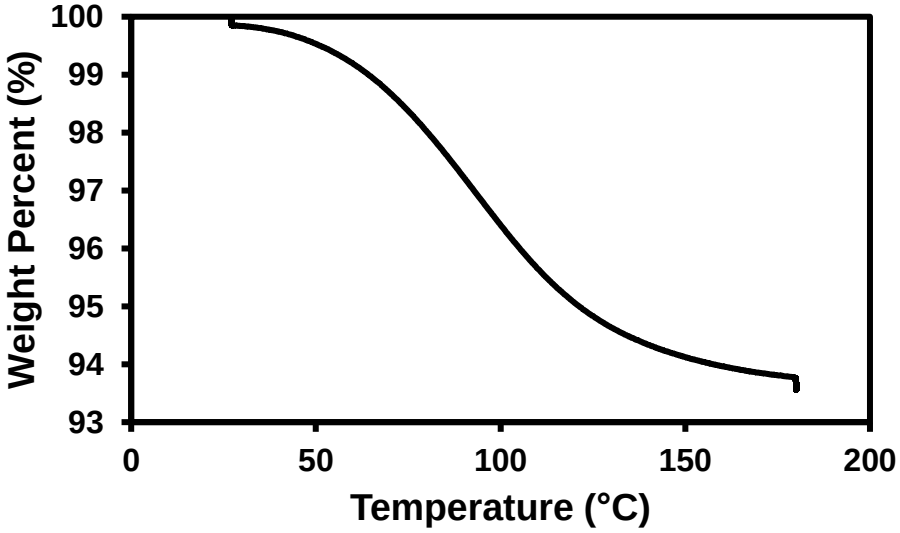

Figure 5.44. TGA graph showing a one-step desorption of C_6H_5Cl from complex **1a**·C_6H_5Cl after the radical regeneration studies. Host-guest ratio was calculated to be 1:0.51.

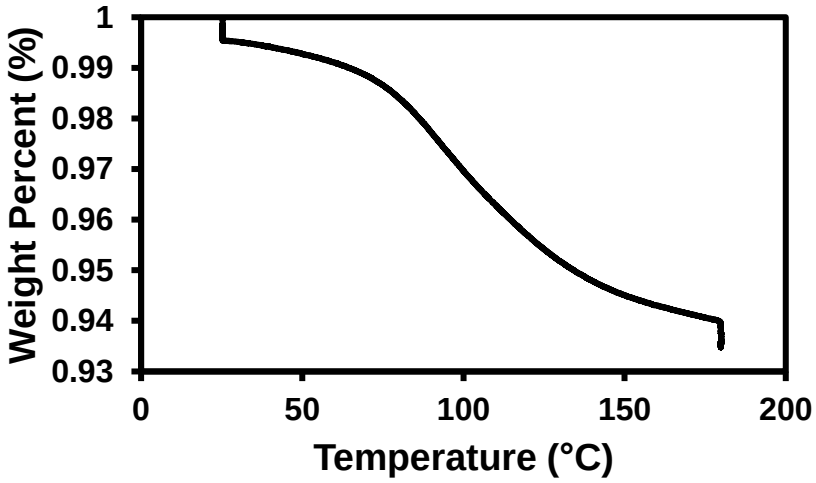

Figure 5.45. TGA graph showing a one-step desorption of DMF from complex **1a**·DMF after the radical regeneration studies. Host-guest ratio was calculated to be 1:0.78.

5.4.6 Absorbance Measurements

UV/Vis data was collected on either a Perkin Elmer Lambda 35 UV/vis spectrometer with UV Winlab software or a SoftMax M2 spectrometer (solid and solution, respectively). Spectra were recorded from either 330-600 nm (solid) or 270-550 nm (solution) at 1 nm steps. 10 μM concentrations were used for solution samples.

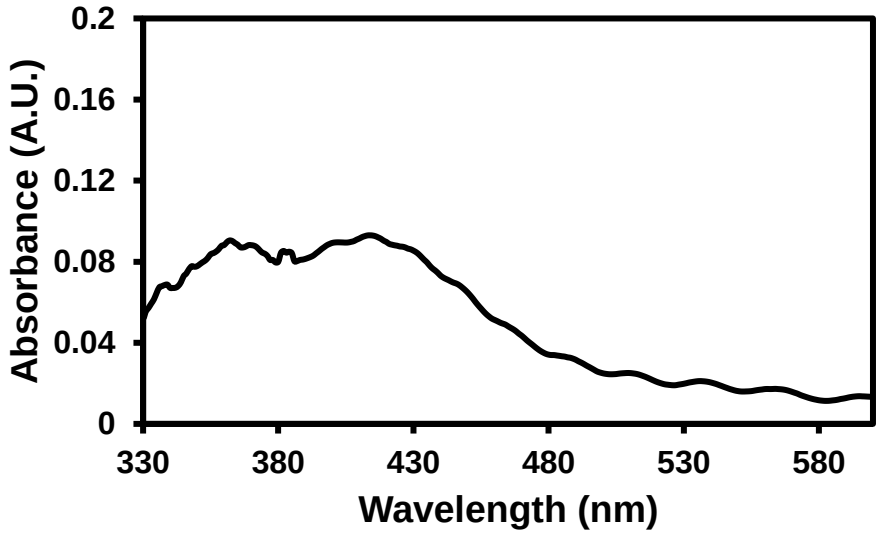

Figure 5.46. UV/Vis absorption spectrum of activated **1** in the solid-state.

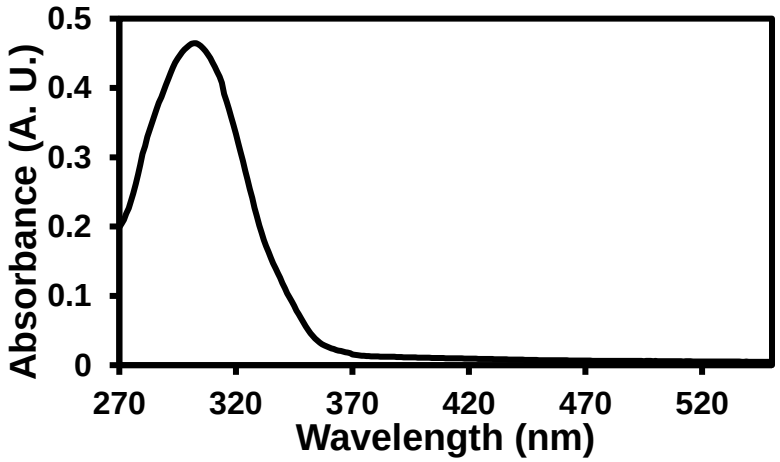

Figure 5.47. UV/Vis absorption spectrum of macrocycle **1a** in DMSO.

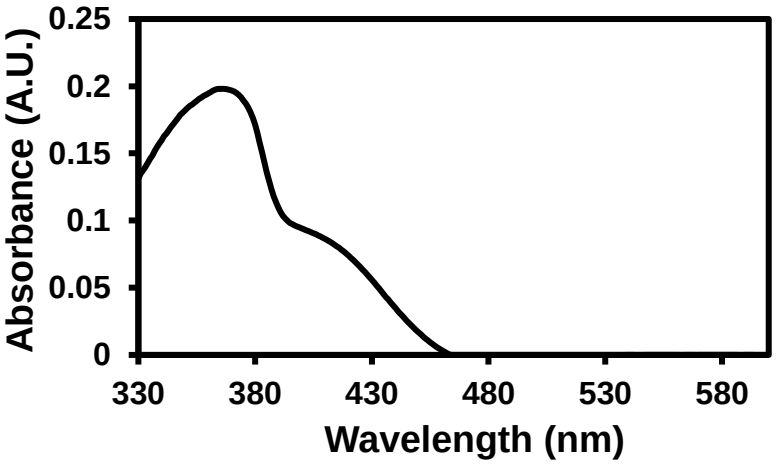

Figure 5.48. UV/Vis absorption spectrum of activated **1a** in the solid-state.

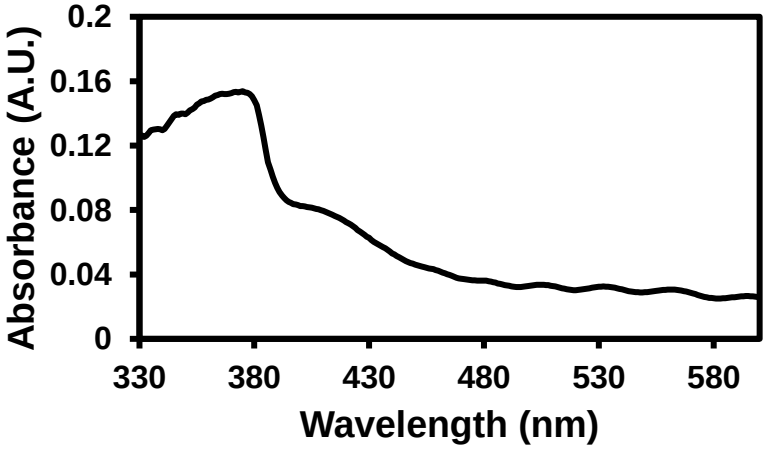

Figure 5.49. UV/Vis absorption spectrum of complex **1a**·C_6H_6 in the solid-state.

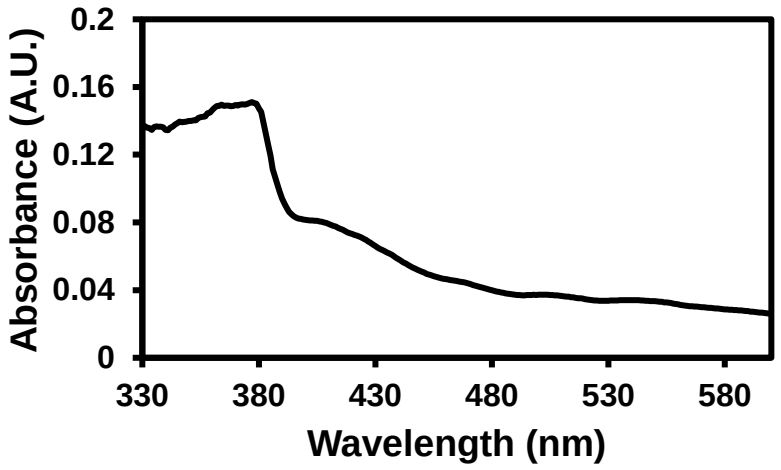

Figure 5.50. UV/Vis absorption spectrum of complex **1a**·DME in the solid-state.

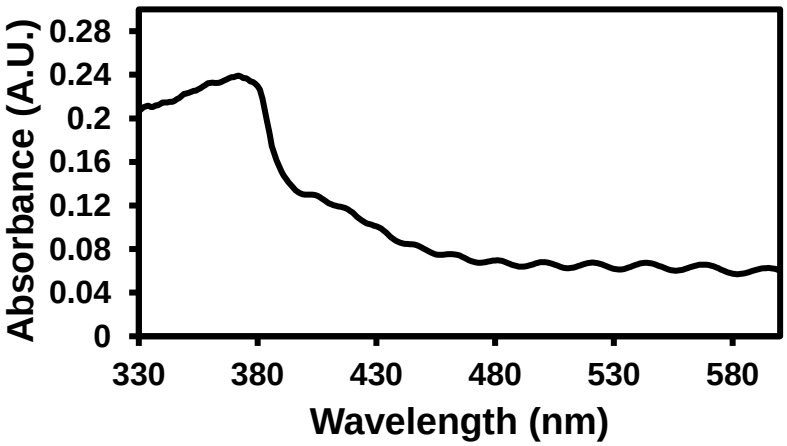

Figure 5.51. UV/Vis absorption spectrum of complex **1a**·DMF in the solid-state.

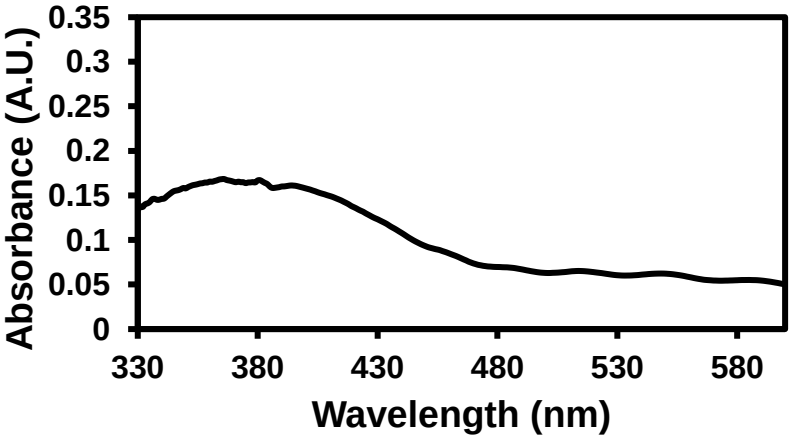

Figure 5.52. UV/Vis absorption spectrum of linear analog **2** in the solid-state.

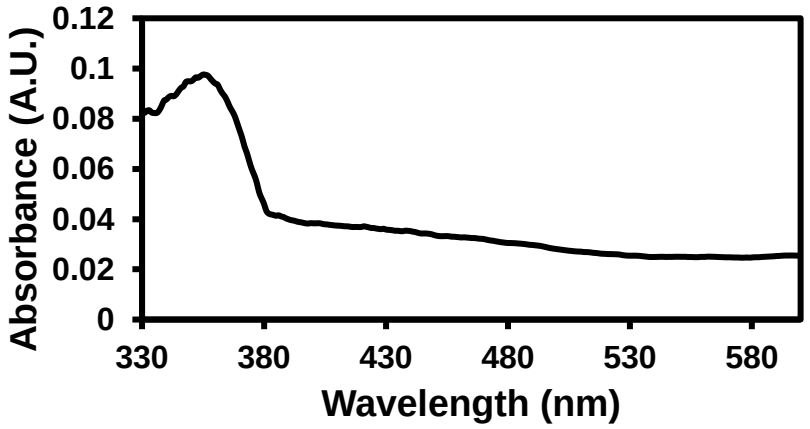

Figure 5.53. UV/Vis absorption spectrum of TPA **3** in the solid-state.

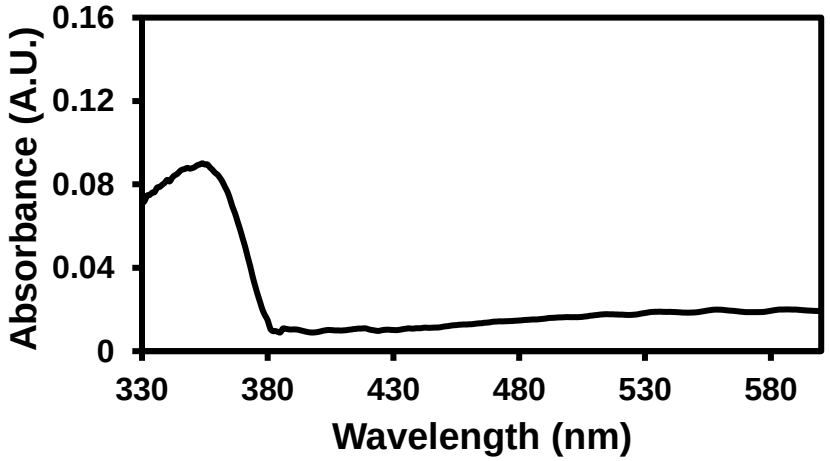

Figure 5.54. UV/Vis absorption spectrum of TPA **3a** in the solid-state.

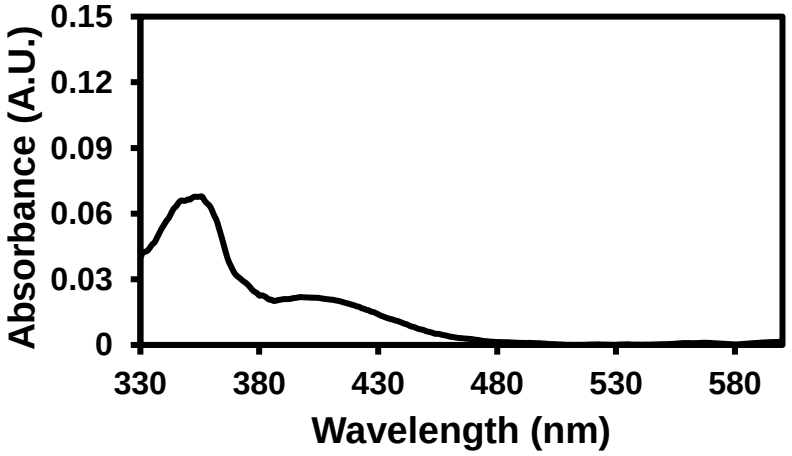

Figure 5.55. UV/Vis absorption spectrum of TPA **4** in the solid-state.

5.4.7 Emission Measurements

Emission data was collected on an Edinburgh FS5 instrument equipped with a 150 W continuous wave xenon lamp source for excitation. Excitations were performed at the λ_{max} of absorbance. Spectra were gathered from 400-650 nm (solid) or 325-800 nm (solution) at 1 nm steps and are an average of three measurements. 10 μM concentrations were used for solution samples.

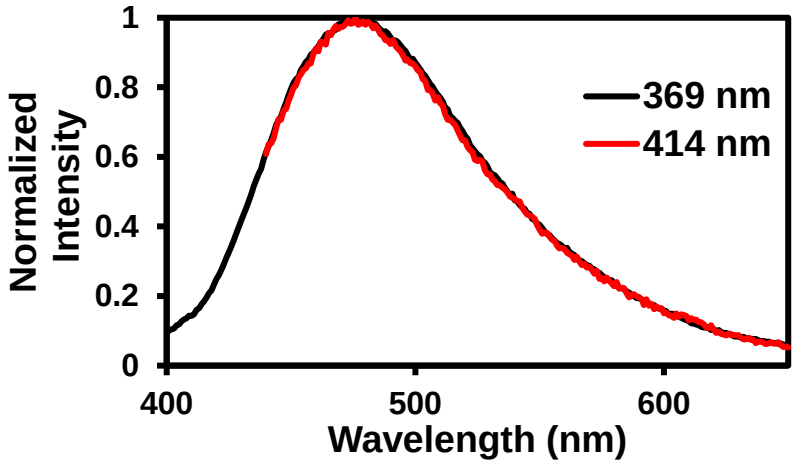

Figure 5.56. UV/Vis emission spectrum of activated **1** in the solid-state. Two different spectra were taken at each λ_{max} of absorption.

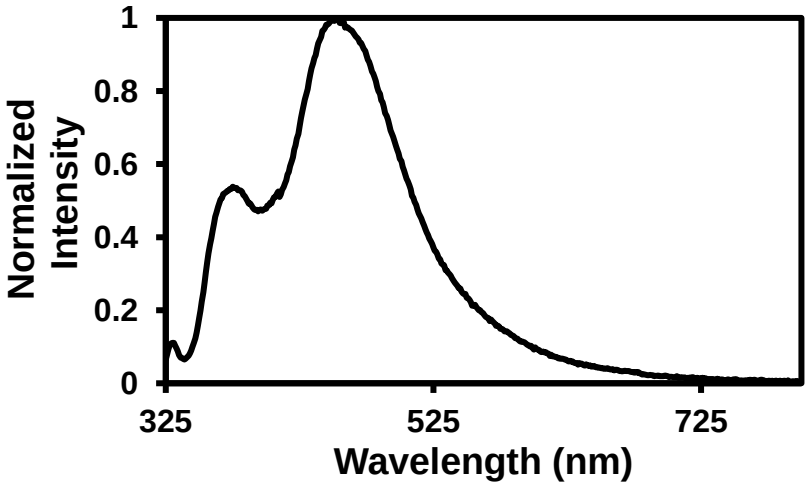

Figure 5.57. UV/Vis emission spectrum of macrocycle **1a** in DMSO.

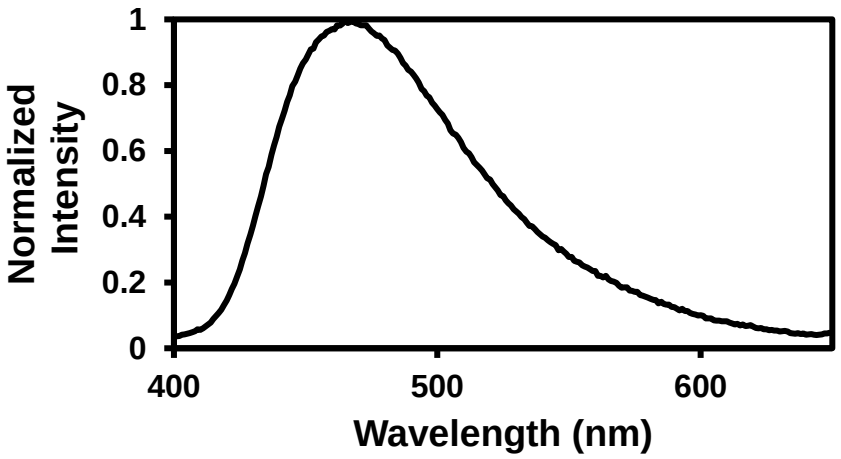

Figure 5.58. UV/Vis emission spectrum of activated **1a** in the solid-state.

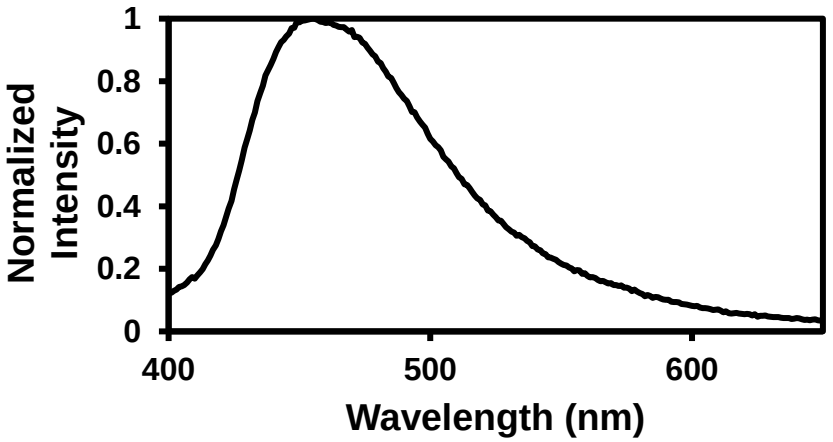

Figure 5.59. UV/Vis emission spectrum of complex **1a**·C_6H_6 in the solid-state.

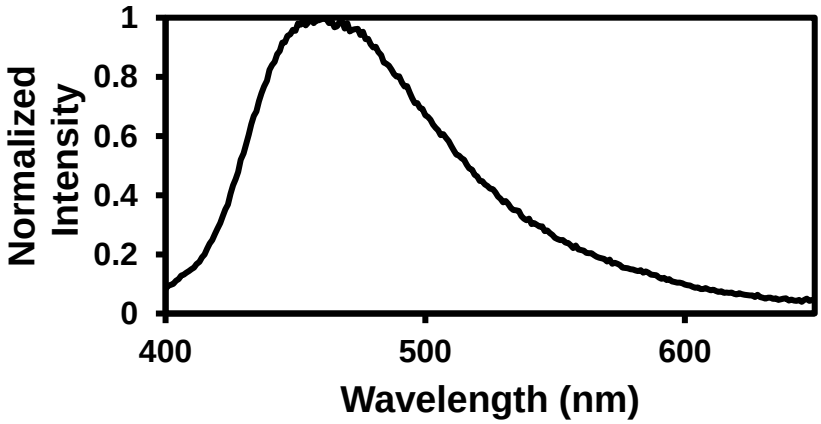

Figure 5.60. UV/Vis emission spectrum of complex **1a**·DME in the solid-state.

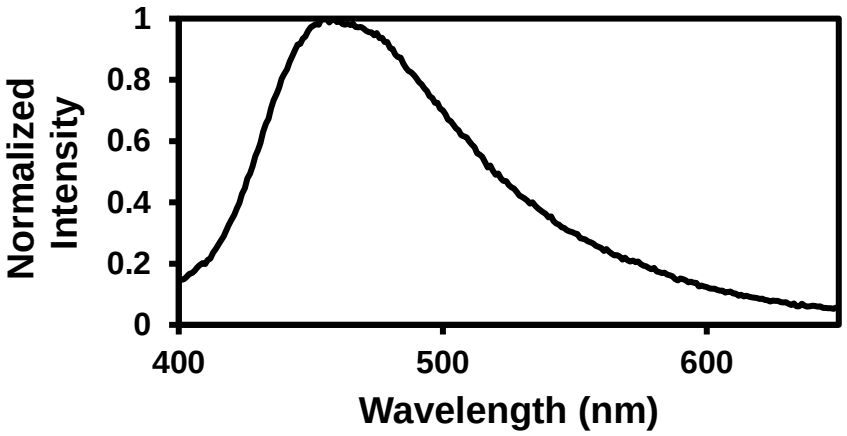

Figure 5.61. UV/Vis emission spectrum of complex **1a**·DMF in the solid-state.

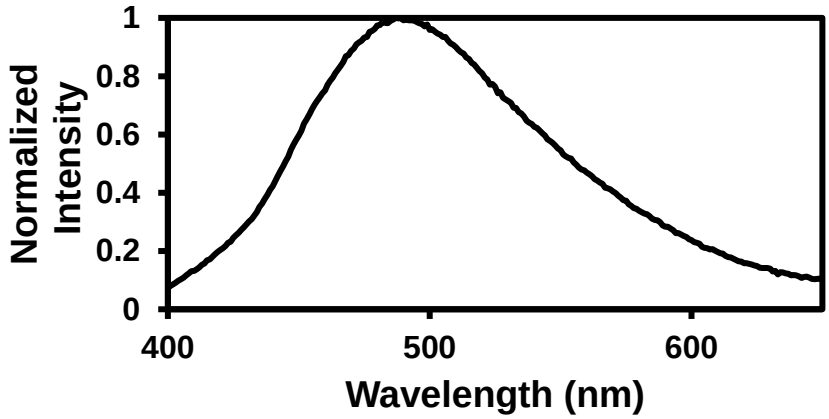

Figure 5.62. UV/Vis emission spectrum of linear analog **2** in the solid-state.

5.4.8 Lifetime Measurements

Lifetimes were measured using a Mini-τ lifetime spectrometer from Edinburgh Instruments equipped with either a 300 nm picosecond-pulsed-light-emitting diode (EPLED 300) or an EPLED 365. The lifetimes were recorded for the largest emission peak given in Table 1. The decays for were fit according to Equation S1 as either a bi- or triexponential function where τ and *B* are the lifetime and amplitude, respectively. 10 μM concentrations were used for solution samples.

$$I(t) = \int_{-\infty}^{t} IRF(t') \sum_{i=1}^{n} B_i e^{-\frac{t-t'}{\tau_i}} dt'$$

Equation 5.1. Fitting equation for fluorescence decay.

The amplitude-weighted average luminescent lifetimes τ_{av} were calculated using Equation S2. B_3 and τ_3 were only used for triexponential fits.

$$\langle \tau_{av} \rangle = \frac{B_1\tau_1 + B_2\tau_2 + B_3\tau_3}{B_1 + B_2 + B_3}$$

Equation 5.2. Equation for amplitude-weighted average lifetime.

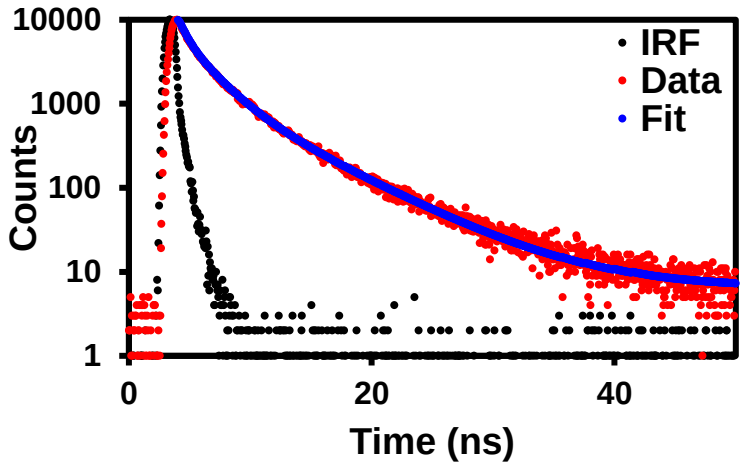

Figure 5.63. Lifetime data for activated **1** in the solid-state.

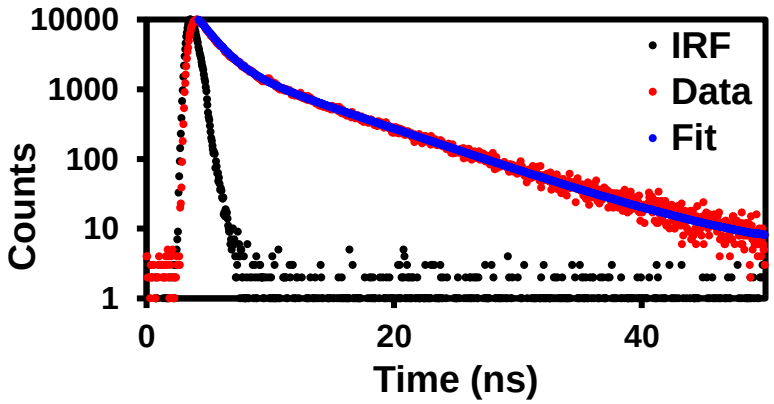

Figure 5.64. Lifetime data for macrocycle **1a** in DMSO.

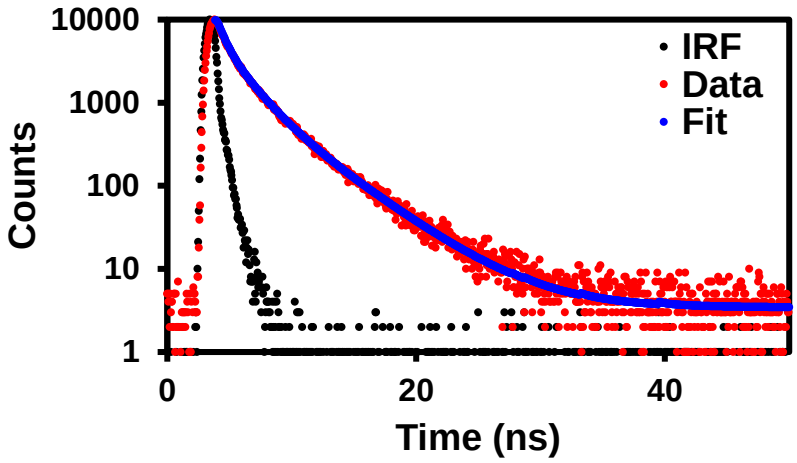

Figure 5.65. Lifetime data for activated **1a** in the solid-state.

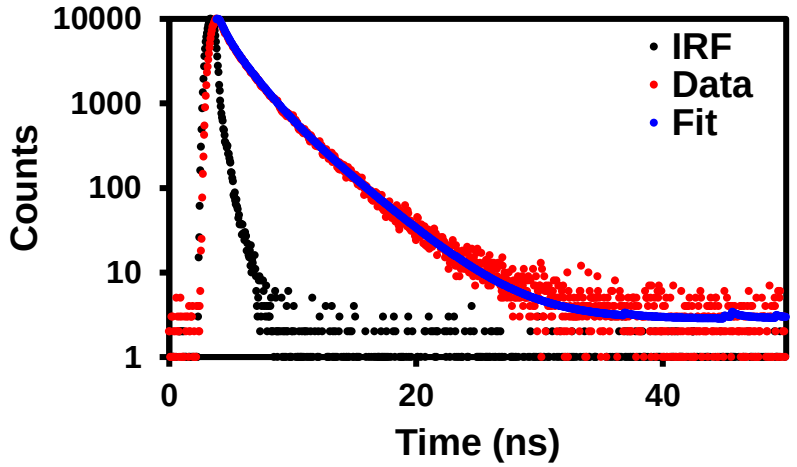

Figure 5.66. Lifetime data for complex **1a**·C_6H_6 in the solid-state.

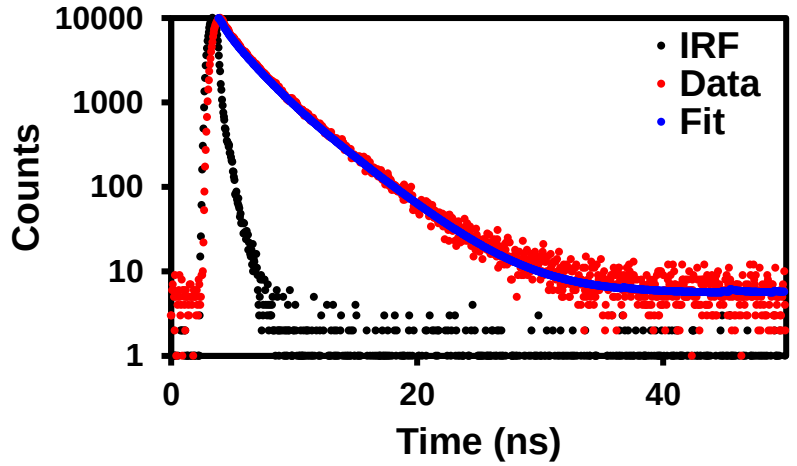

Figure 5.67. Lifetime data for complex **1a**·DME in the solid-state.

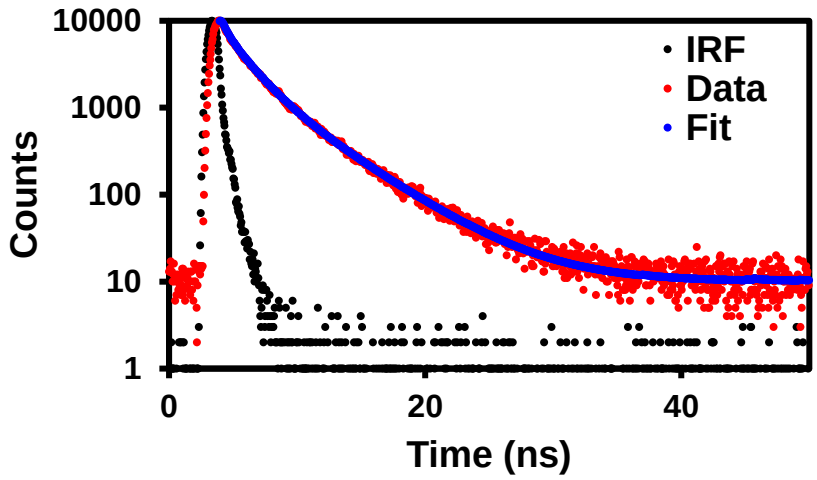

Figure 5.68. Lifetime data for complex **1a**·DMF in the solid-state.

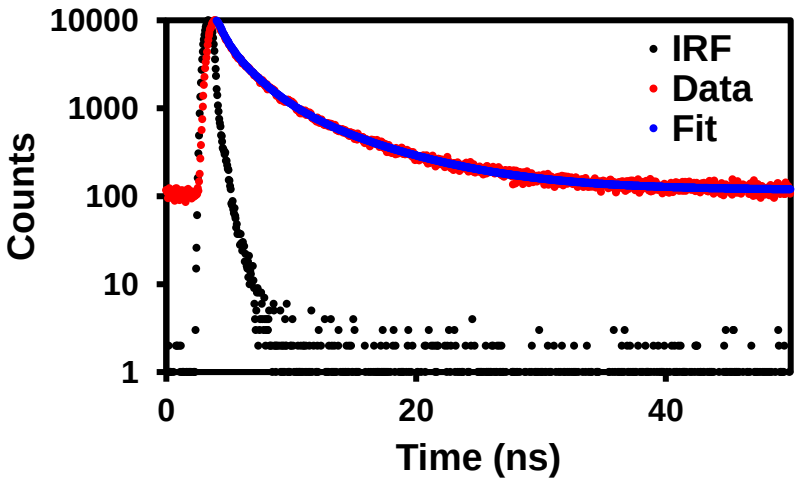

Figure 5.69. Lifetime data for linear analog **2** in the solid-state.

Table 5.6. Data Collection and Refinement for Macrocycle **2** Related Compounds.

Compound	B_1	τ_1 (ns)	B_2	τ_2 (ns)	B_3	τ_3 (ns)	τ_{av} (ns)	X^2
1	0.0614	0.536	0.0437	2.144	0.0096	5.959	1.6	1.290
10 μM **1a** in DMSO	0.0754	1.435	0.0134	7.126			2.3	1.336
1a	0.0749	0.501	0.0301	1.785	0.0096	4.157	1.1	1.327
1a·C_6H_6	0.0644	0.381	0.0374	1.691	0.0150	3.619	1.2	1.275
1a·DME	0.0591	0.328	0.0343	1.790	0.0220	3.866	1.4	1.314

1a·DMF	0.0640	0.347	0.0385	1.773	0.0150	4.491	1.3	1.268
2	0.0652	0.469	0.0348	2.057	0.0093	7.046	1.5	1.164

5.4.9 EPR Measurements

EPR measurements were carried out on a Bruker EMX plus equipped with a Bruker X-band microwave bridgehead and Xenon software (v 1.1b.66). All spectra were recorded at room temperature and a power of ~1.589 mW with a modulation amplitude of 2.0 G. The double integration to obtain peak areas was performed in the Xenon software. Samples were sealed under argon and UV-irradiated in Norell Suprasil Quartz EPR tubes.

One difference from previous studies was the light source used for irradiation.[8] Instead of using a medium pressure mercury arc lamp we used 365 LEDs. This was done because preliminary studies with TPA **1a** showed the formation of quartz impurities using the mercury lamp (the tube itself was generating a radical signal), which was disadvantageous especially at low radical concentrations of **1a**. The 365 LEDs precluded this issue as no radical signal was detected in the EPR tube after irradiation. To investigate if we were still activating the same radical processes as before we irradiated **2a** with the 365 LEDs to ensure the same spectra would be obtained as previously seen with the mercury lamp.[8] Indeed, a nearly identical spectra with the same *g*-value = 2.006 (Figure 9) was obtained. However, the sample did require a longer irradiation time to generate the same signal intensity as previously observed for the mercury lamp. This is likely due to the lower intensity of the LEDs versus the mercury lamp (15 W versus 450 W). Overall, this suggests we are activating the same radical generation process with the LEDs as with the medium pressure Hg lamp just at a slower rate.

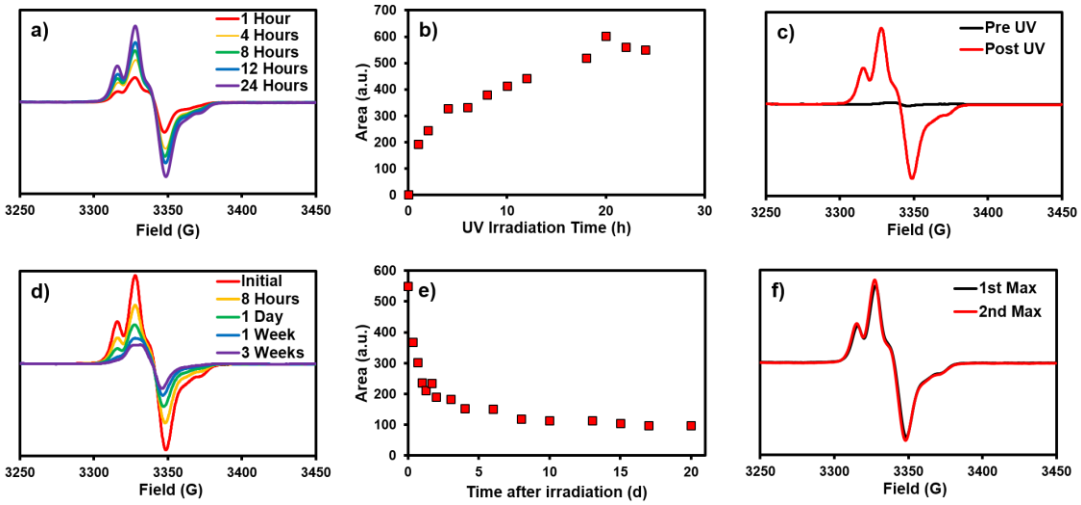

Figure 5.70. EPR data for activated **1a**. (a) EPR after incremental times of UV-irradiation. (b) Double integration over time of UV-irradiation. A maximum radical concentration of 0.69% was found for 9.8 mg of macrocycle by averaging the last four data points. (c) EPR signal pre and post UV irradiation. (d) Dark decay after initial UV-irradiation. (e) Double integration over time after initial UV-irradiation. (f) EPR signal after initial maximum radical concentration was reached (1st Max) versus when the maximum radical concentration was reached again (2nd Max) during the first cycle of radical regeneration (see Figure 5.8).

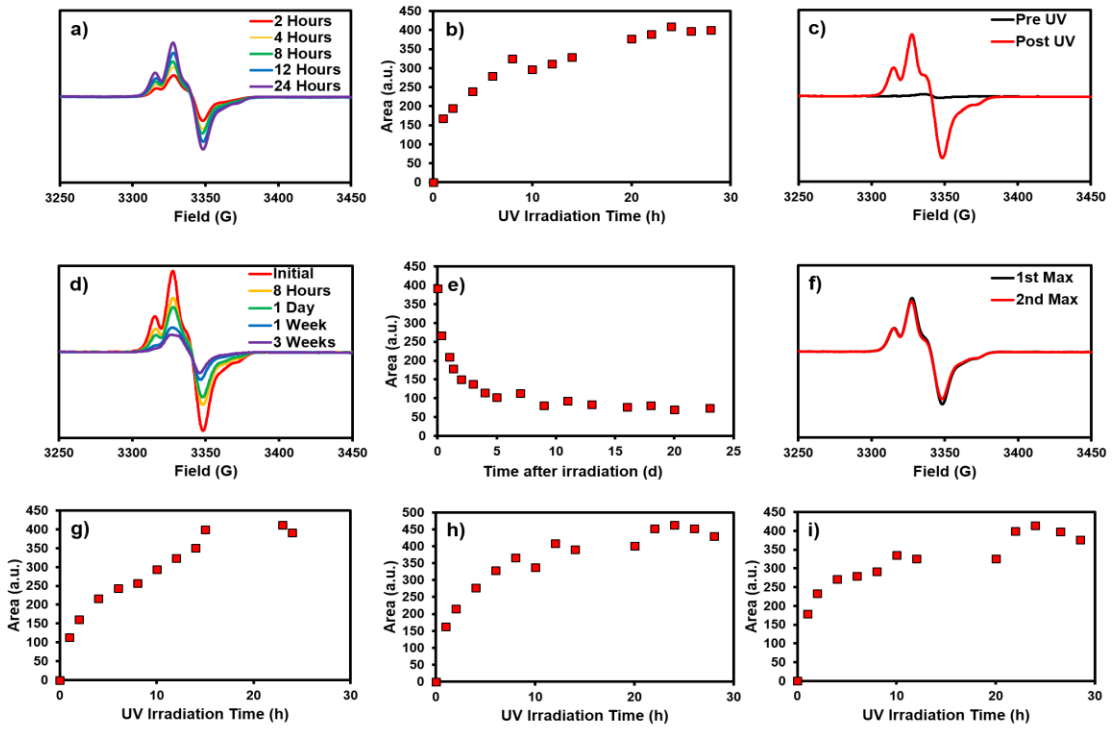

Figure 5.71. EPR data for complex **1a**·C_6H_6. (a) EPR after incremental times of UV-irradiation. (b) Double integration over time of UV-irradiation. A maximum radical concentration of 0.78% was found for 6.5 mg of macrocycle by averaging the last three data points. (c) EPR signal pre and post UV irradiation. (d) Dark decay after initial UV-irradiation. (e) Double integration over time after initial UV-irradiation. (f) EPR signal after initial maximum radical concentration was reached (1st Max) versus when the maximum radical concentration was reached again (2nd Max) during the first cycle of radical regeneration (see Figure 5.8). (g) A second trial of the double integration over time of UV-irradiation. A maximum radical concentration of 0.82% was found for 6.1 mg of macrocycle by averaging the last three data points. (h) A third trial of the double integration over time of UV-irradiation. A maximum radical concentration of 0.88% was found for 6.3 mg of macrocycle by averaging the last four data points. (i) A forth trial of the double integration over time of UV-irradiation. A maximum radical concentration of 0.93% was found for 5.3 mg of macrocycle by averaging the last four data points. An average maximum concentration of 0.85% was found over all four trials with a standard deviation of 0.06%.

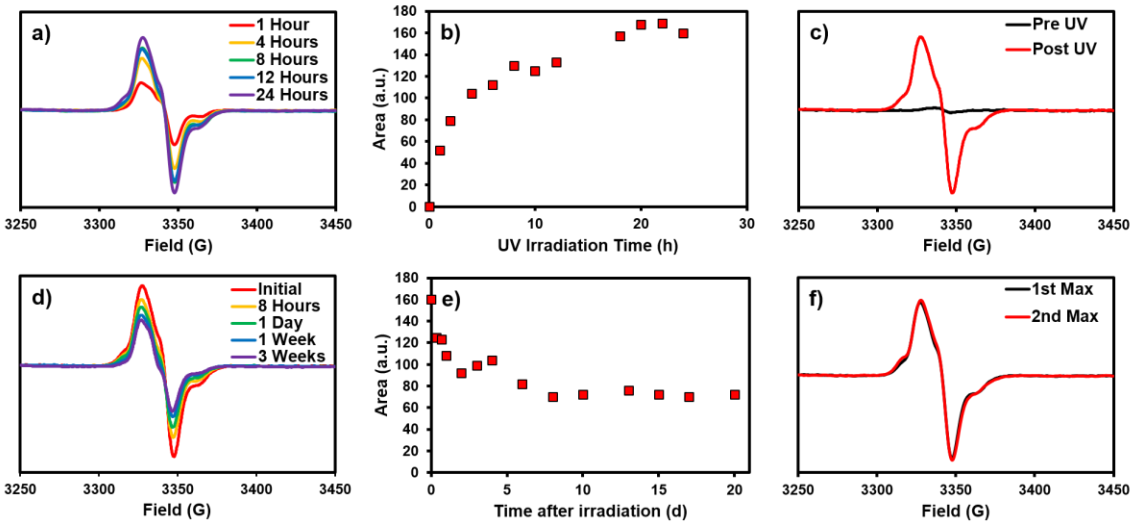

Figure 5.72. EPR data for complex **1a**·DME. (a) EPR after incremental times of UV-irradiation. (b) Double integration over time of UV-irradiation. A maximum radical concentration of 0.28% was found for 8.2 mg of macrocycle by averaging the last four data points. (c) EPR signal pre and post UV irradiation. (d) Dark decay after initial UV-irradiation. (e) Double integration over time after initial UV-irradiation. (f) EPR signal after initial maximum radical concentration was reached (1st Max) versus when the maximum radical concentration was reached again (2nd Max) during the first cycle of radical regeneration (see Figure 5.8).

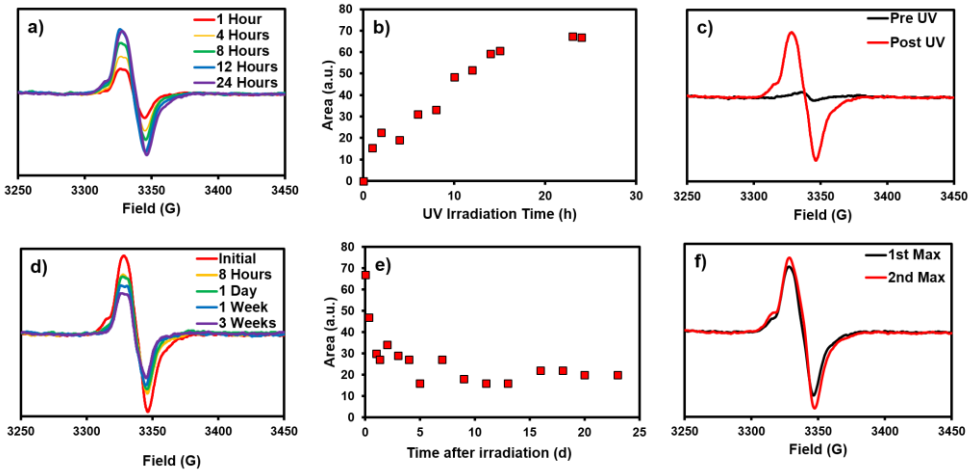

Figure 5.73. EPR data for complex **1a**·DMF. (a) EPR after incremental times of UV-irradiation. (b) Double integration over time of UV-irradiation. A maximum radical concentration of 0.15% was found for 8.1 mg of macrocycle by averaging the last two data points. (c) EPR signal pre and post UV irradiation. (d) Dark decay after initial UV-irradiation. (e) Double integration over time after initial UV-irradiation. (f) EPR signal after initial maximum radical concentration was reached (1st Max) versus when the maximum radical concentration was reached again (2nd Max) during the first cycle of radical regeneration (see Figure 5.8).

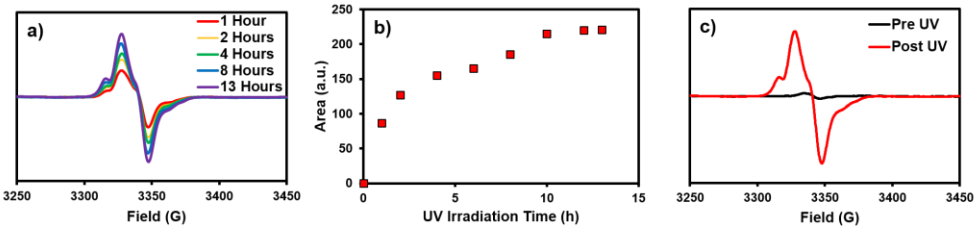

Figure 5.74. EPR data for complex **1a**·C_6H_5F. (a) EPR after incremental times of UV-irradiation. (b) Double integration over time of UV-irradiation. A maximum radical concentration of 0.45% was found for 6.6 mg of macrocycle by averaging the last two data points. (c) EPR signal pre and post UV irradiation.

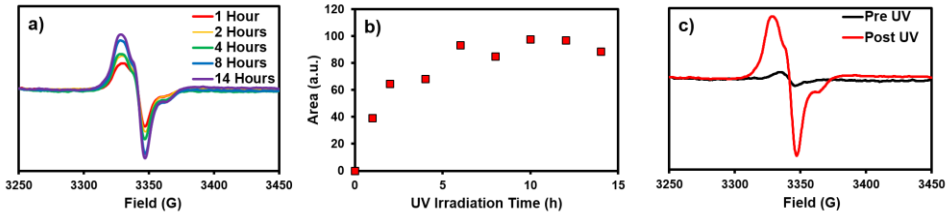

Figure 5.75. EPR data for complex **1a**·C_6H_5Cl. (a) EPR after incremental times of UV-irradiation. (b) Double integration over time of UV-irradiation. A maximum radical concentration of 0.24% was found for 6.2 mg of macrocycle by averaging the last five data points. (c) EPR signal pre and post UV irradiation.

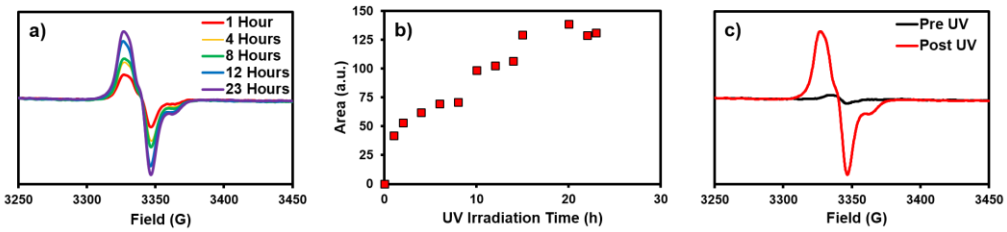

Figure 5.76. EPR data for complex **1a**·C_6H_5Br. (a) EPR after incremental times of UV-irradiation. (b) Double integration over time of UV-irradiation. A maximum radical concentration of 0.23% was found for 8.5 mg of macrocycle by averaging the last four data points. (c) EPR signal pre and post UV irradiation.

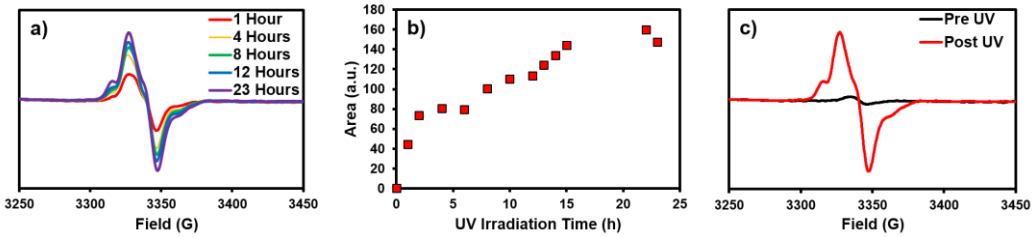

Figure 5.77. EPR data for complex **1a**·1,4-dioxanes. (a) EPR after incremental times of UV-irradiation. (b) Double integration over time of UV-irradiation. A maximum radical concentration of 0.38% was found for 5.6 mg of macrocycle by averaging the last three data points. (c) EPR signal pre and post UV irradiation.

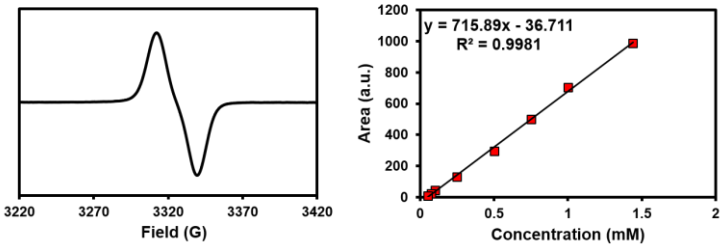

Figure 5.78. EPR data and radical concentration determination for Magic Blue. (A) EPR spectra for Magic Blue as a 1 mM solution in degassed dichloromethane. (B) Calibration curve for radical concentration determination. It should be noted that Magic Blue noticeably degrades after 4-6 weeks, so it must be used quickly once obtained.

5.4.10 NMR Spectra Pre and Post UV

NMR spectra were taken on a Bruker Avance III-HD 300 MHz spectrometer. Measurements were taken after radical regeneration studies were completed.

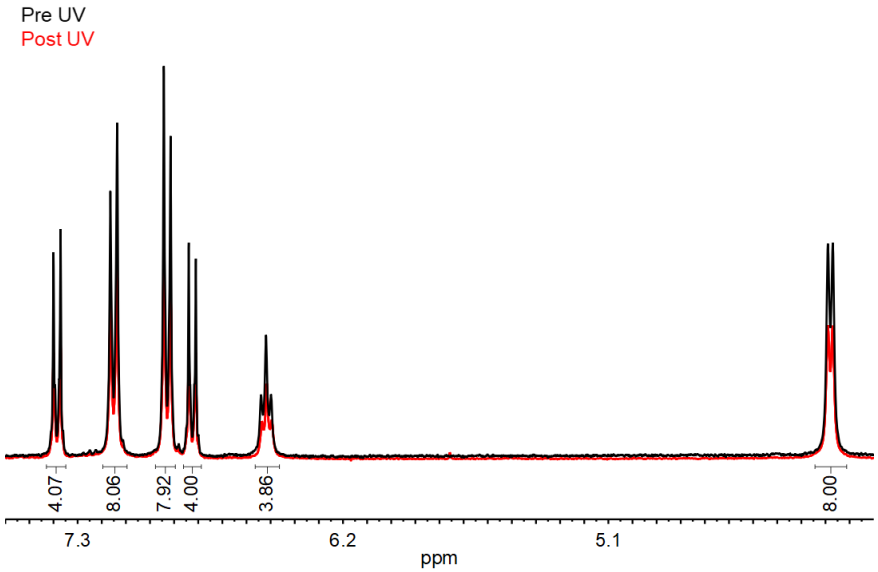

Figure 5.79. ^{1}H NMR of activated **1a** after radical regeneration studies (DMSO-d_6, 300 MHz). Sample was redissolved before measurement. No changes were observed for parent resonances of macrocycle **1a**. Peaks and integrals are for the redissolved sample (red). Black is for comparison represents a freshly synthesized sample of macrocycle **1a**.

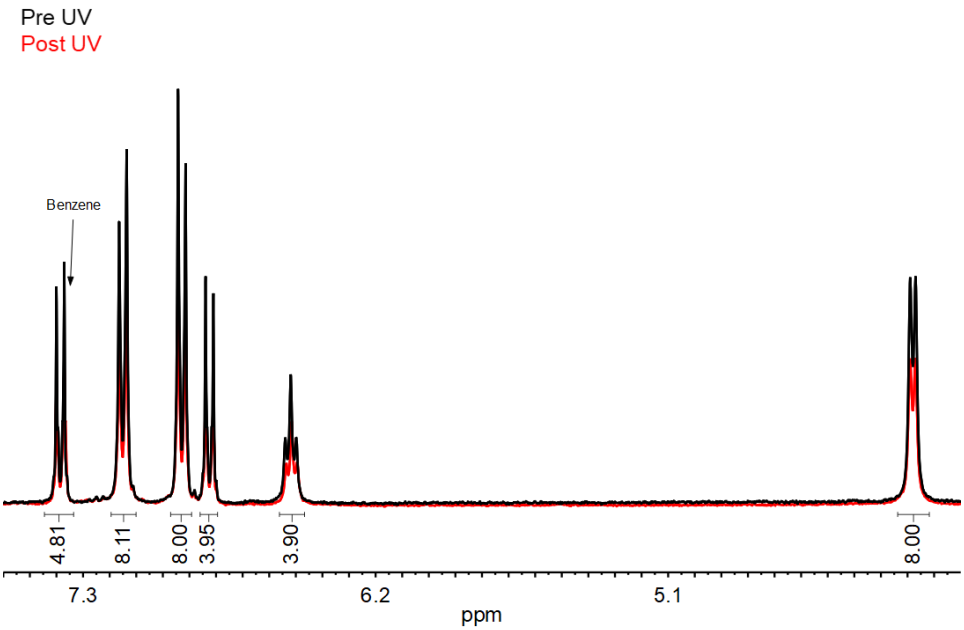

Figure 5.80. ^{1}H NMR of complex **1a**·C_6H_6 after radical regeneration studies (DMSO-d_6, 300 MHz). Sample was redissolved before measurement. No changes were observed for parent resonances of macrocycle **1a** except the benzene is now in the spectra (as it was the guest in complex **1a**·C_6H_6). Peaks and integrals are for the redissolved sample (red). Black is for comparison represents a freshly synthesized sample of macrocycle **1a**.

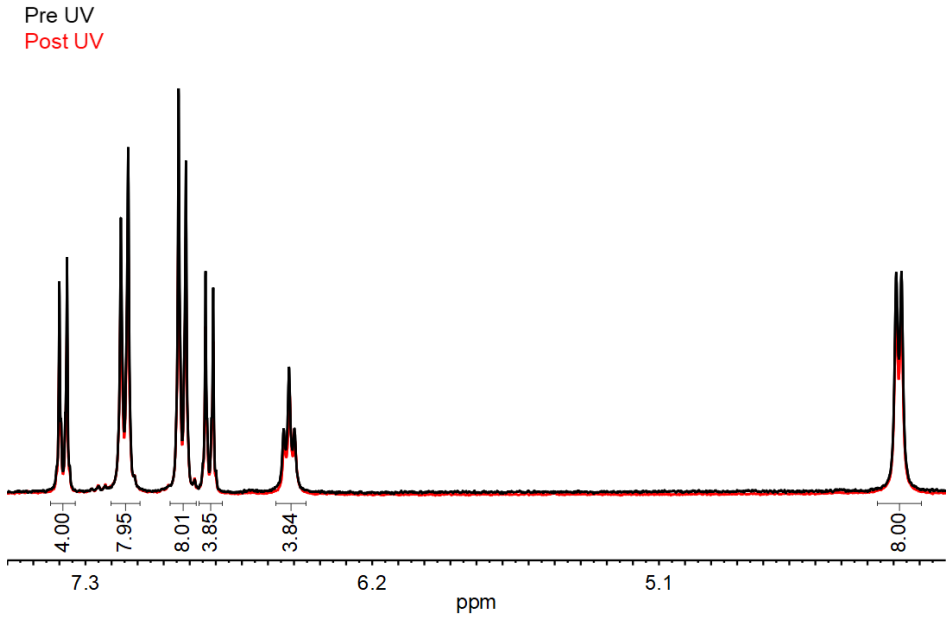

Figure 5.81. ^{1}H NMR of complex **1a**·DME after radical regeneration studies (DMSO-d_6, 300 MHz). Sample was redissolved before measurement. No changes were observed for parent resonances of macrocycle **1a**. Peaks and integrals are for the redissolved sample (red). Black is for comparison represents a freshly synthesized sample of macrocycle **1a**.

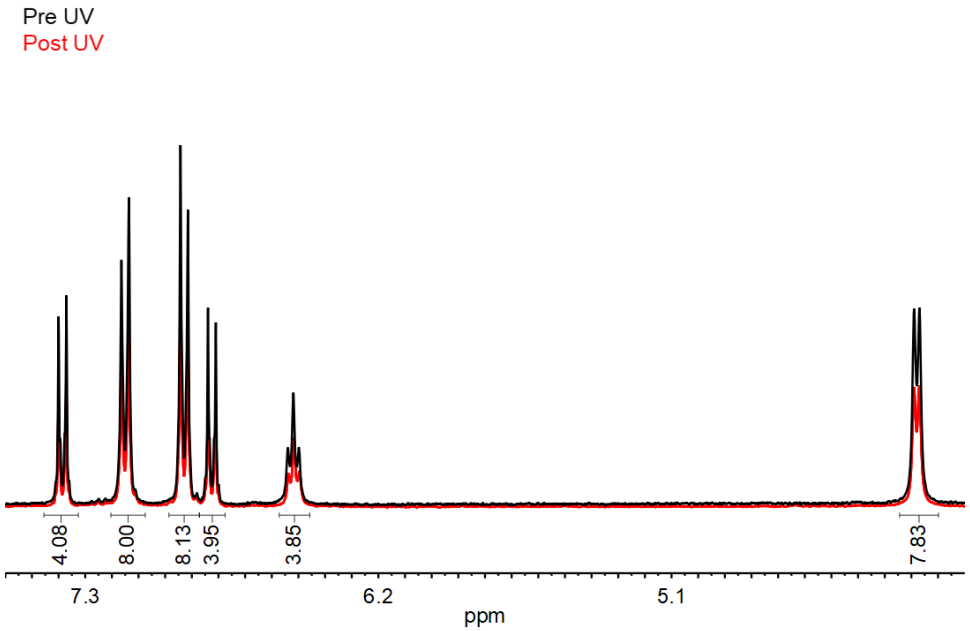

Figure 5.82. ^{1}H NMR of complex **1a**·DMF after photophysical studies (DMSO-d_6, 300 MHz). Sample was redissolved before measurement. No changes were observed for parent resonances of macrocycle **1a**. Peaks and integrals are for the redissolved sample (red). Black is for comparison represents a freshly synthesized sample of macrocycle **1a**.

5.4.11 Solid-state NMR

^{13}C CP MAS NMR were performed at 298 K using a wide-bore Avance III HD 17.6 T spectrometer (Bruker Biospin) at the Advanced Magnetic Resonance Imaging and Spectroscopy (AMRIS) Facility in Gainesville, Florida.

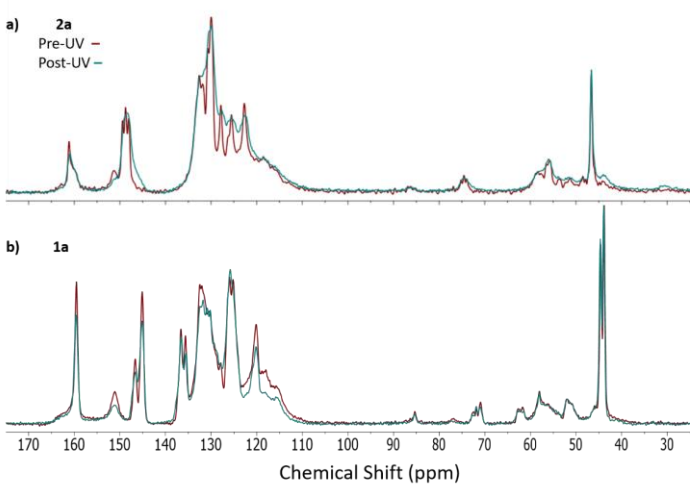

Figure 5.83. Room temperature carbon-13 CP-MAS NMR spectra of the pre and post-UV irradiated (8 hours irradiation) of the linear analog **2a** and activated host **1a** acquired at 17.6 T at a spinning speed of 14 kHz and a recycle delay of 3 s.

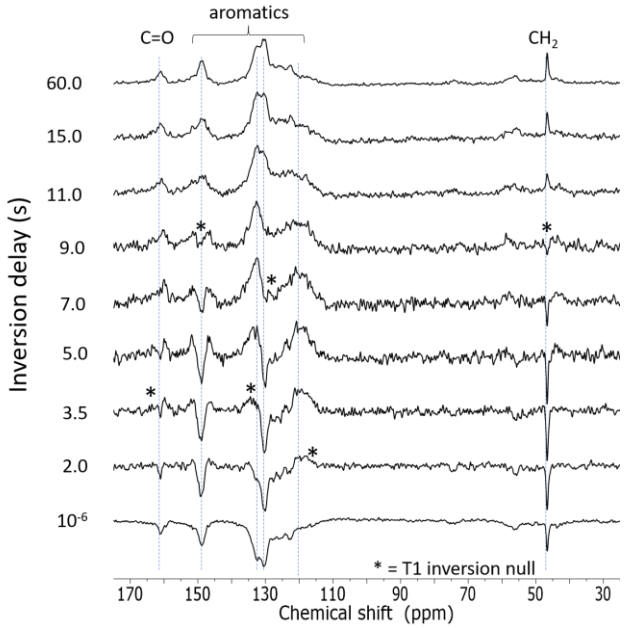

Figure 5.84. Room temperature carbon-13 detected proton T_1 inversion-recovery CP-MAS spectra for varying relaxation delay, acquired at 17.6 T at a spinning speed of 14 kHz.

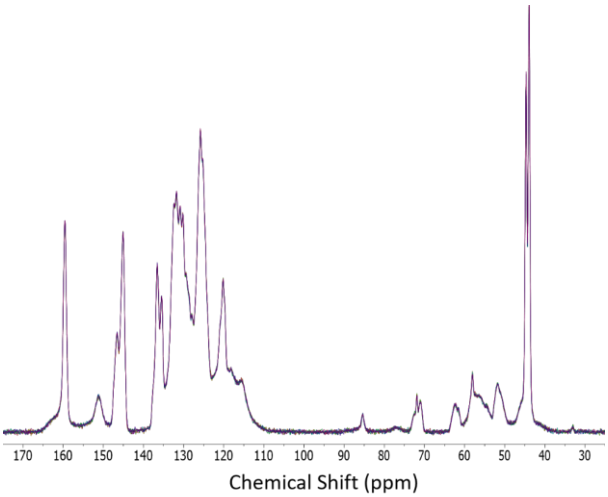

Figure 5.85. Overlay of the room temperature carbon-13 CP-MAS spectra of the post-UV irradiated activated host **1a** acquired at intervals of 106 minutes over the course of approximately 16 hours. The spectra are all identical, indicating the stability of the photoinduced radical on the timescale of the experiment.

5.4.12 Cyclic Voltammetry

Measurements were carried out in dichloromethane using a WaveDriver 20 Bipotentiostat combined with Aftermath software. Solutions contained 1 mM solute and 100 mM $((n\text{-Bu})_4N)^+(PF_6)^-$ as the electrolyte. Measurements were performed in an H cell equipped with a SCE reference, platinum wire counter, and glassy carbon working electrodes. Measurements were conducted at a potential rate of 100 mV/s.

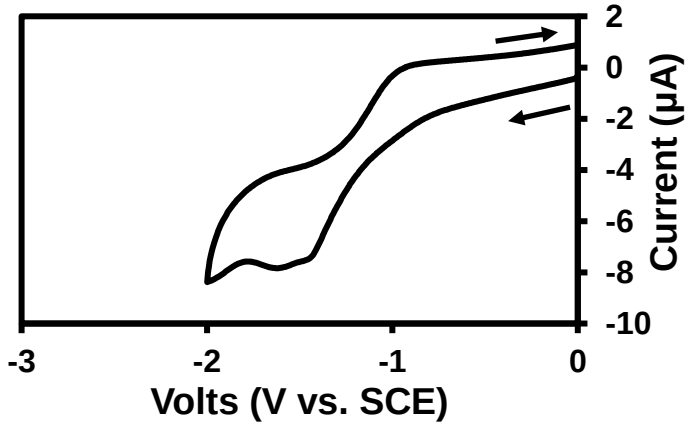

Figure 5.86. Reductive cyclic voltammetry for linear analog **2**.

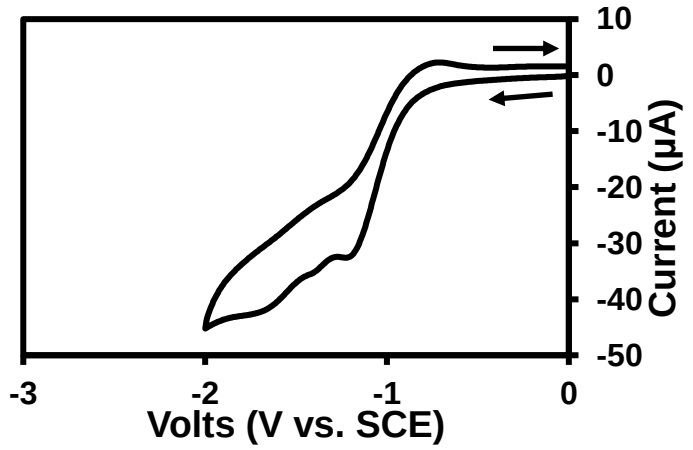

Figure 5.87. Reductive cyclic voltammetry for linear analog **2a**.

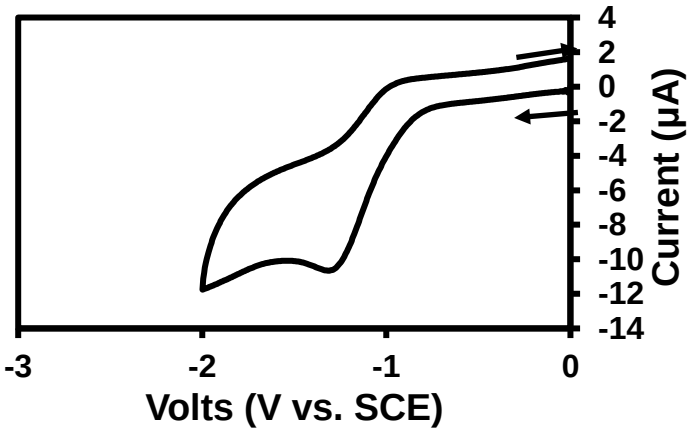

Figure 5.88. Reductive cyclic voltammetry for TPA **3**.

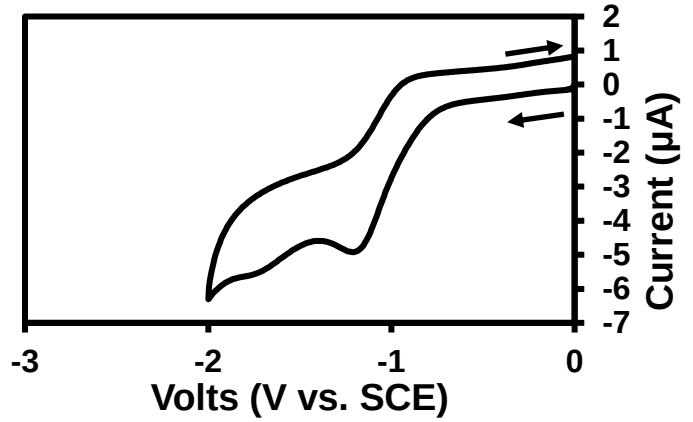

Figure 5.89. Reductive cyclic voltammetry for TPA **3a**.

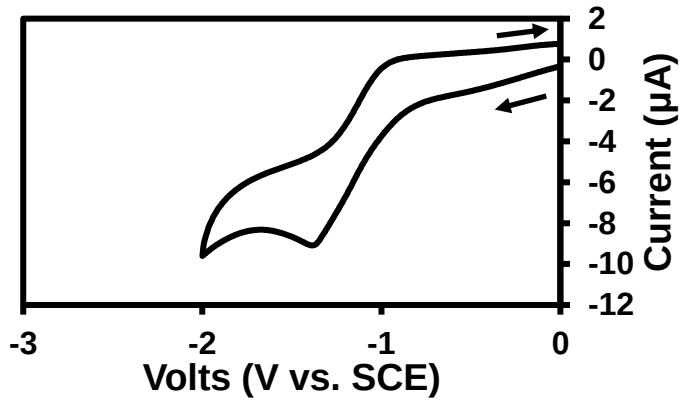

Figure 5.90. Reductive cyclic voltammetry for TPA **4**.

5.5 REFERENCES

1. Mattia, E.; Otto, S. *Nat. Nanotechnol.* **2015**, *10*, 111-119.
2. Mahadevi, A. S.; Sastry, G. N. *Chem. Rev.* **2016**, *116*, 2775-2825.
3. Steed, J. W. *Chem. Commun.* **2018**, 13175-13182.
4. Ogoshi, T.; Kakuta, T.; Yamagishi, T. *Angew. Chem., Int. Ed.* **2019**, *58*, 2197-2206.
5. Würthner, F.; Saha-Möller, C. R.; Fimmel, B.; Ogi, S.; Leowanawat, P.; Schmidt, D. *Chem. Rev.* **2016**, *116*, 962-1052.
6. Mills, M. B.; Wohlhauser, T.; Stein, B.; Verduyn, W. R.; Song, E.; Dechambenoit, P.; Rouzières, M.; Clérac, R.; Preuss, K. E. *J. Am. Chem. Soc.* **2018**, *140*, 16904-16908.
7. Liu, M.; Zhang, L.; Wang, T. *Chem. Rev.* **2015**, *115*, 7304-7397.
8. Das, S.; Heasman, P.; Ben, T.; Qiu, S. *Chem. Rev.* **2017**, *117*, 1515-1563.
9. Lin, R.-B.; He, Y.; Li, P.; Wang, H.; Zhou, W.; Chen, B. *Chem. Soc. Rev.* **2019**, *48*, 1362-1389.
10. Dhakshinamoorthy, A.; Alvaro, M.; Garcia, H. *Chem. Commun.* **2012**, *48*, 11275-11288.

11. Tan, Y.-X.; He, Y.-P.; Yuan, D.; Zhang, J. *Appl. Catal. B-Environ.* **2018**, *221*, 664-669.

12. Lü, J.; Cao, R. *Angew. Chem., Int. Ed.* **2016**, *55*, 9474-9480.

13. Kitagawa, S.; Kitaura, R.; Noro, S. *Angew. Chem., Int. Ed.* **2004**, *43*, 2334-2375.

14. Tabacchi, G. *ChemPhysChem* **2018**, *19*, 1249-1297.

15. Sumida, K.; Rogow, D. L.; Mason, J. A.; McDonald, T. M.; Bloch, E. D.; Herm, Z. R.; Bae, T.-H.; Long, J. R. *Chem. Rev.* **2012**, *112*, 724-781.

16. Li, J.-R.; Sculley, J.; Zhou, H.-C. *Chem. Rev.* **2011**, *112*, 869-932.

17. Kreno, L. E.; Leong, K.; Farha, O. K.; Allendorf, M.; Van Duyne, R. P.; Hupp, J. T. *Chem. Rev.* **2012**, *112*, 1105-1125.

18. Wales, D. J.; Grand, J.; Ting, V. P.; Burke, R. D.; Edler, K. J.; Bowen, C. R.; Mintova, S.; Burrows, A. D. *Chem. Soc. Rev.* **2015**, *44*, 4290-4321.

19. Comotti, A.; Bracco, S.; Sozzani, P. *Acc. Chem. Res.* **2016**, *49*, 1701-1710.

20. Alhamami, M.; Doan, H.; Cheng, C.-H. *Materials* **2014**, *7*, 3198-3250.

21. Yanai, N.; Uemura, T.; Inoue, M.; Matsuda, R.; Fukushima, T.; Tsujimoto, M.; Isoda, S.; Kitagawa, S. *J. Am. Chem. Soc.* **2012**, *134*, 4501-4504.

22. Akakuru, O. U.; Iqbal, M. Z.; Saeed, M.; Liu, C.; Paunesku, T.; Woloschak, G.; Hosmane, N. S.; Wu, A. *Bioconjugate Chem.* **2019**, *30*, 2264-2286.

23. Ratera, I.; Veciana, J. *Chem. Soc. Rev.* **2012**, *41*, 303-309.

24. Forrester, A. R.; Hay, J. M.; Thompson, R. H. *Organic Chemistry of Stable Free Radicals*; Academic Press: New York, 1968.

25. Ito, A.; Ino, H.; Tanaka, K.; Kanemoto, K.; Kato, T. *J. Org. Chem.* **2002**, *67*, 491-498.

26. Yano, M.; Sato, K.; Shiomi, D.; Ichimura, A.; Abe, K.; Takui, T.; Itoh, K. *Tetrahedron Lett.* **1996**, *37*, 9207-9210.

27. Fukui, N.; Cha, W.; Shimizu, D.; Oh, J.; Furukawa, K.; Yorimitsu, H.; Kim, D.; Osuka, A. *Chem. Sci.* **2017**, *8*, 189-199.

28. Bill, N. L.; Ishida, M.; Bähring, S.; Lim, J. M.; Lee, S.; Davis, C. M.; Lynch, V. M.; Nielsen, K. A.; Jeppesen, J. O.; Ohkubo, K.; Fukuzumi, S.; Kim, D.; Sessler, J. L. *J. Am. Chem. Soc.* **2013**, *135*, 10852-10862.

29. Murata, H.; Miyajima, D.; Nishide, H. *Macromolecules* **2006**, *39*, 6331-6335.

30. Skorka, L.; Kurzep, P.; Chauviré, T.; Dubois, L.; Mouesca, J.-M.; Maurel, V.; Kulszewicz-Bajer, I. *J. Phys. Chem. B* **2017**, *121*, 4293-4298.

31. Su, C.; He, H.; Xu, L.; Zhao, K.; Zheng, C.; Zhang, C. *J. Mater. Chem. A* **2017**, *5*, 2701-2709.

32. Chen, Z.; Su, C.; Zhu, X.; Xu, R.; Xu, L.; Zhang, C. *J. Polym. Sci. A: Polym. Chem.* **2018**, *56*, 2574-2583.

33. Agrarwala, P.; Kabra, D. *J. Mater. Chem. A* **2017**, *5*, 1348-1373.

34. Quinton, C.; Alain-Rizzo, V.; Dumas-Verdes, C.; Miomandre, F.; Clavier, G.; Audebert, P. *RSC Adv.* **2014**, *4*, 34332-34342.

35. Saha, A.; Chen, M.; Lederer, M.; Kahnt, A.; Lu, X.; Guldi, D. M. *Chem. Sci.* **2017**, *8*, 1360-1368.

36. Moulin, E.; Armao, J. J.; Giuseppone, N. *Acc. Chem. Res.* **2019**, *52*, 975-983.

37. Shimizu, L. S.; Salpage, S. R.; Korous, A. A. *Acc. Chem. Res.* **2014**, *47*, 2116-2127.

38. DeHaven, B. A.; Goodlett, D. W.; Sindt, A. J.; Noll, N.; De Vetta, M.; Smith, M. D.; Martin, C. R.; González, L.; Shimizu, L. S. *J. Am. Chem. Soc.* **2018**, *140*, 13064-13070.

39. Sindt, A. J.; DeHaven, B. A.; McEachern, D. F.; Dissanayake, D. M. M. M.; Smith, M. D.; Vannucci, A. K.; Shimizu, L. S. *Chem. Sci.* **2019**, *10*, 2670-2677.

40. Sindt, A. J.; Smith, M. D.; Berens, S.; Vasenkov, S.; Bowers, C. R.; Shimizu, L. S. *Chem. Comm.* **2019**, *55*, 5619-5622.

41. Ji, L.; Feng, M.-S.; Liu, Z.-Q.; Shen, Y.-X.; Chen, H.-F. *Org. Lett.* **2010**, *12*, 5192-5195.

42. Xu, D.; Ciszewski, L.; Li, T.; Repič, O.; Blacklock, T. J. *Tetrahedron Lett.* **1998**, *39*, 1107-1110.

43. Sobolev, A. N.; Belsky, V. K.; Romm, I. P.; Chermikova, N. Y.; Guryanova, E. N. *Acta Crystallogr. C* **1985**, *C41*, 967-971.

44. Turro, N. J.; Ramamurthy, V.; Scaiano, J. C. *Modern Molecular Photochemistry of Organic Molecules*; Viva Books: New Delhi, 2017.

45. Miller, J. C.; Meek, J. S.; Strickler, S. J. *J. Am. Chem. Soc.* **1977**, *99*, 8175-8179.

46. Würthner, F. *Chem. Commun.* **2004**, 1564-1579.

47. Yang, M.; Xu, D.; Xi, W.; Wang, L.; Zheng, J.; Huang, J.; Zhang, J.; Zhou, H.; Wu, J.; Tian, Y. *J. Org. Chem.* **2013**, *78*, 10344-10359.

48. Matsuura, T.; Omura, K. *Bull. Chem. Soc. Jpn.* **1966**, *39*, 944-947.

49. Data, P.; Pander, P.; Zassowski, P.; Mimaite, V.; Karon, K.; Lapkowski, M.; Grazulevicius, J. V.; Slepski, P.; Darowcki, K. *Electrochim. Acta* **2017**, *230*, 10-21.

50. Stoll, S.; Schweiger, A. *J. Magn. Reson.* **2006**, *178*, 42-55.

51. Li, Z.; Dong, Q.; Xu, B.; Li, H.; Wen, S.; Pei, J.; Yao, S.; Lu, H.; Li, P.; Tian, W. *Sol. Energy Mater. Sol. Cells* **2011**, *95*, 2272-2280.

52. Wang, Y.-X.; Leung, M.-K. *Macromolecules* **2011**, *44*, 8771-8779.

53. Chen, L.; Qian, G.; Jin, X.; Cui, Y.; Gao, J.; Wang, Z.; Wang, M. *J. Phys. Chem. B* **2007**, *111*, 3115-3121.

54. Paul, G. K.; Mwaura, J.; Argun, A. A.; Taranekar, P.; Reynolds, J. R. *Macromolecules* **2006**, *39*, 7789-7792.

55. Tian, H.; Yang, X.; Chen, R.; Zhang, R.; Hagfeldt, A.; Sun, L. *J. Phys. Chem. C* **2008**, *112*, 11023-11033.

56. Li, Q.-Q.; Zhong, A.-S.; Liu, H.-J.; Peng, M.; Liu, J.; Pei, Z.-G.; Huang, Z.-L.; Qin, J.-G.; Li, Z. *Sci. China Chem.* **2011**, *54*, 625-630.

57. Dubinina, G. G.; Price, R. S.; Abboud, K. A.; Wicks, G.; Wnuk, P.; Stepanenko, Y.; Drobizhev, M.; Rebane, A.; Schanze, K. S. *J. Am. Chem. Soc.* **2012**, *134*, 19346-19349.

58. APEX3 Version 2016.5-0, SAINT+ Version 8.37A; Bruker AXS, Inc.: Madison, WI, 2016.

59. Krause, L.; Herbst-Irmer, R.; Sheldrick, G. M.; Stalke, D. *J. Appl. Crystallogr.* **2015**, *48*, 3–10.

60. Sheldrick, G. M. *Acta Crystallogr. A* **2015**, *71*, 3–8.

61. Sheldrick, G. M. *Acta Crystallogr. C* **2015**, *71*, 3-8.

62. Dolomanov, O. V.; Bourhis, L. J.; Gildea, R. J.; Howard, J. A. K.; Puschmann, H. *J. Appl. Crystallogr.* **2009**, *42*, 339–341.

63. APEX3 Version 2016.9-0, SAINT+ Version 8.37A, TWINABS Version 2012/1, Cell_Now Version 2008/4; Bruker AXS, Inc.: Madison, WI, 2016.

64. APEX3 Version 2018.1-0, SAINT+ Version 8.38A; Bruker AXS, Inc.: Madison, WI, 2016.

CHAPTER 6

CONCLUSIONS AND FUTURE WORK

6.0 ABSTRACT

Self-assembly of small molecules into hierarchal structures can give rise to new properties unseen in solution. This helps create functional materials with emergent properties. To form these materials in high fidelity hydrogen bond directing groups such as ureas, thioureas, and squaramides can be used to guide hydrogen bond assembly in the solid-state. For example, the assembly of *m*-xylene macrocycles containing these directing groups each exhibit different solid-state assemblies with ureas directing the assembly of columnar nanotubes, thioureas directing the assembly of Herringbone sheets, and squaramides directing the assembly of interdigitated rings. Once assembled, hierarchal structures can start to exhibit new properties. For instance, urea tethered assemblies of TPAs display stable photogenerated radical formation upon self-assembly which is not seen in solution. Moreover, the number of radicals formed can be modulated by the substitution on the TPA moiety or by the supramolecular environment around the TPA via guest inclusion. This thesis explored the supramolecular assembly of TPA macrocycles to form robust nanotubes that can facilitate guests exchange via single-crystal-to-single-crystal transformations. This chapter will serve to summarize topics from prior chapters and provide insight on the future work that could be done for each research aim.

6.1 DISCUSSION

6.1.1 Chapter 2

Chapter 2 compared the conformational preferences and subsequent assembly of three hydrogen bonding groups: urea, thiourea and squaramide.[1] This was done by developing synthetic routes to form two small *m*-xylene macrocycles incorporating either two thioureas or two squaramides (Figure 6.1a, right two compounds, respectively). Next,

a large number of crystallization conditions were screened for crystal growth and four new crystal structures incorporating these macrocycles were determined. These new structures were compared and contrasted with previously reported crystal structures of the *bis*-squaramide and *bis*-urea macrocycles.[2,3]

For the thiourea macrocycle two different crystal structures were obtained: one of the pure material and the other as a solvate with ethylene diamine. In the non-solvated material (Figure 6.1b middle), the macrocycle was found in a *trans-trans* arrangement with both thiourea groups oriented approximately perpendicular to the *m*-xylene spacer. This arrangement was due controlled by the thiourea groups propensity to adopt perpendicular hydrogen bonding, which resulted in 2D Herringbone sheets. In the solvated structure, assembly was modulated by interactions with ethylene diamine. Here, the thiourea macrocycles exhibited both *cis-trans* and *trans-trans* arrangements to effectively hydrogen bond with the included amine solvent. This conformational flexibility in the thiourea macrocycle was also observed in solution via 2D Exchange Spectroscopy NMR. Overall, this macrocycle showed more conformational flexibility than the other macrocycles in both solution and the solid-state and afforded significantly different solid-state assembly due to the perpendicular hydrogen bonding motif of the thioureas.

In the squaramide system, two new crystal structures were obtained (one as a pure material and another as a propylene carbonate solvate) in conjunction with an already reported DMSO solvate. In the new structures, the squaramides adopted *trans-trans* arrangements as interdigitated macrocycles interlayered into 2D sheets. The interdigitation arose from bifurcated hydrogen bonding to one of the available two carbonyls hydrogen bonding motif from the squaramide units. The main difference between the new structures

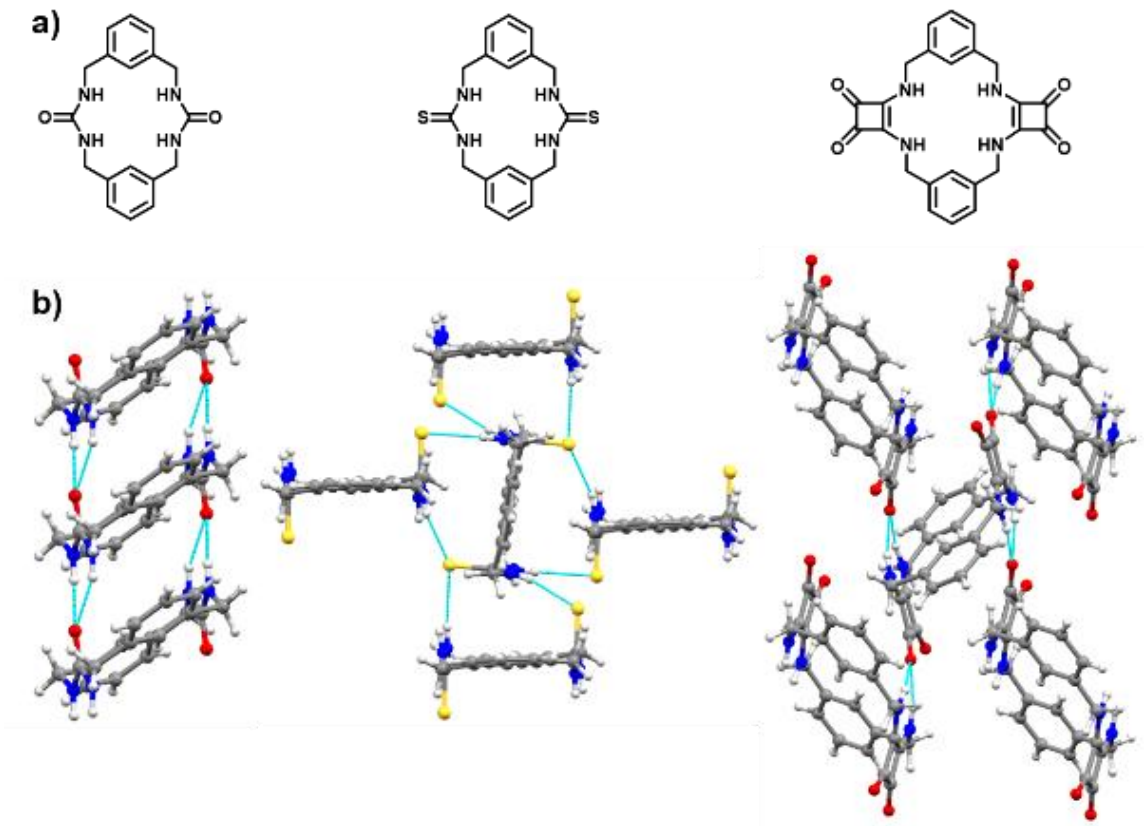

Figure 6.1. Comparison of the self-assembly of small *m*-xylene macrocycles. (a) Molecular structures of macrocycles. From left to right they are *bis*-urea, *bis*-thiourea, and *bis*-squaramide macrocycles. (b) Comparison of self-assembly.

was the addition of a solvate layer for the solvated propylene carbonate crystals. For comparison, the previously solved DMSO solvate also had the macrocycle in a *trans-trans* arrangement.[3] However, the amide hydrogens are engaged in bifurcated hydrogen bonding with DMSO solvent instead of the squaramide carbonyls. Despite this the overall conformation of the macrocycle was very similar to the other two crystal structures indicating this macrocyclic system has less flexibility versus the thiourea macrocycles.

For comparison, the *bis*-urea macrocycle crystallizes as a pure material with the macrocycles found in a *trans-trans* arrangement (Figure 6b, left).[2] This macrocycle organizes into small columnar nanotubes with assembly being driven by three-centered

hydrogen bonding on either side of the macrocycles. This bonding tapes up the sides of the nanotube.

Overall, the hydrogen bonding groups guide the assembly of small *m*-xyelene macrocycles in different ways. Thioureas display more conformational freedom and perpendicular hydrogen bonding. As a pure material it adopts 2D herringbone sheets. Squaramides display less conformational freedom and adopt a bifurcated hydrogen bonding motif. This results in a network of interdigitated macrocycles patterned into 2D sheets when crystallized as a pure compound. Lastly, ureas also display minimal conformational freedom in the solid-state and bifurcated hydrogen bonding. However, this resulted in 1D nanotubes unlike the squaramide macrocycles.

Although hydrogen bonds can be quite predictable when only one interaction is anticipated, it is often more unpredictable if multiple interactions are present. As our studies show, urea, thiourea and squaramide hydrogen bonding groups each have distinct geometric and distance preferences for their association in small macrocycles. Thus, it would be intriguing to see how the assembly of mixed macrocycles, which each contain two different assembly directing groups as seen in Figure 6.2, would play out. A wide screen of crystallization conditions could determine if one of the hydrogen bonding groups have preference over the others or if different crystal forms are obtained, indicating the promiscuity of assembly. This could help identify which hydrogen bonding motif is the most preferred when two different directing groups are in competition with each other. Comparison of the different crystal forms obtained by multiple crystallizations of the three possible mixed macrocycles can help gage how these directing groups interact with each other. These experimental studies could then be combined with computational models

which can check what sites are preferred for hydrogen bonding. By producing an electrostatic map of the molecule, the sites for hydrogen bond donation and acceptation can be predicted. In many cases, the most electropositive site (hydrogen bond donor) interacts with the most electronegative site (hydrogen bond acceptor) in the solid-state.[4] However, this is not always the case as sterics can also play a role. Thus, experimentation and computations combined would allow us to determine if the motif these macrocycles adopt are sterically or electrostatically driven.

Additional experiments in combination with the mixed macrocycles, could include testing the assembly larger *bis*-thiourea and *bis*-squramide macrocycles. In the macrocycles shown above, the directing groups were constrained into small, rigid *m*-xylene which contained no intrinsic pore. Thus, one question that could be posed is, "Does this constrained macrocycle system alter the assembly motif or limit the conformational flexibility of the hydrogen bonding groups?" To probe this question, one could synthesize a series of series of related *bis*-thiourea and *bis*-squaramide macrocycles with larger C-shape spacer units. For the *bis*-urea macrocycles, macrocycles with larger C-shape spacer units still adopted the similar 1D nanotube structure.[5] Thus, it would be interesting to see if thiourea and squaramide macrocycles would follow the same trend or if a new pattern would arise. This could be tested by incorporating phenyl ether or benzophenone C-shape

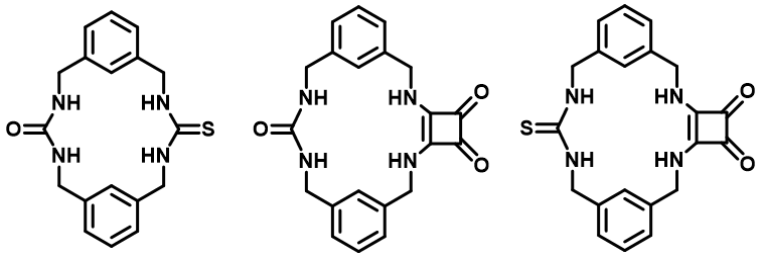

Figure 6.2. Potential mixed *m*-xylene macrocycles incorporating two different hydrogen bonding directing groups. From left to right they are urea/thiourea, urea/squaramide, and thiourea, and squaramide.

units into *bis*-thiourea and *bis*-squaramide macrocycles, as these spacers are larger than the original *m*-xylene unit. Upon assembly, crystal forms could be tested to analyze if the original assembly motifs were still observed (2D Herringbone patters and interdigitated macrocycles, respectively), or if a new framework was found. This would give insight into the origin of assembly motifs observed for *m*-xylene macrocycles. Are these assembled structures reflective of the hydrogen bonding directing groups preferences or are they also influenced by the small xylene spacer? In relation to this, it would also be interesting to see how forming mixed macrocycles with two different C-shape spacers (one phenyl ether C-shape and one benzophenone C-shape) affected the hydrogen bonding networks of these directing groups. Overall, these studies along with the proposed mixed macrocycles could help give better insight into how these hydrogen bond directing groups function and how predictable their structures are.

6.1.2 Chapter 3

In chapter 3, a methylene urea-tethered (TPA) dimer was synthesized and assembled into single crystals.[6] In solution, this molecule exhibited both fluorescence and phosphorescence based on the polarity or hydrogen bonding capability of the solvent. Radicals were observed upon UV-photoirradiation in solution, although these species were unstable and resulted in degradation of the material. However, radicals generated within the crystalline material were remarkably stable, demonstrating that self-assembly is a viable and potentially widely applicable strategy to stabilize photo-generated radicals. Electrochemical evidence and Electron Paramagnetic Resonance (EPR) spectroscopy suggest the radicals were formed through a charge separation process with the formation of a radical cation.

As seen in Figure 6.3, the synthesized TPA had bromine substitution on one *para* site. This played a large role in its photophysics due to the heavy atom effect which increases spin orbit coupling through intersystem crossing.[7] Initially, the molecule had very similar absorbance spectra in every tested solvent with a λ_{max} of absorption around 300 nm. However, the emission spectra were quite different with two bands arising: one around 365 nm and another around 450 nm. The intensity of these bands could change with the polarity of the tested solvent with non-polar solvent promoting the 365 nm band and polar solvents promoting 450 nm band. Literature precedent suggested the 365 nm band was from fluorescence.[8] However, the 450 nm band was more difficult to assign. Using DOSY NMR, monomeric 4-bromotriphenylamine emission studies, and triplet quenching experiments this band was assigned to phosphorescence as it was the most likely cause.

Next, EPR spectra were taken of the TPA molecule pre and post UV-irradiation. This was done to gauge the generation and stability of photogenerated radicals of the material. In solution, the TPA molecule exhibited a radical signal after 4 hours of UV-irradiation. However, an NMR the sample afterwards showed significant degradation of

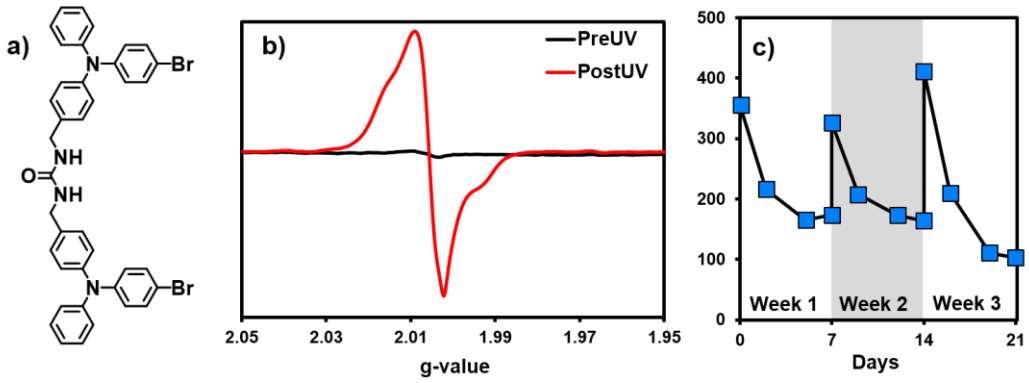

Figure 6.3. (a) Molecular structure of TPA used in radical studies in chapter 3. (b) EPR signal pre and post UV-irradiation in the solid-state. (c) Double integration of the EPR spectra after of UV irradiation. Every week the sample was re-irradiated back to its maximum concentration.

the material suggesting that radical formation for this molecule is unstable in solution. In the solid-state different results were found. Here, the TPA molecule could still form radicals, but the NMR spectra of the sample showed no degradation of the material. This suggested that radical formation in the solid-state was a stable process.

Following this, some of the characteristics of the radical were measured. It was found that an approximate maximum of 1 in 150 molecules could generate a radical after continual UV-irradiation. These radicals could last up to a month with a half-life of one week. Most surprisingly, re-irradiation of the material could regenerate radicals back to their original concentrations. Electrochemical studies suggested that radical generation for this material was a result of charge separation within the TPA molecule with a radical cation residing on the TPA.

Future work of these studies could include screening the assembly of TPA compounds with different halogen substitution, TPA macrocycles, and simple TPAs. This along with radical simulations of the EPR spectrum could help elucidate the structure of the photogenerated anion along with a possible mechanism for this process. Understanding how this process occurs could help in the design of better photoactive materials. The results of these studies for bromine substituted and unsubstituted derivatives were largely explored in Chapter 5.

Additional studies could investigate coupling strategies that employ the bromine as a handle for attaching electron acceptors. Although the anion formed upon UV-irradiation of the TPA has not yet been fully characterized, a covalently bonded known acceptor with the correct potential to accept an electron from the TPA donor host would help elucidate

this process. Two possible compounds for this study are shown in Figure 6.4. Here, the electron acceptor would be a derivative of 2,1,3-benzothiadiazole (BT), which has previously been shown to shown to accept electrons from TPAs via light irradiation.[9] TPA/BT molecules already have uses in the fabrication of OLEDs[10,11] and chemiluminescent materials.[9] By covalently binding these functional groups together, not only could we test their radical generation, we could also test more practical properties such as photoconductivity. Overall, these proposed studies could give insight on the potential applications of these materials.

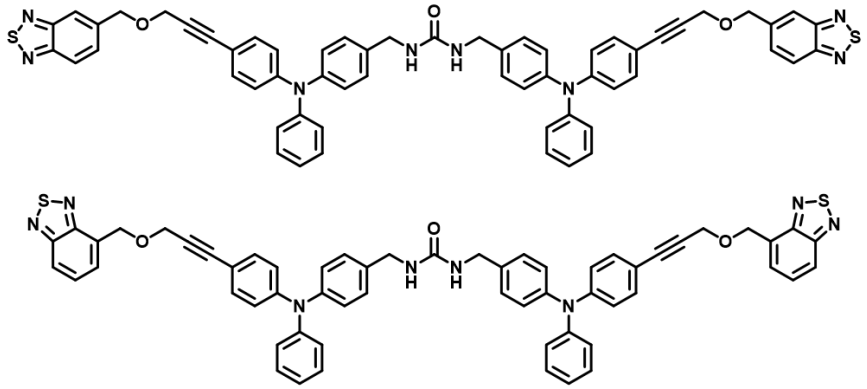

Figure 6.4. Potential TPA/BT covalently bound molecules

6.1.3 Chapter 4

Chapter 4 detailed how a brominated TPA *bis*-urea macrocycle self-assembled into robust nanotubes.[12] These porous tubes could be activated with heat and loaded with guests via single-crystal-to-single-crystal (SC-SC) transformations. Each host-guest complex along with the activated host was isoskeletal in regard to the original macrocycle framework. The activated host exhibited confined ^{129}Xe NMR signals when pressurized under xenon with ^{129}Xe PFG NMR measurements suggesting that the channels are homogeneous. Overall, a new robust porous organic material was formed with 1D porosity that allowed the exchange of guests in a SC-SC manner.

The TPA macrocycle shown in Figure 6.5 organizes into columnar nanotubes. These nanotubes are held together through a combination of offset π-π stacking between phenyl rings of the TPA and hydrogen bonding between the urea tethers. This results in robust nanotubes which have a pore aperture of 6.5 × 4.3 Å. This cross-sectional size was very similar to equivalent phenyl ether and benzophenone *bis*-urea macrocycle hosts.[13,14] Hirshfeld analysis of the TPA host indicated that individual nanotubes were held together with halogen-π stacking interactions. This resulted in unusually large crystals, which facilitated X-ray analysis. This in combination with heavy bromine atoms on the macrocycle makes this TPA host ideally suited for SC-SC transformational studies. Although other *bis*-urea hosts could exchange guests in a SC-SC manner as evidenced by excellent PXRD data[15,16] no single crystal data had been obtained until this TPA host was studied.

To activate the TPA host for guest exchange, a gentle amount of heating was applied to the host to remove the initial glyme (or DME) guest, which was present from the initial crystallization conditions. This resulted in an activated material that was used for two purposes. First, new guests could be added resulting in a new host-guest complex. For this, small benzene derivatives were loaded by soaking the TPA activated host in guest

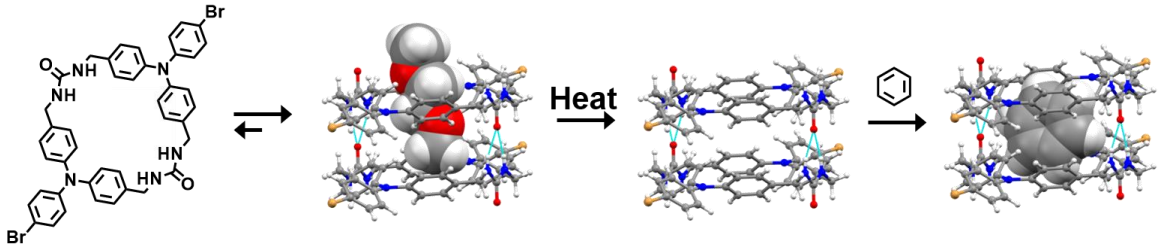

Figure 6.5. Brominated TPA macrocycles self-assembly into robust columnar structures. Heating the crystals results in an activated host. Suspending this host in a neat solution of a new guest results in a new host-guest complex. All of these processes follow SC-SC processes.

solutions. Single crystal data indicated the guests were displaced over four sites for every two macrocycles. This resulted host-guest ratio of approximately 1:0.5. For the second application, activated crystals were pressurized under a xenon atmosphere to probe the architecture of the material. The ^{129}Xe NMR spectra indicated two pore types which were in fast exchange with each other. These pores were tentatively assigned to the nanotubes and inter-columnar pores. ^{129}Xe pulsed filed gradient NMR experiments indicated there was no fast exchange between the columnar Xenon and the outside environment indicating there were no defects in the channel walls. Overall, this host proved useful in analyzing host-guest characteristics inside 1D channels.

Future research directions could explore applications of this new material in molecular separations. For example, one could probe the TPA host's ability to function as a size-exclusion material for the separation of small molecules. Similar work has been carried out with zeolites and metal-organic-frameworks (MOFs).[17] The pore size of these materials can influence how well certain compounds can be absorbed. For instance, the MOF, MIL-101, can absorb ethyl benzene and *p*-xylene at a higher capacity versus the *o*-xylene or *m*-xylene structural isomers.[18] It was suggested the effective molecular size of the absorbed guests was responsible for this observation. In comparison to MOFs and zeolites, the bis-urea hosts have simple homogeneous 1-D nanochannels with sub-nanometer diameters. In particular, the TPA host has a rigid 6.5 × 4.3 Å pore cross-sectional area, which is within the range for separating *meta* and *para* substituted benzenes. We expect the host would show selectivity for separating xylene isomers and aryl didiodides according to their cross-sectional size (Figure 6.6).[19-22] By placing the host in either a 1:1 vapor or liquid of these *meta* and *para* substituted benzenes, the host would be

screened to see if it could function as a size-exclusion material based on if there was selective loading or not. These experiments could give insight onto how rigid the pore of this TPA host is, and what some of its properties and limitations are.

Other bis-urea hosts have been applied as nanochambers for photoreactions of small molecules.[5] The nanotubes of the hosts orient photoactive guests such that selective photoproducts can be obtained. In solution, these molecules can react a number of ways due to free rotation giving rise to a large number of possible different products. However, encapsulation within the nanotubes limits the vibrational freedom of the molecules resulting in altered reactivity. Thus far, crystal structures of these host-guest structures have yet to be obtained and instead molecular modeling has been used to see how the guests orient inside the channels. While this works most of the time, sometimes products unanticipated from the modeling approach appear.[23] This was the case 6-bromochromone loaded inside the *m*-di(phenylethynyl)benzene (PHY) host. While, molecular modeling suggested the *syn*-head-to-head [2+2] photo-dimer was the expected photo-product, an aryl coupled product was obtained instead. Since the SC-XRD of the host-guest complex was

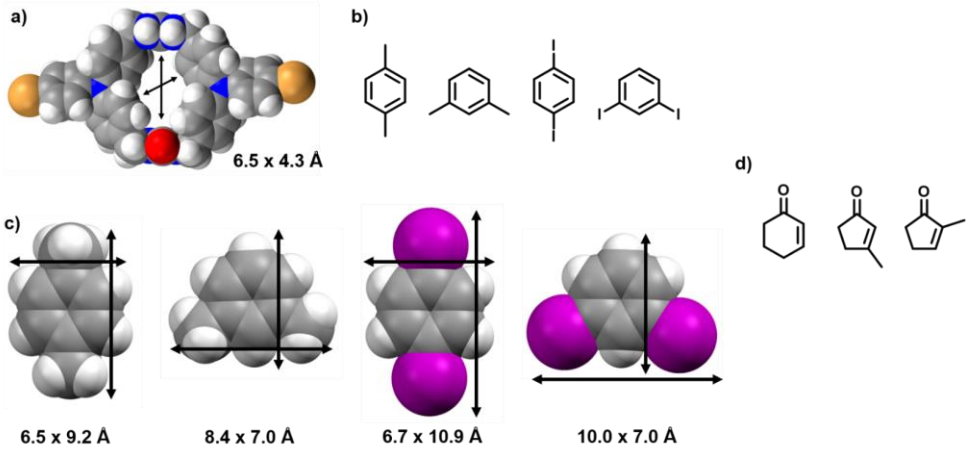

Figure 6.6. (a) Brominated TPA host with a rigid 1D channel with its pore aperture given.[12] (b) Potential guests that could be separated by the macrocycle host. (c) sizes of the guests from their crystal data.[19-22] (d) Potential photo-active guests that could be loaded into the TPA host for selective photo-reactions.[24,25]

not obtained it was not clear if the unexpected photo-product was a result of molecular packing of the guest inside of the host or if the bromine on the chromone was causing an unusual reaction pathway.

Similar studies could be carried out with the TPA system, keeping in mind its propensity for electron transfer. Advantageous, is that the TPA host, forms much larger crystals than prior *bis*-urea hosts and is therefore ideally suited for monitoring SC-SC transformation. Thus, this macrocycle could provide much needed insight into these processes. This would also improve molecular modeling approaches as well since there would be experimental data to better fit the molecular models too. Considering, the similarly sized phenyl ether host could facilitate selective photoreactions of small α, β-unsaturated ketones (Figure 6.6),[24,25] this family of guests are a good starting point for screening photoreactions inside the TPA host. Moreover, these guests should not accept an electron from the TPA host according to their reduction potential.[26] Overall, this new *bis*-urea host gives plenty of new opportunities in understanding how host-guest chemistry works within 1D environments.

6.1.4 Chapter 5

Chapter 5 investigated photophysical properties of columnar assembled TPA macrocycles. Small derivative molecules that contained some of the functional groups of the TPA macrocycle were prepared as controls were self-assembled in the solid-state as well.[27] The photophysical properties of these materials were measured with specific regard to photogenerated radical formation. It was found that polarity or heavy atom inclusion could limit the number of radicals formed and that two TPAs needed to be tethered together for a large amount of radical formation to occur. NMR, EPR, and EPR simulation evidence

suggest the radicals formed were a result of charge separation with a radical cation centered on the nitrogen center of the TPA framework. The other radical showed a broad signal with no identifiable features.

As mentioned above, several control compounds were made and crystallized. These included two TPA macrocycles, two TPA linear analogs, and three TPA controls with minimal substitution. Additionally, the X-ray structure of several host-guest structures of the bromine macrocycle host were reported. As described in chapter 4, this host could be activated and load new guests via SC-SC transformations with the TPA remaining isoskeletal. For these studies, this generated a series of complexes whose properties could be directly compared.

For the macrocycles and linear analogs, the photophysical properties of absorption, emission, and photoluminescent lifetimes were all approximately the same. Moreover, the properties of each host-guest complex of the bromine macrocycle were also similar. However, these trends were broken once the photophysical properties radical formation were considered. For the brominated macrocycle host-guest complexes, it was found that lowering heavy atom substitution or polarity increased the number of radicals observed using EPR spectroscopy (Figure 6.7). The benzene host-guest complex showed the most radical formation after 24 hours of irradiation with 0.78% of the molecules generating a radical while the more polar and heavy atom substituted complexes with *N*,*N*-dimethylformamide and bromobenzene displayed 0.15% and 0.23%, respectively. Overall, these complexes showed persistent radicals with an observable radical signal lasting up to 3 weeks with a half-life of 1 day. Moreover, reirradiation of these materials could regenerate the observed radical species very similarly to the materials in chapter 3 with

radical decay/regeneration processes remaining consistent without degrading the host material.

For the TPA derivatives, simple TPA displayed no radical formation while TPAs with one *para* substituted bromine or methylene urea could generate a small radical signal. To generate large radical signal two TPAs needed to be connected on either side of a methylene urea tether. This was evidenced by the macrocycles and linear analogs, which had this characteristic, as they generated the most radicals during UV-irradiation.

Electrochemical, NMR, and radical simulations suggested that the process of radical formation is a charge separation-based process with radical cation forming on the nitrogen center of the TPA group. Electrochemical studies indicate one TPA is oxidized while the other TPA is initially reduced. NMR studies indicate the TPA core and carbon of the urea carbonyl are the most affected by radical formation while the carbon of methylene bridge is the least affected. EPR simulations were best fit to double radical spectra with one radical being a hyperfine split radical cation on the nitrogen of the TPA core while the other radical was a broad signal. Overall, these studies show how

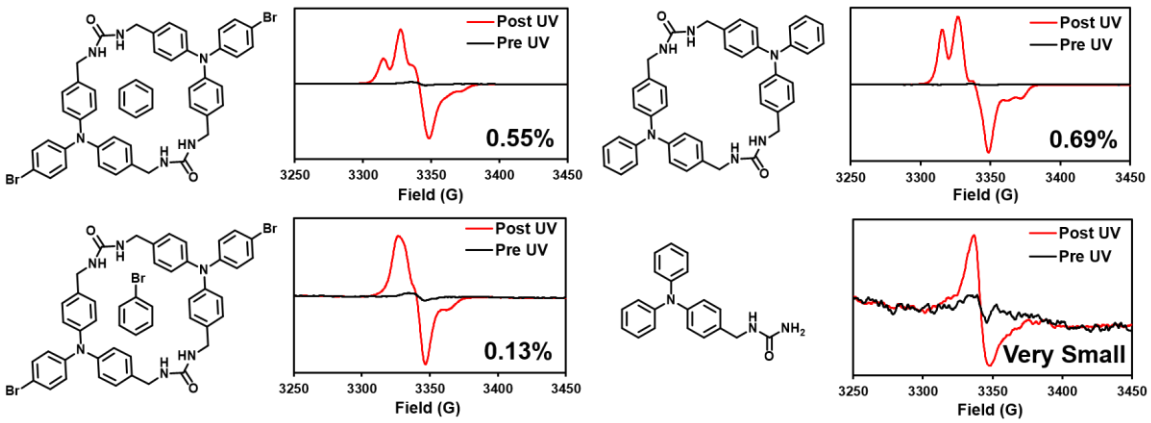

Figure 6.7. Radical formation in TPA materials. EPR spectra show radical signal pre and post UV-irradiation. Numbers in corner indicate what percentage of molecules generated a radical after 4 hours of irradiation.

supramolecular environments and molecular structure can define the photophysical properties of a material.

The next step in these studies is to examine these radicals with Q-Band EPR, electron nuclear double resonance (ENDOR), and electron spin echo envelope modulation (ESEEM). In anticipation of applying these methods, we have already sent samples to the Forbes group at Bowling Green State University and to the Wasielewski group at Northwestern University. Q-Band EPR is taken at a higher frequency that X-Band EPR (which is what was used for these studies) and therefore has a higher sensitivity to the observed radicals resulting in a better spectral resolution which could help differentiate the radical species in the TPA materials.[28] ENDOR and ESEEM both monitor NMR frequencies indirectly through EPR transitions.[29,30] This can give structural information of the radical such as what NMR active nuclei are close to the unpaired electron. The combination of these with Q-Band EPR could help elucidate the structure of the other radical in this system (non-radical cation) and give insight on a possible mechanism for the photogenerated radical process.

Additional work with these materials should include loading electron accepting guests into the host framework of the brominated macrocycle host. Similar to chapter 3, the anion formed upon UV-irradiation of the TPA was not identified in this work. Thus, by adding an electron accepting guest, the anion would be known as it would be located on the guest instead of in the TPA framework. Three possible guests for this include tetracyanoethylene (TCNE), tetracyanoquinodimethane (TCNQ), and 2,1,3-benzothiadiazole (Figure 6.8).[31-33] Although only the latter is small enough to fit inside the nanotubes (as a tilted structure), if molecular separations studies suggested as future work

for chapter 4 indicate the host is more flexible than anticipated then TCNE and TCNQ may be able to load as well since they are only 1 Å wider than the pore (7.2 and 7.5 Å, respectively, versus the 6.5 Å pore size). By loading these guests inside the TPA host, we could screen more practical applications of this material.

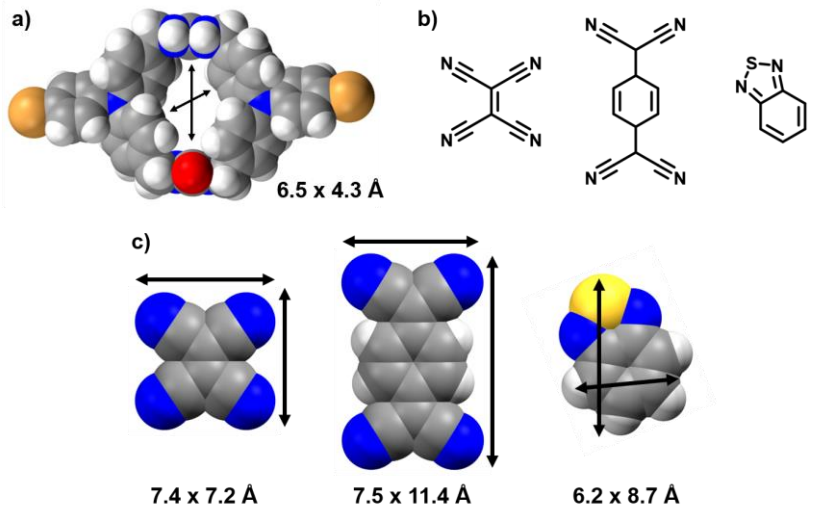

Figure 6.8. (a) Brominated TPA host with a rigid 1D channel with its pore aperture given.[12] (b) Potential electron accepting guests that could into the macrocycle host. (c) sizes of the guests from their crystal data.[31-33]

6.2 CONCLUSIONS

In summary, small molecules can self-assembly into the solid-state to new rise to new properties unseen in solution. These materials can be systematically formed from hydrogen bond directing groups. For example, the self-assembly of *m*-xylene macrocycles containing directing groups such as ureas, thioures, and squaramides each exhibit different structures when assembled. Thiourea macrocycles form Herringbone sheets, squaramide macrocycles form 2D sheets of interdigitated rings, and urea macrocycles form columnar nanotubes. Once assembled, structures can start to exhibit new properties. For instance, in solution, urea tethered assemblies of TPAs display unstable photogenerated radical formation. However, upon self-assembly this process becomes stable. In fact, persistent

radicals are formed whose concentration and persistence can be modulated by the substitution on the TPA moiety or by the supramolecular environment around the TPA. The latter of these can be exclusively examined with self-assembled TPA macrocycles which form robust nanotubes that facilitate guests exchange via SC-SC transformations. Overall, this research shows how emergent properties can be brought about through the directed self-assembly of small molecules.

6.3 REFERENCES

1. Sindt, A. J.; Smith, M. D.; Pellechia, P. J.; Shimizu, L. S. *Cryst. Growth Des.* **2018**, *18*, 1605-1612.
2. Shimizu, L. S.; Smith, M. D.; Hughes, A. D.; Shimizu, K. D. *Chem. Commun.* **2001**, 1592-1593.
3. Qin, L.; Hartley, A.; Turner, P.; Joliffe, K. A. *Chem. Sci.* **2016**, *7*, 4563-4572.
4. Price, S. L. *CrystEngComm* **2004**, *6*, 344-353.
5. Shimizu, L. S.; Salpage, S. R.; Korous, A. A. *Acc. Chem Res.* **2014**, *47*, 2116-2127.
6. Sindt, A. J.; DeHaven, B. A.; McEachern, D. F.; Dissanayake, D. M. M. M.; Smith, M. D.; Vannucci, A. K.; Shimizu, L. S. *Chem. Sci.* **2019**, *10*, 2670-2677.
7. Turro, N. J.; Ramamurthy, V.; Scaiano, J. C. *Modern Molecular Photochemistry of Organic Molecules*. Viva Books: New Delhi, 2017.
8. Kuramoto, Y.; Nakagiri, T.; Matsui, Y.; Ohta, E.; Ogaki, T.; Ideka, H. *Photochem. Photobiol. Sci.* **2018**, *17*, 1157-1168.
9. Omer, K. M.; Ku, S.-Y.; Cheng, J.-Z.; Chou, S.-H.; Wong, K.-T.; Bard, A. J. *J. Am Chem. Soc.* **2011**, *133*, 5492-5499.

10. Peng, Z.; Zhang, K.; Huang, Z.; Wang, Z.; Duttwyler, S.; Wang, Y.; Lu, P. *J. Mater. Chem. C* **2019**, *7*, 2430-2435.
11. Lo, Y.-C.; Yeh, T.-H.; Wang, C.-K.; Peng, B.-J.; Hsiech, J.-L.; Lee, C.-C.; Liu, S.-W.; Wong, K.-T. *ACS Appl. Mater. Interfaces* **2019**, *11*, 23417-23427.
12. Sindt, A. J.; Smith, M. D.; Berens, S.; Vasenkov, S.; Bowers, C. R.; Shimizu, L. S. *Chem. Commun.* **2019**, *55*, 5619-5622.
13. Shimizu, L. S.; Hughes, A. D.; Smith, M. D.; Davis, M. J.; Zhang, B. P.; zur Loye, H.-C.; Shimizu, K. D. *J. Am. Chem. Soc.* **2003**, *125*, 14972-14973.
14. Dewal, M. B.; Xu, Y.; Yang, J.; Mohammed, F.; Smith, M. D.; Shimizu, L. S. *Chem. Commun.* **2008**, 3909-3911.
15. Dewal, M. B.; Lufaso, M. W.; Hughes, A. D.; Samuel, S. A.; Pellechia, P.; Shimizu, L. S. *Chem. Mater.* **2006**, *18*, 4855-4864.
16. Dawn, S.; Dewal, M. B.; Sobransingh, D.; Paderes, M. C.; Wibowo, A. C.; Smith, M. D.; Krause, J. A.; Pellechia, P. J.; Shimizu, L. S. *J. Am. Chem. Soc.* **2011**, *133*, 7025-7032.
17. Yang, Y.; Bai, P.; Guo, X. *Ind. Eng. Chem. Res.* **2017**, *56*, 14725-14753.
18. Yang, K.; Sun, Q.; Xue, F.; Lin, D. *J. Hazard. Mater.* **2011**, *195*, 124-131.
19. Kryukova, M. A.; Sapegin, A. V.; Novikov, A. S.; Krasavin, M.; Ivanov, D. M. *Crystals* **2019**, *9*, 71.
20. Ibberson, R. M.; David, W. I. F.; Parsons, S.; Prager, M.; Shankland, K. *J. Mol. Struct.* **2000**, *524*, 121-128.
21. van Koningsveld, H.; van den Berg, A. J.; Jansen, J. C.; de Goede, R. *Acta Crystallogr. B* **1986**, *42*, 491-497.

22. Sankaran, H.; Sharma, S. M.; Sikka, S. K.; Chidambaram, R. *Pramana J. Phys.* **1986**, *27*, 835-839.

23. Salpage, S. R.; Donevant, L. S.; Smith, M. D.; Bick, A.; Shimizu L. S. *J. Photochem. Photobiol. A-Chem.* **2016**, *315*, 14-24.

24. Yang, J.; Dewal, M. B.; Shimizu, L. S. *J. Am. Chem. Soc.* **2006**, *128*, 8122-8123.

25. Yang, J.; Dewal, M. B.; Profeta, S.; Smith, M. D.; Li, Y.; Shimizu, L. S. *J. Am. Chem. Soc.* **2008**, *130*, 612-621.

26. House, H. O.; Huber, L. E.; Umen, M. J. *J. Am. Chem. Soc.* **1972**, *94*, 8471-8475.

27. Sindt, A. J.; DeHaven, B. A.; Goodlett, D. W.; Hartel, J. O.; Ayare, P. J.; Du, Y.; Smith, M. D.; Mehta, A. K.; Brugh, A. M.; Forbes, M. D. E.; Bowers, C. R.; Vannucci, A. K.; Shimizu, L. S. Guest Inclusion Modulates Concentration and Persistence of Photo-generated Radicals in Assembled Triphenylamine Macrocycles. *Submitted to J. Am. Chem. Soc.* October 25, 2019. ja-2019-115189.

28. Roessler, M. M.; Saladori, E. *Chem. Soc. Rev.* **2018**, *47*, 2534-2553.

29. Murphy, D. M.; Farley, R. D. *Chem. Soc. Rev.* **2006**, *35*, 249-268.

30. Deligiannakis, Y.; Louloudi, M.; Hadjiliads, N. *Coord. Chem. Rev.* **2000**, *204*, 1-112.

31. Little, R. G.; Pautler, D.; Coppens, P. *Acta Crystallogr. B* **1971**, *27*, 1493-1499.

32. Long, R. E.; Sparks, R. A.; Trueblood, K. N. *Acta Crystallor.* **1965**, *18*, 932-939.

33. Suzuki, T.; Tsuji, T.; Okubo, T.; Okada, A.; Obana, Y.; Fukushima, T.; Miyashi, T.; Yamashita, Y. *J. Org. Chem.* **2001**, *66*, 8954-8960.

APPENDIX A

MODELING THE PHOTO EXCITED STATE TRANSTIONS IN SELF-ASSEMBLED METHYLENE UREA TETHERED BENZOPHENONES*

*Adapted with permission from DeHaven, B. A.; Goodlett, D. W.; **Sindt, A. J.**; Noll, N.; De Vetta, M.; Smith, M. D.; Martin, C. R.; González, L.; Shimizu, L. S. *J. Am. Chem. Soc.* **2018**, *140,* 13064-13070.

A.1 INTRODUCTION

Benzophenone is a compound which can be used as photoinitiator for polymerizations,[1,2] antimicrobial coatings,[3,4] and as an oxidant for removing environmental pollutants, thanks to its photosensitizing properties.[5] A photosensitizer is a compound that, after irradiation with light, relaxes to a long-lived triplet excited state. In this triplet state it can react with oxygen forming reactive oxygen species, which can oxidize compounds in the surrounding areas. Recently, the Shimizu group have used this property to selectively oxidize 2-methyl-2-butene to 3-methyl-2-butene-1-ol at a 90% selectivity among other reactions.[6] This was done by self-assembling macrocycle 1 (Figure A.1) into 1D channels. The macrocycles are made with two benzophenone groups in close proximity separated by two methylene urea units which help stack the macrocycles into columns via the three centered urea hydrogen bonding network.[7] Once assembled, the columns form a host with open channels approximately 7 Å in diameter which allow for the loading of guests for selective oxidations. Additionally, upon UV irradiation, this host can relax into the triplet state and undergo a hydrogen abstraction reaction forming a persistent radical species. This radical species can be used, for example, to enhance the NMR signal of guests using the DNP-NMR technique.[8] This phenomenon is not observed for regular benzophenone as its radical form is only detected at low temperatures or using radical trapping techniques.[9,10]

In order to unravel the origin of the outstanding properties showed by the macrocycle, we have examined the excited states its two linear analogues reported in Figure A.1. Although these compounds do not contain any cavity (i.e. channels) like macrocycle 1, they still exhibit the same photophysical behavior and therefore represent a good model system for study. Specifically, we want to examine the excited states of these

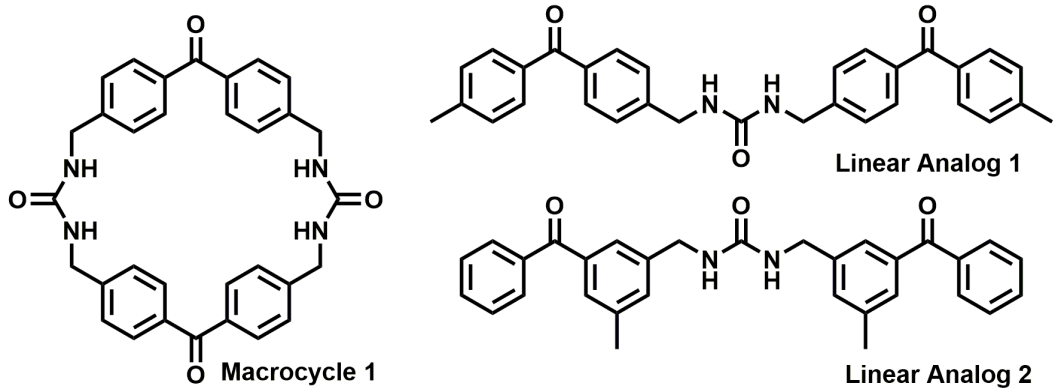

Figure A.1. Compounds to be discussed in this appendix.

molecules in two different conditions: in the solid-state and in a solution of dimethyl sulfoxide (DMSO). This would allow us to identify what is the role of the crystal structure and of the solvent in the unusual photophysics showed by these analogs in the two different states. The simulation of the absorption properties of these compounds in different environments is the first step towards the understanding of the photophysical phenomena observed experimentally.

A.2 COMPUTATIONAL DETAILS

The computational method of choice should provide reasonable energies at a feasible computational cost. We have considered the second order Algebraic Diagrammatic Construction for the polarization propagator (ADC(2))[11] coupled with a single valence polarized basis set that also accounts for dispersion correction (def2-SVPD).[12] Unfortunately, the description of the two linear analogs requires the calculations of a large number of excited states to properly reproduce the features of the experimental absorption band. Therefore, we have employed this more accurate method as reference for time dependent density functional theory (TDDFT). This method introduces larger approximations and is very much dependent by the choice of the exchange and correlation (xc) functional; it also allows, though, to calculate more excited states at lower

computational costs. The TDDFT calculations were performed with the wB97XD[13] xc-functional and the double zeta polarized basis set including diffused functions 6-31+G**.[14] Such a long-range corrected functional can partially describe excitations with charge transfer character and includes dispersion corrections.

Slices from the experimental crystal structures will be examined to distinguish which are of the most relevant moieties for the description of the absorption spectrum. Natural transition orbitals (NTOs) for the most important transitions will also be employed for this purpose, together with a charge transfer descriptor and the electron/hole population analysis available in the TheoDore software package.[15] Then the excited states computed for the crystalline structures in gas phase will be compared to those calculated in solvent.

The solvent dimethyl sulfoxide (DMSO) and its effects on the compounds absorption properties were described by the implicit solvation model PCM.[16] First, the geometry of the linear analogs were optimized at the DFT wB97XD/6-31G** level of theory. Diffused functions prevented the geometry optimization convergence in solvent, so the optimization was done in gas phase. After optimization, the excited states were calculated again with TDDFT, using the same long-range corrected xc-functional and basis set.

To compute the absorption of the half-structures we have calculated 15 excited states. For the other calculations 25 states were sufficient to reproduce the main features of the experimental spectrum.

A.3 THEORETICAL BACKGROUND

TDDFT and ADC vary slightly in how they calculate excited states. For TDDFT it is a modification of DFT which calculates the electronic structure of a system based on a system's electron density instead of its wave function like hartree-fock (HF) or post-HF methods. For DFT an equivalent electron density of non-interacting electrons is calculated for each electron and exchange-correlation functionals are added to recover these interactions to give an approximate solution. This solves the many-body problem and is cheaper (more timely) than many HF methods, but this theory only applies to the ground state.[17] For the calculations of excited states a time-dependent version of DFT was developed which includes additional theorems in its calculation.[18] Overall, this creates a system that can generate accurate spectra at low cost.[19] Unfortunately, TDDFT can run into issues with long-range charge transfer states[20] and requires benchmarks for reliability since TDDFT can be unpredictable at times and is not systematically improvable.[21] ADC on the other hand solves the many-body problem using Green's function theory.[22] Using this method propagators are generated which yield solutions to a certain class of problems.[23,24] Certain propagators like the polarization propagators can be used to find the evolution of a molecule's electronic system. This propagator acts on the ground-state of the wavefunction and propagates the density variances of the many-body system.[25] This insinuates that polarization propagator implicitly contains information on the excited states of molecule. By using this one can extract the excited state information from an ADC calculation.

The environment surrounding a molecule can play a huge role in its absorption properties. However, modeling a compound surrounded by thousands of solvent molecules is unfeasible and expensive. Because of this many solvent models have been developed to

address this issue. One of these, the polarizable continuum model (PCM), addresses this issue by embedding the molecule of interest in a dielectric continuum cavity defined by the atomic radii. The continuum polarizes the molecule to give the effect of being in a solvent.

A.4 RESULTS

For the benchmark of the TDDFT method against the more accurate ADC(2) we have selected the half LA 1 (Figure A.2) and we have computed its absorption spectrum with the two methods. Next, the method of choice will be used on the slices of LA 1's and LA 2's crystal structures reported in Figure A.2.

A.4.1 Linear Analog 1

Between the half LA's absorption calculated with the two computational methods specified above, ADC(2) gives better relative intensities for the main peaks of the

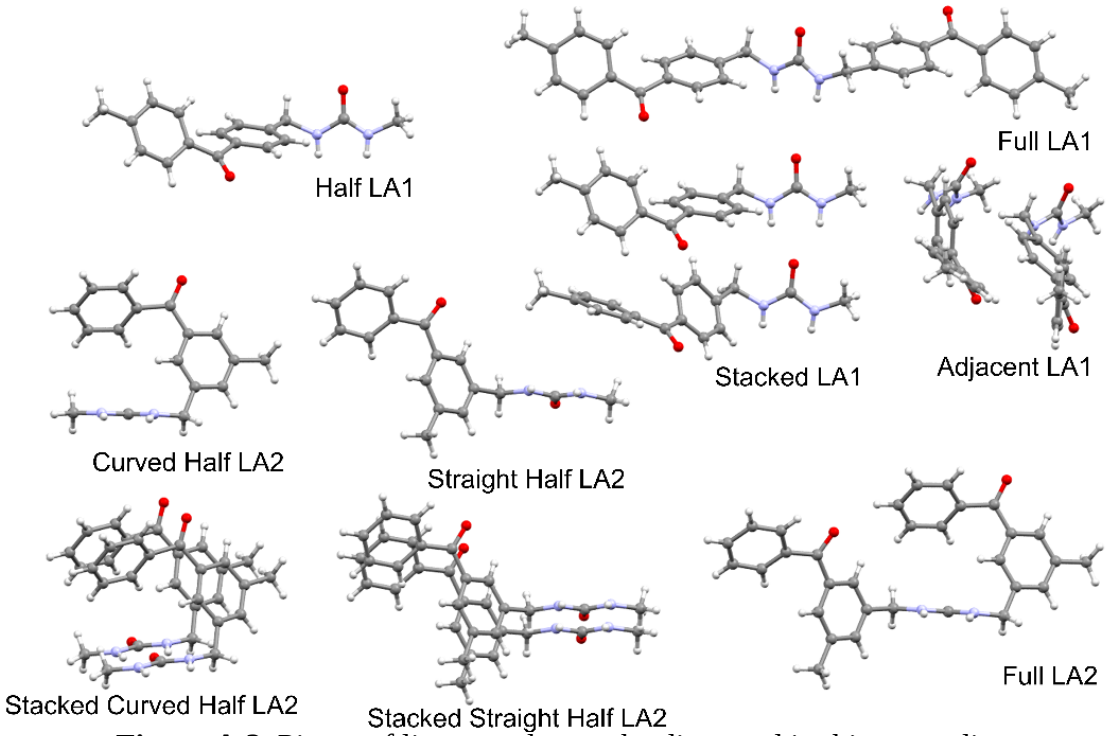

Figure A.2. Pieces of linear analogs to be discussed in this appendix.

absorption spectrum. Nevertheless, both methods are able to reproduce the two main peaks of the absorption spectrum at ~240 (Band 1) and ~200 nm (Band 2) with Band 1 being more intense (Figure A.3). Band 1 is blue-shifted with respect the experimental values by 141 and 129 nm for the ADC(2) and TDDFT calculations, respectively. This is due to the approximations introduced in the simulation: the periodicity of the crystal is not considered since the spectra of the analogue is computed in gas phase and to some extent such shifts are inherent to the theoretical model. In both cases, Band 1 is missing features that characterize the experimental spectra which could be considered as shoulders of the most intense peak. It is clear that half LA is a poor model to accurately represent the whole crystal, although it produces the most intense peak raised by ππ* transitions. Both methods are also able to find the nπ* excitation as lowest singlet excited state. Although being a dark transition, it is the one responsible for the radical formation in the solid-state and therefore important for further considerations on the photophysical properties of these compounds. The agreement between the two methods is then considered satisfactory and united with the gain in computational cost, allowed us to conveniently use TDDFT for all the other compounds studied.

To qualitatively reproduce the shape of the experimental spectrum several slices of the crystal were taken into account (Figure A.2). These included: the full linear analog connected through the methylene urea spacer, two stacked half linear analogs connected to one another with hydrogen bonds through the urea moiety, and two adjacent half linear analogs which were spatially close to one another with minor π-stacking interactions. Of these, the full LA gave the spectrum that best matches the experimental one (Figure A.4a). It reproduces in fact one of the features of Band 1 missing in the previous simulations

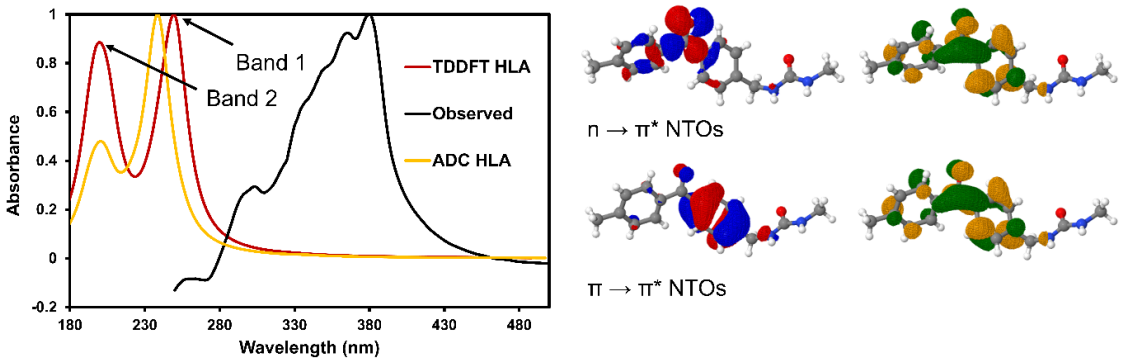

Figure A.3. Comparison between the ADC(2) and TDDFT calculations. On the left hand side the is the comparison between the ADC(2), TDDFT, and experimental absorption spectra. The back curve is the experimental spectrum recorded form the crystal state while the spectra computed with ADC(2) and TDDFT are reported in yellow and red respectively. On the right hand side are reported the NTO pairs for the n→π* and π→π* transitions from the ADC(2) calculation.

which is labelled as Band 1' in Figure A.4a. Upon closer inspection this peak is raised by three π→π* excitations (Figure A.4a). The first of these π→π* excitations, described by the NTOs pairs reported in panel b, was contributing to the main peak, Band 1, for the half LA absorption. Now, for the full analogue, it has shifted to higher energies, so it appears separately from Band 1 and contributes to Band 1'. The second π→π* excitation (Figure A.4c) contributing to this feature, was a dark state in the half model whereas in the full analogue it shows some absorption intensity. The third π→π* excitation is a new excited state, described by the NTOs reported in Figure A.4d. Even though we have improved the shape of the calculated spectra modelling the full analogue, the predicted energies are still significantly blue-shifted (119 nm) with respect the experimental one. Also for the full LA, the n→π* transitions are the lowest lying excited states, but this time there exists two distinct excitations, one for each benzophenone unit on either side of the urea spacer.

The adjacent and stacked LAs, gave similar absorption spectra to the half LA model. Most of their transitions are local excitations, with no charge transfer between one

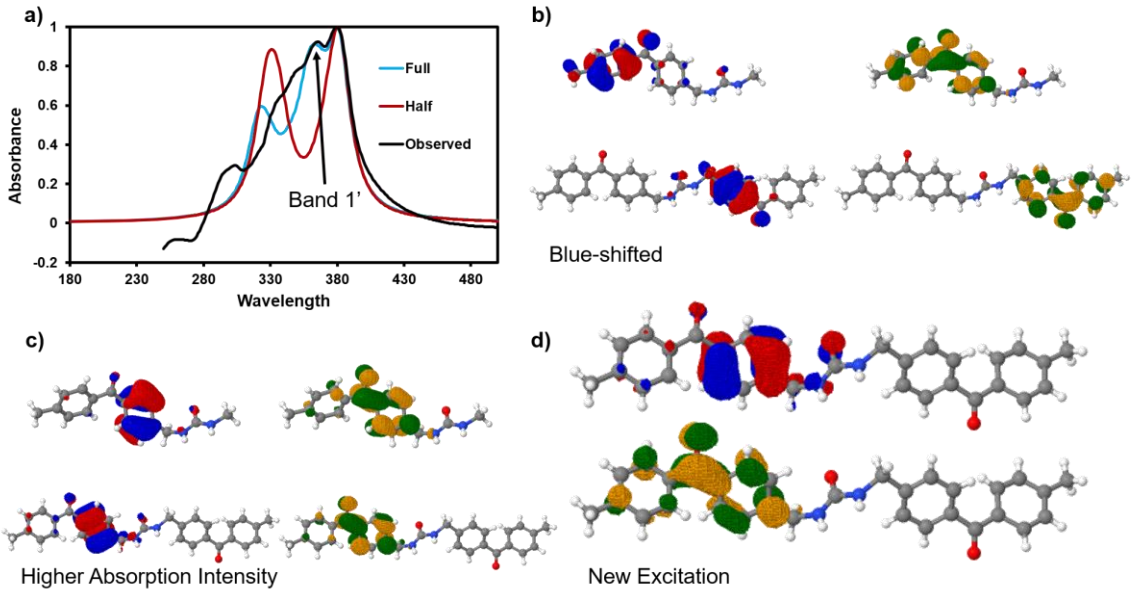

Figure A.4. Comparison between the spectra computed for half and the full linear analog. (a) Experimental and shifted computed spectrum for the LA. (b) NTOs from the blue-shifted excitation contributing to the Band 1' peak. (c) NTOs involved in the bright excited state of the full LA that was dark for the half model. (d) NTOs of the excitation contributing to the Band 1' that is present in the full LA spectrum but not in the half model one.

unit to the other, as visible also from the NTOs reported in Figure A.5. Both spectra are also not able to reproduce Band 1', just like the half LA model. For both of these models, 25 singlet excitations may have not been enough to fully describe the higher energy part of the spectrum. For example, the stacked LAs had major contributions from the 24th and 25th root for its higher energy peak, so it is unclear if more roots would change its shape or not.

To understand the effects of the solvent clearly visible from the experimental spectra reported in Figure A.6a we have compared the full LA absorption calculated in gas phase and in solvent. For the solvent calculation, the geometry was minimized using the PCM implicit model starting from the crystal structure geometry. In the geometry optimization, the two benzenes in the benzophenone unit rotate with respect to each other which can be monitored by measuring the average dihedral angle between the two, in this

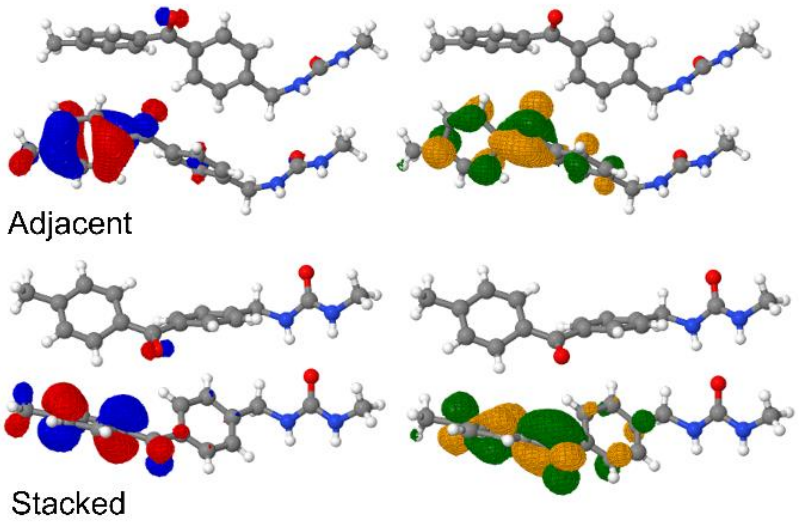

Figure A.5. Comparison between stacked and adjacent models of the linear analog. The NTOs clearly show that the transitions contributing to the main absorption features are local excitation on single benzophenone units.

case from 26.9˚ to 31.3˚. More noticeably, the benzene rings directly connected to the urea spacer move from being in plane with each other and roughly perpendicular to the urea to an out of plane arrangement. Such motion can also be monitored with the dihedral, but now the dihedral is measured between the benzene and the urea unit. In this case the shift is from 81.5˚ to 67.6˚. These structural modifications are visualized in Figure A.4b. The calculated spectrum in solvent is blue-shifted by only 5 nm with respect the experimental solvent spectra which itself is blue-shifted by 120 nm from the one recorded in the solid-state. The theoretical and experimental spectra in solution are therefore in very good agreement.

The main difference between the excited states in solution, with respect to the solid state ones, is the participation of both benzene rings of the benzophenone unit in the excitations raising the main absorption feature as opposed to only one in the solid state. Another significant difference is that there is the loss of all the fine structures that were

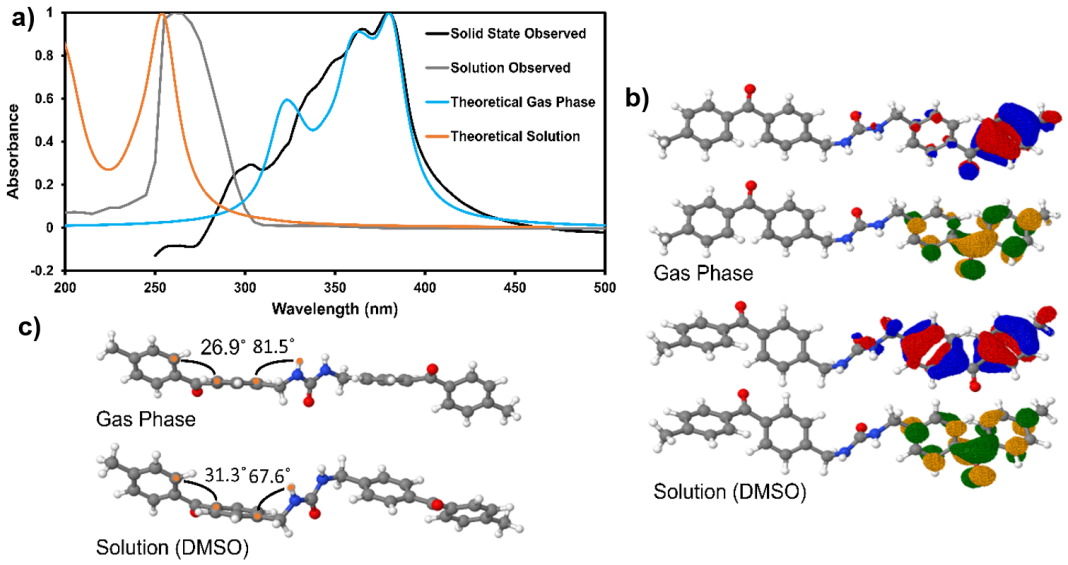

Figure A.6. Comparison between the full (gas phase) and solvent LA 1. (a) Experimental (solution and solid state), shifted theoretical gas phase, and unshifted theoretical solution spectra of LA 1. (b) The prominent NTOs for the major absorption band for both calculations. (c) Differences in geometry between the gas phase unoptimized (top) and solution optimized (bottom) structures for 2. Also shown are the average torsion angle between the benzene units of the benzophenone (left) and the benzophenone and urea group (right).

characterizing Band 1, such as the feature named Band 1'. Overall, such broader absorption bans could be attributed to the additional degrees of freedom of the compound in solution. In the crystal structure, the geometry of the linear analog is constrained and forces each part of the benzophenone unit to act independently. This gives rise to more uncoupled excitations from the single chromophores that form the analogue which contributes to the fine structure visible in the experimental absorption in the solid state. In the solution case on the other hand, the freedom of motion gained allows the linear analog to orient itself to where both benzenes can participate in the excitation of the π bands resulting in a loss of independent chromophores and therefore a loss of fine structure.

A.4.2 Linear Analog 2

In addition to LA 1, the absorption spectra for LA 2 were measured as well. LA 2 varies from LA 1 in that the connection to the methylene urea connector is through the *meta* position instead of the *para* position on the benzophenone units with respect to the carbonyl (Figure A.1). LA 2 is also different in that in the solid state one benzophenone has a 'curved' orientation compared to the urea while the other is 'straight' orientation similar to LA 1. This gives the linear analog much less overall symmetry than LA 1 making more difficult to work with. Just like for LA 1 different slices of linear analog 2's crystals structure were taken to see if any pieces were indicative of the whole (Figure A.2). For this the following slices were taken: the full linear analog connected through the methylene urea spacer, one half of the linear analog with the 'curved' orientation, two 'curved' half pieces hydrogen bonding to each other through the urea moiety, one half of the linear analog which had the 'straight' orientation, and two 'straight' half pieces hydrogen bonding to each other through the urea moiety. Because of the more complicated crystal structure no adjacent slices were taken as there were too many combinations for this study (unlike for LA 1).

The computed absorption spectra for all the model systems considered for this analog, roughly gave the same shape, with two intense absorption bands (Band 1 and Band 2) raised by $\pi \rightarrow \pi^*$ transitions. Also, for this analog, the lowest excited state is the $n \rightarrow \pi^*$ transition, which is again a dark state.

For the two half pieces (curved [C-Half] and straight [S-Half]), Band 2 is now more intense than Band 1, which is the opposite of the previous analog. The main contribution

to Band 1 is a $\pi \rightarrow \pi^*$ transitions involving the entirety of the benzophenone unit (Figure A.7). The main difference in this band between the two model systems is that while for S-Half the band is raised by a single excitation; the C-Half has many contributions from several excitations which also results in a slightly broader absorption peak. In contrast to Band 1, Band 2 for the C-Half is generated by a single major excitation while for the S-Half model has two main excitations contributing to its band. The two halves models also differ in the Band 2 excitation because the S-Half has much more n character in its occupied NTOs compared to the C-Half (Figure A.7). When comparing to the experimental data it can be seen that the intensities of Bands 1 and 2 are flipped in the calculations and that the peaks are blue shifted (for Band 1 blue-shifts are 131 and 135 nm for C-Half and S-Half, respectively). This is likely due to the gas phase issues again. Additionally, it may be that in this case the calculations may be over-estimating the higher energy absorption peaks as well.

Stacking via hydrogen bonding for both halves resulted in very similar results. The first band of the spectra (Band 1), in both cases is raised by local excitations confined on one of the half pieces. Band 2 on the other hand presents some contributions from excited states with charge transfer (CT) character, as clearly visible by the NTOs reported in Figure A.8. The CT descriptor available from the wavefunction analysis performed with TheoDore has a value of 0.2 for this bright transition contributing to the absorption band. Other states presented higher CT numbers but those are dark states and therefore not included in this discussion. Unfortunately, further description of this second band of the spectrum suffers from the limited number of excited states calculated. It would be

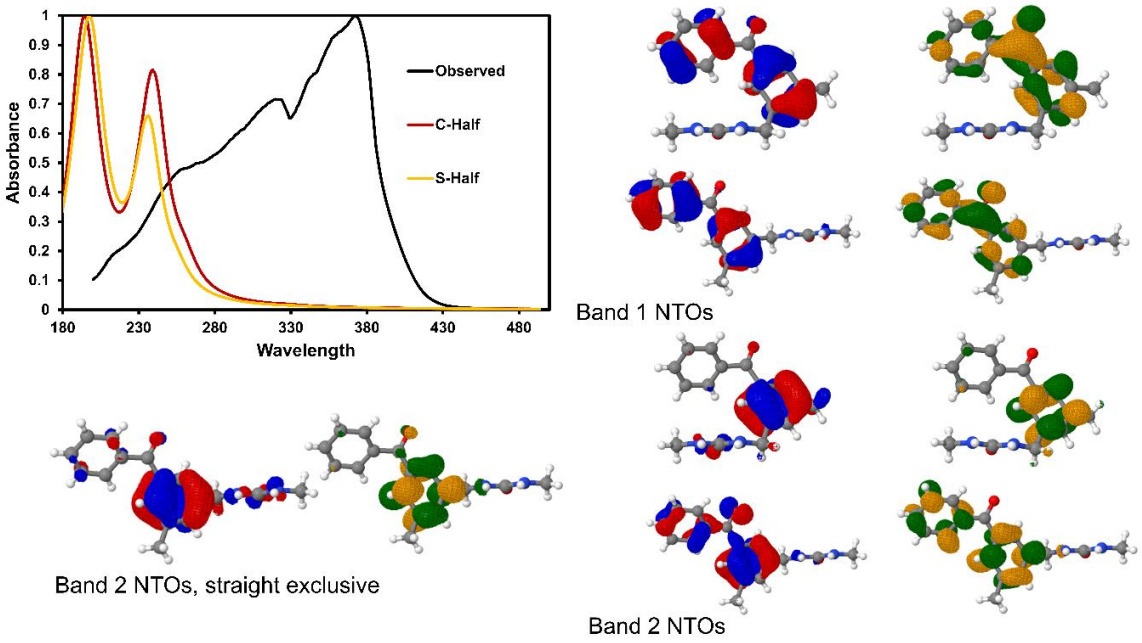

Figure A.7. Comparison between the two halves of LA 2. In the top left are the experimental and unshifted computed spectrum for the LA. Everywhere else, are the prominent NTOs corresponding to excited states that make the additional absorption maxima seen for the C-Half and S-Half. In the top right are the NTOs responsible for Band 1 for both halves. On the bottom, are the NTOs responsible for Band 2. The S-Half has an extra set NTOs corresponding to another major excitation for this band.

interesting for future work to increase the number of states as well as the number of stacked analog to consider exciton states.

Similar to LA 1, the comparison between the absorption in solution and solid state (crystal), the full LA was used. Also similar to LA 1, Band 1 of the calculated solution spectrum is blue-shifted by 5 nm with respect to the experimental solution spectrum which itself is blue-shifted by 116 nm compared to the experimental solid-state absorption. The

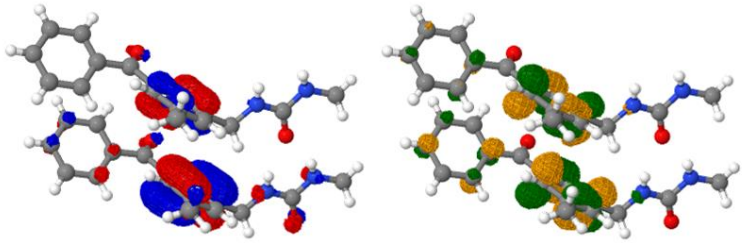

Figure A.8. NTOs for interesting excitation for the Stacked S-Half LA. The NTOs for this excitation correspond to the major excitation in Band 2 for the Stacked S-Half.

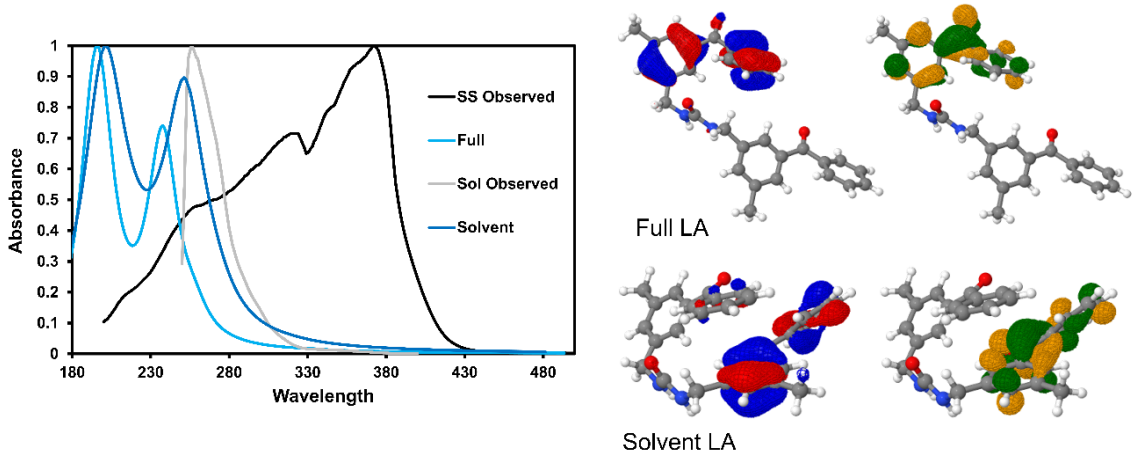

Figure A.9. Comparison between full and solvent LAs. On the left are the experimental and unshifted computed spectra, on the right are the prominent NTOs for Band 1 for both calculations.

gas phase calculation (which used the crystal geometry) is blue-shifted compared to the solid-state absorption by 135 nm. Both calculations and the experimental solution absorption lack the fine features seen for the solid-state absorption. For the geometry optimization in solution, LA 2 bended on itself to make an apparent π-π stacking between the two benzophenone units. Despite this, the NTOs for the major excitation in Band 1 are almost identical to that of the gas phase calculation. This is opposite from LA 1 in which the solution calculation had different occupied NTOs than the gas phase calculation. This may help explain why in the solid-state LA 1 and LA2 have different photophysical characteristics in their experimental data.

A.5 CONCLUSIONS

In conclusion, the absorption spectra for two different compounds containing benzophenones units separated by a methylene spacer were calculated. This included also a small benchmark of the computational method on half of the moieties forming the analogs. Different slices form the crystal structure were afterwards considered to identify

the most important moieties contributing to the absorptions of these compounds. The full linear analog absorption spectra were computed both in gas phase (using crystal geometry) and in solution (using a geometry optimization) to identify the origin of the different absorptions observed experimentally in solution and the solid-state. In all computed spectra, the excitations contributing to the absorption bands were analyzed through the examination of the main natural transition orbitals and the charge transfer descriptors to distinguish local excitations to charge transfer ones. We have found in most of the cases the excitations are local.

The origin of the different absorption spectra in the two different conditions for LA 1 were attributed to structural rearrangement experience by the compound in solution, where it is no longer constrained by the periodicity of the crystal structure. This is also the reason why the absorption peak in solution is broader and does not present any fine features. For LA 2, none of the pieces gave spectra that matched the experimental data well. It could be for this LA that TDDFT over estimates the higher energy transitions. As for the orbitals both the solution and solid-state NTOs were very similar.

When comparing the two LAs as a whole it can be seen that the NTOs that make the major transitions between the two LAs appear to be slightly different. While for LA 2 the NTO for Band 1 is a $\pi \rightarrow \pi^*$ transition which includes the entire benzophenone unit, for LA 1 it only includes one half of the benzophenone. This could help explain why LA 1 and LA 2 exhibit different behavior in the solid-state. Overall, these calculations give a basis of where some of the photophysical properties of these linear analogs derive.

A.6 REFERENCES

1. Griesser, M.; Rosspeintner, A.; Dworak, C.; Höfer, M.; Grabner, G.; Liska, R.; Gescheidt, G. *Macromolecules* **2012**, *45*, 8648-8657.
2. Tehfe, M.-A.; Dumur, F.; Graff, B.; Morlet-Savary, F.; Fouassier, J.-P.; Gigmes, D.; Lalevée, J. *Macromolecules* **2012**, *45*, 8639-8647.
3. Lim, K. S.; Oh, K. W.; Kim, S. H. *Polym. Int.* **2012**, *61*, 1519-1524
4. Dhende, V. P.; Samanta, S.; Jones, D. M.; Hardin, I. R.; Locklin, J. *ACS Appl. Mater. Interfaces* **2011**, *3*, 2830-2837.
5. Marin, M. L.; Santos-Juanes, L.; Arques, A.; Amat, A. M.; Miranda, M. A. *Chem. Rev.* **2012**, *112*, 1710-1750.
6. Geer, M. F.; Walla, M. D.; Solntsev, K. M.; Strassert, C. A.; Shimizu, L. S. *J. Org. Chem.* **2013**, *78*, 5568-5578.
7. Dewal, M. B.; Xu, Y. W.; Yang, J.; Mohammed, F.; Smith, M. D.; Shimizu, L. S. *Chem Commun* **2008**, 3909-3911.
8. DeHaven B. A.; Tokarki, J. T.; Korous, A. A.; Mentink-Vigier, F.; Makris, T. M.; Brugh, A. M.; Forbes, M. D. E.; van Tol, J.; Bowers, C. R.; Shimizu, L. S. *Chem. Eur. J.* **2017**, *23*, 8315-8319.
9. Barash, L.; Wasserman, E.; Yager, W. A. *J. Am. Chem. Soc.* **1967**, *89*, 3931-3932.
10. Lin, T.-S. *J. Chem. Phys.* **1972**, *57*, 2260-2264.
11. Dreuw, A.; Wormit, M. *Wiley Interdiscip. Rev. Comput. Mol. Sci.* **2015**, *5*, 82-95.
12. Hellweg, A.; Rappoport, D. *Phys. Chem. Chem. Phys.* **2015**, *17*, 1010-1017.
13. Chai, J.-D.; Head-Gordon, M. *Phys. Chem. Chem. Phys.* **2008**, *10*, 6615-6620.
14. Ditchfield, R.; Hehre, J. W.; Pople, J. A. *J. Chem. Phys.* **1971**, *54*, 724-728.

15. Plasser, F.; Bäppler, S. A.; Wormit, M.; Dreuw, A. *J. Chem. Phys.* **2014**, *141*, 024107-024112.
16. Mennucci, B. *Wiley Interdiscip. Rev. Comput. Mol. Sci.* **2012**, *2*, 386-404.
17. Koch, W.; Holthausen, M. C. *A Chemist's Guide to Density Functional Theory*. Wiley-VCH: Weinheim, 2001.
18. Casida, M.; Huix-Rotllant, M. *Annu. Rev. Phys. Chem.* **2012**, *63*, 287-323.
19. Dierksen, M.; Grimme, S.; *J. Chem. Phys.* **2004**, *120*, 3544-3554.
20. Dreuw, A.; Weisman, J. L.; Head-Gordon, M. *J. Chem. Phys.* **2003**, *119*, 2943-2946.
21. Harbach, P. H. P.; Dreuw, A. *Modeling of Molecular Properties*. Wiley-VCH: Weinheim, 2011.
22. Ridley, J. E.; Zerner, M. C. *Theor. Chim. Acta* **1973**, *32*, 111-134.
23. Fetter, A. L.; Walecka, J. D. *Quantum Theory of Many-Particle Systems*. McGraw Hill: New York, 1971.
24. Dickoff, W. H.; van Neck, D. *Many-Body Theory Exposed!: Propagator Description of Quantum Mechanics in Many-Body Systems*. World Scientific: Singapore, 2005.
25. Dreuw, A.; Wormit, M. *Comput. Mol. Sci.* **2015**, *5*, 82-95.

APPENDIX B

SYNTHESIZING CHIRAL MACROCYCLES AND USING THE BORROWING HYDROGEN STRATEGY TO FORM UREA BRIDGED MOLECULES

B.1 INTRODUCTION

The borrowing hydrogen (BH) strategy is a powerful tool that combines hydrogen transfer with intermediate reactions to form more complex molecules in one step. The key in this strategy is it avoids the direct use of molecular hydrogen with the added benefit of reducing the number of steps in a synthetic procedure. This method finds uses in the activation of alkanes, alcohols, and amines for the formation of new C-C and C-N bonds.[1] For the activation of alcohols, the BH strategy is used for Aza-Wittig reactions,[2] the amination of alcohols to form either primary[3] or higher order amines (Figure B.1a),[4,5] and heterocyclization.[6] For the amination of alcohols to higher order amines, reactions are ran in anaerobic conditions although high yields can be found in aerobic conditions with the right systems.[7,8] For the latter, molecular oxygen converts the alcohol to the corresponding aldehyde speeding up the rate limiting step. These systems have the ability to *N*-alkylate amides in high yields. This type of alkylation is usually harder due to the nitrogen being less activated in an amide versus a normal amine. This reaction works under anaerobic systems too, but again it is much less common due to the deactivation of the amine.[9] A potential use for these systems is the ability to reduce the number of reactions in a synthetic scheme. In the Shimizu group, we make *bis*-urea macrocycles which include a bromine substitution step to form the cycles as the key step.[10] The BH strategy gives the option of skipping the bromination step and employing the alcohol instead. Although the BH strategy for ureas is rare compared to regular amines, it has been employed. Examples include the formamide/alcohol[11] and mono-substituted urea/alcohol[12] coupling to form di-substituted ureas. Unfortunately, ureas can also act as an ammonia surrogates to form an upwards of tri-substituted amines from alcohol couplings.[13]

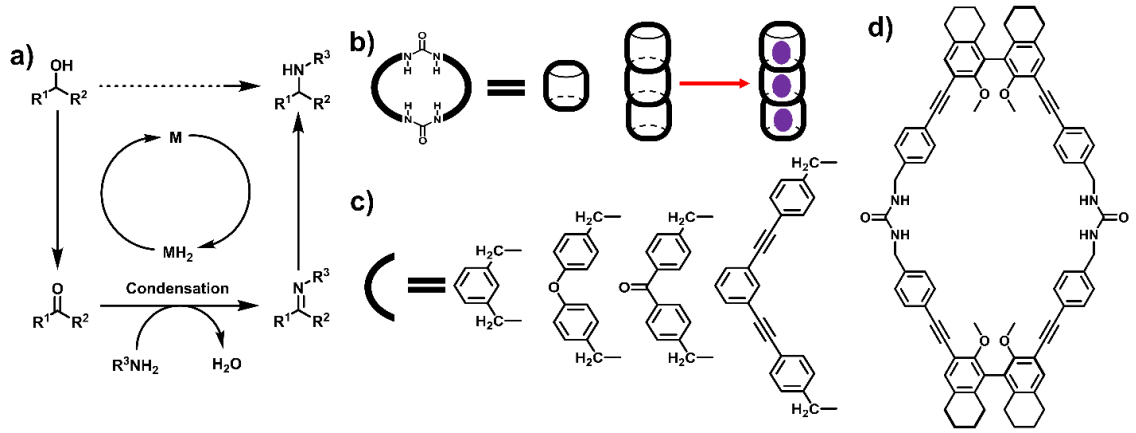

Figure B.1. BH strategy and *bis*-urea macrocycles. (a) Catalytic condensation using the BH strategy for the *N*-alkylation of amines using alcohols. (b) Macrocycles are made from two ureas and two C-shape spacers, which self-assemble into straws (or channels) which can uptake small guests. (c) Examples of C-shape spacers. (d) A chiral *bis*-urea macrocycle using a *R*-BINOL derivative as the chiral C-shape spacer.

Chiral *bis*-urea macrocycles are of interest to the Shimizu group. Typically, our group makes macrocycles from two urea groups and two C-shape spacers which connect the macrocycle together (Figures B.1b and c).[10] The urea groups assemble through a three centered urea hydrogen bond interaction aligning the macrocycles into 1D columns in the solid-state. The C-shape spacers help define the features of the column including size (small or large channel), internal polarity, and functionality as in the case with benzophenones.[14] Another feature could be handedness, or chirality of the channel.

Typically, chiral nanochannels find applications in the electronics industry where they define properties such as magnetochiral dichroism, magnetic skyrmions, and nonreciprocal carrier transport in conductors.[15-17] Channels are usually made from chiral macrocycle precursors.[18] Although new electronic materials are not currently our goal, we are interested in how chirality would affect the nanotubes ability load guests and act as a photochamber for photoreactions of small molecules. Typically, we use our macrocycles

as photochambers (or hosts) to promote the selectivity in photoreactions for small molecules.[19,20] We are interested the handedness of the channel would influence the photoreactivity and modulate the product selectivity. Our approach targets chiral BINOL precursors as building blocks for chiral *bis*-urea macrocycles (Figure B.1d). Then we will crystallize the macrocycle to afford columnar assemblies with accessible channels to examine the before mentioned properties.

In order to examine the feasibility of the BH strategy to minimize the number of steps in the formation *bis*-urea macrocycles and the possibility for forming chiral macrocycles the following methods will be employed. Firstly, benzyl alcohol will be coupled to amide and urea derivatives using a catalyst supplied by the Hultzsch group (Figure B.2) to methodically derive an ideal system for the formation of macrocycles. This will help eliminate a step in the synthesis of these macrocycles. Secondly, precursors for the formation of the chiral macrocycles derived from both *R* and *S* BINOL will be synthesized. This will supply materials necessary to form chiral macrocycles.

B.2 CATALYSIS BACKGROUND

As seen in Figure B.1a the BH strategy is a three-step reaction that results in the loss of water. These steps include the oxidation of the substrate, imine formation, and reduction of the imine. As its name indicates, the catalyst in this system 'borrows' a hydrogen from the substrate and 'returns' it later eliminating the need for molecular hydrogen being added to the system. For the amination of alcohols, direct condensation is highly unfavorable. However, the alternative route the BH strategy allows lets the condensation to carry forward. In the activation step a catalyst removes an equivalent of

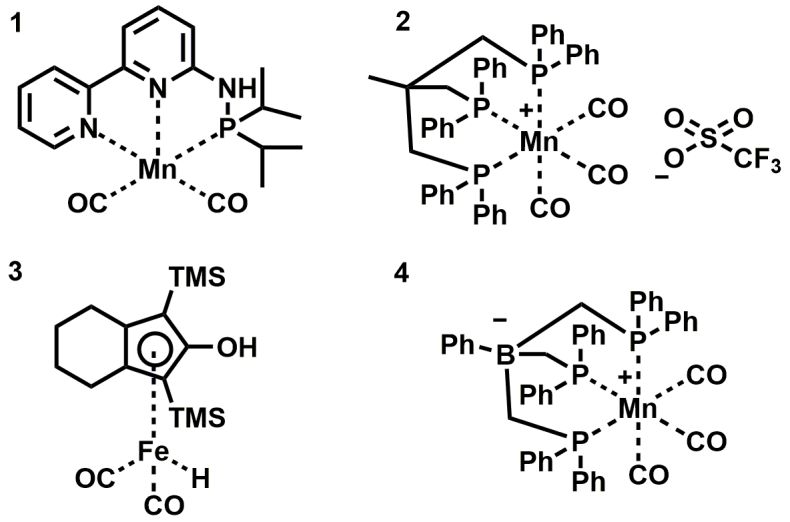

Figure B.2. Catalysts supplied by the Hultzsch group.

hydrogen from the substrate oxidizing the alcohol to its corresponding aldehyde. This is typically the rate limiting step in these reactions. Next, the favorable imine formation from the reaction of an aldehyde (or ketone) with an amine can occur resulting in the loss of water. This imine can then be reduced by the 'borrowed' hydrogen resulting in alkylated amine product. This strategy has the benefit of being atom efficient, green (only side-product is water), and time efficient (cuts out additional synthetic steps). Unfortunately, this reaction usually requires high temperatures, may have unselective activation (alpha carbons), and the catalyst may interact with the reagents in an undesirable way (side reactions).

In comparison to other methods the BH strategy stands out. Reductive amination is usually done at lower temperatures, but there is a net loss in the oxidation state of the substrate and requires toxic reagents. Substitution reactions tend to have higher yields, but an appropriate substrate with a leaving group must be synthesized. This results in a stoichiometric amount of byproducts. The Mitsunobu reaction exhibits the same net reaction as a BH reaction, but also forms stoichiometric byproducts and is restricted to

specific nucleophiles. Once issues with regioselectivity are addressed, the BH strategy may become the best option for *N*-alkylation of amines.

B.3 RESULTS

B.3.1 Catalysis

Our first study was to determine which catalyst system was best suited for amide or urea coupling with benzyl alcohol. This was done by investigating the four Hultzsch group catalyst systems with their idealized protocols and examining their activity to couple acetamide with benzyl alcohol to form *N*-benzylacetamide. An aerobic palladium reaction was used as a control with established coupling conditions.[8] As seen in Table B.1, only **1** and the control produced the desired product. The two exhibited the same yield of N-benzylacetamide at 13%. Interestingly, both of these systems produced an alpha substituted product as well in similar yields. This set of reactions was our starting point for the following examinations.

Table B.1. Initial Reactions for Amide/Alcohol Coupling.

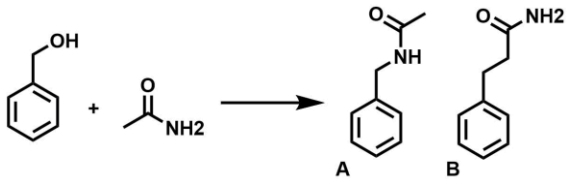

Catalyst Conditions*	Yield for A (%)	Yield for B (%)
1	13	15
2	0	0
3	0	0
4	0	0
Control*	13	11

*Conditions varied by catalyst depending on the catalyst's ideal protocol.

To create better conditions for the coupling reaction of benzyl alcohol and acetamide, **1** was chosen for further optimization. Four new conditions probed with the

first running the reaction neat with an excess of acetamide. This resulted in a slightly higher yield of 21% for A and a lower yield for B at 13%. Next, two reactions were set up with diglyme instead of dimethoxyethane as the solvent. This allowed the reactions to be run at higher temperatures (150˚C versus 120˚C) while still using a non-cyclic ether as the solvent. The difference between these reactions was the base used which was either potassium hydride or potassium *tert*-butoxide. This resulted in B as the only product at 44% and 40%, respectively. Seen here, the stronger base gave the product in higher yield. To check reaction feasible, the back half of the reaction was set up with benzaldehyde and acetamide only. It was found that only a 28% yield could be obtained. From this it is was concluded that acetamide was a poor candidate for reaction optimization since even in the most ideal conditions yields were poor. Interestingly, very few catalysts made for amide/alcohol coupling ever use acetamide as a coupling partner. In one of the few cases in which it was reported, the maximum yield was 45%.[9]

Table B.2. Reaction optimizations for acetamide substrates.

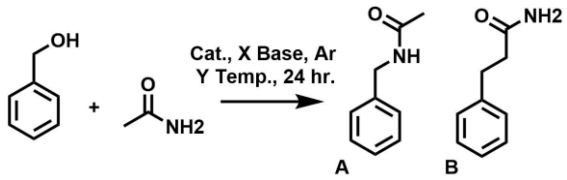

Trial	Yield for A (%)	Yield for B (%)	Base	Temperature (°C)	Solvent
1	21	13	KH	120	DME
2	0	44	KH	150	Diglyme
3	0	40	KO-*t*Bu	150	Diglyme
4	28	0	$NaBH_4$	rt	Acetic Acid

*This reaction is significantly different than the others. General conditions are as follows. Aldehyde, 20 eq. amide, and 1.5 eq. TMSCl were dissolved in acetic acid and stirred overnight. 1.5 of $NaBH_4$ were added in the morning. A GC-MS was taken after TLC showed no presence of aldehyde (~1 hour).

Because the alpha carbon substitution was competing with the amine substitution, three urea analogs were next studied. These structures substitute the alpha carbon position from carbonyl to nitrogen. Additionally, this answers the question of whether or not the urea is going to act as an ammonia surrogate or act as a whole unit. The urea analogs chosen include urea (control), tetrahydropyrimidin-2(1*H*)-one (cyclic urea derivative), and 5-(*tert*-butyl)-1,3,5-triazian-2-one (urea derivative used in macrocycle synthesis). In the former two cases none of the desired product was observed. Analysis of the GC-MS fragments indicated that the urea ring systems were severed under the *N*-alkylation conditions. This indicates that either the urea is acting as an ammonia surrogate or activated alpha carbons are forming next to the urea nitrogens, both of which pose critical problems for this system. This suggests that this system would be a poor candidate for macrocycle synthesis. For unsubstituted urea, a 35% yield was found. Likely, additional optimization could increase this yield, but due to time constraints this was not further optimized. Overall, these studies indicate that the BH strategy could be employed for macrocycle synthesis, but the *bis*-urea macrocycle would have to be made directly from the urea instead of protected urea.

Table B.3. Reactions with urea spacers.

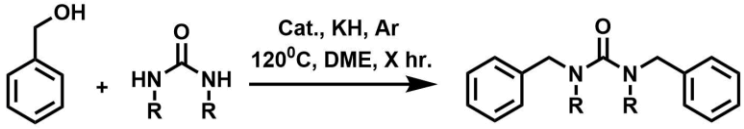

Urea Analog	Yield (%)	Time (h)
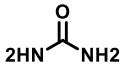	35	72
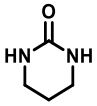	0	24
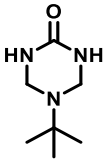	0	24

As both acetamide and ureas were poor analogs for the BH strategy using **1**, benzamide was chosen for future studies since it is more commonly used in this reaction. As Table B.4 indicates, benzamide gave much more favorable yields than its counterparts. Next, we tried to optimize base reagent used. The strongest base, potassium hydride gave the best yield at 71%, followed by potassium *tert*-butoxide at 67% then tribasic potassium phosphate at 57% which was the weakest of the bases. Next, we investigated longer reaction times. Unfortunately, this only increased the yield by 2% to 73% overall. Due to time constraints, this reaction could not be further optimized. Future work would likely include changing catalyst loading, equivalents of base, solvent, temperature, and using other benzamide analogs. Already, this reaction compares favorably with the literature (75%)[8], (83%)[9], (90%)[7], and (99%)[7] with the latter of these two using rare metals in rhodium and iridium. Further optimization of this reaction would likely put it among the best catalytic systems as the unoptimized conditions already compare very favorably.

Table B.4. Reactions with benzamide.

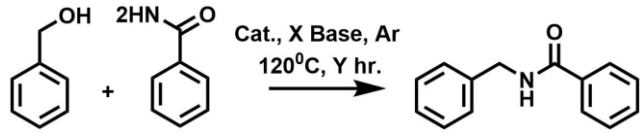

Trial	Yield (%)	Base	Time (h)
1	71	KH	24
2	67	KO-*t*Bu	24
3	57	K_3PO_4	24
4	73	KH	72

B.3.2 Chiral Macrocycles

As Figure B.3 indicates we wanted to make *R* and *S* BINOL derivatives as chiral macrocycle precursors. The plan of study was to make **R3** and **S3** in Vienna and complete the macrocycle in South Carolina. The precursors were made as planned and were shipped off to South Carolina for further synthetic work. The steps performed in Vienna include

reducing the back half of the BINOLs to allow for the preferred iodination at the *ortho* positions to the alcohols. Then the alcohols were alkylated into ethers to prevent side reactions further on in the synthesis. The planned steps to be performed in South Carolina include the Sonagashira coupling of ethynylenebenzyl alcohol to the BINOL derivatives, the bromination of the free alcohols, cyclization with 5-(*tert*-butyl)-1,3,5-triazian-2-one, and the deprotection of the protected ureas. Crystallization of the final product will indicate if chiral channels will be formed, allowing for the further work of studies in photoreactivity and absorption spoken of in the introduction to take place.

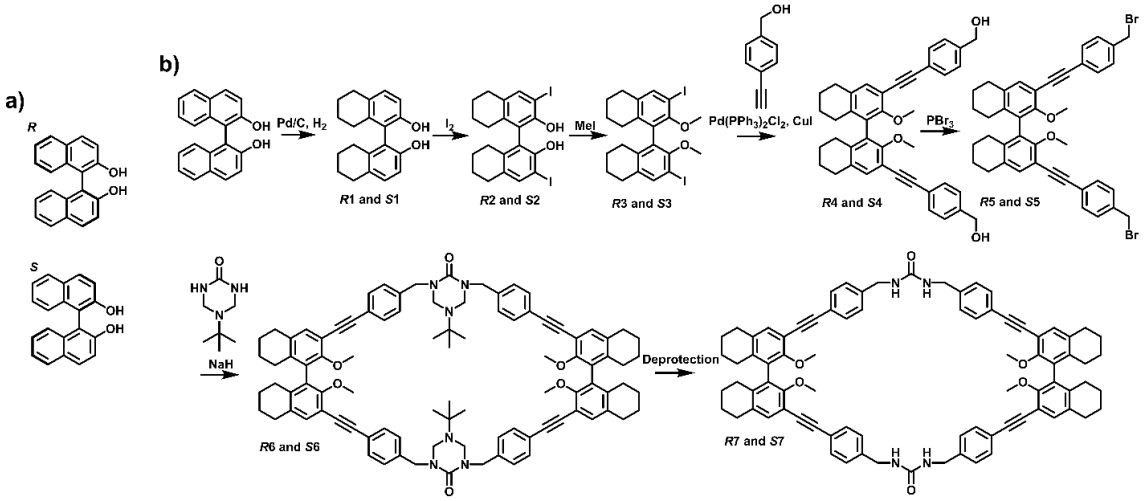

Figure B.3. Plan for making chiral macrocycles. (a) BINOL derivatives from which the macrocycles are made. (b) Synthetic scheme for the macrocycles.

B.4 CONCLUSIONS

In conclusion, a BH strategy was used to couple different amide and urea derivatives with benzyl alcohol and chiral macrocycle precursors were made. It was seen that **1** was the best catalyst for this reaction and that benzamide was the best amide surrogate for the BH strategy as it only produced the desired product. This reaction compared favorably to previous literature even before optimization. Further optimization

would likely put it among the best. Unfortunately, for acetamide and urea derivatives not as much luck was found as alpha carbon activation was a stressing issue. For the chiral macrocycles, the desired precursors were made and shipped off to South Carolina.

B.5 EXPERIMENTAL DETAILS

Catalysis for **1** in General: Under an Argon atmosphere, potassium hydride (0.5 eq.) and amide (1.1 eq.) were added to a 1 mL vial. Then benzyl alcohol (0.5 mmol) was added dropwise. A catalyst solution was added after (0.025 eq. in 100 μL of DME) and the vial was sealed. The sealed vial was heated at 120˚C for 24 hours and was cooled to room temperature. An internal standard of 100 μL of *p*-xylene was added followed by the addition of 0.5 mL of water. After mixing for 5 minutes, the solution was extracted with ethyl acetate (3 × 0.5 mL) and was put on the GC column for yield analysis.

Catalysis for **2** in General: Under an Argon atmosphere, potassium hydride (1.0 eq.), amide (1.0 eq.), catalyst (0.05 eq.), and 100 μL of dry THF were added to a 1 mL vial. Then benzyl alcohol (0.5 mmol) was added dropwise. The sealed vial was heated at 120˚C for 24 hours and was cooled to room temperature. An internal standard of 100 μL of *p*-xylene was added followed by the addition of 0.5 mL of water. After mixing for 5 minutes, the solution was extracted with ethyl acetate (3 × 0.5 mL) and was put on the GC column for yield analysis.

Catalysis for **3** in General: Under an Argon atmosphere, potassium *tert*-butoxide (1.0 eq.), amide (1.0 eq.), catalyst (0.05 eq.), and 100 μL of dry DMF were added to a 1 mL vial. Then benzyl alcohol (0.5 mmol) was added dropwise. The sealed vial was heated at 120˚C for 24 hours and was cooled to room temperature. An internal standard of 100 μL

of *p*-xylene was added followed by the addition of 0.5 mL of water. After mixing for 5 minutes, the solution was extracted with ethyl acetate (3 × 0.5 mL) and was put on the GC column for yield analysis.

Catalysis for **4** in General: Under an Argon atmosphere, amide (0.25 mmol), catalyst (0.05 eq.), molecular sieves, and 100 μL of dry toluene were added to a 1 mL vial. Then benzyl alcohol (10 eq.) was added dropwise. The sealed vial was heated at 120˚C for 24 hours and was cooled to room temperature. An internal standard of 100 μL of *p*-xylene was added followed by the addition of 0.5 mL of water. After mixing for 5 minutes, the solution was extracted with ethyl acetate (3 × 0.5 mL) and was put on the GC column for yield analysis.

Control Catalysis in General:[8] Alcohol (6.0 eq.), amide (0.5 mmol), $Pd(OAc)_2$ (0.05 eq.), and potassium carbonate (1.0 eq.) were added to a 5 mL flask. This mixture was heated to 180˚C for 36 hours. After cooling, the reaction was quenched with ethyl acetate, and an internal standard of 100 μL of *p*-xylene was added. This mixture was put on the GC column for yield analysis.

***R*1:** This compound was made according to previous procedures.[21] *R*-BINOL (2.0000 g, 6.99 mmol), 10% Pd/C (0.5000 g), 20 mL of absolute ethanol were added to a 50 mL autoclave and was stirred under 60 bar H_2 at 70˚C for 16 hours. After cooling, the Pd/C was filtered off and was washed with ethyl acetate (5 mL). The combined filtrate was concentrated via rotary evaporation leaving behind the white solid (91%). Spectra matched that as previously recorded.[22] ^{1}H NMR (400 MHz, $CDCl_3$): δ (ppm) 7.07 (d, J = 8.3 Hz,

2H), 6.83 (d, *J* = 8.3 Hz, 2H), 4.53 (s, 2H), 2.78-2.72 (m, 4H), 2.35-2.11 (m, 4H), 1.78-1.63 (m, 8H).

***S*1:** This compound was made according to previous procedures.[23] *R*-BINOL (2.0000 g, 6.99 mmol), 10% Pd/C (0.5000 g), 20 mL of absolute ethanol were added to a 50 mL autoclave and was stirred under 60 bar H_2 at 70˚C for 16 hours. After cooling, the Pd/C was filtered off and was washed with ethyl acetate (5 mL). The combined filtrate was concentrated via rotary evaporation leaving behind the white solid (81%). The spectra matched that as previously recorded.[23] ^{1}H NMR (400 MHz, $CDCl_3$): δ (ppm) 7.07 (d, *J* = 8.3 Hz, 2H), 6.83 (d, *J* = 8.4 Hz, 2H), 4.53 (s, 2H), 2.79-2.72 (m, 4H), 2.35-2.11 (m, 4H), 1.79-1.64 (m, 8H).

***R*2:** This compound was made according to previous procedures.[24] ***R*1** (1.8680 g, 6.35 mmol) was dissolved in 60 mL of dry dichloromethane. Then morpholine (3.3 mL, 38.07 mmol) and iodine (3.3014 g, 13.01 mmol) were added sequentially. The solution turned red. After 5 hours of stirring at room temperature 100 mL of dichloromethance and 100 mL of 1 N HCl were added. The mixture was extracted with dichloromethane (3 × 60 mL) and was washed with saturated sodium thiosulfate (3 × 60 mL) and brine (1 × 60 mL). The organics were removed via rotary evaporation leaving behind the white solid (86%). The spectra matched that as previously recorded.[24] ^{1}H NMR (400 MHz, $CDCl_3$): δ (ppm) 7.51 (s, 2H), 4.96 (s, 2H), 2.77-2.69 (m, 4H), 2.32-2.04 (m, 4H), 1.76-1.61 (m, 8H).

***S*2:** This compound was made according to previous procedures.[24] ***S*1** (0.2500 g, 0.85 mmol) was dissolved in 7.5 mL of dry dichloromethane. Then morpholine (0.44 mL, 5.10 mmol) and iodine (0.4418 g, 1.74 mmol) were added sequentially. The solution turned

red. After 5 hours of stirring at room temperature 100 mL of dichloromethance and 100 mL of 1 N HCl were added. The mixture was extracted with dichloromethane (3 × 7.5 mL) and was washed with saturated sodium thiosulfate (3 × 7.5 mL) and brine (1 × 7.5 mL). The organics were removed via rotary evaporation leaving behind the white solid (87%). The spectra matched that as previously recorded.[25] ^{1}H NMR (400 MHz, $CDCl_3$): δ (ppm) 7.51 (s, 2H), 4.96 (s, 2H), 2.76-2.69 (m, 4H), 2.32-2.04 (m, 4H), 1.76-1.61 (m, 8H).

***R*3:** This compound was made according to previous procedures.[25] ***R*2** (2.9700 g, 5.44 mmol) was dissolved in 42 mL of acetone and was heated to 50˚C. Then potassium carbonate (2.6303 g, 19.03 mmol) and methyl iodide (2.1 mL, 19.03 mmol) were added sequentially. This reaction stirred for 24 hours then an additional amount of methyl iodide (1.0 mL) was added. After 12 more hours the reaction was cooled and 30 mL of water was added. This mixture stirred for 4 hours then was extracted with dichloromethane (3 × 50 mL). The organics were removed via rotary evaporation. Then 50 mL of THF and 50 mL of 1 N NaOH was added to the solid. This mixture stirred for 4 hours and was extracted with dichloromethane (3 × 50 mL). The organics were dried with $MgSO_4$, and were filtered. The organics were removed again via rotary evaporation leaving behind a pale yellow solid (95%). ^{1}H NMR (400 MHz, $CDCl_3$): δ (ppm) 7.56 (s, 2H), 3.50 (s, 6H), 2.79-2.71 (m, 4H), 2.33-2.03 (m, 4H), 1.77-1.60 (m, 8H). Further characterization for this compound is still required.

***S*3:** This compound was made according to previous procedures.[25] ***S*2** (2.0461 g, 3.75 mmol) was dissolved in 28 mL of acetone and was heated to 50˚C. Then potassium carbonate (1.8121 g, 13.11 mmol) and methyl iodide (1.5 mL, 13.11 mmol) were added

sequentially. This reaction stirred for 24 hours then an additional amount of methyl iodide (0.75 mL) was added. After 12 more hours the reaction was cooled and 21 mL of water was added. This mixture stirred for 4 hours then was extracted with dichloromethane (3 × 30 mL). The organics were removed via rotary evaporation. Then 30 mL of THF and 30 mL of 1 N NaOH was added to the solid. This mixture stirred for 4 hours and was extracted with dichloromethane (3 × 30 mL). The organics were dried with $MgSO_4$, and were filtered. The organics were removed again via rotary evaporation leaving behind a pale yellow solid (95%). The spectra matched that as previously recorded.[25] ^{1}H NMR (400 MHz, $CDCl_3$): δ (ppm) 7.57 (s, 2H), 3.51 (s, 6H), 2.78-2.72 (m, 4H), 2.33-2.03 (m, 4H), 1.77-1.60 (m, 8H).

B.6 REFERENCES

1. Corma, A.; Navas, J.; Sabater, M. J. *Chem. Rev.* **2018**, *118*, 1410-1459.
2. Cami-Kobeci, G.; Williams, J. M. J. *Chem. Commun.* **2004**, 1072-1073.
3. Gunanathan, C.; Milstein, D. *Acc. Chem. Res.* **2011**, *44*, 588-602.
4. Grigg, R.; Mitchell, T. R. B.; Sutthivaiyakit, S.; Tongpenyai, N. *J. Chem. Soc., Chem. Commun.* **1981**, 611-612.
5. Watanabe, Y.; Tsuji, Y.; Ohsugi, Y. *Tetrahedron Lett.* **1981**, *22*, 2667-2670.
6. Marichev, K. O.; Takacs, J. M. *ACS Catal.* **2016**, *6*, 2205-2210.
7. Liu, C.; Liao, S.; Li, Q.; Feng, S.; Sun, Q.; Yu, X.; Xu, Q. *J. Org. Chem.* **2011**, *76*, 5759-5773.
8. Yu, X.; Jiang, L.; Li, Q.; Xie, Y.; Xu, Q. *Chin. J. Chem.* **2012**, *30*, 2322-2332.
9. Das, J.; Banerjee, D. *J. Org. Chem.* **2018**, *83*, 3378-3384.
10. Shimizu, L. S.; Salpage, S. R.; Korous, A. A. *Acc. Chem. Res.* **2014**, *47*, 2116-2127.
11. Lane, E. M.; Hazari, N.; Bernskoetter, W. H. *Chem. Sci.* **2018**, *9*, 4003-4008.

12. Li, F.; Sun, C.; Shan, H.; Zou, X.; Xie, J. *ChemCatChem* **2013**, *5*, 1543-1552.

13. Yamaguchi, K.; He, J.; Oishi, T.; Mizuno, N. *Chem. Eur. J.* **2010**, *16*, 7199-7207.

14. DeHaven B. A.; Tokarki, J. T.; Korous, A. A.; Mentink-Vigier, F.; Makris, T. M.; Brugh, A. M.; Forbes, M. D. E.; van Tol, J.; Bowers, C. R.; Shimizu, L. S. *Chem. Eur. J.* **2017**, *23*, 8315-8319.

15. Rikken, G. L. J. A.; Raupach, E. *Nature* **1997**, *390*, 493-494.

16. Nagaosa, N.; Tokura, Y. *Nat. Nanotechnol.* **2013**, *8*, 899-911.

17. Naaman, R.; Waldeck, D. H. *Annu. Rev. Phys. Chem.* **2015**, *66*, 263-281.

18. Nitti, A.; Pacini, A.; Pasini, D. *Nanomaterials* **2017**, *7*, 167-189.

19. Dawn, S.; Salpage, S. R.; Koscher, B. A.; Bick, A.; Wibowo, A. C.; Pellechia, P. J.; Shimizu, L. S. *J. Phys. Chem. A* **2014**, *118*, 10563-10574.

20. Yang, J.; Dewal, M. B.; Profeta, S. J.; Smith, M. D.; Li, Y.; Shimizu, L. S. *J. Am. Chem. Soc.* **2008**, *130*, 612-621.

21. Huang, H.; Liu, X.; Zhou, L.; Chang, M.; Zhang, X. *Angew. Chem., Int. Ed.* **2016**, *55*, 5309-5312.

22. Takasaki, M.; Motoyama, Y.; Yoon, S.-H.; Mochida, I.; Nagashima, H. *J. Org. Chem.* **2007**, *72*, 10291-10293.

23. Wang, P.; Liu, Y.; Zhang, Y.-L.; Da, C.-S. *Chirality* **2017**, *29*, 443-450.

24. Pousse, G.; Devineau, A.; Dalla, V.; Humphreys, L.; Lasne, M.-C.; Rouden, J.; Blanchet, J. *Tetrahedron* **2009**, *65*, 10617-10622.

25. Brenet, S.; Minozzi, C.; Clarens, B.; Amiri, L.; Berthiol, F. *Synthesis* **2015**, *47*, 3859-3873.

APPENDIX C

PERMISSION TO REPRINT CHAPTER 2

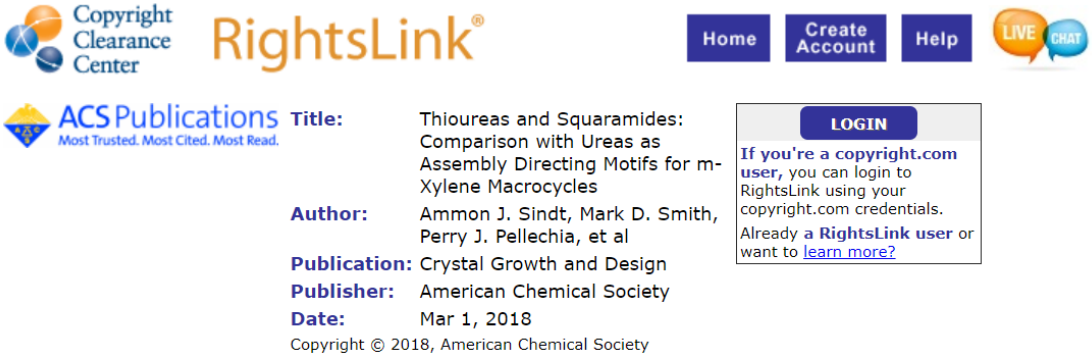

Copyright Clearance Center RightsLink®

Home | Create Account | Help | LIVE CHAT

ACS Publications
Most Trusted. Most Cited. Most Read.

Title: Thioureas and Squaramides: Comparison with Ureas as Assembly Directing Motifs for m-Xylene Macrocycles

Author: Ammon J. Sindt, Mark D. Smith, Perry J. Pellechia, et al

Publication: Crystal Growth and Design

Publisher: American Chemical Society

Date: Mar 1, 2018

Copyright © 2018, American Chemical Society

LOGIN

If you're a copyright.com user, you can login to RightsLink using your copyright.com credentials.

Already **a RightsLink user** or want to learn more?

PERMISSION/LICENSE IS GRANTED FOR YOUR ORDER AT NO CHARGE

This type of permission/license, instead of the standard Terms & Conditions, is sent to you because no fee is being charged for your order. Please note the following:

- Permission is granted for your request in both print and electronic formats, and translations.
- If figures and/or tables were requested, they may be adapted or used in part.
- Please print this page for your records and send a copy of it to your publisher/graduate school.
- Appropriate credit for the requested material should be given as follows: "Reprinted (adapted) with permission from (COMPLETE REFERENCE CITATION). Copyright (YEAR) American Chemical Society." Insert appropriate information in place of the capitalized words.
- One-time permission is granted only for the use specified in your request. No additional uses are granted (such as derivative works or other editions). For any other uses, please submit a new request.

APPENDIX D

PERMISSION TO REPRINT CHAPTER 3

Sindt, A. J.; DeHaven, B. A.; McEachern, D. F.; Dissanayake, D. M. M. M.; Smith, M. D.; Vannucci, A. K.; Shimizu, L. S. *Chem. Sci.* **2019**, *10,* 2670-2677. Published by The Royal Society of Chemistry.

The following excerpt was taken the Royal Society of Chemistry's website.[1]

Author reusing their own work published by the Royal Society of Chemistry

You do not need to request permission to reuse your own figures, diagrams, etc, that were originally published in a Royal Society of Chemistry publication. However, permission should be requested for use of the whole article or chapter except if reusing it in a thesis. If you are including an article or book chapter published by us in your thesis please ensure that your co-authors are aware of this.

Reuse of material that was published originally by the Royal Society of Chemistry must be accompanied by the appropriate acknowledgement of the publication. The form of the acknowledgement is dependent on the journal in which it was published originally, as detailed in 'Acknowledgements'.

1. Royal Society of Chemistry Licences, Copyrights and Permissions. https://www.rsc.org/journals-books-databases/journal-authors-reviewers/licences-copyright-permissions/ (accessed Oct 9, 2019)

APPENDIX E

PERMISSION TO REPRINT CHAPTER 4

* Sindt, A. J.; Smith, M. D.; Berens, S.; Vasenkov, S.; Bowers, C. R.; Shimizu, L. S. *Chem. Commun.* **2019**, *55*, 5619-5622. Reproduced by permission of The Royal Society of Chemistry.

The following excerpt was taken the Royal Society of Chemistry's website.[1]

Author reusing their own work published by the Royal Society of Chemistry

You do not need to request permission to reuse your own figures, diagrams, etc, that were originally published in a Royal Society of Chemistry publication. However, permission should be requested for use of the whole article or chapter except if reusing it in a thesis. If you are including an article or book chapter published by us in your thesis please ensure that your co-authors are aware of this.

Reuse of material that was published originally by the Royal Society of Chemistry must be accompanied by the appropriate acknowledgement of the publication. The form of the acknowledgement is dependent on the journal in which it was published originally, as detailed in 'Acknowledgements'.

1. Royal Society of Chemistry Licences, Copyrights and Permissions. https://www.rsc.org/journals-books-databases/journal-authors-reviewers/licences-copyright-permissions/ (accessed Oct 9, 2019)

APPENDIX E

PERMISSION TO REPRINT APPENDIX A

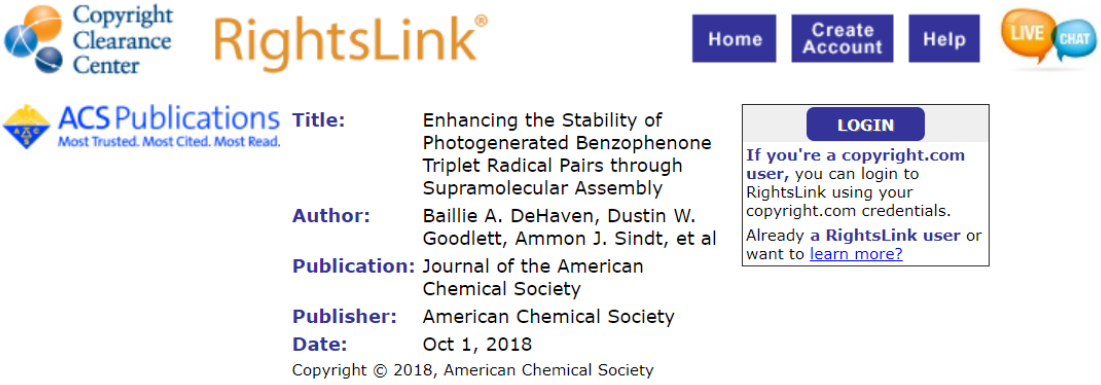

Copyright Clearance Center RightsLink®

Home | Create Account | Help | LIVE CHAT

ACS Publications
Most Trusted. Most Cited. Most Read.

Title: Enhancing the Stability of Photogenerated Benzophenone Triplet Radical Pairs through Supramolecular Assembly

Author: Baillie A. DeHaven, Dustin W. Goodlett, Ammon J. Sindt, et al

Publication: Journal of the American Chemical Society

Publisher: American Chemical Society

Date: Oct 1, 2018

Copyright © 2018, American Chemical Society

LOGIN

If you're a copyright.com user, you can login to RightsLink using your copyright.com credentials.

Already a RightsLink user or want to learn more?

PERMISSION/LICENSE IS GRANTED FOR YOUR ORDER AT NO CHARGE

This type of permission/license, instead of the standard Terms & Conditions, is sent to you because no fee is being charged for your order. Please note the following:

- Permission is granted for your request in both print and electronic formats, and translations.
- If figures and/or tables were requested, they may be adapted or used in part.
- Please print this page for your records and send a copy of it to your publisher/graduate school.
- Appropriate credit for the requested material should be given as follows: "Reprinted (adapted) with permission from (COMPLETE REFERENCE CITATION). Copyright (YEAR) American Chemical Society." Insert appropriate information in place of the capitalized words.
- One-time permission is granted only for the use specified in your request. No additional uses are granted (such as derivative works or other editions). For any other uses, please submit a new request.